FABRICATION OF ULTRAFINE GRAINED STEELS WITHOUT SEVERE PLASTIC DEFORMATION AND THEIR APPLICATION TO AUTOMOBILE BODY STRUCTURES(Dissertation_全文)

AUTHOR(S):

Okitsu, Yoshitaka

FABRICATION OF ULTRAFINE GRAINED STEELS WITHOUT SEVERE PLASTIC DEFORMATION AND THEIR APPLICATION TO AUTOMOBILE BODY STRUCTURES

2012

Yoshitaka Okitsu

TABLE OF CONTENTS

CHAPTER 5: APPLICATION OF ULTRAFINE GRAINED STEELS TO AUTOMOBILE BODY STRUCTURES

CHAPTER 1

INTRODUCTION

1.1 Background of this study

1.1.1 Demands for weight reduction of automobiles for decreasing CO_2 emission

Nowadays, improvement of fuel efficiency of automobiles is a very important subject, which comes from the global demands for reducing emission of greenhouse gasses such as CO_2 [1, 2]. For this purpose, not only an improvement of fuel efficiency of engines, but also reduction of body weight, rolling drag force, friction, etc. are necessary in automobiles. Figure 1.1 shows relationship between fuel efficiency and weight in commercial gasoline engine cars with various types of transmissions, including hybrid electric vehicles (driven by gasoline engine and electric motor) [1]. The weight of cars certainly affects the fuel efficiency, in other words, the CO_2 emission. On the other hand, demands for crash worthiness of automobiles in car collisions have been also increased. The crash worthiness of new cars is evaluated through various safety assessment programs in each country or area in the world [3-5]. Figure 1.2 shows examples of test modes in the car-safety assessment programs in EU, North America and Japan. Recent cars are required to satisfy various modes in the safety assessment programs, including those which are not shown in Fig. 1.2.

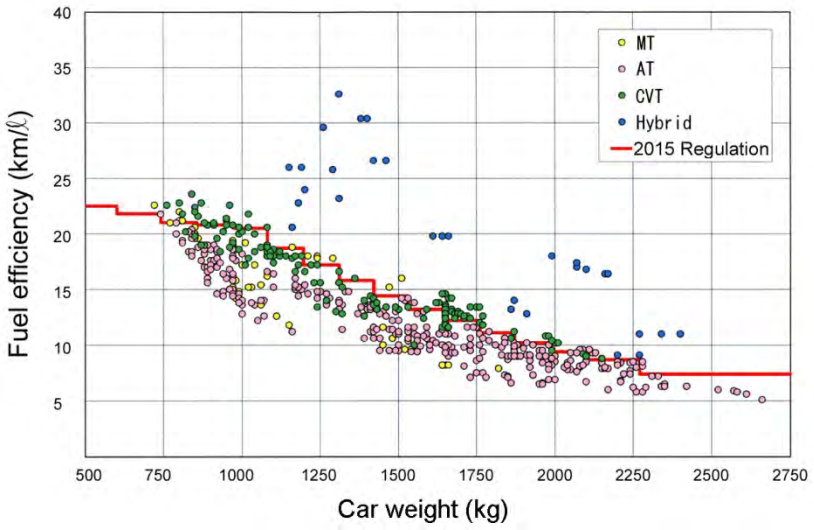

Figure 1.1 Relationship between the weight and fuel efficiency evaluated by “JC08 mode” in commercial gasoline engine cars in Japan with various types of transmissions, including hybrid electric vehicles [1]. MT, AT and CVT mean manual transmission, automatic transmission, and continuously valuable transmission, respectively.

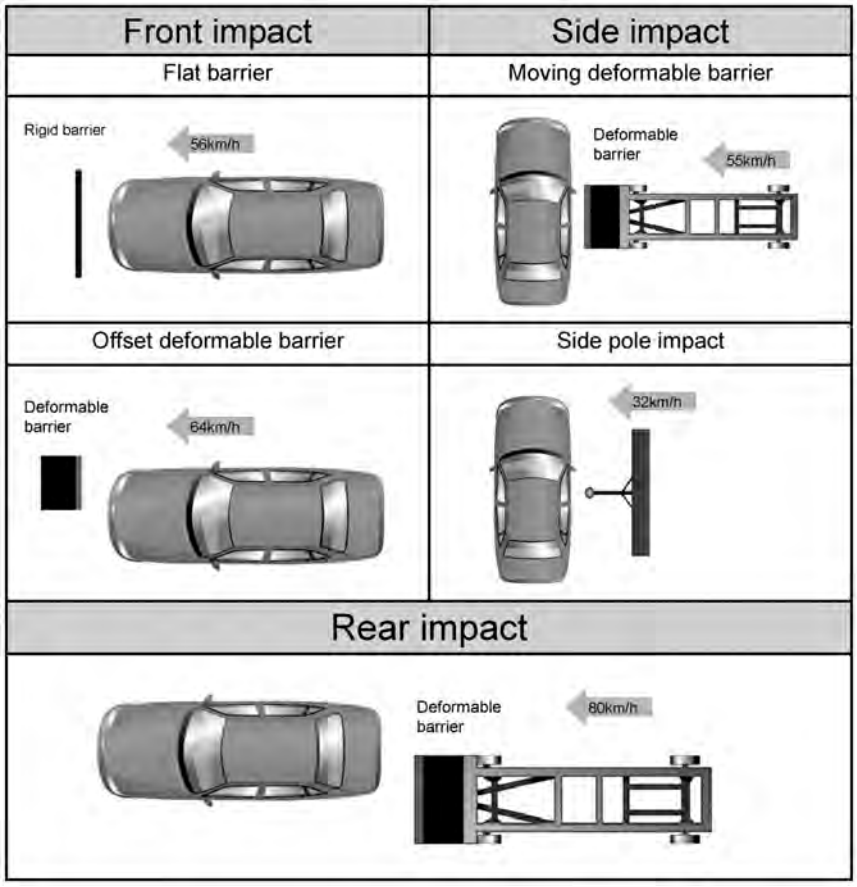

Figure 1.2 Examples of test modes in the car-safety assessment programs in EU, North America and Japan.

For improving the crash worthiness, actual body weight has increased gradually since 1990's [6]. In order to suppress the increase in body weight, considerable efforts have been carried out. Figure 1.3 shows an example for the change in body weight of commercial cars (per car projection area) and the ratio of high strength steels (HSS) among the steels applied to body structures since 1979 [6]. The application of HSS started in 1980's, due to the demands for improving fuel efficiency. The thickness of steel sheets applied to body structures was reduced by increasing strength of the steels. Therefore, the body weight gradually decreased in 1980's. The strength of the HSS applied in 1980's was not very high, for example, 440 MPa in tensile strength (it is so-called "440 MPa class"). However, significant increase in the body weight is seen in 1990's, which is due to the global demands for the crash worthiness, as mentioned before. Simultaneously the HSS ratio has been increased since 1995. Various kinds of HSS [7, 8] with higher strengths have been developed since 1990's and applied to body structures, which contributed to the suppression of the weight increase. As a result, more than 50% of body parts are made of HSS in recent cars [9]. The application of HSS, as well as the optimization of the body structure, has been contributed to the suppression of the body weight increase. The average weight of commercial cars in Japan has not been increased so much in 2000's [1], however in 2010's, due to the global demands for reducing greenhouse gasses emission, greater efforts for reducing the weight of commercial cars are required.

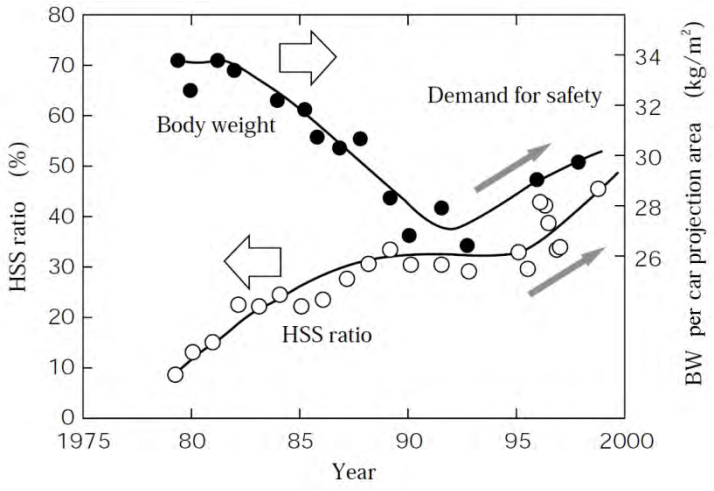

Figure 1.3 Change in car body weight per car projection area and application ratio of high strength steels (HSS) in body structures (HSS weight / whole body weight) [6].

1.1.2 Potential demands for ultrafine grained steels for automobile body structures

Low-density metals such as aluminium and magnesium have been also applied to premium or sports cars. However, steels are still widely used for various kinds of commercial cars due to their high cost performance and varieties in mechanical properties. In order to utilize the performance of steels more effectively, some projects studying lightweight steel body have been operated. One of the lightweight body projects, the ULSAB (Ultra-Light Steel Auto Body) project [10] has shown that significant weight reduction could be achieved by applying AHSS (advanced high strength steels) as well as advanced manufacturing methods, such as tailor-welded blanks (TWB: steel sheets assembled from a number of single sheets having various thickness and strength by laser welding), tubular hydroforming (forming of a metal pipe by hydro pressure applied to the inside of it) and laser-welding assembly. Such technologies in manufacturing, as well as the AHSS have been applied to actual body structures after the ULSAB project and contributed to the suppression of the weight increase of body structures. Figure 1.4 shows a picture of a prototyped body-in-white manufactured in the ULSAB project, demonstrating an optimized body structure with new manufacturing methods [10]. In the ULSAB project, various kinds of HSS were applied to more than 90 percent of the body parts, and weight reduction of 25% compared with the benchmark cars was achieved. As post-ULSAB, advanced lightweight steel bodies, which adapt to more variations of automobile safety assessments, were proposed in the ULSAB-AVC (advanced vehicle concept) project [11]. New AHSS including DP (dual-phase) steels and TRIP (transformation induced plasticity)-assisted steels were applied to the body structure in the ULSAB-AVC project. However, due to the increasing demands for improving the fuel efficiency and reducing the CO_2 emission, further weight reduction is required in recent days.

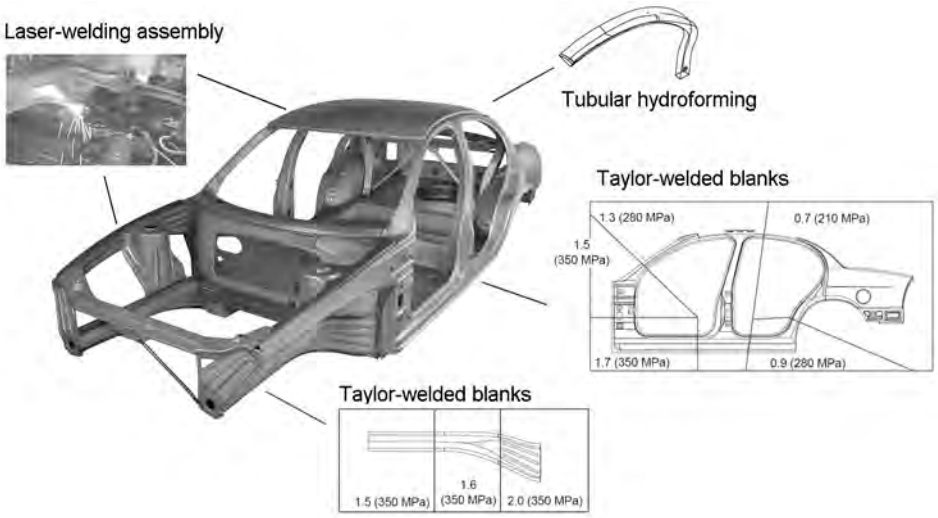

Figure 1.4 A body-in-white prototyped in the ULSAB project demonstrating a light-weight body concept with new manufacturing methods [10].

In order to achieve further weight reduction by expanding the application of HSS, new steels having new microstructures and superior properties have been widely studied [7, 8]. An example is the high-Mn TWIP (Twinning induced plasticity) steels [12, 13], which have austenite microstructures and superior combinations of tensile strength and elongation. This steel is classified as “second generation AHSS” [14]. Recent target, so-called “third generation AHSS” [14], is the steels having intermediate elongation between conventional HSS and TWIP steels but less alloying elements than the TWIP steels. Figure 1.5 shows the position of the “third generation AHSS” in a strength-elongation map. Also various types of conventional HSS and the “second generation AHSS” including austenitic steels and TWIP steels are indicated in the figure. Those new AHSS are under development in many research laboratories and steel industries. The examples for the third generation AHSS under development are the “quench and partitioning (Q-P)” steels [15, 16] which are composed of fine bainite/martensite matrix and retained austenite, and the ultrafine multi-phase steels having microstructures composed of ferrite matrix and hard second phases [17]. In the alloy and microstructure designing of such new AHSS, the grain refinement of ferrite or other phases down to sub-micrometer sizes is thought to be one of the important microstructural controlling methods [14]. Actually, improvement of mechanical properties by ultra grain refinement of steels, such as such as high strength [18], good toughness in low temperature [19] and high stretch formability [20], has been reported. Therefore, superior mechanical properties are also xpected in new HSS with the technology of ultra grain refinement. In this study, the “ultrafine” grain size corresponds to that between 100 nm and 1 μm. Materials having grain sizes smaller than 100 nm are generally called as “nanocrystalline” materials [21].

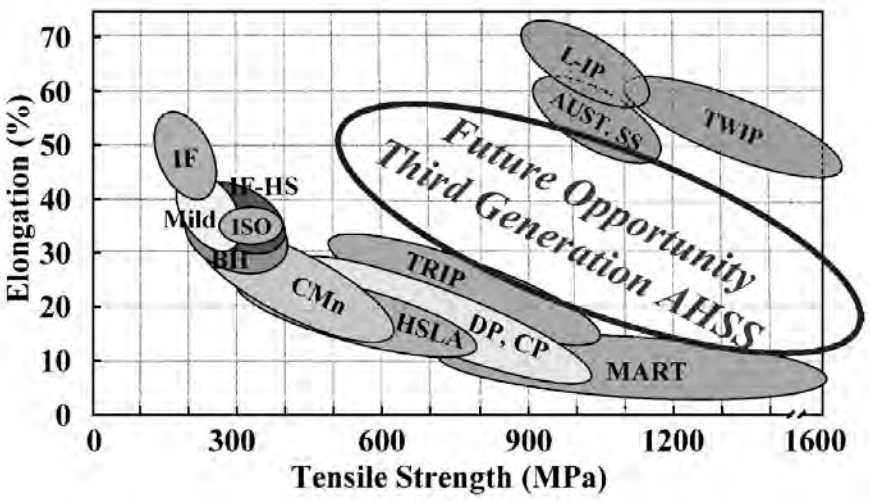

Figure 1.5 Schematic illustration indicating the position of the "third generation AHSS (advance high strength steels)" in a strength-elongation map for steels. Also various types of conventional HSS and the "second generation AHSS" including austenitic steels and TWIP steels are indicated [14].

1.2 New routes to fabricate ultrafine grained steels without severe plastic deformation

In order to fabricate ultrafine grained (UFG) or nanocrystalline metals, severe plastic deformation (SPD) processes [22] have been generally applied. First, the procedures of typical SPD processes are reviewed in this section. Figure 1.6 shows the procedures of high pressure torsion (HPT) [23, 24], equal channel angular extrusion (ECAE) [25, 26], and accumulative roll bonding (ARB) [27, 28] which are all SPD processes. In the HPT (Fig. 1.6 (a)), disc-shaped specimens with a diameter ranging from 10 to 20 mm and ring-shaped specimens with a diameter up to 100 mm [24] are applied. The thickness of the specimens is usually below 1 mm. The specimen is put between the plunger and support shown in Fig. 1.6 (a), and compressed under an applied pressure of several GPa. The lower support turns, and shear strain is introduced to the specimen by friction forces. Figure 1.6 (b) shows the procedure of the ECAE. A bar-shaped specimen is pressed in a special die having two channels with equal cross section intersecting usually at an angle of 90 degrees. Shear strain is introduced to the specimen through the pressing, and by repeating the pressing, very high strain is applied to the specimen. Figure 1.6 (c) shows the procedure of the ARB. In the ARB process, two sheets that usually have the same thickness are firstly degreased and wire-brushed on the contact surfaces, to achieve good bonding between two stacked sheets. The stacked sheets are then bonded by rolling. The roll-bonding is sometimes carried out at elevated temperatures below recrystallization temperature of the material, in order to make the bonding better and to reduce the rolling force. By repeating the procedure, very high

plastic strain is introduced to the sheet. When the rolling reduction in thickness through one cycle of the roll-bonding is set to be 50%, a heavily deformed specimen having the same dimensions as the initial sheet can be obtained after the repetition of the cycle. In all the SPD processes shown here, the shape and dimensions of the specimens are almost the same before and after the processing. Only the ARB can provide sheet-shaped UFG specimens. As mentioned in the previous section, some studies using the ARB have revealed superior mechanical properties of UFG steels [18-20]. However, it has been difficult to apply the UFG steel sheets to automobile body parts. This is due to the limited dimensions of the UFG steels fabricated by SPD processes. In addition, the SPD processes do not seem adaptive to the conventional mass production routes for steels. Therefore, in order to apply the UFG metals to commercial automobiles, more simple process with high productivity that provides large-sized UFG steels has been required.

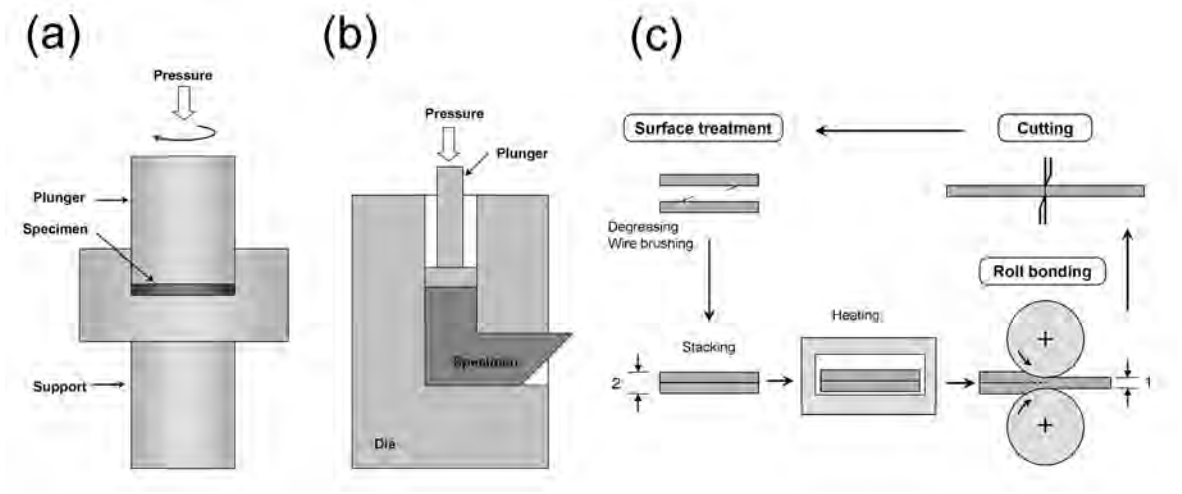

Figure 1.6 Schematic illustrations of various SPD (severe plastic deformation) processes for fabricating bulk ultrafine grained or nanocrystalline metals. (a) HPT (high pressure torsion), (b) ECAE (equal channel angular extrusion) and (c) ARB (accumulative roll bonding).

It is well known that very high plastic strain over 4 or 5 should be applied to the specimens in order to refine the grain sizes down to sub-micrometer [29]. In order to produce UFG metals with high productivity, it is necessary to reduce the required plastic strain. In case of steels, the matrix has phase transformation, which means that various combinations of transformed phases and plastic deformation can be considered [30]. From this point of view, studies to reduce the plastic strain required for fabricating UFG structures have been reported using various combinations of transformed phases and plastic deformation [31-35]. Through those studies, UFG ferrite microstructures have been obtained. However the processes proposed in the previous studies [31-35] have not been commercially applied, because the productivity is still insufficient in those processes. In this study, a new route to fabricate low-C UFG steel sheets with high productivity [36, 37] is

introduced. The feature of the newly developed route is conventional rolling of a duplex microstructure composed of ferrite and martensite, which has not been studied before. In Chapter 2, the concept of this process, microstructural evolution, the effect of process conditions, and the effect of the starting microstructures are shown and discussed.

1.3 Dynamic deformation of ultrafine grained steels

As mentioned in section 1.1, the crash worthiness is one of the required performances for automobile body structures. The body parts are deformed at very high strain rates in cases of car collisions. The materials in the body structures are required to absorb crash energy in dynamic deformation (deforming at high strain rates). For example, the strain rates of the material reach over 10^2 s^{-1} in the dynamic deformation of tubular automobile body parts [38, 39]. Therefore dynamic deformation properties of materials are important for the parts in automobile body structures. One of the characteristics of materials for evaluating the dynamic strength is the difference in flow stress between high and low strain rates, $\Delta\sigma$. Generally the strength of metals increases when the strain rate increases [40-42]. Figure 1.7 shows the relationship between yield shear stress and strain rate in a low-C steel at various temperatures [42]. It has been shown that the flow stress at room temperature has significant strain rate dependence at a strain rate range between 10^{-1} and 10^3 s^{-1}. Among various metals, especially bcc metals including iron have high strain rate dependence of flow stress compared with fcc/hcp metals. In bcc metals the principal barrier for dislocation motion is the Peierles-Nabarro stress [41] that is known to have large temperature (and strain rate) dependence. Therefore iron and steels naturally have high $\Delta\sigma$. However, it generally decreases when the steels are strengthened by alloying elements, precipitates and second phases [43-45]. On the other hand, dynamic deformation properties of UFG ferrite microstructures has not been studied systematically. Only a few studies have been reported [46, 47]. Therefore it is required to clarify the dynamic deformation properties of UFG steels, when considering the application to automobile body structures. However, the limited dimensions of the specimens obtained in the SPD processes have prevented the systematic investigation of the dynamic deformation properties of UFG metals. In addition, another difficulty in investigating the dynamic tensile properties is the fact that the strain rates applied in conventional high-speed test methods were limited to narrow range. In this study, using the UFG sheet steels having sufficient dimensions fabricated by the newly developed process, and using a special high-speed tensile test equipment recently developed, dynamic tensile deformation properties of the UFG ferrite steels are investigated systematically.

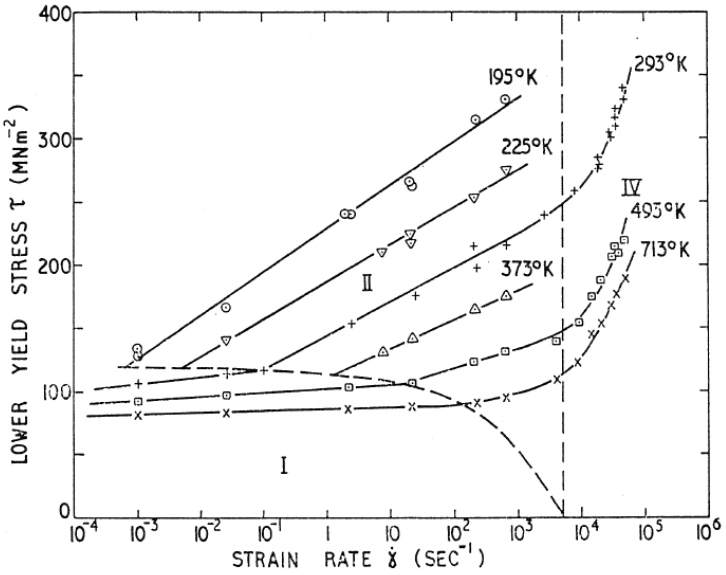

Figure 1.7 The relationship between lower yield stress and strain rate in a low-C steel at various temperatures [42]. The data shows significant strain rate dependence of yield stress at room temperature at strain rates between 10^{-1} and 10^{3} s^{-1}.

1.4 Improvement of tensile ductility in ultrafine grained steels

The ultra grain refinement of steels significantly increases their strength. On the other hand, it decreases the elongation, especially uniform elongation of steels [18, 48]. This behavior is common in other metals such as aluminium [18]. Figure 1.8 shows that uniform elongation significantly decreases down to a few percent when the grain size decreases to about 1 μm both in IF (interstitial free) steel and 1100 aluminium [18]. This is due to the insufficient work hardening rate in UFG single-phase microstructures [49, 50]. The plastic instability theory in tensile deformation, which will be described in detail in Chapter 3, shows that highly strengthened materials require larger work hardening rate to keep uniform deformation. Considering the stamping process of automobile body parts, adequate uniform elongation is required. Therefore in order to apply UFG steels widely to automobile body parts, uniform elongation should be improved. For this demand, an effective way is an introduction of hard second phases to the UFG microstructures [51]. Generally in the conventional HSS, dual-phase (DP) and multi-phase (MP) steels including TRIP-assisted steels show improved uniform elongation by enhanced work hardening rate due to the introduction of hard phases. In case of fine grained steels, improvement of elongation is expected by an introduction of hard phase as well [52]. In this study, trials to introduce hard second phases into the UFG ferrite microstructures are carried out. The effect of volume fraction and properties of the hard second phases on mechanical properties of the UFG ferrite microstructures are investigated systematically.

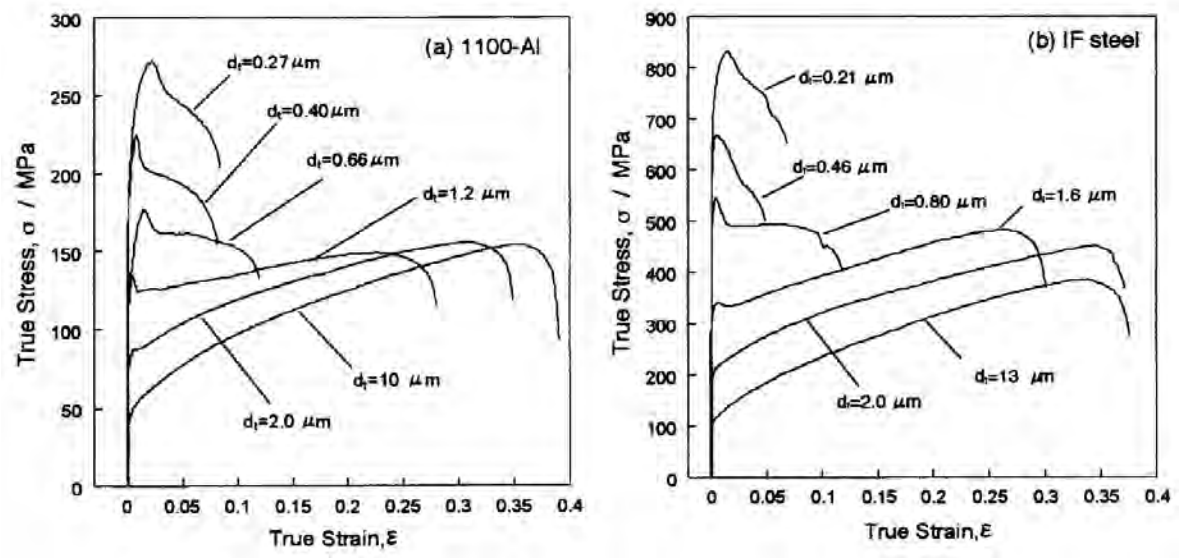

Figure 1.8 Tensile stress-strain curves of the 1100-aluminium (a) and IF steel (b) fabricated by accumulative roll bonding (ARB) and subsequent annealing, and having various grain sizes [18].

1.5 Application of ultrafine grained steels to automobile body structures

Figure 1.9 shows an example of recent automobile body structure indicating the tensile strength of applied sheet steels [53]. The application ratio of HSS is nearly 50% in weight of the body. By the way, the body parts are categorized into two groups having different functions. The one is the parts surrounding passengers' cabin, so-called "pillars" and "rails". They are required to keep the space for the passengers by preventing deformation of the cabin during car collisions. Recently, ultra high strength steels (UHSS) stronger than 980 MPa are applied to those parts [54]. Additionally, the application of "hot-stamping" [55, 56] to the parts in the cabin section has been expanding. The process of the "hot-stamping" is composed of stamping of a steel sheet at high temperatures of austenite region in order to form the part shape, and subsequent rapid cooling in the stamping die for forming martensite microstructure. Through this process, the tensile strength of 1500 MPa is obtained with relatively high formability due to the high stamping temperature.

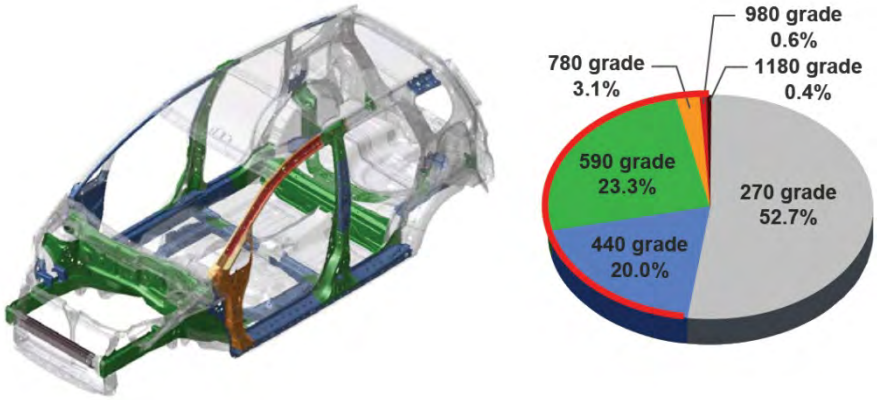

Figure 1.9 An example of automobile body structure indicating tensile strength of applied steels, and weight ratio of the applied steels having various tensile strengths [53].

The other group in body structures contains the frame parts in front and rear sections. They are required to absorb impact energy by deforming during car collisions. However, as shown in Fig. 1.9, the strength of the steels that are applied to the front and rear frames is limited to 600 MPa in typical commercial cars [9, 53, 57]. Therefore, in order to achieve further weight reduction in automobile body structures, the application of stronger steels, such as UHSS to the front and rear sections should be considered. Generally the parts in the front and rear sections are required to absorb impact energy through heavy deformation along longitudinal direction of the frames (axial collapse). Actually, sometimes the ability of energy absorption even decreases when conventional UHSS are applied to such parts. This is because of the change in deformation shapes in the axial collapse. The ideal deformation shape of the frames in the axial collapse is “compact-mode” [58, 59], which means a stable deformation through the formation of a series of continuous folds like accordion. The typical appearance of a square tube deformed in the “compact-mode” achieved in axial collapse is shown in Fig. 1.10 (a) [59]. However, when conventional UHSS are applied, “non-compact” mode, which decreases the efficiency of impact energy absorption, tends to occur. Figure 1.10 (b, c) show typical appearances of the “non-compact” mode observed in axial collapse of steel tubes. The “non-compact” mode is principally caused by the inadequate dimensions of the tubes, i.e. under the condition of small section, thin wall and long tube length. Additionally it has been reported that the poor work hardening (low *n*-value) in the material causes the “non-compact” mode [60]. Here, it is indicated again that the improvement of work hardening in the UHSS are important. Therefore, the improvement of work hardening rate of UFG ferrite steels is expected to show good performance in crash energy absorption as well. In this study, the crash worthiness, especially axial collapse properties of the fabricated UFG ferrite microstructures are investigated and discussed.

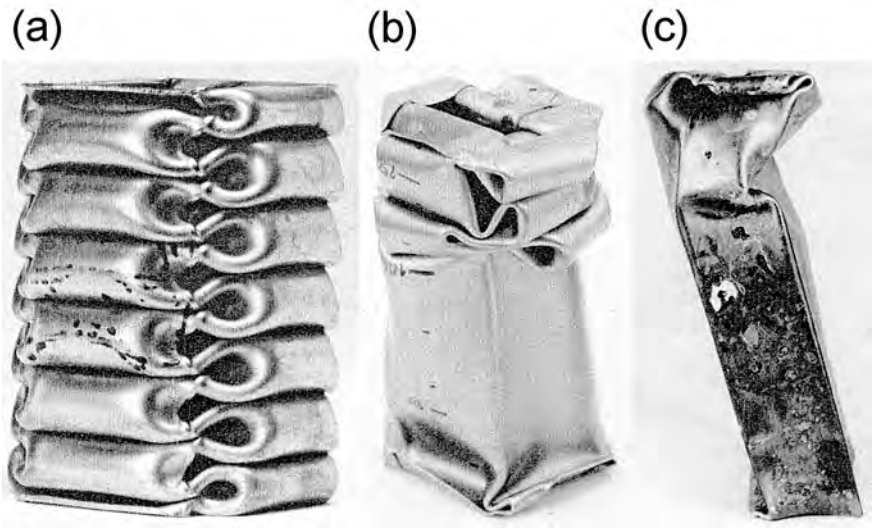

Figure 1.10 Examples of rectangular tubes dynamically deformed by the load along longitudinal direction of the tubes (axial collapse) showing (a) “compact mode” deformation with continuous folds, and (b, c) “non-compact mode” deformation. The tube in (b) shows straight non-deformed region as well as partly compact folds, and the tube in (c) shows falling down of the tube without forming compact folds [59].

1.6 The structure of this thesis

In this thesis, overall results of the study on fabrication and evaluation of the UFG steel sheets are shown and discussed. In Chapter 1, this chapter, the background and the aim of this study were introduced. In Chapter 2, the new route to fabricate bulky UFG steel sheets without SPD, which was developed in this study, is introduced. The mechanism of microstructural evolution, the effect of process conditions, and the effect of variations of the starting microstructures are shown and discussed. In Chapter 3, quasi-static and dynamic mechanical properties of the fabricated UFG steels, as well as UFG-IF steels and conventional HSS are shown. In Chapter 4, the concept and test results for the improvement of uniform elongation of the UFG ferrite microstructures by introducing hard second phases are shown. The TRIP effect by retained austenite, and the effect of ferrite grain size on the mechanical properties of UFG multi-phase microstructures are shown and discussed. In Chapter 5, focusing on the dynamic collapse of hat columns, crash worthiness of two UFG steels, UFG-FC and UFG-MP steels are clarified, and the potential of UFG steels as automobile body applications for further weight reduction are shown and discussed. In Chapter 6, overall results in this study are summarized.

1.7 References

[1] Ministry of Land, Infrastructure and Transport, Fuel efficiency of automobiles, Available at: http://www.mlit.go.jp/jidosha/nenpi/nenpilist/nenpilist.html [Accessed 14 October 2011].

[2] National Highway Traffic Safety Administration (NHTSA), Light-Duty Vehicle Greenhouse Gas Emission Standards and Corporate Average Fuel Economy Standards; Final Rule (2010) pp. 225, Available at: http://www.nhtsa.gov [Accessed 14 October 2011].

[3] European New Car Assessment Programme (Euro-NCAP), Assessment Protocol – Adult Occupant Protection Version 5.2 (2010), Available at: http://www.euroncap.com [Accessed 14 October 2011].

[4] U.S. Department of Transportation, Federal Motor Vehicle Safety Standards and Regulations (FMVSS) Standard No. 208, Available at: http://www.nhtsa.gov [Accessed 14 October 2011].

[5] National Agency for Automotive Safety & Victim's Aid (NASVA), Safe Car Choosing Guide Book (New Car Assessment Japan 2010), Available at: http://www.nasva.go.jp [Accessed 14 October 2011].

[6] Y. Kuriyama, M. Takahashi, H. Ohashi, J. Soc. Automotive Eng. Jpn. 55 No.4 (2005) 51.

[7] H. Takechi, JOM 60 No.12 (2008) 22.

[8] World Steel Association, Advanced High Strength Steel (AHSS) Application Guidelines Version 4.1, 2009. Available at: http://www.worldautosteel.org [Accessed 14 October 2011].

[9] B. Lüdke, M. Pfestorf, Functional design of a "Lightweight body in white" – How to determine body in white materials according to structural requirements. in: S. Hashimoto, S. Jansto, H. Mohrbacher, F. Siciliano (Eds.), International Symposium on Niobium Microalloyed Sheet Steel for Automotive Applications. TMS, Warrendale, 2006, pp. 27.

[10] ULSAB Consortium, ULSAB Engineering Report, 1998, Available at: http://www.worldautosteel.org [Accessed 14 October 2010].

[11] ULSAB-AVC Consortium, ULSAB-AVC Advanced Vehicle Concepts Technical Transfer Dispatch #6 – ULSAB-AVC Body Structure Materials, 2001, available at www.worldautosteel.org [Accessed 14 October 2010].

[12] O. Grässel, L. Krüger, G. Frommeyer, L. W. Meyer, Int. J. Plast. 16 (2000) 1391.

[13] D. Cornette, P. Cugy, A. Hildenbrand, M. Bouzekri, G. Lovato, SAE Technical Paper 2005-01-1327, SAE International, Warrendale, 2005.

[14] D. K. Matlock, J. G. Speer. Third generation of AHSS: microstructure design concepts. in: A. Haldar, S. Suwas, D. Bhattacharjee (Eds.), Microstructure and Texture in Steels and Other materials, Springer, London, 2009. pp. 185.

[15] J. G. Speer, D. V. Edmonds, F. C. Rizzo, D. K. Matlock, Current Opinion in Solid State & Materials Science 8 (2004) 219.

[16] K. Sugimoto, M. Murata, S. M. Song, ISIJ Int. 50 (2010) 162.

[17] D-W. Suh, S-J. Park, T-H. Lee, C-S. Oh, S-J. Kim, Mater. Trans. A 41 (2010) 397.
[18] N. Tsuji, Y. Ito, Y. Saito, Y. Minamino, Scripra Mater. 47 (2002) 893.
[19] N. Tsuji, S. Okuno, Y. Koizumi, Y. Minamino, Mater. Trans. 45 (2004) 2272.
[20] R. Yoda, K. Shibata, T. Morimitsu, D. Terada, N. Tsuji, Scripra Mater. 65 (2011) 175.
[21] C. C. Kock, I. A. Ovid'ko, S. Seal, S. Veprek, Structural Nanocrystalline Materials, Chambridge Universtiy Press, Cambridge, 2007, pp. 292.
[22] B. S. Altan (Ed.), Severe Plastic Deformation toward Bulk Production of Nanostructured Materials, NOVA Science Publishers, New York, 2005.
[23] R. Z. Valiev, A. V. Korznikov, R. R, Mulyukov, Mater. Sci. Eng. A,168 (1993)141.
[24] K. Edalati, Z. Horita, Mater. Trans. 50 (2009) 92.
[25] V.M . Segal, Mater. Sci. Eng. A 197 (1995) 157.
[26] Y. Iwahashi, J. Wang, Z. Horita, M. Nemoto, T. G. Langdon, Scripta Mater. 35 (1996) 143.
[27] Y. Saito, N. Tsuji, H. Utsunomiya, T. Sakai, R. G. Hong, Scripta Mater. 39 (1998) 1221.
[28] Y. Saito, H. Utsunomiya, N Tsuji, T. Sakai, Acta Mater. 47 (1999) 579.
[29] N. Tsuji, Adv. Eng. Mater.12 (2010) 701-707.
[30] N. Tsuji, T. Maki, Scripta Mater. 60 (2009) 1044.
[31] N. Tsuji, R. Ueji, Y. Minamino, Y. Saito, Scripta Mater. 46 (2002) 305
[32] R. Ueji, N. Tsuji, Y. Minamino, Y. Koizumi, Acta Mater. 50 (2002) 4177.
[33] A. Ohmori, S. Torizuka, K. Nagai, ISIJ Int. 44 (2004) 1063.
[34] T. Furuhara, T. Mizoguchi, T. Maki, ISIJ Int. 45 (2005) 392.
[35] R. Song, D. Ponge, D. Raabe, R. Kaspar, Acta Mater. 53 (2005) 845.
[36] Y. Okitsu, N. Takata, N. Tsuji: Scripta Mater. 60 (2009) 76.
[37] Y. Okitsu, N. Takata, N. Tsuji: J. Mater. Sci. 43 (2008) 7391.
[38] S. Simunovic, P. Kumar, V. Nukala, J. Fekete, D. Meuleman, M. Milititsky, SAE Technical Paper, 2003-01-1383, SAE International, Warrendale, 2003.
[39] A. Otubushin, Int. J. Impact Eng. 21 (199) 349.
[40] M. A. Meyers, Dynamic behavior of materials, John Wiley & Sons, Inc., New York, 1994, pp. 340.
[41] J. Harding, The effect of high strain rate on material properties, in: T. Z. Blazynski (Ed.), Materials at high strain rates, Elsevier, London, 1987, pp. 133.
[42] J. D. Campbell, W. G. Ferguson, Phil. Mag. 21 (1970) 63.
[43] D. M. Bruce, D. K. Matlock. J. G. Speer, A. K. De, SAE Technical Paper, 2004-01-0507, SAE International, Warrendale, 2004.
[44] M. Takahashi, A. Uenishi, H. Yoshida, Y. Kuriyama, SAE Technical Paper 2003-01-2765, SAE International, Warrendale, 2003.
[45] S. Takagi, Y. Tokita, K. Sato, T. Shimizu, K. Hashiguchi, K. Ogawa, K. Mimura, S. Tanimura, SAE Technical Paper 2005-01-0494, SAE International, Warrendale, 2005.
[46] D. Jia, K.T. Ramesh, E. Ma, Acta Mater. 51 (2003) 3495.
[47] N. Tsuchida, H. Masuda, Y. Harada, K. Fukaura, Y. Tomota, K. Nagai, Mater. Sci. Eng. A 488 (2007) 446.
[48] S. Takaki, K. Kawasaki, Y. Kimura, in: R. S. Mishra, S. L. Semiatin, C. Suryanarayana, N. N. Thadhani, T. C. Lowe (Eds.), Ultrafine Grained Materials, TMS, Warrendale,

2000, pp. 247.
[49] Y. M. Wang, E. Ma, Acta Mater. 52 (2004) 1699.
[50] N Tsuji, Fabrication of bulk nanostructured materials by accumulative roll bonding (ARB). in: M. J. Zehetbauer, Y. T. Zhu (Eds.), Bulk Nanostructured materials, WILEY-VCH, Weinheim, 2009, pp. 235.
[51] Y. Tomota, A, Narui, N. Tsuchida, ISIJ Int. 48 (2008) 1107.
[52] N Tsuchida, Y. Tomota, K. Nagai, Tetsu-to-Hagané 89 (2003) 1170.
[53] In: Euro Car Body 2008, Automotive Circle International, Bad Nauheim, 2008.
[54] R. Z. Mallen, J. Odell, B. O'Hara, SAE Technical Paper, 2009-01-0088, SAE International, Warrendale, 2009.
[55] D. W. Fan, B. C. De Cooman, ISIJ Int. 50 (2010) 1713.
[56] T. Nishibata, N. Kojima, Tetsu-to-Hanané 96 (2010) 378 (in Japanese).
[57] R. Sohmshetty, K. Malella, O. Faruque, P. Geck, P. A. Elliott, SAE Technical Paper, 2006-01-1587, SAE International, Warrendale, 2006.
[58] H. F. Mahmood, A. Paluszny, SAE Technical Paper 811302, SAE International, Warrendale, 1981.
[59] S. R. Reid, T. Y. Reddy, M. D. Gray, Int. J. Mech. Sci. 28 (1986) 295.
[60] A. Uenishi, Y. Kuriyama. M. Takahashi, High-Strength Steel Sheets Offering High Impact Energy-Absorption Capacity. Nippon Steel Technical Report 81 (2000) 17.

CHAPTER 2

FABRICATION OF ULTRAFINE GRAINED MICROSTRUCTURES WITHOUT SEVERE PLASTIC DEFORMATION

2.1 A new route to fabricate ultrafine grained microstructures in carbon steels without severe plastic deformation

2.1.1 Introduction

As mentioned in Chapter 1, the severe plastic deformation (SPD) processes to fabricate uniform ultrafine grained (UFG) microstructures require very large plastic strain over 4 or 5 in logarithmic equivalent strain [1]. In case of straining by rolling, the equivalent strain, ε_{eq} introduced to specimens during the rolling assuming the plane strain compression is described as

$$\varepsilon_{eq} = -\frac{2}{\sqrt{3}} ln \frac{t}{t_0} \quad (2.1)$$

where t_0 and t are the thickness of sheet specimens before and after rolling. In order to introduce a plastic strain of 4 during the rolling, a thickness reduction of 96.9% is required. This reduction seems not to adapt to the practical production of structural sheet metals. In order to reduce the plastic strain and to produce UFG microstructures with high productivity, various processes without SPD have been proposed [1, 2]. In case of steels, which have phase transformation of the matrix, various processes composed of phase transformation and plastic deformation have been studied [3-7]. As a result, it has become possible to obtain UFG microstructures by plastic strains of 1 to 3, which are much smaller than those in the typical SPD processes. Here, some examples for plastic deformation of various kinds of transformed microstructures of steels are described. Table 2.1 summarizes the conditions and obtained microstructures in the previous studies [3-7].

Ueji et al. [3, 4] have shown that 50% cold-rolling and annealing of as-quenched martensite in low-C steel (JIS-SS400) can produce equiaxed and ultrafine ferrite containing finely dispersed cementite. In this case, the plastic strain accumulated into the specimen is 0.8. However cold-rolling of as-quenched martensite, which is very hard and has less cold

workability, gives difficulty in practical production. Other starting microstructures (microstructures before rolling), tempered martensite [5], ferrite-pearlite (F-P) [6] and pearlite [7] have been used in other studies. In the cases of martensite [3, 4], tempered martensite [5] and F-P [6] as starting microstructures before rolling, ultrafine/fine ferrite microstructures have been obtained, but the ferrite grains contained residual dislocations inside. The dislocation density was decreased by annealing at elevated temperatures, but coarsening of ferrite grains occurred simultaneously to make the grain sizes over 1 μm. Furuhara et al. [7] have obtained fully annealed sub-micrometer ferrite with large amount of cementite particles by 90% cold-rolling of high-C pearlite and subsequent annealing at 700 °C. The microstructure they obtained showed a good balance of tensile strength and tensile elongation (950 MPa, 14%). However, it seems to be difficult to apply high-C pearlite steels to automobile body parts because of poor spot-weldability due to the high carbon content.

Based on these results, we propose a new route to fabricate UFG ferrite microstructure in low-C steels, which is composed of cold-rolling and annealing of ferrite-martensite duplex microstructure [8, 9]. In this section, the new route to fabricate UFG ferrite microstructures is introduced, and the microstructures at each stage of the process are shown. The mechanism of UFG ferrite formation in this process is discussed.

Table 2.1 Starting microstructures, deformation condition, subsequent heat-treatment condition, and obtained microstructures in the previous studies for fabricating UFG steels.

Starting micro-structure	Chemical composition (mass%)	Deformation method and temperature	Applied equivalent strain	Heat- treatment condition	Obtained ferrite grain size (μm)	Ref. No.
M	0.13C-0.37Mn	CR, RT	0.8	500 °C, 1.8 ks	0.18	[3, 4]
TM	(0.1-0.3)C-1.5Mn	WR, 500 °C	3.1	500 °C, 3.6 ks	0.5-0.8	[5]
F-P	0.22C-0.74Mn	PC, 550 °C	1.6	550 °C, 7.2 ks	1.2	[6]
P	1.0C-1.4Cr	CR, RT	2.7	700 °C, 120 sec	0.2-0.4	[7]

F: Ferrite, C: Cementite, M: Martensite, TM: Tempered Martensite, P: Pearlite,

CR: Cold-rolling, WR: Warm-rolling, PC: Plane strain compression, RT: room temperature

2.1.2 Experimental procedure

Table 2.2 summarizes the chemical composition of the steel used in this section, which is named “UFG-FC1 steel” hereafter. Based on a low-C steel, slight amount of Nb and B were added in this material. The transformation temperatures on cooling from austenite, which were important for fabricating a duplex starting microstructure, were measured by dilatometer. The two-phase region of ferrite and austenite at cooling rate of 2 °Cs^{-1} was between 465 °C and 625 °C. Figure 2.1 shows a schematic illustration describing the fabricating process and conditions. The fabricating process consists of conventional hot-rolling, cold-rolling and annealing. An ingot prepared by vacuum-melting was

hot-rolled to a thickness of 6.8 mm at a finishing temperature (FT: the temperature after the final pass in the hot-rolling) of 770 °C in austenite region. After that, the sheet was air-cooled to 540 °C corresponding to the intercritical region of ferrite and austenite, and then water-cooled to room temperature for obtaining a duplex microstructure of ferrite and martensite. The hot-rolled sheet was cold-rolled at room temperature using a four-high rolling mill with lubrication. Cold-rolled sheets having 150 mm width and 0.6 mm thicknesses were obtained. The total reduction in thickness through cold-rolling was 91 %. The equivalent plastic strain through cold-rolling, calculated using the equation (2.1), was 2.8. The cold-rolled sheets were annealed at various temperatures ranging from 620 to 680 °C for 120 s in a salt bath followed by water-cooling.

Table 2.2 Chemical composition (mass%) of the low-C (UFG-FC1) steel used for fabricating ultrafine grained ferrite-cementite microstructures.

C	Si	Mn	P	S	Al	Nb	B	N
0.10	0.01	1.98	0.002	0.001	0.018	0.018	0.0015	0.0011

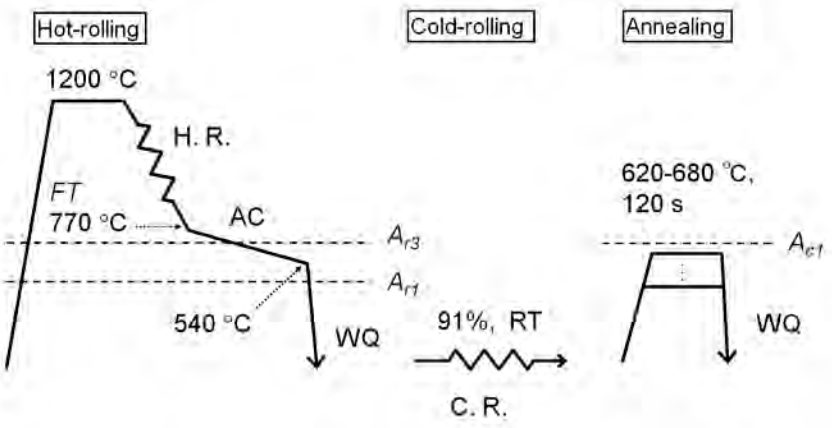

Figure 2.1 Schematic drawing of the process for fabricating the UFG ferrite-cementite microstructures by cold-rolling and annealing of a duplex microstructure. A_{r1}, A_{r3}, and A_{c1} mean the transformation temperatures measured by dilatometer. The A_{r1}, A_{r3}, and A_{c1} are 465 °C, 625 °C and 700 °C, respectively.

Microstructural observations were carried out for the specimens at each stage of the process. All the specimens were observed from the transverse direction (TD) of the sheets. The samples for optical microscopy (OM) or scanning electron microscopy (SEM) were etched with a 3% nital. SEM observations were conducted in Hitachi S-4300E/N SEM operated at 15 kV. Thin foils for transmission electron microscopy (TEM) were prepared by twin-jet electropolishing in a 10% $HClO_4$ + 90% CH_3COOH solution, and observed by JEOL JEM-2010HC TEM operated at 200 kV. An electron backscatter diffraction (EBSD) analysis was also carried out by using FEI XL30S SEM equipped with TSL (TexSEM Laboratories, Inc.) orientation image microscope (OIM) system operated at 15 kV. The

EBSD scanning was carried out at the thickness center on the longitudinal section perpendicular to TD (TD section). The mapping was carried out at a step size of 0.05 or 0.1 μm on a hexagonal grid. The data were analyzed using the OIM analysis version 4.7 software. Vickers hardness was measured on the TD section of the specimens at each stage of the process. Using a load of 1 kg, the hardness was measured at least three times for each specimen, and the data were averaged.

2.1.3 Microstructural change during the process

An optical micrograph of the hot-rolled sheet is shown in Fig. 2.2. The hot-rolled sheet showed a duplex microstructure composed of ferrite matrix (bright region) and martensite islands (dark region). The mean intersection lengths along the normal direction (ND) of the both regions, measured using the optical micrograph, were 5.55 μm for the ferrite and 2.47 μm for the martensite. The area fraction of martensite measured by point-counting method was 42%. The TEM observation confirmed that the martensite was typical “lath-martensite” including high density of dislocations. The average thicknesses of martensite laths and blocks were 0.4 μm and 1.5 μm, respectively. Cementite particles were not observed in the hot-rolled specimen. Figure 2.3 shows a SEM microstructure of the 91% cold-rolled specimen. The ferrite matrix (dark gray region) exhibited wavy microstructure elongated roughly to the rolling direction (RD) and bent along the diamond-shaped martensite islands (light gray region). It is indicated that complex plastic flow occurred and higher strain was introduced into the softer ferrite matrix owing to the existence of hard martensite phase. The martensite regions were also deformed to some extent during the cold-during, and exhibited diamond-like shapes in Fig. 2.3. The strain introduced into martensite should be smaller than that into ferrite matrix, because martensite is much harder than ferrite. Such a strain distribution between soft phase (ferrite) and hard phase (martensite) is the key factor for the formation of ultrafine grains in the present thermomechanical treatment, as will be discussed later.

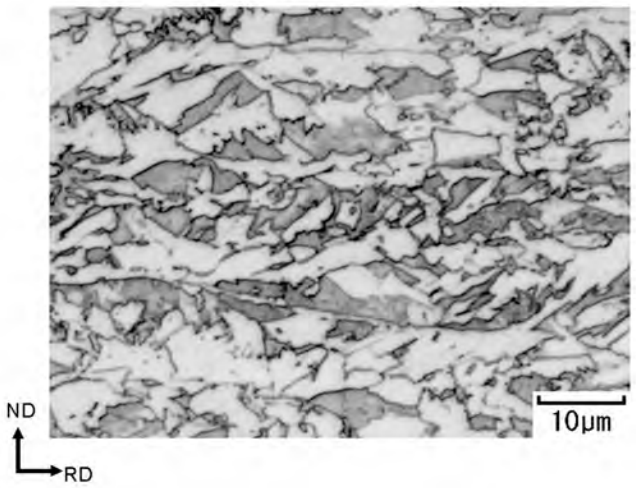

Figure 2.2 Optical micrograph of the hot-rolled sheet as starting material. After the hot-rolling, the sheet was air-cooled to 540 °C and then water-cooled to room temperature. Observed from TD.

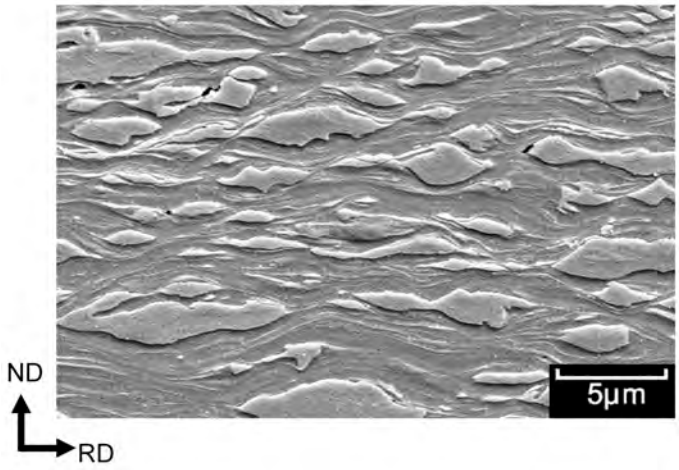

Figure 2.3 SEM microstructure of the low-C (UFG-FC1) steel cold-rolled by 91% reduction. Starting microstructure was a duplex structure composed of ferrite and martensite shown in Fig. 2.2. Observed from TD.

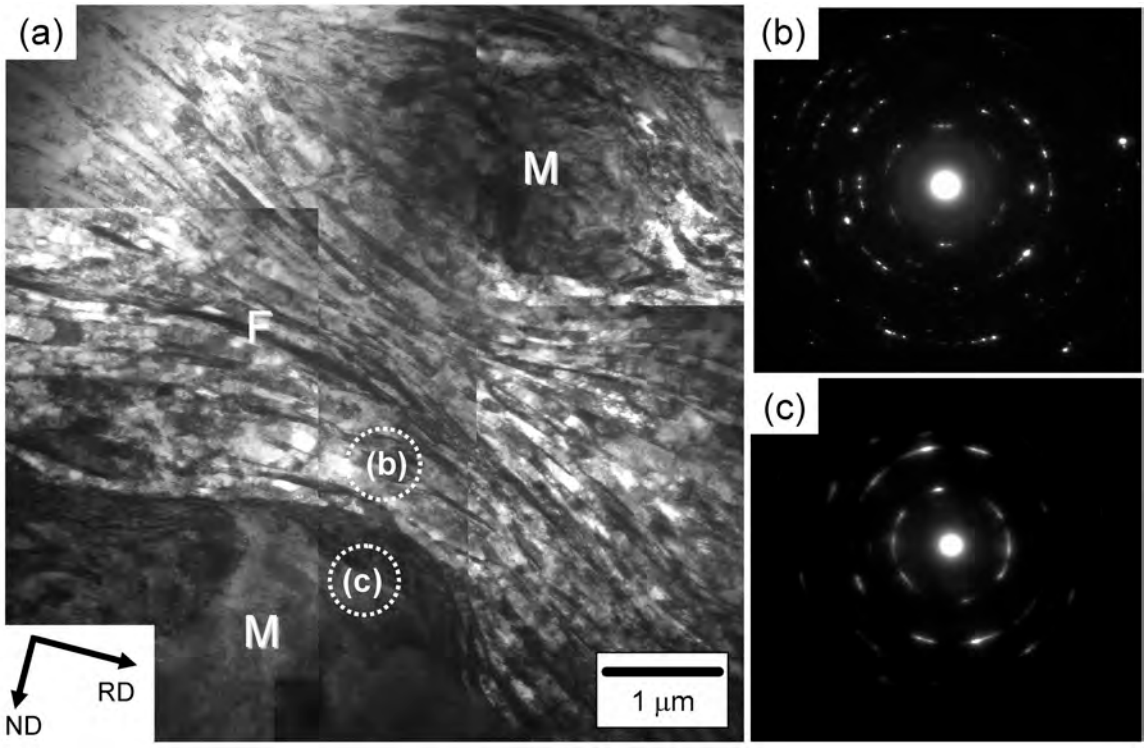

Figure 2.4 (a) TEM Microstructure of the low-C (UFG-FC1) steel cold-rolled by 91% reduction. Starting microstructure was a duplex structure composed of ferrite and martensite. Observed from TD. (b) SAD pattern taken from ferrite. (c) SAD pattern taken from martensite.

Figure 2.4 shows a TEM microstructure of the 91% cold-rolled specimen. The “F” and “M” in the figure indicate ferrite and martensite, respectively. In the ferrite region neighboring to martensite islands, fine lamellar structure of ferrite with mean spacing of 0.14 μm was observed. Figure 2.4 (b) shows a selected area diffraction (SAD) pattern taken

from the ferrite region indicated by the dotted circle (b) in Fig.2.4 (a). The SAD pattern shows ring-like spots, which indicates that various orientations existed within the selected area. Figure 2.4 (c) shows a SAD pattern taken from the martensite region indicated by the dotted circle (c) in Fig. 2.4 (a). The pattern is again ring-like, which suggests large local misorientations in the martensite regions as well.

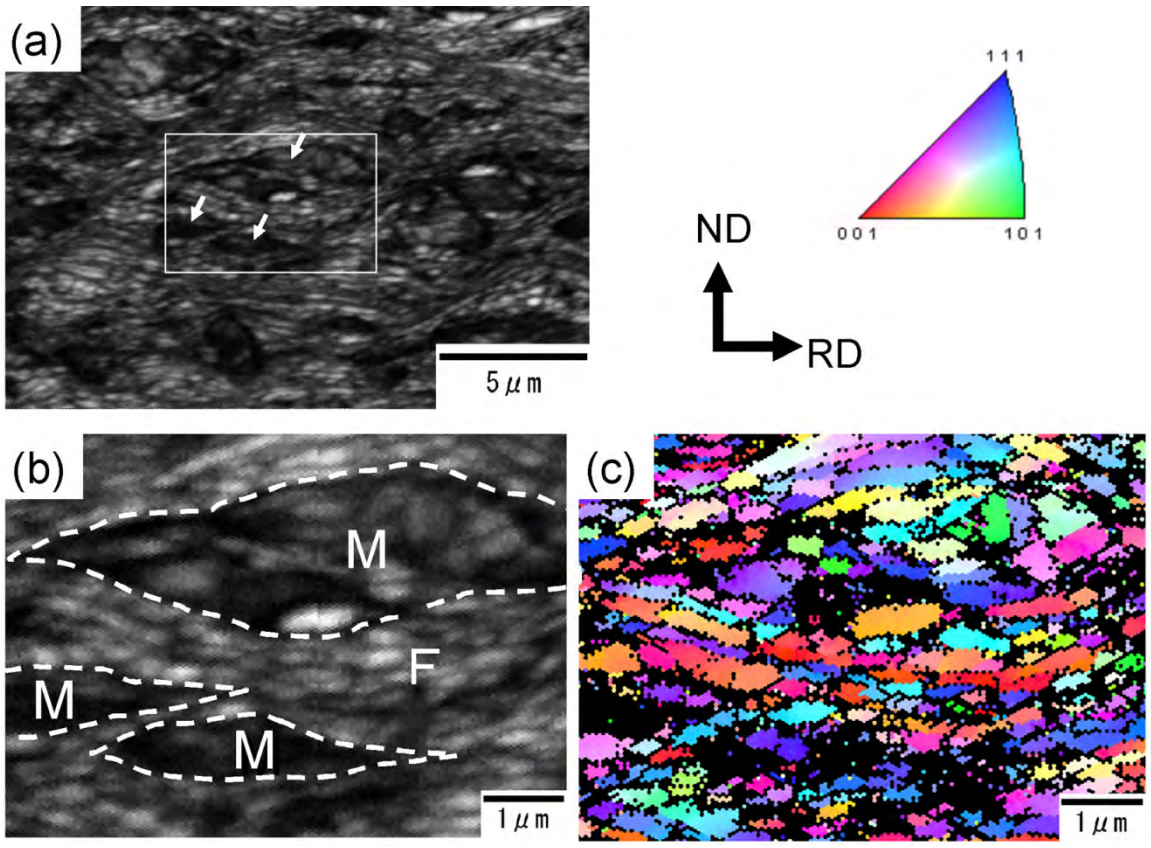

Figure 2.5 Orientation imaging microstructures obtained by EBSD analysis of the low-C (UFG-FC1) steel cold-rolled by 91% reduction. Observed from TD. (a) Image quality (IQ) map of a large area. White arrows indicate martensite. (b) Enlarged IQ map of the rectangular area in (a). M and F indicate martensite and ferrite, respectively. (c) ND orientation color map of the same area as (b). The measured points in which confidence index (CI) is smaller than 0.1 are colored in black in (c).

The microstructure of the cold-rolled specimen was also investigated by EBSD analysis. Figure 2.5 (a) shows an image quality (IQ) map obtained by the EBSD measurement for a 20 μm × 14 μm rectangular area on TD section of the 91% cold-rolled specimen. The ferrite matrix (relatively bright region) and martensite (dark region) are recognized. Martensite regions are indicated by white arrows in Fig.2.5 (a). Figure 2.5 (b) shows an enlarged IQ map of the rectangular area with a size of 5 μm × 7 μm in Fig.2.5 (a). The “F” and “M” in the figure indicate ferrite and martensite, respectively. Broken white lines indicate the boundaries between ferrite and martensite. Figure 2.5 (c) shows an ND orientation color map of the same area as Fig.2.5 (b). The measured pixels having CI (confidence index) values smaller than 0.1 are colored in black, because the orientation analysis was not accurate in those pixels. The ferrite matrix exhibited wavy microstructure

elongated roughly to RD and bent along the diamond-shaped martensite islands. It was also suggested that complex plastic flow occurred and high strain was introduced into the ferrite matrix owing to the existence of the hard martensite phase. A lamellar structure of ferrite with mean spacing of 0.22 μm was observed in Fig.2.5 (b). The lamellar structure contained ultrafine grains with large misorientations, as is indicated by various colors in Fig.2.5 (c). Also in the martensite, small regions having various colors were observed. This result indicates that ultrafine grains with large misorientations also formed in the martensite, corresponding to the SAD pattern shown in Fig. 2.4 (c). Consequently, it was revealed that a kind of UFG microstructure in ferrite matrix was already achieved in the cold-rolled state, in both ferrite matrix and martensite regions.

Next, microstructures after annealing of the 91% cold-rolled specimen are shown. Figure 2.6 (a-d) shows SEM microstructures of the specimens after annealing at 620 °C, 635 °C, 655 °C and 680 °C for 120 s. The cold-rolled microstructure shown in Fig. 2.3 changed to equiaxed UFG ferrite grains including fine cementite particles during the annealing. Cementite particles were homogeneously dispersed within the UFG ferrite matrix. Figure 2.7 (a-d) shows boundary misorientation maps obtained by EBSD analysis of the specimens annealed at 620 °C, 635 °C, 655 °C and 680 °C for 120 sec. The bold lines show high-angle grain boundaries (HAGBs) of which misorientation angles are higher than 15 degrees, while the narrow gray lines show low-angle grain boundaries (LAGBs) having misorientation angles between 2 and 15 degrees. The EBSD analysis revealed that the ultrafine grains in the annealed specimens were mostly surrounded by HAGBs, and contained few dislocation substructures within the grains.

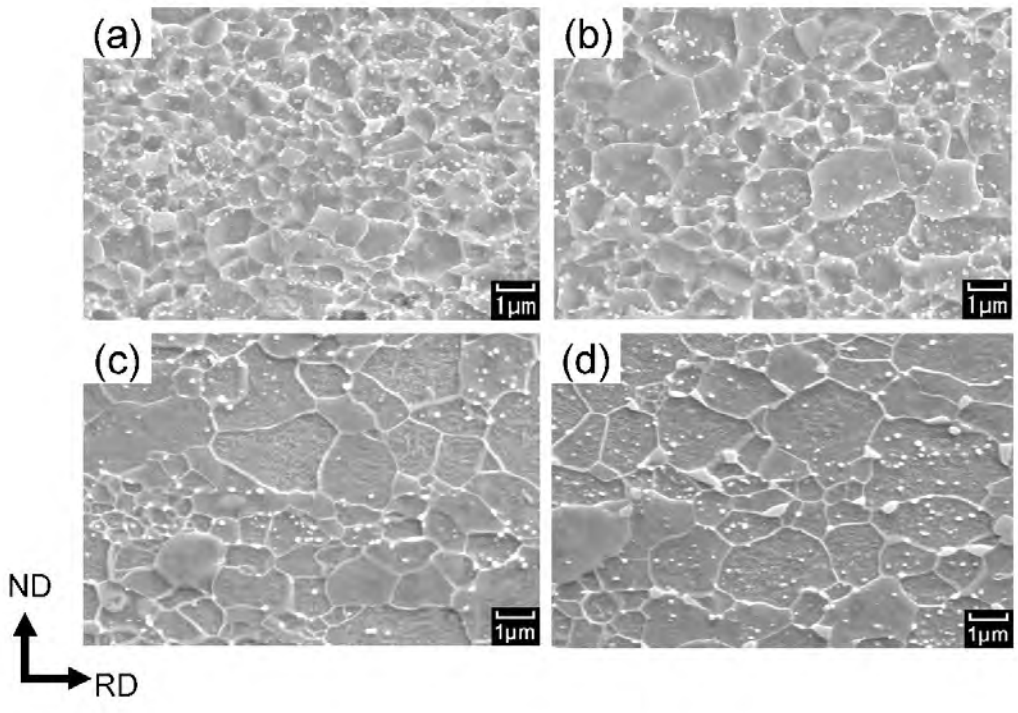

Figure 2.6 SEM microstructures of the low-C (UFG-FC1) steel cold-rolled by 91% reduction and annealed at (a) 620 °C, (b) 635 °C, (c) 655 °C and (d) 680 °C for 120 s followed by water-cooling to room temperature.

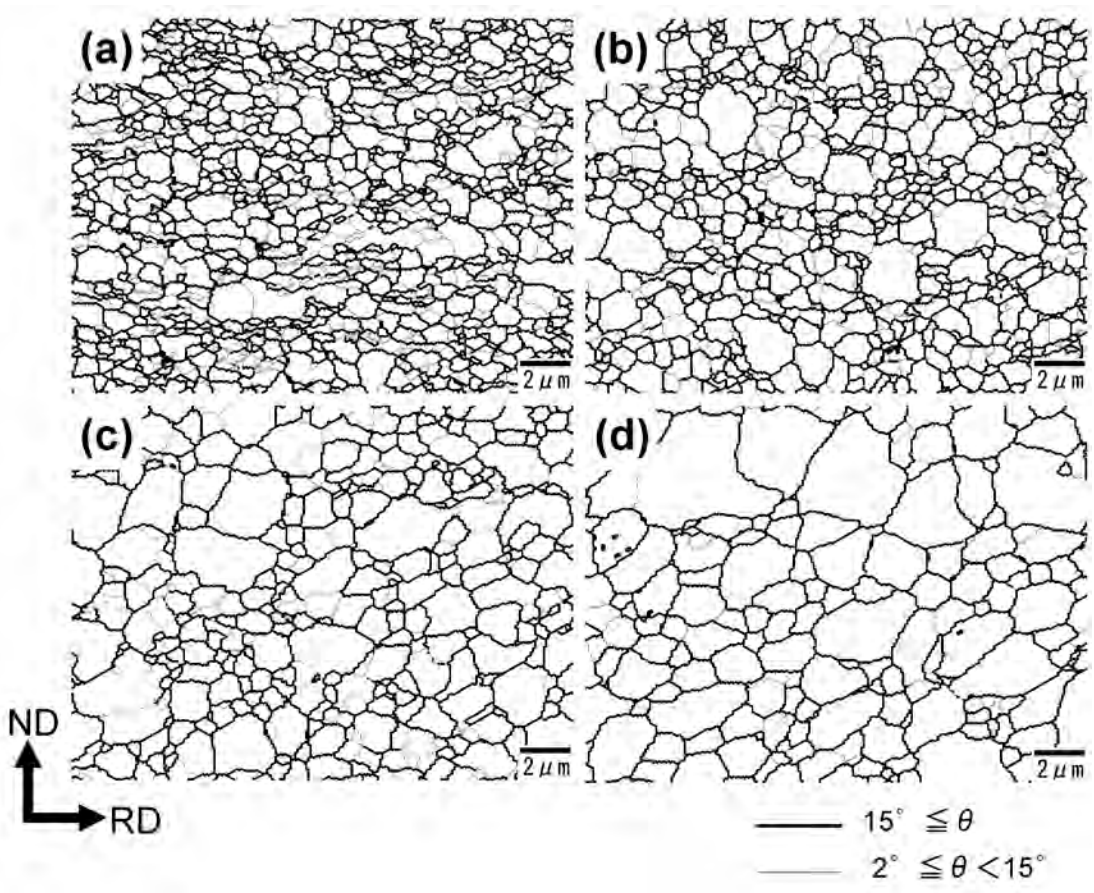

Figure 2.7 Boundary misorientation maps obtained by EBSD analysis of the low-C (UFG-FC1) steel cold-rolled by 91% reduction and annealed at (a) 620 °C, (b) 635 °C, (c) 655 °C and (d) 680 °C for 120 s followed by water-cooling to room temperature. Observed from TD. The bold lines show high angle grain boundaries and the narrow gray lines show low angle grain boundaries.

Figure 2.8 shows distributions of boundary misorientation angles obtained by the EBSD analysis of the annealed specimens. The fraction of HAGBs of the specimen annealed at 620 °C was 77.4%, and it gradually increased with increasing the annealing temperature. It should be emphasized that the fraction of HAGBs in the present UFG microstructures was high even at low annealing temperatures such as 620 °C, and it was higher than those in the UFG microstructures fabricated by other processes [3-6].

Figure 2.9 shows distributions of grain diameter obtained by the EBSD analysis of the annealed specimens. As the grain diameter, the diameter of a circle having equivalent area as the grain was used. The distributions of the grain diameter were rather broad. For example, some coarse grains larger than 2 μm existed in the specimen annealed at 620 °C, however the average grain diameter was 0.49μm. The average grain diameters of other annealed specimens at 635 °C, 655 °C and 680 °C were 0.62 μm, 0.85 μm and 1.03 μm, respectively.

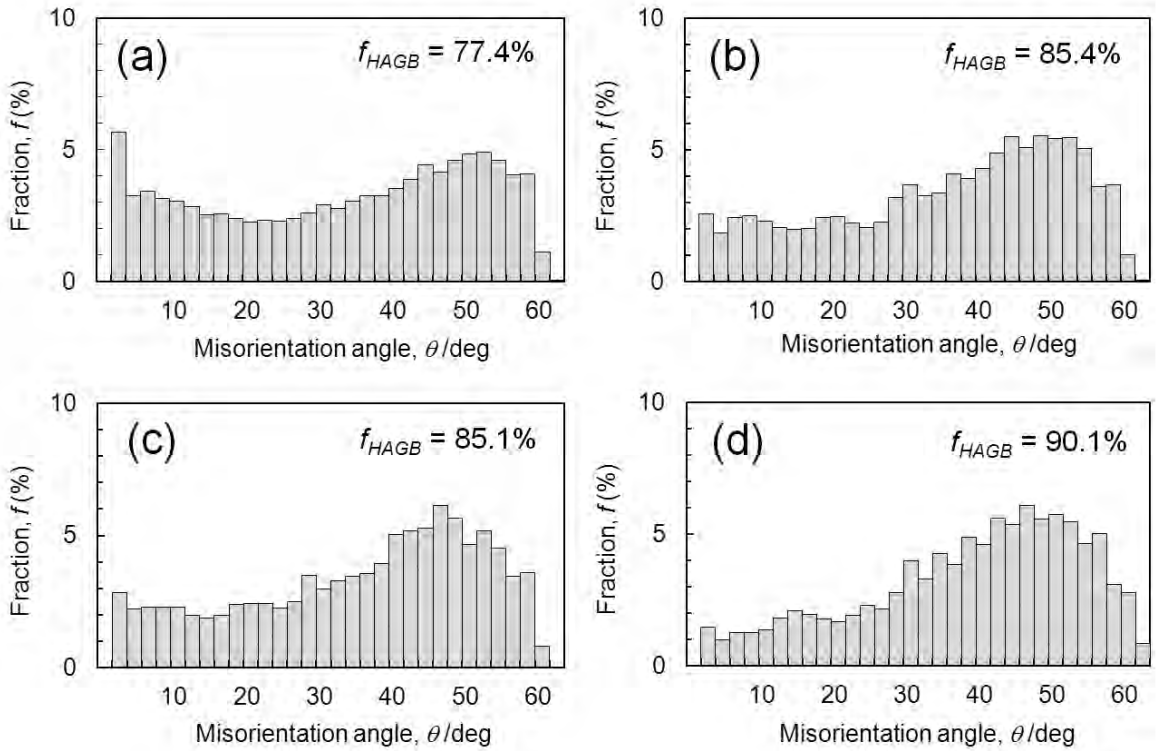

Figure 2.8 Misorientation angle distributions of the low-C (UFG-FC1) steel cold-rolled by 91% reduction and annealed at (a) 620 °C, (b) 635 °C, (c) 655 °C and (d) 680 °C for 120 s followed by water-cooling. f_{HAGB} indicates the fraction of high angle grain boundaries (HAGBs) in the microstructures.

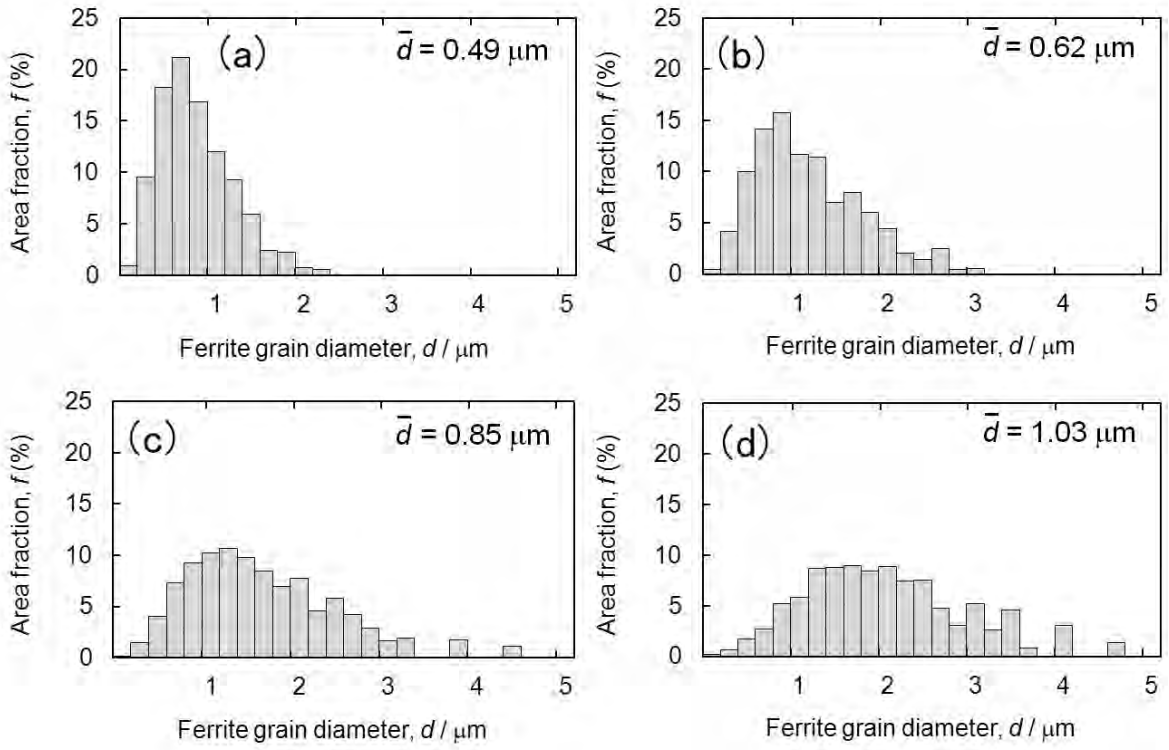

Figure 2.9 Grain diameter distributions indicated by area fraction in the low-C (UFG-FC1) steel cold-rolled by 91% reduction and annealed at (a) 620 °C, (b) 635 °C, (c) 655 °C and (d) 680 °C for 120 s followed by water-cooling. Average ferrite grain diameters, $\bar{d}$, are also indicated in the figures.

2.1.4 Textural change during the process

Figure 2.10 shows ND orientation color maps of the annealed specimens. The displayed regions are the same as those shown in Fig. 2.7. It is shown that the ferrite grains which have crystal orientations near <001> (colored in red) and <111> (colored in blue) were dominant in the specimens annealed at 620 °C and 635 °C (Fig. 2.10 (a) and (b)). In the specimen annealed at 655 °C (Fig. 2.10 (c)), coarse grains having orientations near <110> (colored in green) appeared, and the fraction of such coarse grains increased when annealed at 680 °C (Fig. 2.10 (d)).

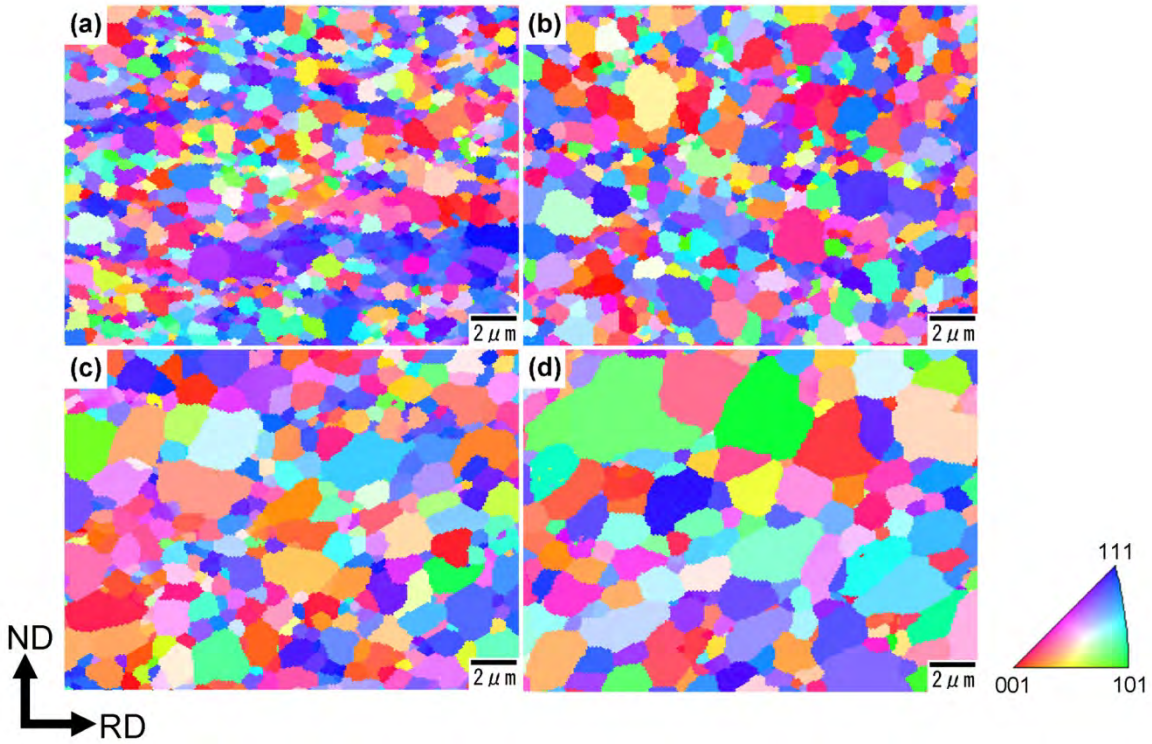

Figure 2.10 ND orientation color maps obtained by EBSD analysis of the low-C (UFG-FC1) steel cold-rolled by 91% reduction and annealed at (a) 620 °C, (b) 635 °C, (c) 655 °C and (d) 680 °C for 120 s followed by water-cooling. Observed from TD. The colors indicate the crystal orientation parallel to ND.

The textures of the fabricated specimens are discussed using pole figures. Figure 2.11 shows typical textures in cold-rolled low-C steels (Fig. 2.11 (a)) [10], and cold-rolled and annealed IF (interstitial free) steels (Fig. 2.11 (b)) [11] indicated by (001) pole figures. It has been well known that the cold-rolling texture of steels is composed of two fiber components: α-fiber (<110> parallel to RD of the sheet) and γ-fiber (<111> parallel to ND of the sheet) [11, 12]. On the other hand, in the texture of the cold-rolled and annealed steels (recrystallization texture), the γ-fiber component becomes dominant. Figure 2.12 shows (001) pole figures constructed by using the orientation data obtained in the EBSD analysis of the present cold-rolled specimen (Fig. 2.12 (a)) and cold-rolled and subsequently annealed specimens (Fig. 2.12 (b-e)). As shown in Fig. 2.12 (a), the cold-rolled specimen

had typical cold-rolling texture observed in low-C steels shown in Fig. 2.11 (a). After annealing at 620 °C (Fig. 2.12 (b)), the texture was still composed of two fiber components, and the intensity of the α-fiber rather increased. As the annealing temperature increased up to 680 °C, the intensity of the two fiber components gradually decreased, and the texture became more random (Fig. 2.12 (d, e)).

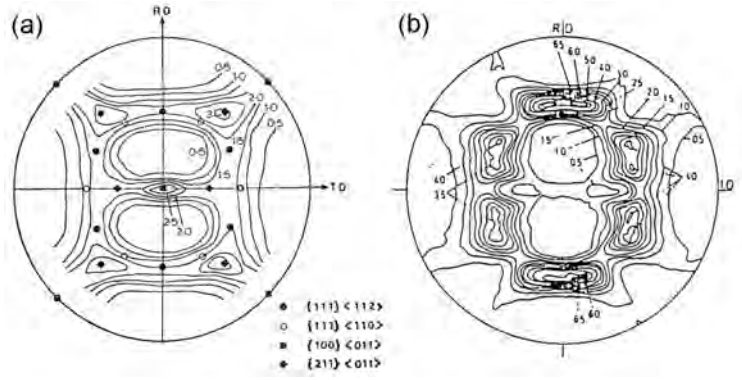

Figure 2.11 Typical (001) pole figures for (a) cold-rolled low-C steels [10], and (b) cold-rolled and annealed IF steels [11].

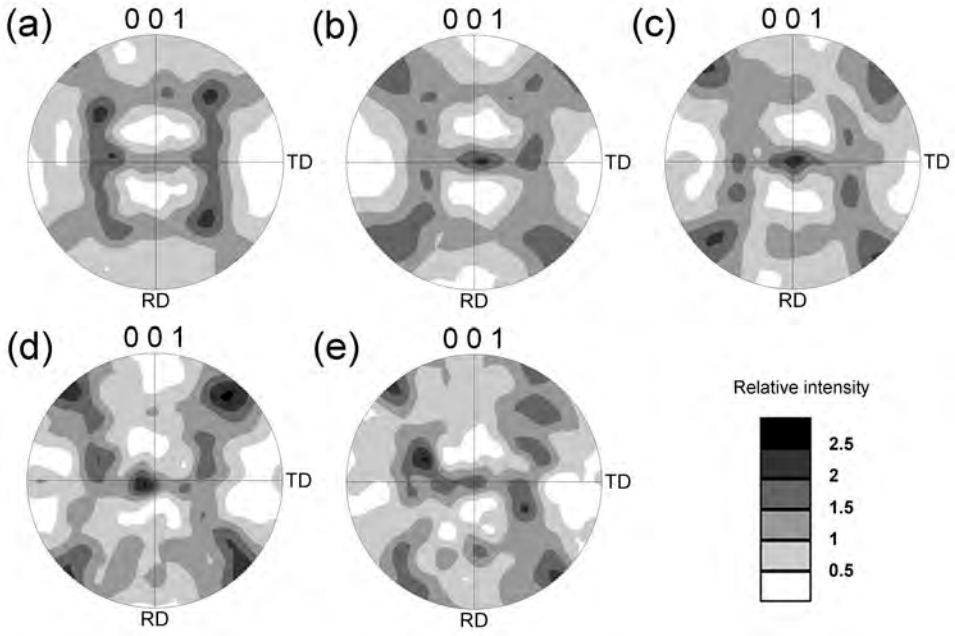

Figure 2.12 (001) Pole figures obtained by EBSD analysis of the low-C (UFG-FC1) steel. (a) After cold-rolling by 91 % reduction, (b-e) cold-rolled and annealed at various temperatures for 120 s followed by water-cooling to room temperature. The annealing temperatures are (b) 620 °C, (c) 635 °C, (d) 655 °C and (e) 680 °C.

In order to evaluate the change in the texture more quantitatively, ODF (orientation distribution function) analysis was carried out using the orientation data. The Bunge notation, in which the crystal rotations are described by three Euler angles, φ_1, Φ and φ_2, was employed. Figure 2.13 shows the $\varphi_2 = 0°$, 45° and 90° sections (in Bunge notation) of ODFs indicating major orientations in cubic crystals [13]. The two fiber components in the

cold-rolling or recrystallization texture in ferritic steels described above are seen in the φ_2 = 45° section of ODF. Other crystal orientations, i. e. <110> parallel to ND, appear in the φ_2 = 0°, 45° and 90° sections. Figure 2.14 shows φ_2 = 45° sections of ODFs showing typical cold-rolling and recrystallization textures in IF steels [12]. The ODF of the cold-rolled state (Fig. 2.14 (a)) shows the two fiber components (α-fiber and γ-fiber). On the other hand, in the recrystallization texture (Fig. 2.14 (b)), the crystal orientation near $(001)[1\bar{1}0]$ in the α-fiber is eliminated, and the orientations concentrate on the γ-fiber, compared with the cold-rolling texture. This is the case in IF steels, but it has been shown that low-C steels have similar cold-rolling and recrystallization textures to those in IF steels [10].

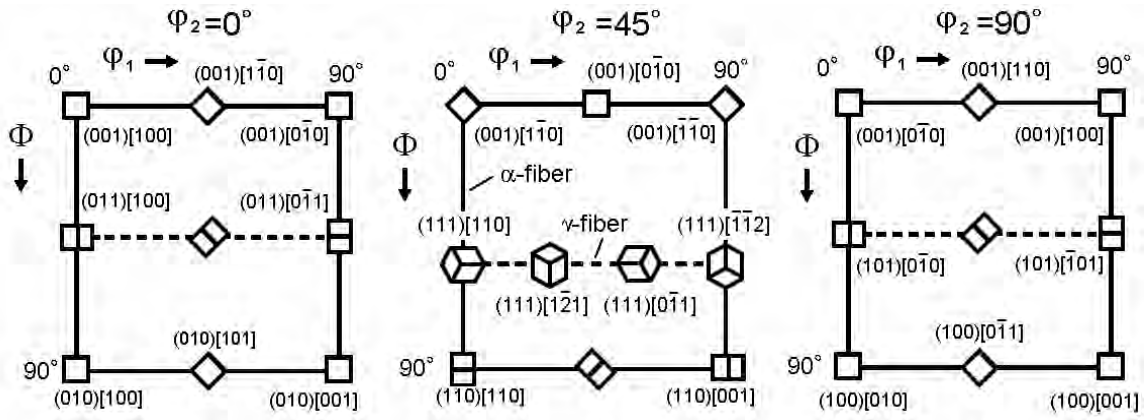

Figure 2.13 φ_2 = 0°, 45° and 90°sections (in Bunge notation) of ODFs and location of important cold-rolling and recrystallization texture components in ferritic steels [13].

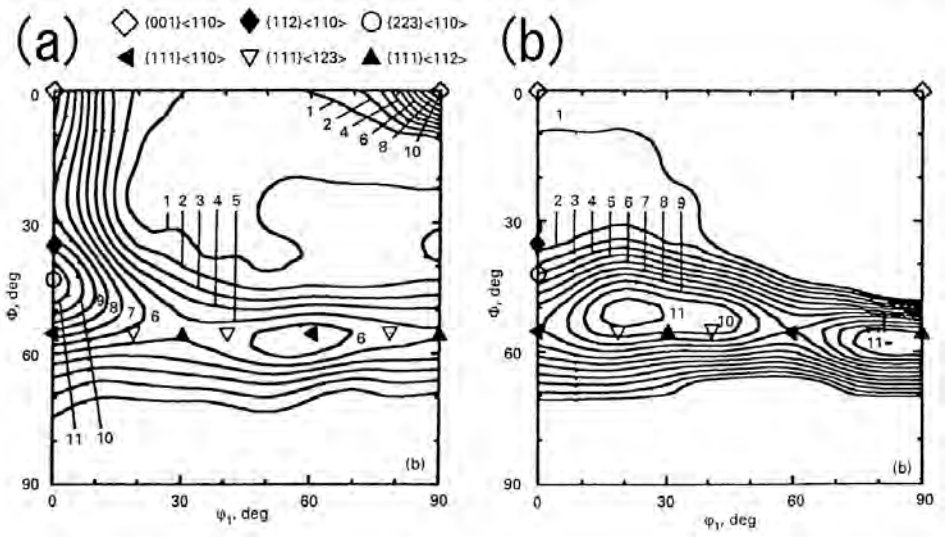

Figure 2.14 φ_2 = 45° sections (in Bunge notation) of ODFs of an IF steels. (a) After cold-rolling to 85% reduction and (b) after cold-rolling and subsequent annealing. Important texture components are also shown in the figures [12].

Next, the textures of the fabricated UFG ferrite microstructures in this study are shown. Figure 2.15 shows the ODFs (in Bunge notation) at various φ_2 values between 0 and 90° constructed by using the EBSD data of the fabricated UFG-FC1 steel after the 91% cold-rolling. The texture was close to the typical cold-rolling textures in low-C steels. For example, the $\varphi_2 = 45°$ section showed the concentration of crystal orientations on the α-fiber and γ-fiber, which was close to the cold-rolling texture in IF steel shown in Fig. 2.14 (a). Figure 2.16 shows the ODFs of the present UFG-FC1 steel cold-rolled and annealed at 620 °C. The texture was close to that of the cold-rolled specimen and different from the recrystallization texture of the conventional IF steels (Fig. 2.14 (b)) where the γ-fiber is dominant. On the contrary, the crystal intensity in the α-fiber was even enhanced in the present UFG ferrite microstructure. Figure 2.17 shows the texture of the specimen cold-rolled and annealed at 680 °C. The concentration of crystal orientations on the α-fiber and γ-fiber decreased, and other crystal orientations appeared. For example, the Euler angles of new orientations were (φ_1=0°, Φ =50-55°, φ_2 = 0°), (φ_1=0°, Φ =50-55°, φ_2 = 90°) and (φ_1= 60°, Φ =90°, φ_2= 45°). As seen in Fig. 2.13, these orientations had <110> poles close to ND. The appearance of these new orientations in Fig. 2.17 is consistent to the result in the ND orientation color map in Fig. 2.10 (d), showing the increase in the green and yellow grains.

Consequently, the UFG ferrite in the fabricated specimens in this study showed a texture close to the typical cold-rolled one, and it changed to that having relatively random orientation distributions during grain growth by increasing the annealing temperature.

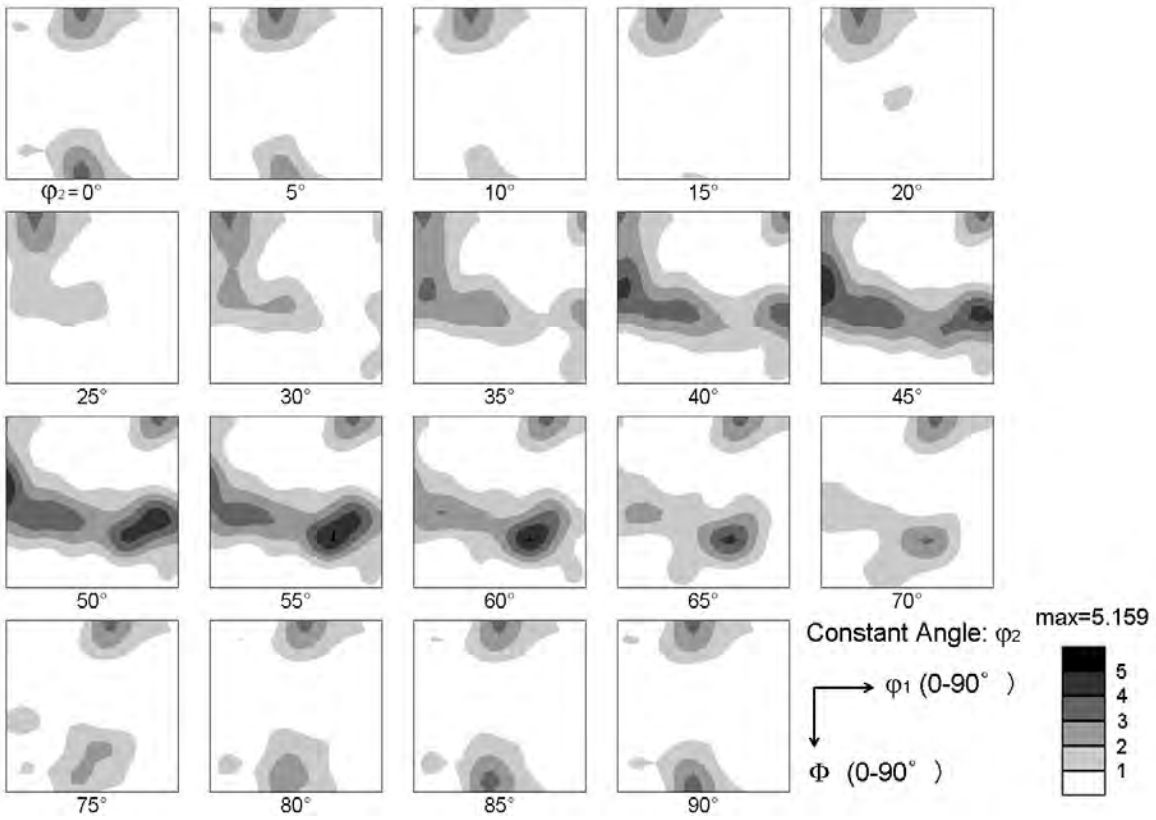

Figure 2.15 ODFs (in Bunge notation) of the low-C (UFG-FC1) steel cold-rolled by 91% reduction.

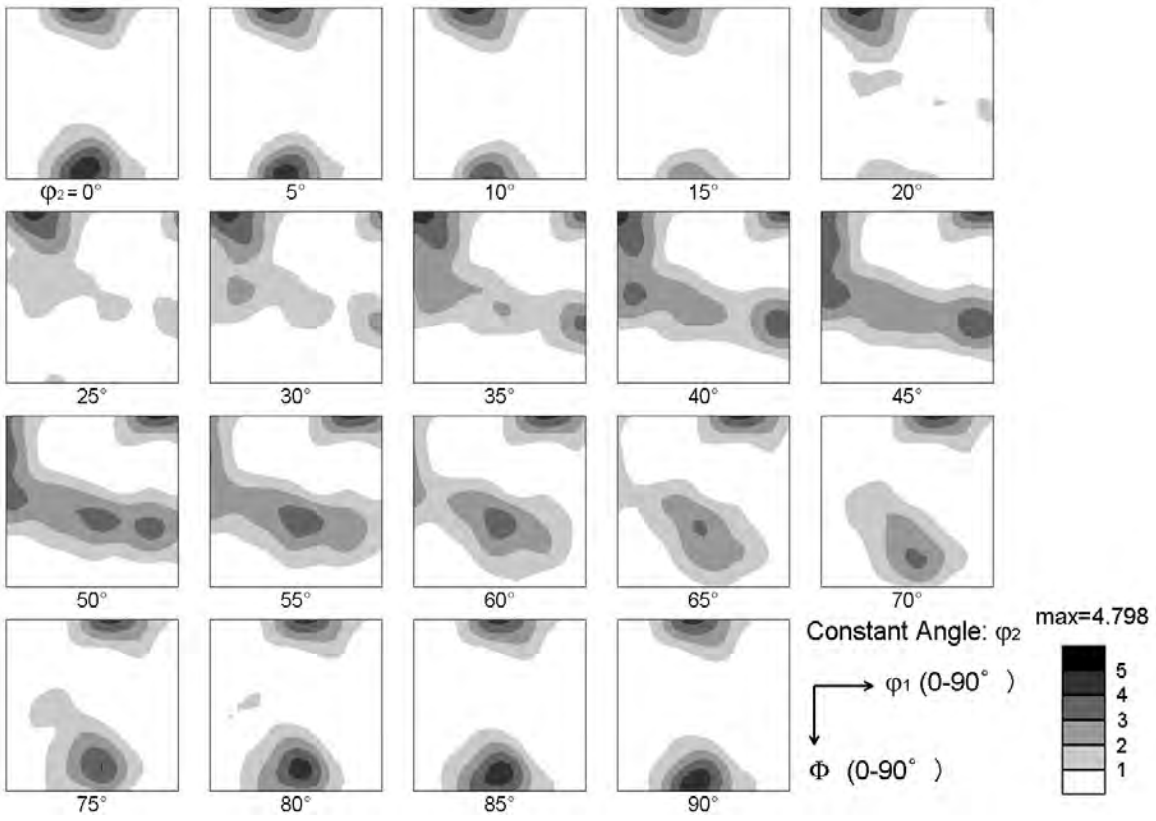

Figure 2.16 ODFs (in Bunge notation) of the low-C (UFG-FC1) steel cold-rolled by 91% reduction and annealed at 620 °C for 120 s.

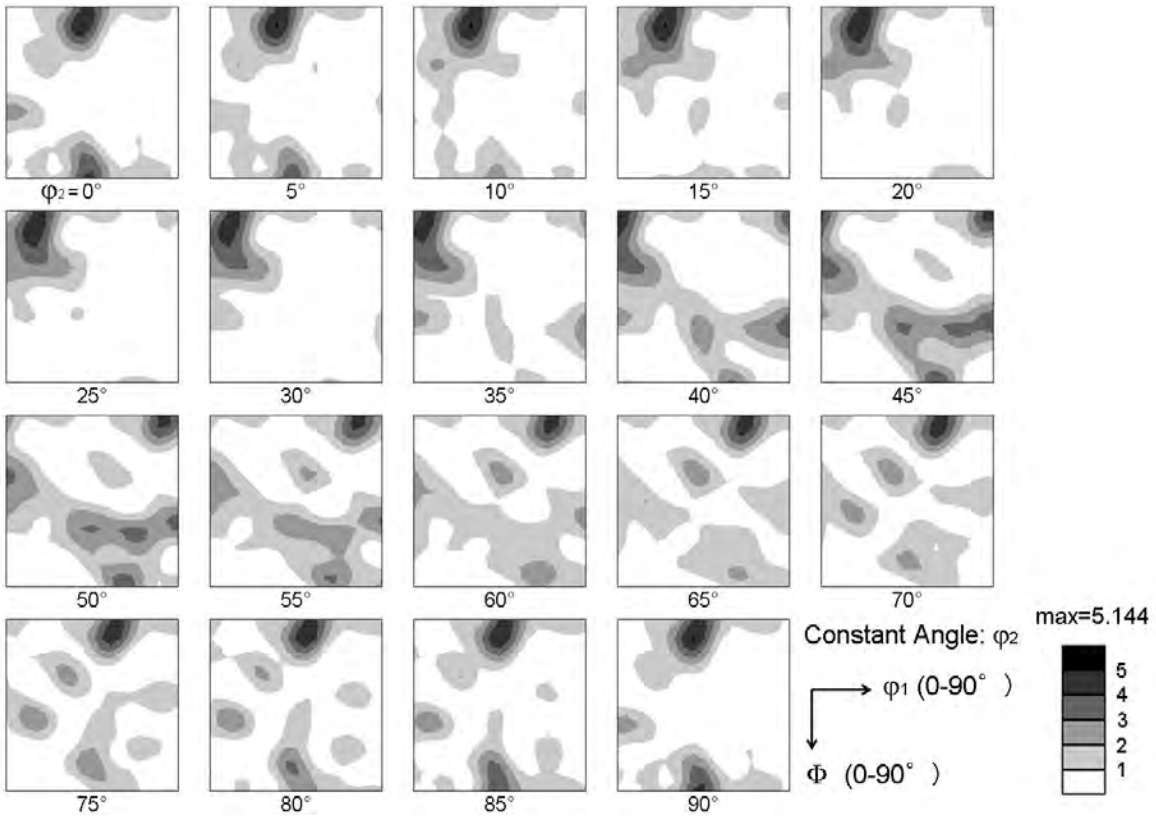

Figure 2.17 ODFs (in Bunge notation) of the low-C (UFG-FC1) steel cold-rolled by 91% reduction and annealed at 680 °C for 120 s.

2.1.5 Discussion

In the present process, UFG ferrite microstructures were obtained by relatively low plastic strain through conventional cold-rolling and annealing procedures. It is known that extremely high equivalent strain over 4 or 5 is required for producing the UFG microstructure through SPD [1]. However, the microstructural analysis of the present cold-rolled specimen revealed that large misorientations existed at the cold-rolled state although the equivalent strain applied was only 2.8. Fine lamellar structure was observed in the deformed ferrite (Fig. 2.4 and Fig. 2.5). Similar lamellar structures have been previously observed in heavily deformed metals. Hansen et al. [14] have shown a lamellar boundary structure with mean boundary spacing of about 0.3 μm in a commercial-purity aluminium heavily cold-rolled to a strain of 5. Tsuji et al. [15] have reported an elongated UFG microstructure with mean grain thickness of 0.21 μm in an ultra-low-C IF steel ARB processed by 5 cycles (equivalent plastic strain of 4.0) at 773K. It is noteworthy that the fine structure including large misorientations, which had been found in SPD processed materials, already existed in the cold-rolled state of the present material in spite of the relatively low plastic strain of 2.8. This result is attributed to the existence of hard martensite in the starting microstructure.

It is well known that hard second particles increase the rate of formation of HAGBs in the matrix through inhomogeneous deformation in two-phase metals and alloys [16]. This is because of the large local misorientation caused by local lattice rotations in the vicinity of the hard particles. In addition, shear strain should be closely related to the significant grain refinement of ferrite matrix. Kamikawa et al. [17] have reported that redundant shear strain introduced at sheet subsurface regions owing to large friction in rolling accelerates the microstructure refinement in the ARB of IF steel. The wavy-shaped ferrite and diamond-shaped martensite in Fig.2.3 suggested that large plastic strains including shear strain components were introduced into the ferrite matrix. It can be concluded that the local lattice rotations in the vicinity of the hard martensite, and the shear strain component introduced to the wavy microstructure accelerated the UFG ferrite formation.

On the other hand, the strain introduced to the martensite islands in the starting microstructure seemed not so high. Nevertheless, the deformed martensite had various orientations. Ueji et al. [3] have reported that 50% cold-rolled low-carbon martensite exhibited fine lamellar structure involving large misorientations, which was equivalent to the microstructure in SPD processed steels. This is thought to be attributed to the complicated and fine microstructure of the as-transformed martensite also involving high density of dislocations and grain boundaries. It can be concluded therefore that the strain applied to martensite in the present study was not very large but probably enough to introduce large local misorientations into the microstructure.

It is supposed that continuous coarsening of the finely subdivided regions together with recovery during the subsequent annealing formed the UFG equiaxed microstructure shown in Fig. 2.6. It is difficult to distinguish clearly which area in Fig. 2.6 was originally ferrite or martensite, but according to the supposed mechanism discussed above, the UFG ferrite could originate from both ferrite and martensite. On the other hand, some coarse

grains larger than 1 μm located in an arc-like row seen in the lower region of Fig. 2.6 (a) probably formed mainly by recovery of the elongated and bent ferrite regions such as that seen in the lower region of Fig. 2.3. Those ferrite regions in the cold-rolled microstructure seem to be deformed to smaller plastic strain because of the relatively low density of surrounding martensite islands. Also the fact that the coarse ferrite grains in the annealed microstructure contained few cementite particles suggests that they were originally ferrite.

In addition, it should be noted that the equiaxed ultrafine ferrite grains do not involve substructures within the grains, as shown in Fig. 2.7. That is, the obtained UFG structures having sub-micrometer grain size are equivalent to fully recrystallized grains. Such a structure has not been achieved before. Basically the ultrafine structures with sub-micrometer grain sizes formed through SPD processes are simultaneously deformation structures, and naturally contain dislocation substructures inside [18] even though they are subdivided by high-angle boundaries in sub-micrometer scales. As a result, it has been difficult to separate the effects of grain refinement and dislocation substructures on the mechanical properties of the UFG materials fabricated through SPD. In previous studies, when fully annealed and equiaxed grain structures were obtained through SPD and subsequent annealing, the grain sizes became over 1 μm [18]. In contrast, in the present study, the grain growth of the ultrafine ferrite grains during annealing was considerably suppressed at 620 to 635 °C. This is probably because of the high density of finely subdivided regions in the cold-rolled microstructure and the fact that the ferrite grains formed during annealing were already surrounded mostly by HAGBs.

Recently, Azizi-Alizamini et al. [19] fabricated a ferrite microstructure with bimodal ferrite grain size distribution by 50% cold-rolling and subsequent annealing of a ferrite-martensite dual-phase microstructure. The “bimodal” microstructure means that having two peaks in the grain size distribution profile. That study [19] aimed for improving strength-ductility combination, based on the results reported by Wang et al. [20] showing an improvement of strength without loss of ductility in “bimodal” microstructure of Cu. The microstructure obtained in reference [19] was a mixture of fine ferrite grains with grain sizes of 2 μm and coarse grains with sizes of 3 to 15 μm. Unfortunately, the strength of the material was not so high (tensile strength of 550 MPa) and the combination of strength and ductility was not so good. Uniform UFG ferrite was not obtained in that study [19], probably because the rolling reduction they took (50%) was smaller than that in the present case (91%), and not enough to get uniform UFG structures.

As seen in the boundary misorientation maps (Fig. 2.7), the present UFG ferrite microstructures had equiaxed ultrafine ferrite grains without dislocation substructures already, indicating the ferrite grains were equivalent to recrystallized ones. However, the texture analysis, that the textures of the present specimens at relatively lower annealing temperatures (620 to 635 °C) were close to the cold-rolling texture observed in low-C and IF steels. This result supports the mechanism discussed above. That is, the present UFG ferrite microstructures were formed mainly by continuous coarsening (or grain growth) of the very fine regions surrounded by HAGBs seen in the cold-rolled specimen (Fig. 2.4 and Fig. 2.5). Previous studies on the texture of UFG steels have shown similar behavior. Kamikawa [21] has shown that the texture of IF steel specimen ARB processed by 7 cycles

did not change so much during subsequent annealing up to 700 °C. It has been explained in Ref. [21] that the ultrafine ferrite grains existed at ARB processed state homogeneously grew with recovery at grain interior during the subsequent annealing, because the as ARB-processed specimen contained sufficient HAGB fraction. Song et al. [6] have shown, in the study on UFG low-C steel fabricated by warm-compression and subsequent annealing, that the texture of heavily deformed and annealed specimen still contained strong α-fiber component, and was different from that in IF steels [12]. They [6] have pointed out this behavior was due to microstructural formation by recovery and not by conventional recrystallization. The present results in the low-C UFG-FC1 steel annealed at 620 °C and 635 °C agree with the previous results [6, 12].

In the conventional recrystallization from deformed microstructures in steels, the change in hardness during the annealing is useful for confirming the occurrence of recrystallization (appearance of new grains without dislocation substructures). Generally the hardness suddenly drops at the "recrystallization temperature", which is around 650 °C in Nb-added IF steels [11]. Figure 2.18 shows Vickers hardness of the present UFG-FC1 specimens before and after the cold-rolling, and after the annealing at various temperatures for 120 sec. As annealing temperature increased up to 670 °C, the hardness continuously decreased. No sudden decrease in hardness was observed. This result supports the mechanism of the formation of the present UFG microstructures discussed above, e.g. continuous coarsening together with recovery of the fine regions having different crystal orientations in the cold-rolled microstructure.

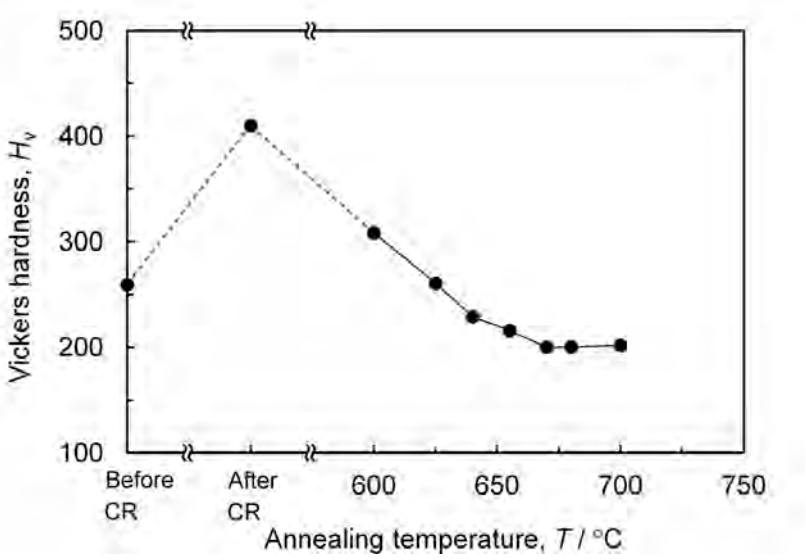

Figure 2.18 Vickers hardness of the UFG-FC1 steel before and after cold-rolling, and after the salt-bath annealing at various temperatures.

2.1.6 Summary

A new route to fabricate ultrafine grained ferrite microstructure through conventional cold-rolling and annealing was shown in this section. The obtained results are summarized below.

(1) UFG ferrite-cementite steel sheets with sufficiently large dimensions could be produced by conventional cold-rolling and subsequent short-time annealing, starting from duplex microstructure composed of ferrite and martensite. Only a plastic strain of 2.8 by cold-rolling was enough to obtain the equiaxed UFG ferrite throughout the specimen.

(2) During the cold-rolling, very fine lamellar structure containing small regions having various crystal orientations was formed in the ferrite matrix. Also the martensite was deformed to some extent through the cold-rolling. The strain introduced to the martensite was not so high, however various crystal orientations existed in the deformed martensite.

(3) The texture analysis revealed that the cold-rolling texture remained after the annealing at 620 °C. This result suggested that the fine regions having various orientations in the cold-rolled specimen grew continuously during the subsequent annealing and formed the equiaxed UFG ferrite microstructure.

(4) The strain distribution between soft ferrite matrix and hard martensite in this process was the key factor for fabricating the UFG microstructures. That is, large and complex strain was introduced to the soft phase (ferrite), while the strain introduced to the hard phase (martensite) was not so high but sufficient to form the ultrafine regions having various crystal orientations.

It can be concluded that the present process effectively provides the UFG steel sheets with sufficient dimensions, and is not only applicable to industrial production of UFG steel sheets (from practical viewpoint) but also useful for the further systematic study on the mechanical properties of the UFG steels (from academic viewpoint).

2.2 Effect of process conditions on ultrafine grained ferrite formation in rolling and annealing of duplex microstructures

2.2.1 Introduction

In the former section, it was shown that UFG ferrite microstructures could be obtained through a simple process composed of rolling and annealing of a duplex microstructure. The key factor in this process is the strain distribution between soft phase (ferrite) and hard phase (martensite). Therefore, it is necessary to clarify the amount of the strain distribution between those phases. In the first part of this section, strain distribution between ferrite and martensite is investigated by analyzing the microstructures before and after cold-rolling (CR). Next, the effects of process conditions on the UFG ferrite formation are investigated and discussed. Two important factors in this process, CR reduction and spacing of martensite islands in the starting microstructure, are varied and their effects are shown. The first factor, CR reduction directly affects the plastic strain applied to ferrite matrix and martensite. Therefore, it seems that a critical CR reduction for obtaining the UFG ferrite exists. In the second part of this section, the effect of CR reduction on the microstructural changes during CR and annealing is shown. The spacing of martensite islands in the starting microstructure seems to affect the amount of strain concentration in ferrite grains surrounding the martensite islands. In the third part of this section, using a refined duplex microstructure as starting material, the effect of the spacing of martensite islands on the UFG microstructure formation is shown and discussed.

2.2.2 Experimental procedure

Three kinds of hot-rolled steel sheets having various duplex microstructures were prepared in this section for the different purposes: (1) A low-C steel prepared for investigating the strain distribution between ferrite and martensite during CR, which is called “LC steel” hereafter. (2) The same hot-rolled steel sheets as used in section 2.1 (UFG-FC1 steel) for investigating the effect of CR reduction. (3) Another low-C steel named "UFG-FC2 steel" which had the same chemical composition as the UFG-FC1 steel, but had a refined duplex microstructure, for investigating the effect of microstructural refinement before CR.

Figure 2.19 shows the procedure for investigating the strain distribution between ferrite and martensite during CR. The LC steel of which chemical composition is shown in Table 2.3 was melted and cast in a vacuum furnace. The ingot was hot-rolled at a FT of 775 °C in austenite region, and cooled by water to room temperature. The 10 mm thick hot-rolled sheet was cold-rolled to a thickness of 4 mm with lubrication, and then heat-treated at 765 °C corresponding to intercritical region of ferrite and austenite for 60 minutes, and then water-quenched. By this heat treatment, a duplex microstructure

composed of ferrite and martensite was obtained. After pickling in HCl in order to remove the oxide layer, the heat-treated sheets were cold-rolled with lubrication. The thicknesses of the specimens after the CR were 2.0, 1.2, 0.8 and 0.6 mm, corresponding to reductions in thickness of 50%, 70%, 80% and 85%, respectively.

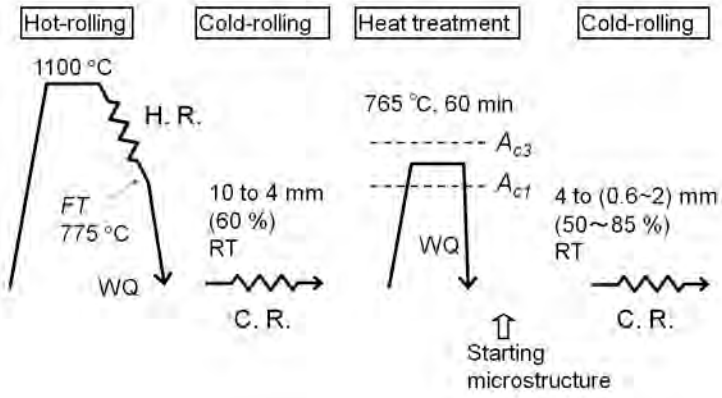

Figure 2.19 Schematic drawing of the procedure for fabricating the starting microstructure having a duplex microstructure and cold-rolling, to investigate the strain distribution between soft and hard phases. A_{c1} and A_{c3} mean the transformation temperatures measured by dilatometer. The A_{c1} and A_{c3} are 720 °C and 825 °C, respectively.

Table 2.3 Chemical composition (mass%) of the low-C (LC) steel used for investigating the effect of cold-rolling reduction on strain distribution between ferrite and martensite.

C	Si	Mn	P	S	Al	Nb	N
0.099	0.01	2.00	0.001	0.002	0.023	0.053	0.0005

Figure 2.20 shows the process for investigating the effect of CR reduction by using the UFG-FC1 steel. The chemical composition is summarized in Table 2.4. The conditions before the CR are the same as those described in section 2.1. An ingot prepared by vacuum-melting was hot-rolled to a thickness of 6.8 mm at a FT of 770 °C in austenite region, air-cooled to 540 °C corresponding to the intercritical region of ferrite and austenite, and then water-cooled to room temperature. The hot-rolled sheet having a duplex microstructure was cold-rolled with lubrication to various thicknesses. The cold-rolled sheets having various total CR reductions from 85 to 94 % were prepared. The cold-rolled sheets were annealed at various temperatures ranging from 525 to 700 °C for 120 sec in a salt bath and cooled by water to room temperature.

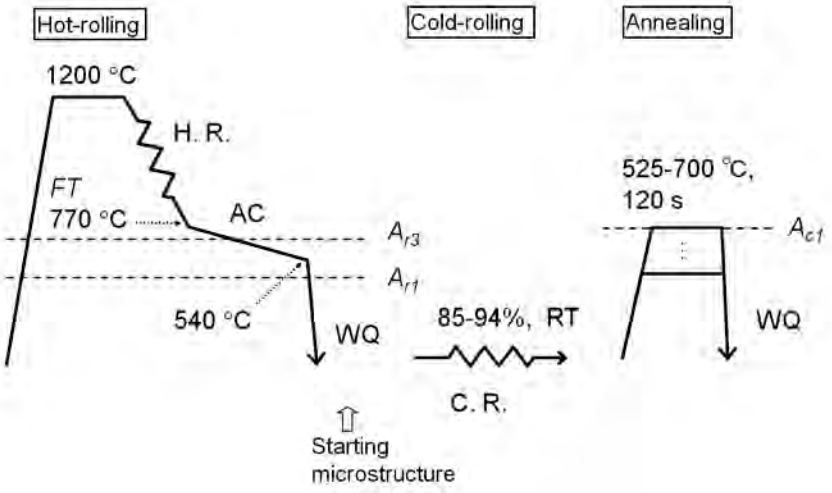

Figure 2.20 Schematic drawing of the process for investigating the effect of cold-rolling reduction on the UFG microstructure formation using the UFG-FC1 steel. A_{r1}, A_{r3}, and A_{c1} mean the transformation temperatures measured by dilatometer. The A_{r1}, A_{r3}, and A_{c1} are 465 °C, 625 °C and 700 °C, respectively.

Table 2.4 Chemical composition (mass%) of the low-C (UFG-FC1) steel used for fabricating ultrafine grained ferrite-cementite microstructures.

C	Si	Mn	P	S	Al	Nb	B	N
0.10	0.01	1.98	0.002	0.001	0.018	0.018	0.0015	0.0011

Figure 2.21 shows a schematic drawing of the procedures for investigating the effect of microstructural refinement before CR. Table 2.5 summarizes the chemical composition of the steel, named "UFG-FC2 steel", of which chemical composition is substantially the same as that of the UFG-FC1 steel shown in Table 2.4. The ingot was hot-rolled to a thickness of 10 mm at a FT of 900 °C in austenite region and immediately cooled to room temperature by water. The hot-rolled sheet was then annealed at 1000°C for 90 minutes and water-quenched to room temperature in order to form uniform martensite microstructure. Next, the sheet was again reheated to 770°C, corresponding to intercritical region of ferrite and austenite for 60 minutes, and water-quenched to room temperature. Finally, the sheet showed a fine duplex microstructure composed of ferrite and martensite. The hot-rolled and intercritically annealed sheet was mechanically grinded to a thickness of 8 mm and cold-rolled by various reductions from 71 to 88%. The final thickness varied from 1 to 2.3 mm. The cold-rolled sheets were annealed at various temperatures ranging from 525 to 700 °C for 120 sec in a salt bath.

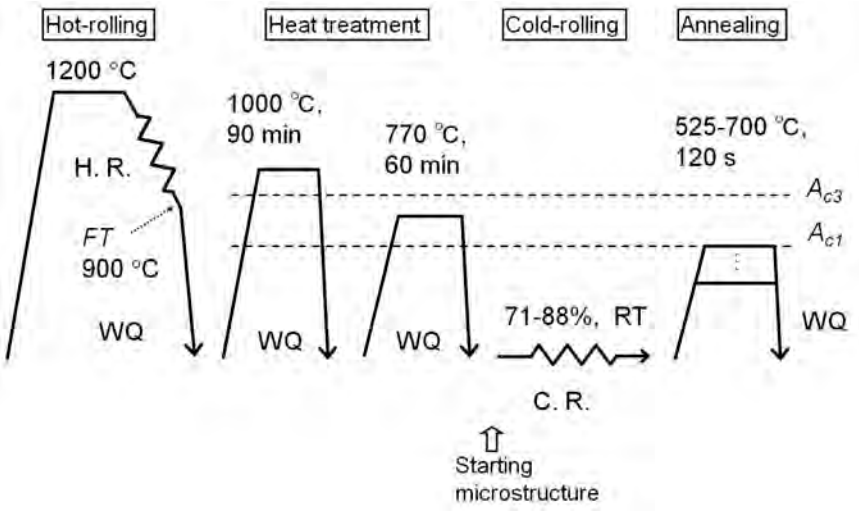

Figure 2.21 Schematic drawing of the procedures for investigating the effect of microstructural refinement before cold-rolling on the UFG microstructure formation using the UFG-FC2 steel. A_{c1} and A_{c3} mean the transformation temperatures measured by dilatometer. The A_{c1} and A_{c3} are 699 °C and 832 °C, respectively.

Table 2.5 Chemical composition (mass%) of the low-C (UFG-FC2) steel used for fabricating ultrafine grained ferrite-cementite microstructures.

C	Si	Mn	P	S	Al	Nb	B	N
0.10	0.01	2.00	0.002	0.001	0.035	0.022	0.0015	0.0007

Microstructural observations were carried out for the specimens at each stage of the processes. All the specimens were observed from TD of the sheets. The samples for OM or SEM were etched with a 3% nital. SEM observations were conducted on Hitachi S-4300E/N SEM operated at 15 kV. EBSD analysis was also carried out by using Hitachi S-4300E/N SEM equipped with TSL OIM system operated at 15 kV. The EBSD scanning was carried out at thickness center on the TD section. The mapping was carried out at a step size of 0.05 μm on a hexagonal grid. For evaluating the ferrite grain size, mean intersection method, using the optical micrographs and SEM micrographs, was employed. The lines parallel to ND and those parallel to RD were drawn on the micrographs, and the intersection lengths of ferrite grains on the lines along both directions were measured and averaged. Also the mean thicknesses of ferrite and martensite were measured by using the mean intersection method, for evaluating the change in thickness of each phase after the CR. The lines parallel to ND were drawn on the optical micrographs or SEM micrographs before and after the CR, and the intersection lengths of ferrite and martensite were measured. Using the data for average thickness of each phase before and after CR, equivalent strains in each phase were calculated by using the equation (2.1) assuming plane strain compression. The volume fractions of each phase were measured by point-counting method using the optical micrographs and SEM micrographs.

2.2.3 Strain distribution between ferrite and martensite during rolling deformation of duplex microstructure

First, the strain distribution between ferrite and martensite during CR is shown. Figure 2.22 shows an optical micrograph of the starting microstructure (before CR) of the LC steel. A duplex microstructure composed of ferrite (white region) and martensite (dark gray region) was obtained. The martensite existed mainly at ferrite grain boundaries and had network-shape. This is because the microstructure was fabricated by reheating a deformed microstructure to the intercritical region. During the heat treatment at intercritical region, austenite formed mainly at ferrite grain boundaries or triple junctions, and then transformed to martensite in the subsequent water-quenching, resulting in the network-shape of the martensite. The mean thicknesses of ferrite and martensite along ND were 2.88 and 1.85 μm, respectively. The martensite volume fraction was 46%.

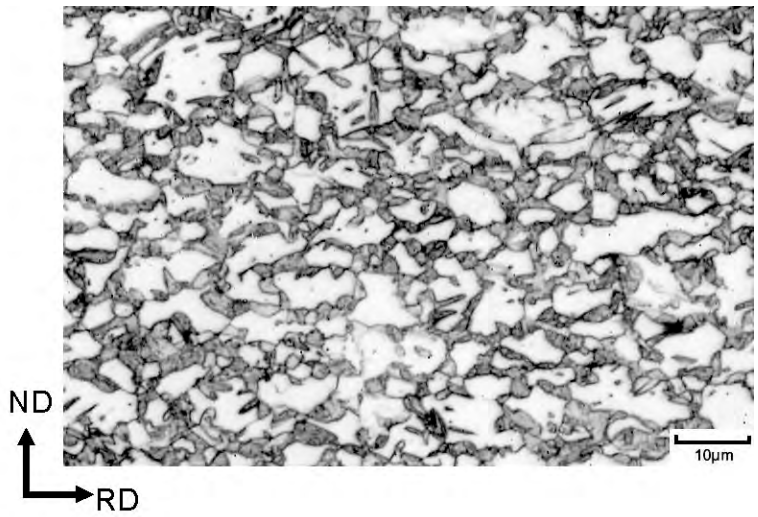

Figure 2.22 Optical micrograph of the LC steel before cold-rolling. The microstructure was composed of ferrite (white region) and martensite (gray region). Observed from TD.

Figure 2.23 shows SEM microstructures after CR of the starting microstructure shown in Fig. 2.22, by various CR reductions. The dark gray region and the light gray region are ferrite and martensite, respectively. It was shown that the spacing of martensite (light gray islands) decreased as the CR reduction increased from 50 to 85%. The wavy flow of the ferrite, as shown in Fig. 2.3, was not clear at the CR reduction of 50%, however it was observed at the CR reductions of 70% or higher. As well as the ferrite matrix, the martensite regions were also deformed to some extent even at low CR reduction of 50%. Figure 2.24 shows equivalent strains in ferrite and martensite, ε_F and ε_M, as a function of CR reduction of the specimen, R. The ε_F was always higher than ε_M at all the CR reductions, indicating the strain concentration to the softer ferrite during CR.

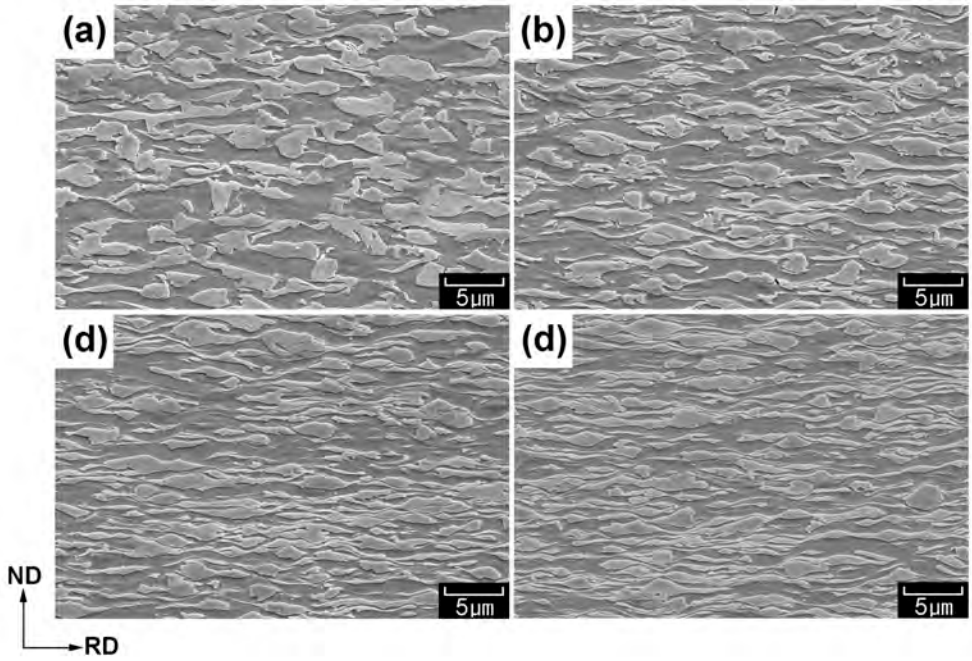

Figure 2.23 SEM microstructures after cold-rolling of the duplex microstructure shown in Fig. 2.22 by reductions of (a) 50%, (b) 70%, (c) 80% and (d) 85%. Observed from TD.

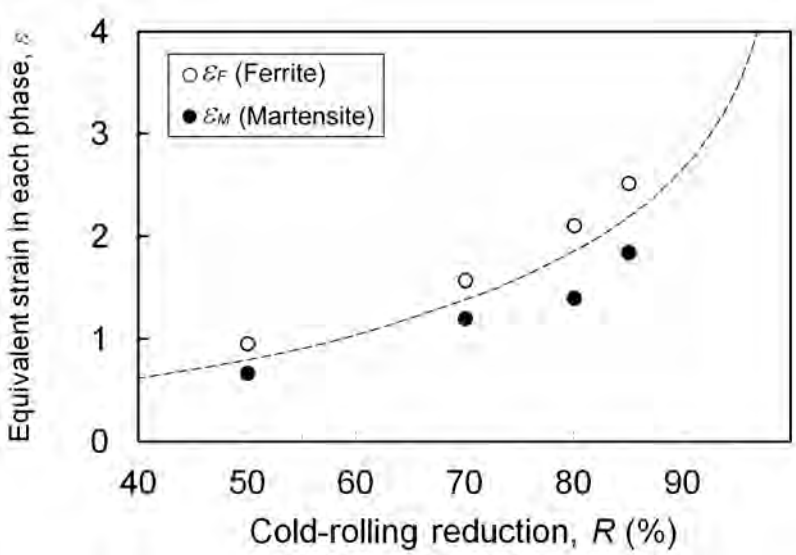

Figure 2.24 Equivalent strain in ferrite and martensite, ε_F and ε_M, as a function of cold-rolling reduction, R, of the LC steel. The ε_F and ε_M were calculated using mean thickness of each phase measured on the OM image before cold-rolling (Fig. 2.22) and the SEM microstructures after cold-rolling (Fig. 2.23). The broken line indicates equivalent strain of the specimen assuming plane strain compression.

2.2.4 Effect of cold-rolling reduction on ultrafine grained ferrite formation

The effect of CR reduction on the UFG ferrite formation after the subsequent annealing is investigated using the UFG-FC1 steel. The hot-rolled sheet of which microstructure was shown in Fig. 2.2 was used as starting material. Figure 2.25 (a, d, g)

show SEM microstructures of the specimens cold-rolled by reductions of 85%, 91% and 94% in thickness, respectively. The dark gray region and the light gray region are ferrite and martensite, respectively. The ferrite matrix exhibited wavy microstructure elongated roughly to RD and bent along the martensite islands having diamond-shapes. In the 85% cold-rolled specimen (Fig. 2.25 (a)), some regions had relatively larger spacings between martensite islands (i.e. the large ferrite area with small amount of martensite islands in the center left region of the SEM micrograph). In those regions, the ferrite did not show significant wavy shape. When the CR reductions were 91% and 94%, almost all the ferrite regions showed wavy and complex shape, and the spacing of martensite significantly decreased (Fig. 2.25 (d, g)).

Figure 2.25 (b, e, h) show the microstructures after annealing at 600 °C of the three kinds of cold-rolled sheets. In the specimen 85 % cold-rolled and annealed at 600 °C (Fig. 2.25 (b)), many equiaxed ultrafine ferrite grains were observed. However, elongated ferrite grains in an arc-like raw were also observed. When the CR reduction was 91 % or larger, the specimens were filled mostly with equiaxed ultrafine ferrite grains (Fig. 2.25 (e, h)). At the annealing temperature of 650 °C (Fig. 2.25 (c, f, i)), significant grain growth occurred in all the CR reductions. Fine cementite particles dispersed in ferrite grains were also observed in all annealed specimens in Fig.2.25.

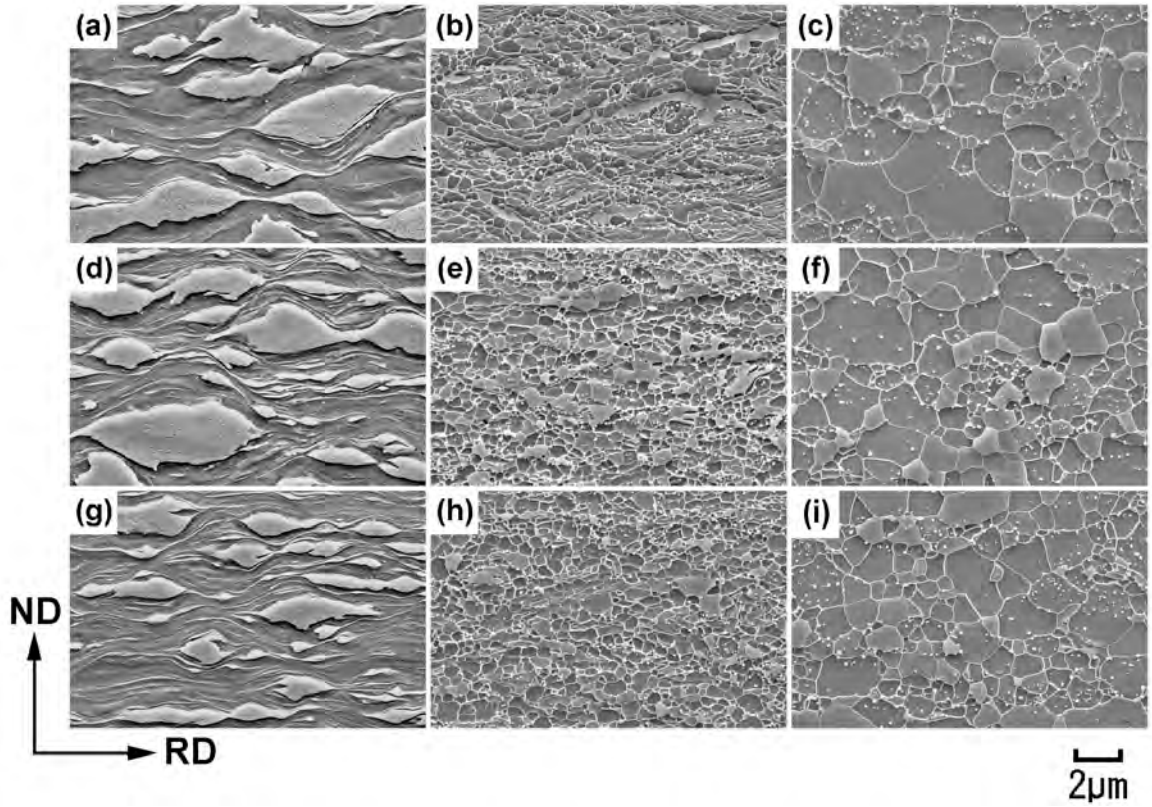

Figure 2.25 SEM microstructures of (a, d, g) cold-rolled specimens, (b, e, h) specimens annealed at 600 °C after cold-rolling, and (c, f, i) specimens annealed at 650 °C after cold-rolling of the UFG-FC1 steel. The cold-rolling reductions are (a, b, c) 85%, (d, e, f) 91% and (g, h, i) 94%. Observed from TD.

Figure 2.26 shows the relationship between annealing temperature and mean ferrite grain size measured on the SEM micrographs. The larger the CR reduction was, the smaller the obtained ferrite grain size was. However, the effect of annealing temperature on the ferrite grain size was more significant. The minimum grain size of the homogeneous grain structures obtained was 0.43 μm in the specimen 94 % cold-rolled and then annealed at 600 °C (Fig. 2.25 (h)).

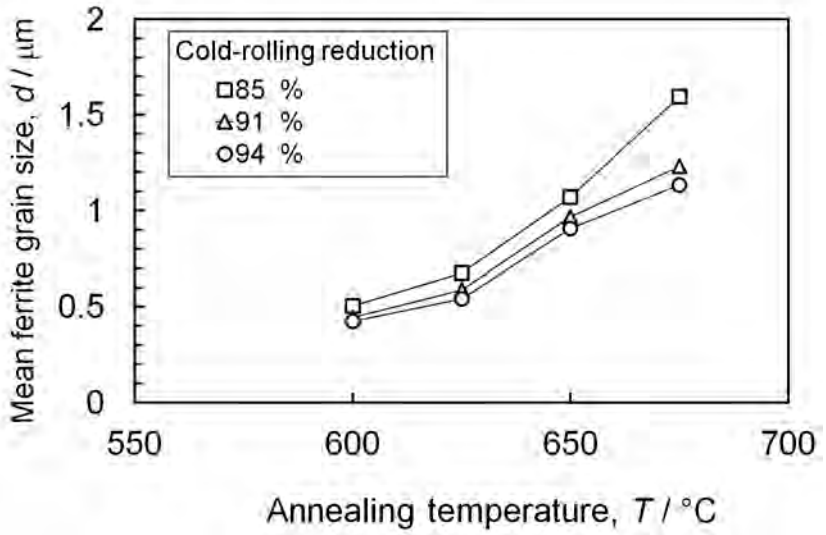

Figure 2.26 Relationship between annealing temperature and mean ferrite grain size of the UFG-FC1 steel.

Figure 2.27 shows a microstructure of the specimen (UFG-FC1) after 94% CR and subsequent annealing at 525 °C for 120 sec. Dotted lines roughly indicate the former martensite islands, which had already changed to fine-grained ferrite and cementite. In the ferrite matrix, UFG ferrite formed along the wavy microstructure in the vicinity of the former martensite. The ferrite grain size was finer at the interface regions between former martensite and ferrite matrix. This result suggests that the interface region is one of the important nucleation sites of UFG ferrite during annealing.

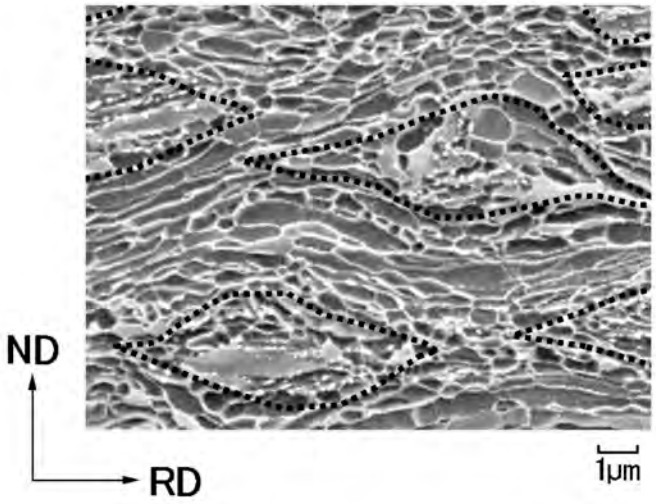

Figure 2.27 SEM microstructure of the low-C (UFG-FC1) steel cold-rolled by 94% reduction, annealed at 525 °C for 120 s and water-cooled to room temperature.

2.2.5 Effect of grain refinement in starting microstructures on ultrafine grained ferrite formation

Figure 2.28 shows a SEM microstructure of the hot-rolled and heat-treated UFG-FC2 steel sheet (starting microstructure before CR). It showed a duplex microstructure composed of fine ferrite (dark gray region) and martensite (light gray region). The martensite islands in the ferrite matrix showed fine lamellar or needle-shapes. It has been reported that similar microstructure was obtained in low-C steels by quenched from austenite region and subsequently annealed at intercritical region [22, 23]. The formation process of the fine microstructure shown in Fig. 2.28 is described below. Through the heat-treatment at 1000 °C for 90minutes followed by water-cooling, "lath-martensite" formed. During the subsequent heating to intercritical region, first, the martensite changed to ferrite-cementite microstructure keeping the needle-like shape, and then austenite formed at the boundaries of the fine ferrite grains as the temperature of the specimen exceeded the A_{c1} transformation temperature. Finally the austenite transformed to martensite again during water-quenching. The mean intersection lengths along ND of the ferrite and martensite regions on the SEM microstructure shown in Fig. 2.28 were 1.72 μm and 1.96 μm, respectively. The spacing of the martensite islands (mean intersection length of the ferrite region) was quite smaller than that in the UFG-FC1 steel after hot-rolling shown in Fig. 2.2. The area fraction of martensite was 43%, which was close to that in the hot-rolled UFG-FC1 steel. Consequently, a refined duplex microstructure composed of ferrite and martensite was obtained by annealing of the hot-rolled sheet.

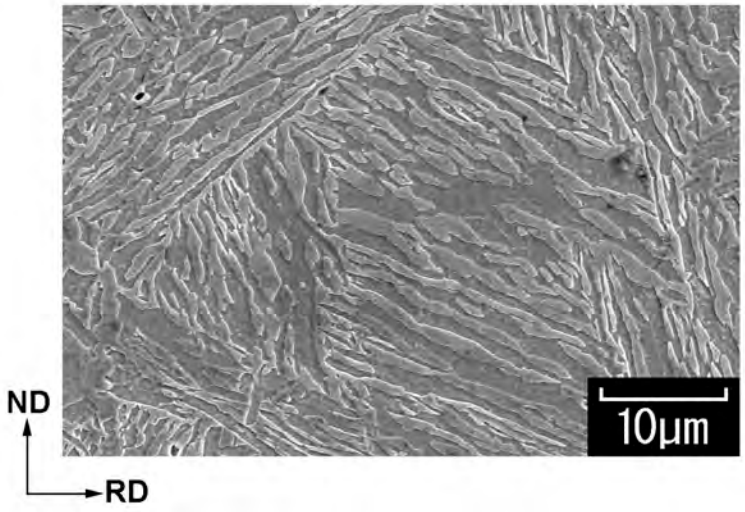

Figure 2.28 SEM microstructure of the starting microstructure (before cold-rolling) of the UFG-FC2 steel, showing a refined duplex microstructure. Observed from TD.

Figure 2.29 (a, d, g) show SEM microstructures of the specimens cold-rolled by reductions of 71%, 80% and 88% in thickness, respectively. The ferrite matrix (dark gray region) exhibited wavy microstructure elongated roughly to RD and bent along the martensite islands (light gray region). This feature was similar to that in the microstructures after CR of the UFG-FC1 steel shown in Fig. 2.3 and Fig. 2.25. However, the spacing of the

martensite islands was much smaller than that in the UFG-FC1 steel cold-rolled. For example, the martensite spacing in the specimen cold-rolled by 71% reduction (Fig. 2.29 (a)) was much smaller than that of the UFG-FC1specimen cold-rolled to 85% (Fig. 2.25 (a)). The martensite islands were also deformed to some extent during the CR and showed diamond-shapes. Although the martensite islands in the starting microstructure (Fig. 2.28) had various angles from RD, the martensite regions in the cold-rolled specimens were almost parallel to RD. This fact indicates that large amount of rotation in the lamellar microstructure occurred during CR.

Figure 2.29 (b, e, h) show SEM microstructures after CR and subsequent annealing at 575 °C. In the 71 % cold-rolled and annealed specimen (Fig. 2.29 (b)), the microstructure was filled mostly with equiaxed ultrafine ferrite grains. At higher CR reductions of 80 and 88 % (Fig. 2.29 (e, h)), also equiaxed UFG ferrite was observed throughout the specimens. When the specimens were annealed at 650 °C, significant grain growth occurred in all specimens (Fig. 2.29 (c, f, i)), which was similar to the former case shown in Fig. 2.25. The minimum CR reduction and annealing temperature for obtaining the equiaxed UFG ferrite microstructure was 71% and 575 °C, respectively. The necessary CR reduction and annealing temperature in order to form uniform UFG ferrite were significantly decreased by the refinement the starting microstructure.

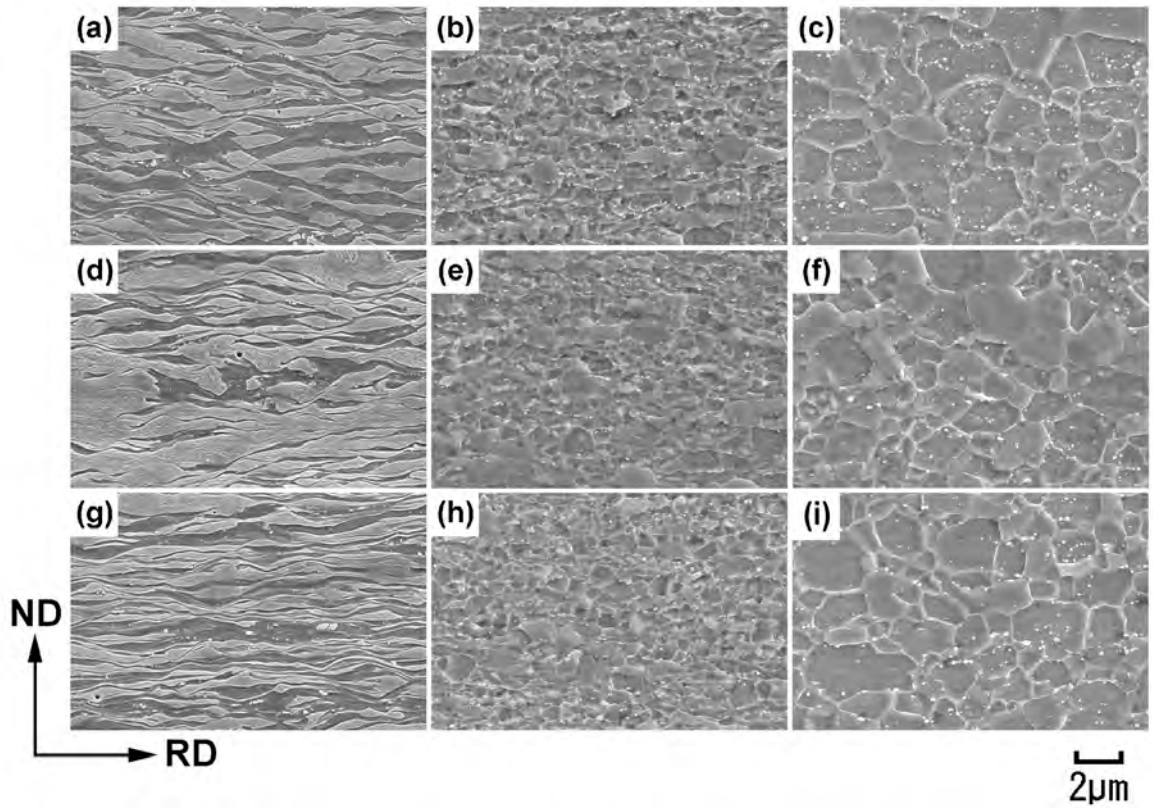

Figure 2.29 SEM microstructures of (a, d, g) cold-rolled specimen, (b, e, h) specimens annealed at 575 °C after cold-rolling and (c, f, i) specimens annealed at 650 °C after cold-rolling of the UFG-FC2 steel. The cold-rolling reductions are (a, b, c) 71%, (d, e, f) 80% and (g, h, i) 88%. Observed from TD. The starting microstructure is shown in Fig. 2.28.

Next, the data obtained by EBSD analysis are shown. Figure 2.30 shows IQ maps, grain boundary (GB) maps and ND orientation color maps of the specimens annealed at 575 °C after CR. Three specimens having CR reductions of 71%, 80% and 88%, were investigated. The narrow gray lines in the GB maps (Fig. 2.30 (b, e, h)) indicate LAGBs of which misorientation angles are 2 to 15 degrees, and the bold lines indicate HAGBs of which misorientation angles are larger than 15 degrees. The fraction of HAGBs in the annealed specimens at CR reductions of 71%, 80% and 88% were 83%, 78% and 68%, respectively. The decrease in the HAGBs fraction by increasing the CR reduction will be discussed later. The mean ferrite grain sizes calculated in the EBSD analysis (the diameter of equivalent circle) of the annealed specimens at CR reductions of 71%, 80% and 88% were 0.39, 0.39 and 0.36 μm, respectively. The ferrite grain size did not change regardless the CR reduction. The EBSD analysis revealed that the equiaxed ultrafine ferrite mostly surrounded by HAGBs was formed even at low CR reduction of 71%. The refinement of the starting microstructure certainly decreased the critical CR reduction and annealing temperature for forming the equiaxed UFG ferrite microstructure. In the ND orientation maps in Fig. 2.30 (c, f, i), it was shown that all specimens having various CR reductions showed various orientations. In addition, it is seen that the orientations near <111> gradually increased as the CR reduction increased up to 88%.

Figure 2.31 shows (001) Pole figures constructed from the EBSD data of the specimens annealed at 575 °C. The specimen having CR reduction of 71% (Fig. 2.31 (a)) exhibited relatively random texture having dispersed crystal orientations, which was close to that in the UFG-FC1 steel 91% cold-rolled and annealed at 680 °C (Fig. 2.12 (e)). When the CR reduction increased up to 88%, the orientations on the γ-fiber component seemed to increase, and became close to the recrystallization texture in conventional low-C steels (Fig. 2. 11 (b)).

In order to clarify the texture change more quantitatively, ODF analysis was also carried out using the orientation data. Typical CR and recrystallization textures in φ_2= 45° section of the ODFs have been shown already (see Fig. 2.14). Figure 2.32 shows ODFs (in Bunge notation) at various φ_2 values between 0 and 90 degrees of the UFG-FC2 steel cold-rolled to 71% and annealed at 575 °C. The orientations on the α-fiber and γ-fiber components were observed in φ_2= 45° section of the ODFs (see typical textures in Fig. 2.14), however the concentration was not so high. The texture seemed to be close to that in the UFG-FC1 specimen cold-rolled to 91% and annealed at 680 °C (Fig. 2.17). Figure 2.33 shows the ODFs of the UFG-FC2 steel cold-rolled to 88% and annealed at 575 °C. The concentration of orientations along γ-fiber was clearly observed. Also the orientations on α-fiber were observed, but the intensity was relatively weak at the orientation {001} <110> (for example, φ_1= 0°, Φ =0°, φ_2= 45°). The increase in the {111} grains by the increase in the CR reduction, shown in the ODF analysis is consistent to the increase in the blue grains in the ND orientation color map (Fig. 2.30 (i)).

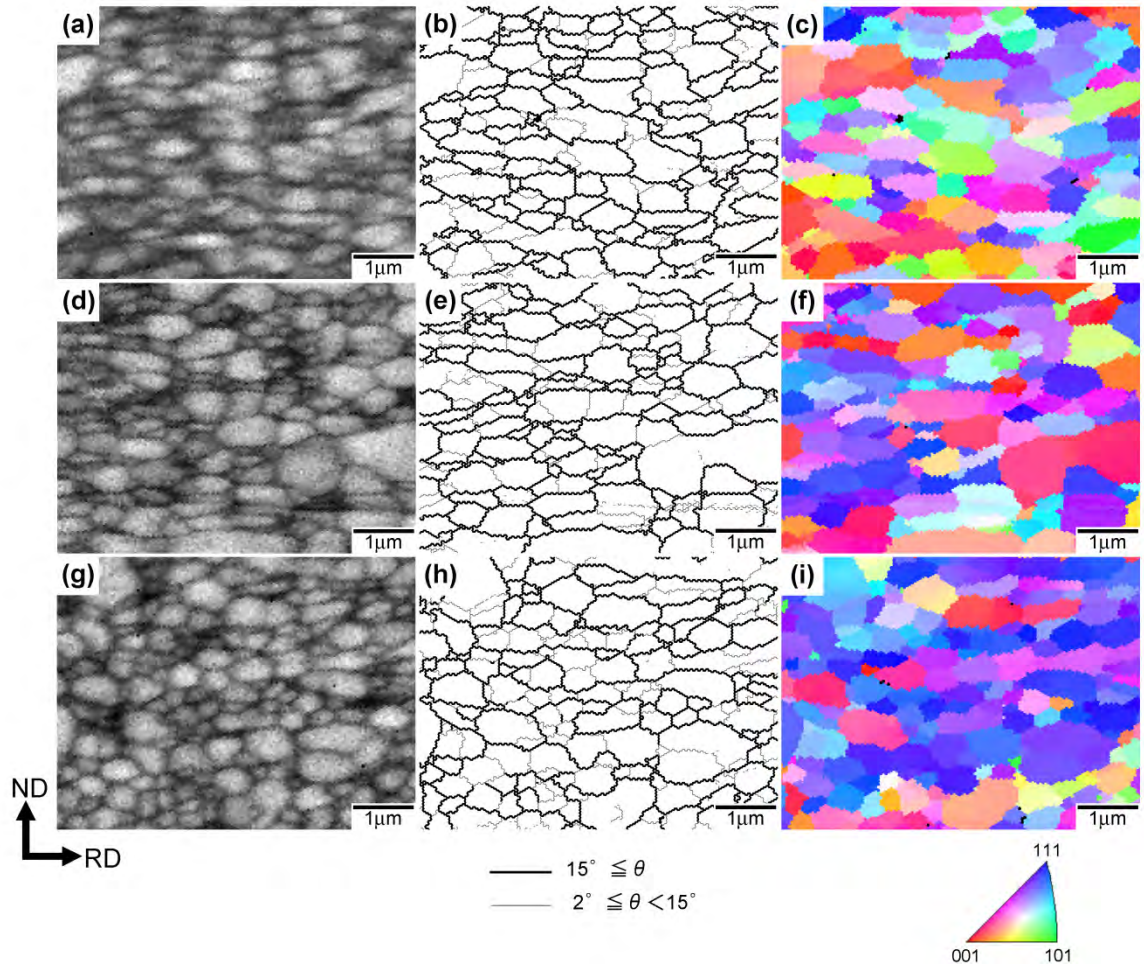

Figure 2.30 (a, d, g) Image quality (IQ) maps, (b, e, h) grain boundary (GB) maps and (c, f, i) ND orientation color maps obtained by EBSD analysis of the UFG-FC2 specimens annealed at 575 °C. The cold-rolling reductions are: (a, b, c) 71%, (d, e, f) 80% and (g, h, i) 88%. The narrow gray lines in (b, e, h) indicate low-angle grain boundaries (LAGBs) and the bold lines indicate high-angle grain boundaries (HAGBs).

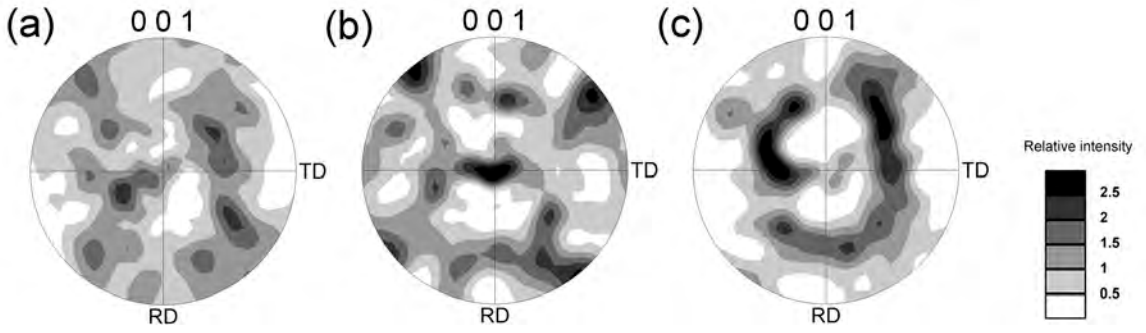

Figure 2.31 (001) Pole figures obtained by EBSD analysis of the low-C (UFG-FC2) steel cold-rolled by various reductions, annealed at 575 °C for 120 s and water-cooled to room temperature. The cold-rolling reductions are (a) 71%, (b) 80% and (c) 88%.

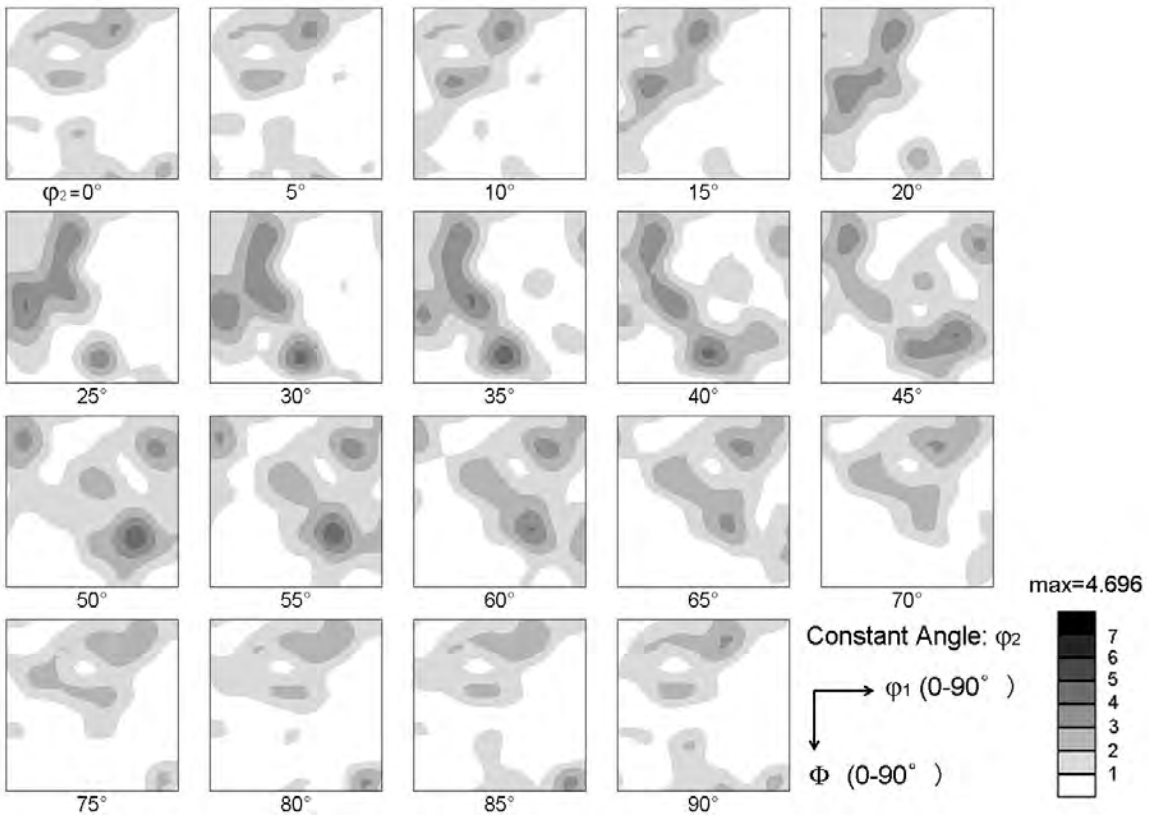

Figure 2.32 ODFs (in Bunge notation) of the UFG-FC2 steel cold-rolled by 71% reduction and annealed at 575 °C for 120 s and water-cooled to room temperature.

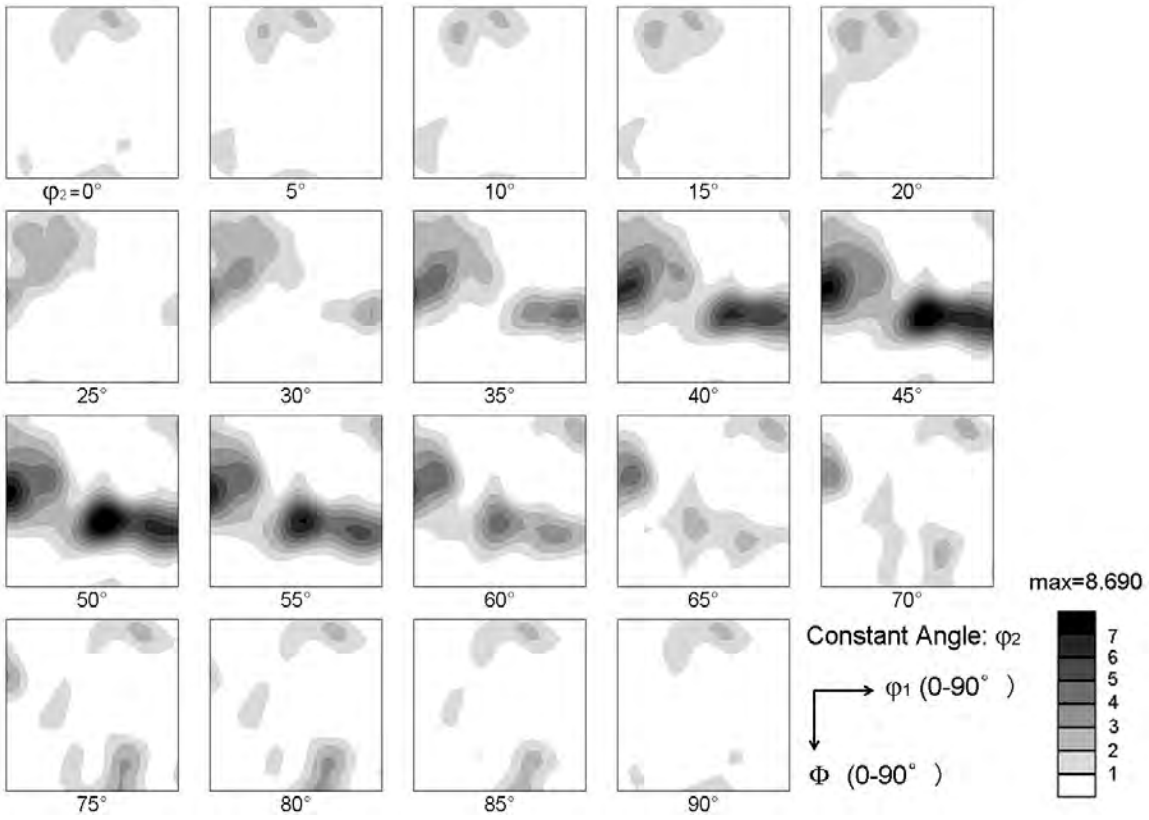

Figure 2.33 ODFs (in Bunge notation) of the UFG-FC2 steel cold-rolled by 88% reduction and annealed at 575 °C for 120 s and water-cooled to room temperature.

2.2.6 Discussion

In section 2.2.3, strain distribution between soft ferrite and hard martensite during the CR was investigated. As shown in Fig. 2. 24, it was clarified that the strain distribution certainly occurred during CR of the duplex microstructure. When the duplex microstructure of the LC steel was cold-rolled, the equivalent strain in the soft ferrite regions was larger than that in the hard martensite regions at all the CR reductions between 50 and 85%. This result was caused by the difference in hardness between those two phases. As the CR reduction increased, the wavy microstructures in the ferrite matrix appeared. This result indicated that the strain introduced into the ferrite matrix became more complex when the CR reduction increased. This was because the complex plastic flow such as shearing and bending in the ferrite regions in the vicinity of hard martensite happened more often at higher CR reductions.

Next, the effects of CR reduction and annealing temperature on microstructural formation in the UFG-FC1 steel were investigated. The critical CR reduction for achieving uniform UFG ferrite was 91%. In the case of 85% reduction, some ferrite grains having elongated and arc-like shape were observed after annealing (Fig. 2. 25 (b)). These grains seemed to be formed by recovery of the deformed ferrite grains having relatively smaller strain concentration during CR. For example, nearly straight morphology of cold-rolled ferrite matrix seen at the left center region in Fig. 2.25 (a) which probably had relatively small plastic strain seemed to change to the elongated and arc-like ferrite in subsequent annealing. Consequently, the strain concentration in the ferrite regions was insufficient at the CR reduction of 85%.

Here, the strain introduced into the ferrite regions in the UFG-FC1 steel during the CR is evaluated by the same way as described in section 2.2.3. Figure 2.34 shows equivalent strain in ferrite and martensite, ε_F and ε_M, as a function of CR reduction, R. Data of the LC steel are plotted again, and data of the UFG-FC2 steel, which will be discussed later, are also plotted. It is seen that ε_F was always higher than ε_M. However, when R was 91% in the UFG-FC1 steel, ε_F was about 3. The measured equivalent strain values might contain some errors, i.e., probably under-estimation of the equivalent strain in ferrite, due to the simple measurement of thickness of each phase using SEM micrographs. The equivalent strain around 3 was still smaller than the necessary plastic strain for obtaining UFG microstructures in typical SPD processes, i.e. 4 to 5. In spite of relatively low strain, uniform UFG ferrite microstructure formed in the present process.

As discussed in section 2.1.5, the additional shear strain component introduced into the ferrite regions due to the existence of hard martensite seemed to accelerate the UFG ferrite formation effectively. When the ferrite regions in the present duplex microstructures were deformed in shear, the interface regions between ferrite and martensite seemed to be deformed heavily because hard martensite did not deform so much. It is well known that hard second particles increase the rate of formation of HAGBs in the matrix through inhomogeneous deformation in two-phase metals and alloys [14]. This is due to local lattice rotations in the vicinity of the hard phase, resulting in large local misorientations [14]. In Fig. 2.27, it was shown that finer ferrite grains formed at the interface regions between former

martensite and ferrite matrix. This result indicated that the formation of UFG regions having various orientations in CR effectively occurred at the interface regions of ferrite and martensite, and that the interface region was one of the important nucleation sites of UFG ferrite grains in annealing. It is expected that the increase in the interface regions may accelerate the formation of UFG ferrite.

In practice, the increase in the area of the interface region in the starting microstructure was achieved by refining the duplex starting microstructure. For this purpose, the refined duplex microstructure shown in Fig. 2.28 was prepared. Using this microstructure, the critical CR reduction required for the uniform UFG ferrite formation decreased down to 71%. This result can be explained by the increase of the interface regions between ferrite and martensite through the microstructural refinement, and the increase of UFG ferrite formation by local lattice rotation at the interface regions. In addition, the small spacing of the martensite islands seemed to concentrate effectively the plastic strain introduced into the ferrite matrix.

The ε_F and ε_M in the UFG-FC2 steel are shown in Fig. 2.34. When R was 71%, ε_F was about 1.8, which was very small. Here, as shown in Fig. 2.28, the directions of the fine lamellar in the duplex microstructure before the CR were random. On the other hand, in the cold-rolled microstructure (Fig. 2.29 (a)), the directions of the lamellar of the deformed martensite and ferrite were almost parallel to RD of the specimen. Therefore, some lamellar regions perpendicular to RD in the starting microstructure rotated by nearly 90 degrees during CR. The strain introduced to such regions should be very high. It is assumed that in the UFG-FC2 steel, in addition to the refinement of the starting microstructure, the random directions of the lamellar duplex structure in the starting microstructure accelerated the formation of the UFG regions, resulting in the decrease in the critical CR reduction for forming the uniform UFG ferrite microstructure.

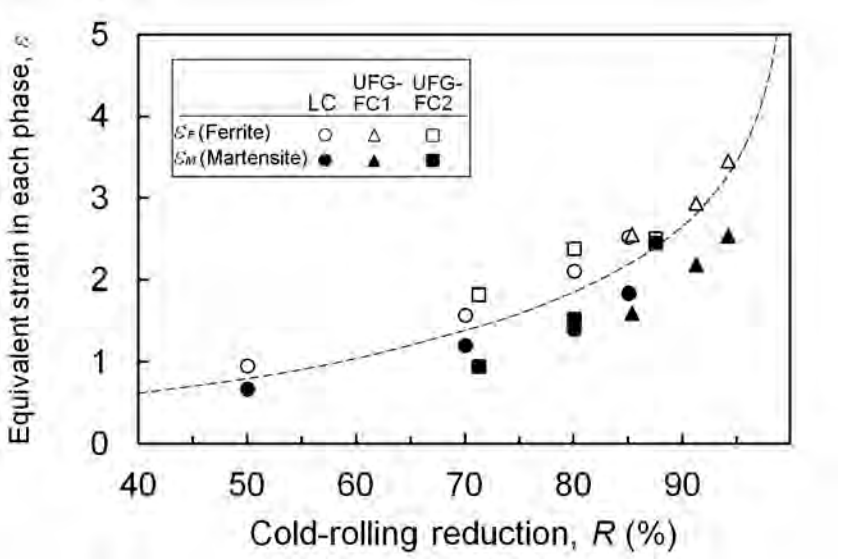

Figure 2.34 Equivalent strain in ferrite and martensite, ε_F and ε_M, as a function of cold-rolling reduction, R, of the LC, UFG-FC1 and UFG-FC2 steels. The ε_F and ε_M were calculated using mean thickness of each phase measured on OM image before cold-rolling and the SEM microstructures after cold-rolling. The broken line indicates equivalent strain of the specimen assuming plane strain compression.

The textures of the annealed specimens of the UFG-FC2 steel shown in Fig. 2.30 to 2.33 are discussed here. The texture significantly changed depending on the CR reduction. As the CR reduction increased up to 88%, the intensity of γ-fiber component significantly increased. In the ODF maps of the 88% cold-rolled and annealed specimen shown in Fig. 2.33, the texture component in the conventional recrystallization texture seen in IF steels (Fig. 2.14 (b)) seemed to be dominant, rather than the cold-rolling texture (Fig. 2.14 (a)). In section 2.1.5, it has been pointed out that the UFG ferrite microstructures in the present UFG-FC1 steel were formed by continuous coarsening together with recovery of the deformed grains having sub-micrometer sizes and cold-rolling texture. This was because the textures after the annealing were close to that in the cold-rolled specimen. However, in the UFG-FC2 specimen cold-rolled to 88%, the texture after the annealing was different, suggesting that the microstructural formation behavior changed at the CR reduction of 88% in the UFG-FC2 steel. In the conventional recrystallization of cold-rolled sheet steels (nucleation and growth process), it is thought that the regions having {111} orientations parallel to ND in the cold-rolled microstructures have higher stored energy, and recrystallization nuclei appear preferentially in such regions during subsequent annealing [10]. In addition, it is well known that the fraction of {111} grains increases as the CR reduction increases [10]. Therefore, it is possible to consider as follows. In the UFG-FC2 specimen cold-rolled to 88%, due to the very fine starting microstructure and high CR reduction, {111} regions in the cold-rolled microstructure had very high stored energy, in other words, high driving force for the recrystallization. It might result in the preferential growth of the {111} region during subsequent annealing. Here, as seen in Fig. 2.31 (h, i), many LAGBs existed at the interfaces between blue grains. It can be assumed that the {111} regions having similar crystal orientations in the cold-rolled microstructure grew and contacted to each other during annealing, remaining LAGBs at the interface.

2.2.7 Summary

In section 2.2.3, the strain distribution between ferrite and martensite during cold-rolling of a duplex microstructure was investigated. Next, the effects of process conditions on the UFG ferrite formation were investigated in sections 2.2.4 and 2.2.5. The effects of cold-rolling reduction, annealing temperature and refinement of the starting microstructure were shown and discussed. The obtained results are summarized below.

(1) During cold-rolling of a duplex microstructure composed of ferrite and martensite, strain distribution between these two phases was observed at cold-rolling reductions higher than 50%. Introduced strain into ferrite was always higher than that into martensite at all the cold-rolling reductions.

(2) The critical cold-rolling reduction required for forming uniform UFG ferrite microstructure after cold-rolling and subsequent annealing was 91% in case of the UFG-FC1 steel. At this cold-rolling reduction, the equivalent strain in ferrite during cold-rolling was about 3. This value was still smaller than the typical plastic strain required in the SPD processes for fabricating UFG microstructures. It was supposed that the additional shear strain component in the ferrite region effectively accelerated the UFG ferrite formation.

(3) In the microstructure after cold-rolling and annealing at low temperature, the ferrite grains were finer at the interface regions between ferrite and former martensite. This result indicated that relatively high strain was introduced into the interface regions.

(4) Based on the result above, a refined duplex microstructure was prepared in order to accelerate the UFG ferrite formation by increasing interface regions between ferrite and martensite, and decreasing the spacing of martensite. The critical cold-rolling reduction for forming uniform UFG ferrite microstructure was reduced down to 71% in this case.

2.3 Effect of martensite volume fraction in starting microstructures on ultrafine grained ferrite formation

2.3.1 Introduction

In the former sections, the martensite volume fractions in the starting duplex microstructures were almost constant (42 to 46%). The martensite fraction in the starting microstructure is expected to affect the behavior of microstructure formation, however its effect has not been clarified yet. In this section, using a low-C steel similar to those in the former sections, the volume fraction of martensite in the starting microstructures was changed from 0 to 100 % by heat-treatment at various temperatures. The obtained microstructures were cold-rolled and annealed, and final microstructures were investigated in order to clarify the optimum martensite fraction in the starting microstructures for the UFG ferrite formation.

2.3.2 Experimental procedure

The chemical composition of the steel used in this section is shown in Table 2.6. The two-phase region of ferrite and austenite during heating at 2 °Cs^{-1} was between 700 °C and 820 °C in this steel according to dilatometer measurement. Figure 2.35 shows the process applied in this investigation. First, an ingot of the steel prepared by vacuum-melting was hot-rolled to a thickness of 10 mm at a FT of 800 °C in austenite region, air-cooled to room temperature and cold-rolled to a thickness of 6 mm. The 6 mm thick sheets were heat-treated at various temperatures ranging from 680 to 1000 °C and water-quenched to room temperature in order to obtain various starting microstructures. Some sheets were additionally heat-treated at 500 °C. The 6 mm thick sheets having various microstructures were mechanically grinded to a thickness of 5 mm and cold-rolled to a thickness of 1 mm at room temperature. The cold-rolling (CR) was carried out in multi-passes using a four-high rolling mill with lubrication. The total reduction in thickness through the cold-rolling was 80%, corresponding to an equivalent plastic strain of 1.86. Finally the cold-rolled sheets were annealed at various temperatures ranging from 400 to 750 °C in a salt bath followed by water-cooling to room temperature.

Microstructural observations for the specimens at each stage of the process were carried out by SEM. All the microstructures were observed on the longitudinal sections perpendicular to TD (TD section) of the sheets. EBSD analysis was also carried out by using HITACHI S-4300SE/N FE-SEM equipped with TSL orientation image microscope (OIM) system. The EBSD scanning was carried out at the thickness center on the TD section, in a 12 μm × 8 μm area at a step size of 0.05 μm on a hexagonal grid. Mean ferrite grain size was measured by mean intersection method using the optical micrographs and SEM micrographs. The lines parallel to ND and the lines parallel to RD were drawn on the micrographs, and

the intersection lengths of ferrite grains by the lines along both directions were measured and averaged. Vickers hardness of the specimens was measured on the TD section, using the specimens prepared for SEM observation. The measurement was carried out for three times at the thickness center with a load of 1 kgf.

Table 2.6 Chemical composition (mass%) of the low-C steel used for investigating the effect of martensite volume fraction in the starting microstructures on UFG ferrite formation after cold-rolling and annealing.

C	Si	Mn	P	S	Al	Nb	Mo
0.099	0.004	1.98	0.002	0.001	0.016	0.021	0.30

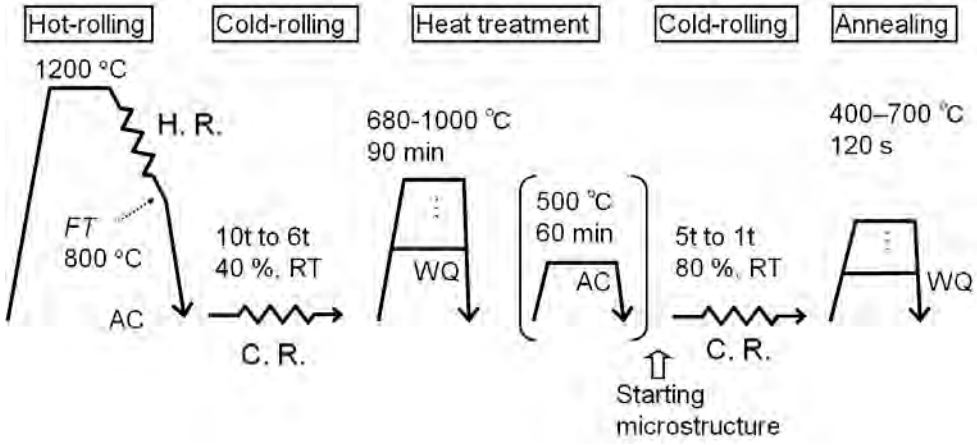

Figure 2.35 Schematic drawing of the process for investigating the effect of martensite volume fraction in the starting microstructures on UFG ferrite formation after cold-rolling and annealing.

2.3.3 Microstructural change during the process

The heat-treatment conditions of the 6 mm thick sheets and obtained starting microstructures are summarized in Table 2.7. The specimen A, heat-treated at 680 °C that is below A_{c1} transformation temperature, showed fully ferrite-cementite (FC) microstructure. The specimens B, C and D were heat-treated at intercritical regions of ferrite and austenite, therefore they had dual-phase (DP) microstructures composed of ferrite and martensite. The specimen E was heat-treated at austenite region and water-quenched to room temperature, therefore it showed full-martensite. The specimen F, which was heat-treated in the same condition as that in the specimen C and then additionally heat-treated at 500 °C, had a microstructure composed of ferrite and tempered martensite. The purpose for making of the specimen F is to confirm the effect of hardness of the second phase on the UFG ferrite formation after cold-rolling and annealing.

Table 2.7 Heat-treatment conditions of the hot-rolled sheets and obtained microstructures as starting microstructures before cold-rolling.

Specimen No.	Heat- treatment condition	Post-heat-treatment condition	Microstructure	Martensite volume fraction (%)
A	680 °C, 90 min.	-	F-C	0
B	720 °C, 90 min.	-	F-M	29
C	750 °C, 90 min.	-	F-M	45
D	800 °C, 90 min.	-	F-M	64
E	1000 °C, 90 min.	-	M	100
F	750 °C, 90 min.	500 °C, 60 min.	F-TM	(44*)

F: Ferrite, C: Cementite, M: Martensite, TM: Tempered Martensite

*Volume fraction of tempered martensite for the specimen F.

Figure 2.36 shows SEM microstructures of the 6 mm thick sheets after the heat-treatment (starting microstructures). The heat-treatment conditions of the specimens are summarized in Table 2.7. The specimen A showed ferrite-cementite (FC) microstructure. The specimens B, C and D showed DP microstructures composed of soft ferrite matrix (dark gray regions) and hard martensite islands (light gray regions). The martensite fraction of the starting microstructures was measured by point-counting method using the SEM microstructures shown in Fig.2.36, and the results are summarized in Table 2.7. The martensite volume fraction in the starting microstructures of the specimens B, C and D were 29%, 45% and 64%, respectively. The specimen E showed 100% martensite microstructure (Fig. 2.24 (e)). The martensite volume fraction varied widely from 0 to 100 % depending on the heat-treatment temperature. The microstructure of the specimen F, shown in Fig.2.36 (f), was composed of ferrite and tempered martensite. The volume fraction of the tempered martensite in the whole microstructure was 44% in the specimen F, which was almost the same as that of martensite in the specimen C.

Figure 2.37 shows SEM microstructures after 80% CR of the microstructures shown in Fig. 2.36. In the cold-rolled microstructure of the specimen A (Fig. 2.37 (a)), elongated ferrite grains containing dispersed cementite particles were observed. This is common in cold-rolling of FC microstructures. In the specimens B, C and D (Fig. 2.25 (b, c, d), the ferrite matrix (dark gray region) exhibited wavy microstructure elongated roughly to RD and bent along the martensite islands (light gray region). It was indicated that complex plastic flow occurred and higher strain was introduced into the softer ferrite matrix owing to the existence of hard martensite phase. This behavior has been already observed in former sections. In the specimen E (Fig. 2.37 (e)) of which starting microstructure was full-martensite, elongated martensite laths were observed. In the specimen F (Fig. 2.37 (f)), ferrite matrix was elongated roughly to RD and showed wavy microstructure, however the bent in the ferrite matrix was not so significant, compared with the specimen C. The tempered martensite islands in the specimen F did not show obvious diamond-like shapes, indicating that the

tempered martensite deformed to larger amount than the “as-quenched” martensite in the specimen C.

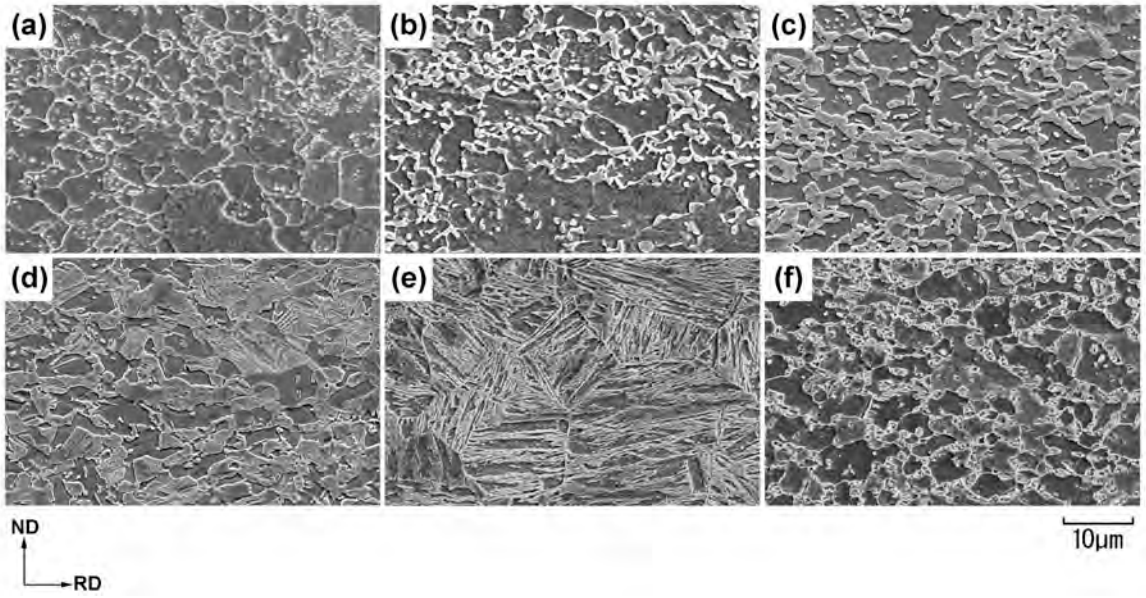

Figure 2.36 SEM Microstructures of the 6 mm thick sheets after the heat-treatment (starting microstructure). (a) Specimen A, (b) specimen B, (c) specimen C, (d) specimen D, (e) specimen E and (f) specimen F. Observed from TD.

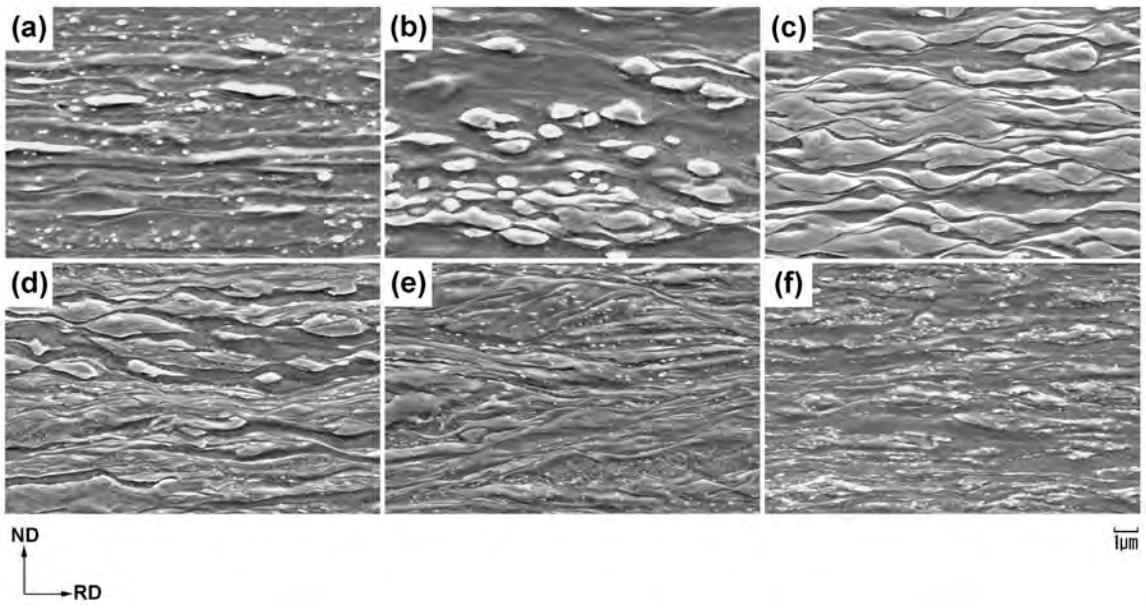

Figure 2.37 SEM Microstructures after 80% cold-rolling of (a) specimen A, (b) specimen B, (c) specimen C, (d) specimen D, (e) specimen E and (f) specimen F. Observed from TD.

Figure 2.38 shows SEM microstructures after annealing at 625 °C for 120 sec of the cold-rolled sheets having a thickness of 1 mm, of which microstructures are shown in Fig. 2.37. In the specimen A (Fig. 2.38 (a)), elongated lamellar ferrite grains were observed, but obvious recrystallized grains were not observed at all. In the specimen B (Fig. 2.38 (b)), both elongated ferrite grains and equiaxed UFG grains were observed. The elongated and

wavy-shaped ferrite region shown in the middle of Fig. 2.38 (b) was probably formed by recovery of the cold-rolled ferrite that was surrounded by small amount of martensite (Fig. 2.37 (b)). The microstructures of the specimens C and D were mostly filled with equiaxed UFG ferrite. The mean ferrite grain sizes in the specimens C and D annealed at 625 °C (Fig. 2.38 (c) and (d)) were 0.40 μm and 0.38 μm, respectively.

In the specimen E (Fig. 2.38 (e)), elongated ferrite grains containing cementite particles were observed, which seemed to be formed by recovery of the deformed martensite. Obvious recrystallized grains were not observed at all in the specimen E. The microstructure of the specimen F (Fig. 2.38 (f)) was mostly elongated ferrite but contained small amount of equiaxed ferrite grains. This means that the tempered martensite in the starting microstructure of the specimen F was less effective to form UFG ferrite compared with the specimen C. This seemed to be because of the lower hardness of the tempered martensite than the as-quenched martensite.

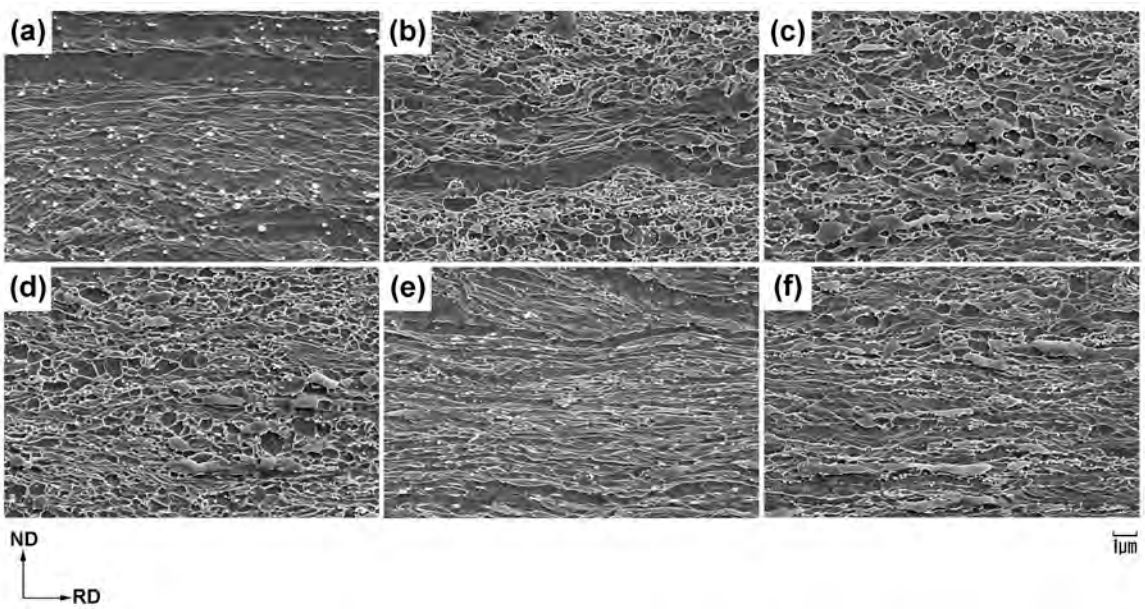

Figure 2.38 SEM Microstructures after annealing at 625 °C of the cold-rolled 1 mm thick sheets of (a) specimen A, (b) specimen B, (c) specimen C, (d) specimen D, (e) specimen E and (f) specimen F. Observed from TD.

In order to investigate the fine microstructure after the annealing at 625 °C in detail, the EBSD analysis was carried out. Figure 2.39 (a, b) show magnified SEM image of the specimens A annealed at 625 °C and ND orientation color map of the same area, respectively. The ND orientation map shows the crystal orientation parallel to ND. A large elongated ferrite grain involving slight contrast in color was observed in Fig. 2.39 (b). This is a recovered ferrite grain, which is commonly observed in low-C steels cold-rolled and annealed below the recrystallization temperature. The elongated grain had an orientation near <001> parallel to ND, and other grains having <111> orientation were observed beside the elongated large grain. Those orientations belong to typical cold-rolling texture of low-C steels [10, 12], which means that the ferrite grains were formed by recovery of the cold-rolled

microstructure. Figure 2.39 (c, d) show magnified SEM image and ND orientation color map of the specimen C annealed at 625 °C, respectively. In the ND orientation map, many equiaxed and fine ferrite grains having various colors were observed, indicating that those grains had various crystal orientations.

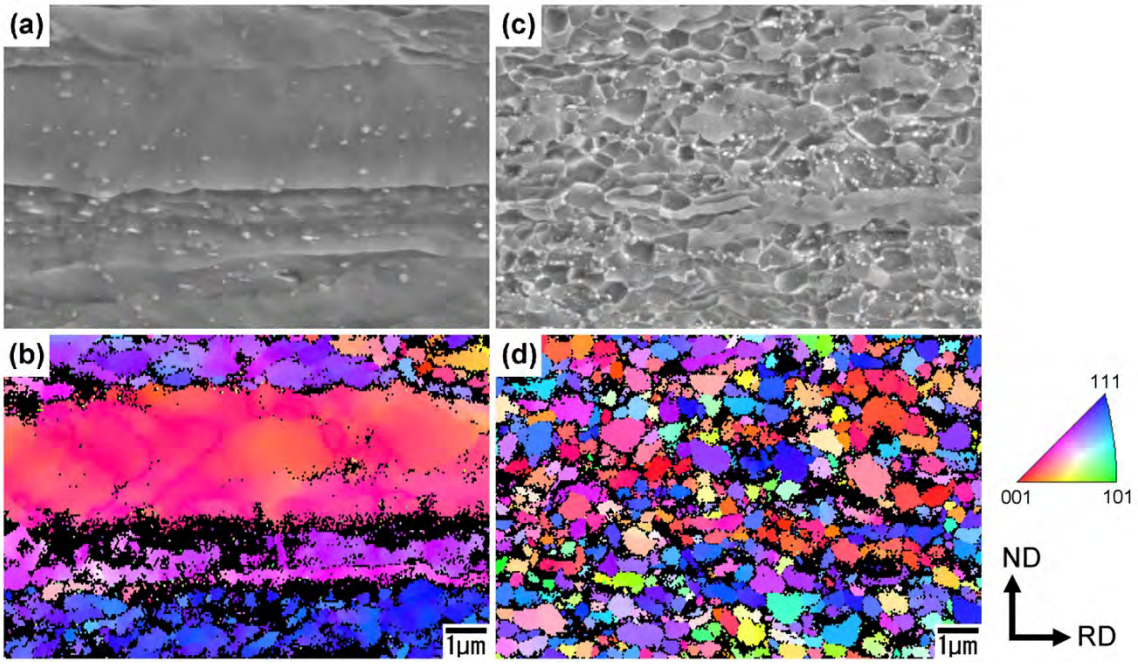

Figure 2.39 (a, c) Magnified SEM images after annealing at 625 °C and (b, d) ND orientation color maps measured by EBSD analysis of the same areas as the SEM images. (a, b) For the specimen A, and (c, d) for the specimen C. The measured points which have lower CI (confidence index) than 0.1 are colored in black.

Figure 2.40 shows the ODFs of the specimen C annealed at 625 °C, constructed using the EBSD data shown in Fig. 2.39 (d). In the $\varphi_2 = 45°$ section of ODF, the α-fiber and γ-fiber components (see Fig. 2. 14) were observed. In addition, the ODFs were close to those in the UFG-FC1 steel having equiaxed UFG ferrite grains shown in Fig. 2.16. These results meant that the equiaxed ferrite grains in the specimen C annealed at 625 °C formed through the same mechanism as the UFG-FC1 steel. That is, the continuous coarsening of the very fine regions having various orientations in the cold-rolled microstructure. Although the specimens A and C have the same chemical composition, only the specimen C showed the UFG ferrite microstructure after the annealing at 625 °C. This result meant that cold-rolling of the DP microstructure certainly accelerated the formation of UFG ferrite during annealing.

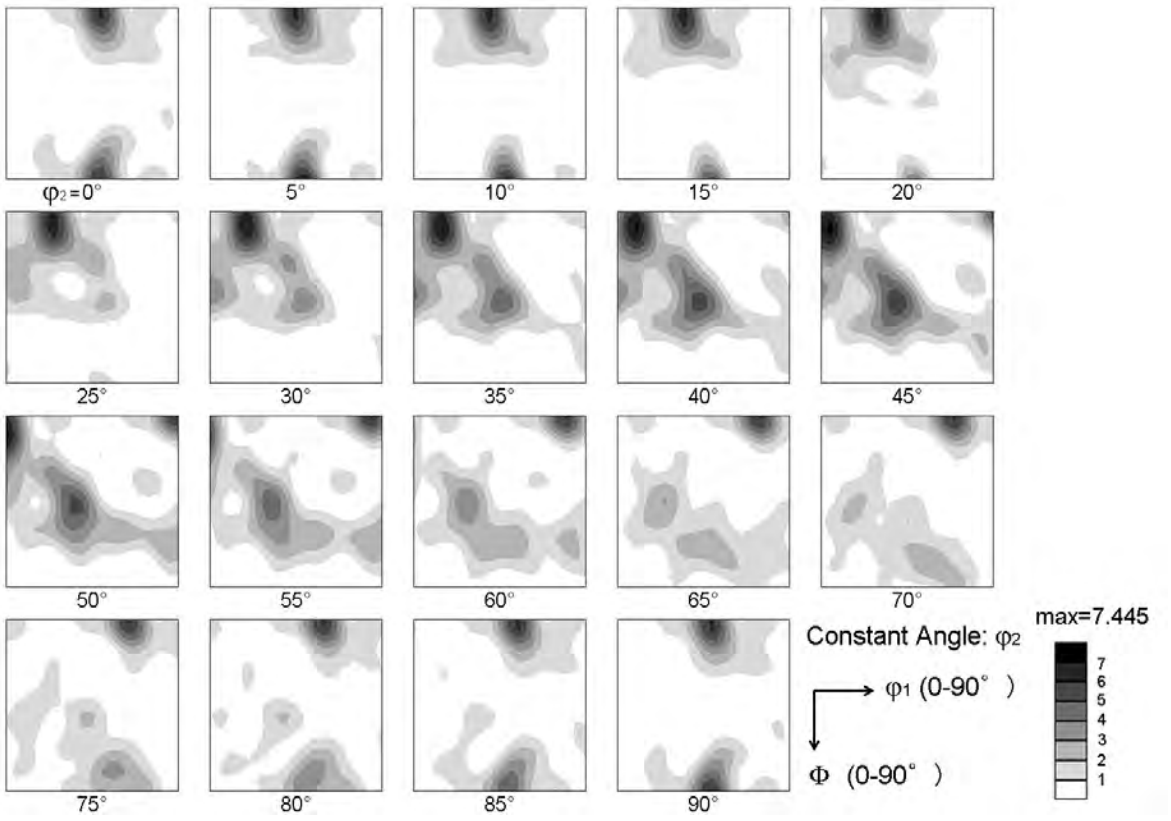

Figure 2.40 ODFs (in Bunge notation) of the specimen C cold-rolled by 80% reduction and annealed at 625 °C for 120 s followed by water-cooled to room temperature.

Figure 2.41 shows microstructures of the specimens annealed at 675 °C. The microstructures of the specimens can be classified into two groups: the specimens A, E and F, and the specimens B, C and D. In the specimens A, E and F, coarse ferrite grains appeared in the elongated ferrite matrix. The coarse grains are recrystallized ones, which appeared from the deformed ferrite matrix. On the other hand, in the specimens C and D, equiaxed and fine ferrite grains containing finely dispersed cementite particles were observed. Those fine ferrite grains seemed to form by growth of the UFG ferrite in the microstructure annealed at 625 °C (Fig. 2.38 (c, d)). The specimen B contained some coarse grains as well as ultrafine ferrite grains. The coarse grains in the specimen B seemed to form by recovery of the elongated ferrite grains existed at 625 °C (Fig. 2.38 (b)). The mean ferrite grain sizes in the specimens B, C and D annealed at 675 °C (Fig. 2.41 (b, c, d) were, 0.74 μm, 0.78 μm and 0.98 μm, respectively. The mean ferrite grain size in the specimen B was not so large, because many ultrafine ferrite grains existed in the microstructure as well as the coarse ferrite grains.

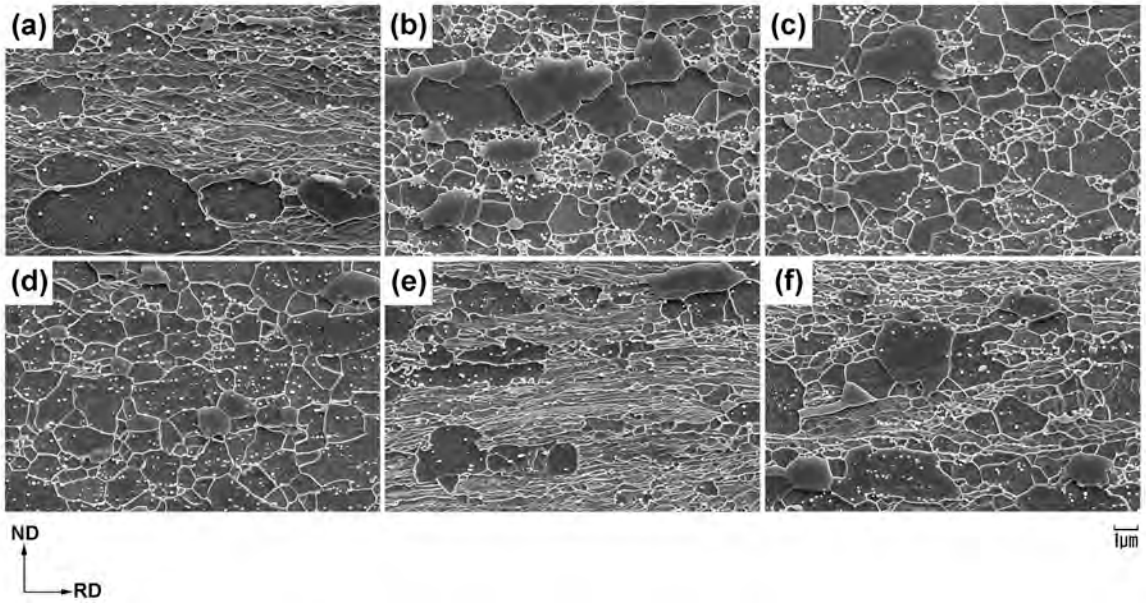

Figure 2.41 SEM Microstructures after annealing at 675 °C of the cold-rolled 1 mm thick sheets of (a) specimen A, (b) specimen B, (c) specimen C, (d) specimen D, (e) specimen E and (f) specimen F. Observed from TD.

Figure 2.42 shows the microstructures of the specimens A to F annealed at 700 °C. In all the specimens, the microstructures were filled with equiaxed ferrite grains. Finely dispersed cementite particles were also observed in the microstructures. In addition, fine martensite islands (light gray regions) were observed mainly at ferrite grain boundaries or triple junctions in all the specimens. As mentioned before, the A_{c1} transformation temperature during heating was approximately 700 °C. During the holding at 700 °C, austenite formed to some extent, and then transformed to martensite during the water-quenching. Figure 2.43 shows the microstructures of the specimens annealed at 725 °C. All the specimens showed duplex microstructures composed of ferrite (dark gray region) and martensite (light gray region). The martensite volume fraction increased in all the specimens compared with the specimens annealed at 700 °C. Figure 2.44 shows the microstructures of the specimens annealed at 750 °C. As the annealing temperature increased, martensite became dominant in the microstructures.

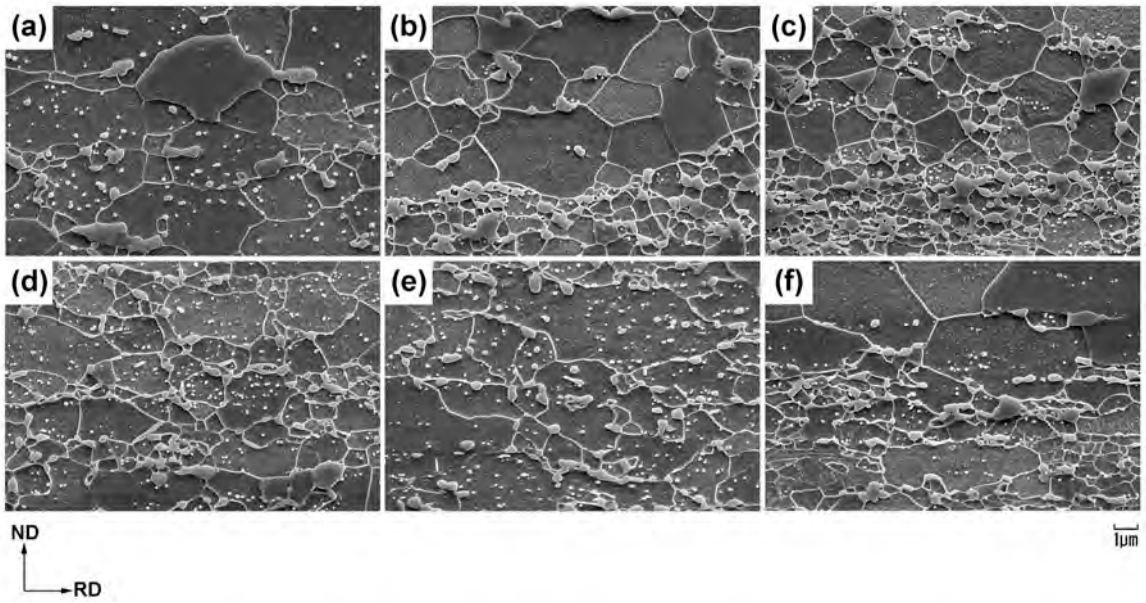

Figure 2.42 SEM Microstructures after annealing at 700 °C of the cold-rolled 1 mm thick sheets of (a) specimen A, (b) specimen B, (c) specimen C, (d) specimen D, (e) specimen E and (f) specimen F. Observed from TD.

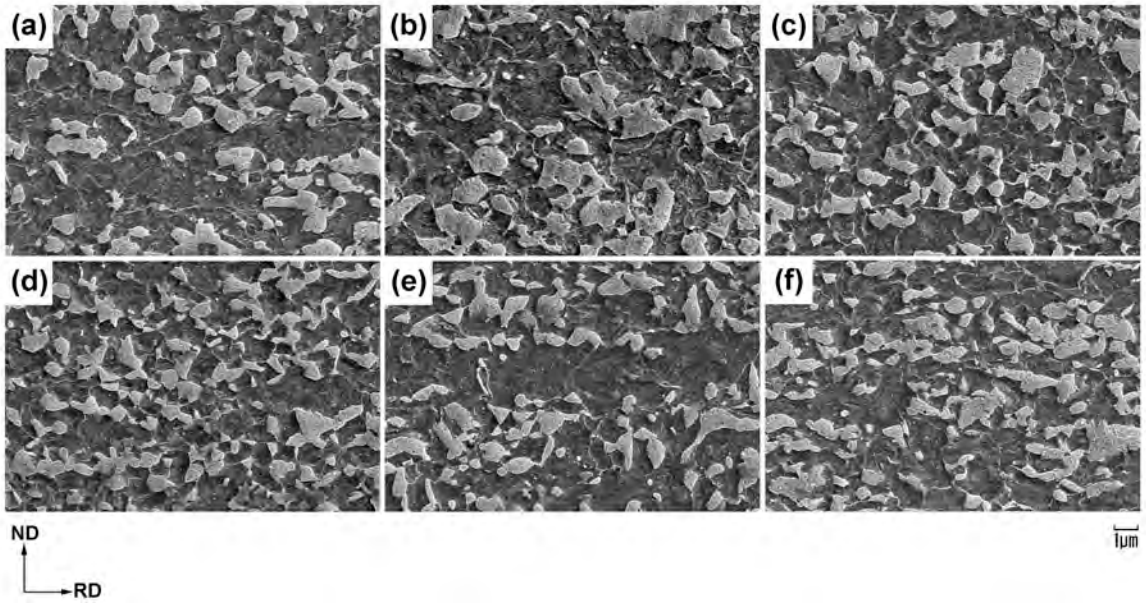

Figure 2.43 SEM Microstructures after annealing at 725 °C of the cold-rolled 1 mm thick sheets of (a) specimen A, (b) specimen B, (c) specimen C, (d) specimen D, (e) specimen E and (f) specimen F. Observed from TD.

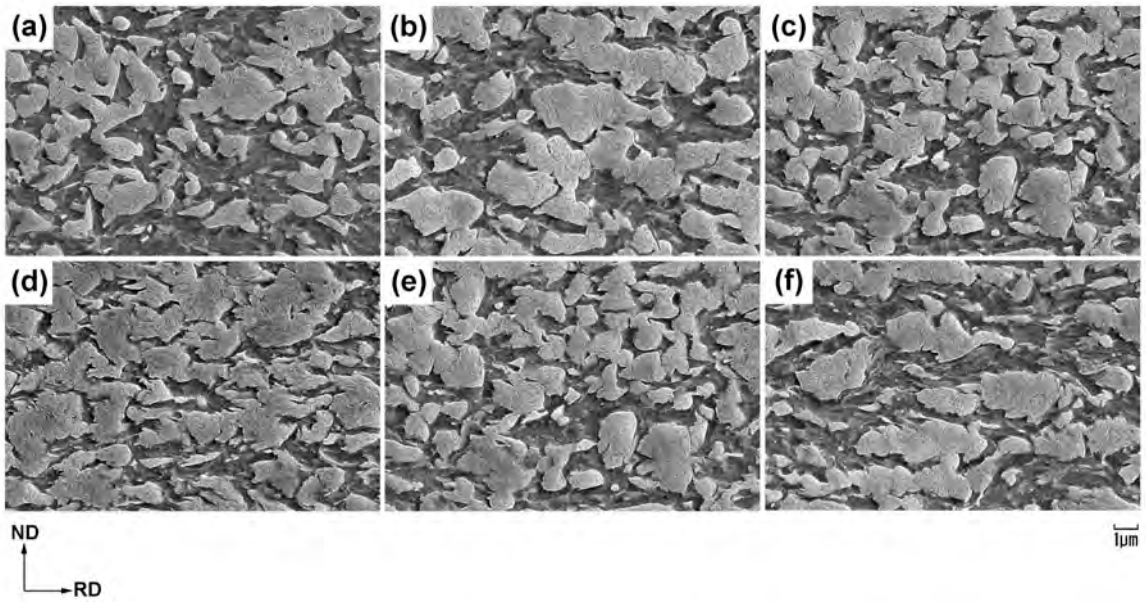

Figure 2.44 SEM Microstructures after annealing at 750 °C of the cold-rolled 1 mm thick sheets of (a) specimen A, (b) specimen B, (c) specimen C, (d) specimen D, (e) specimen E and (f) specimen F. Observed from TD.

Figure 2.45 shows the relationship between mean ferrite grain size and annealing temperature in the specimens A to F cold-rolled to 80% and annealed at various temperatures. Only the grain sizes of the equiaxed ferrite grains in the microstructures were measured. It is seen that the grain sizes of equiaxed ferrite in the specimens B, C, D and E were almost the same at annealing temperatures between 600 and 650 °C. The ferrite grain size in the specimen F annealed at 650 °C was also the same. At annealing temperatures of 675 °C or higher, significant grain growth occurred in the specimens B and F, while the grain growth was moderate in the specimens C and D, resulting in the smaller ferrite grain sizes at 700 °C and 725 °C. In the specimens A and E, the ferrite grain sizes could be measured at the annealing temperatures of 675 °C or higher. The ferrite grain sizes in these specimens were always larger than those in other specimens, corresponding to the SEM microstructures shown in Fig. 2.41 to 2.43. Figure 2.46 shows the martensite volume fraction in the microstructures after intercritical annealing, as a function of the martensite volume fraction in the starting microstructures before CR. The data correspond to the specimens A, B, C, D and E. At annealing temperatures between 700 to 750 °C, the martensite fraction in the annealed specimens were relatively higher when started from duplex microstructures (specimens B, C and D).

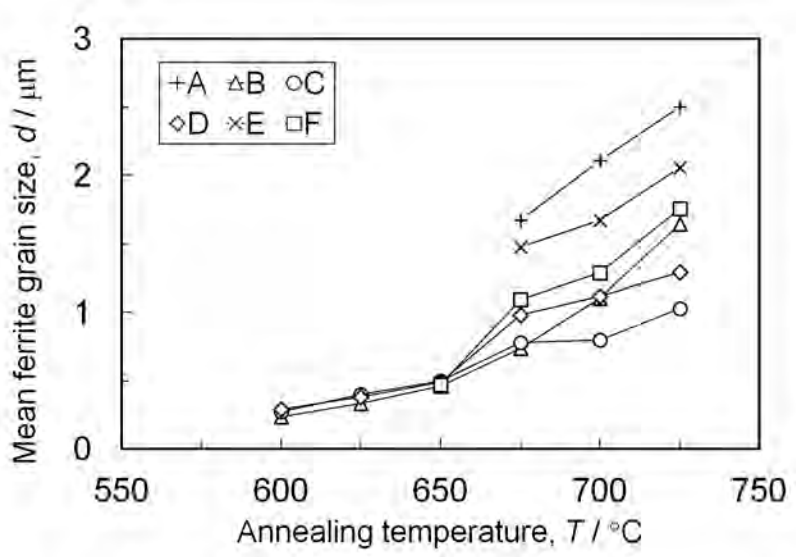

Figure 2.45 Relationship between mean ferrite grain size and annealing temperature of the specimens A to F cold-rolled to 80% and annealed at various temperatures. Only the grain sizes of equiaxed ferrite grains in the microstructures were measured.

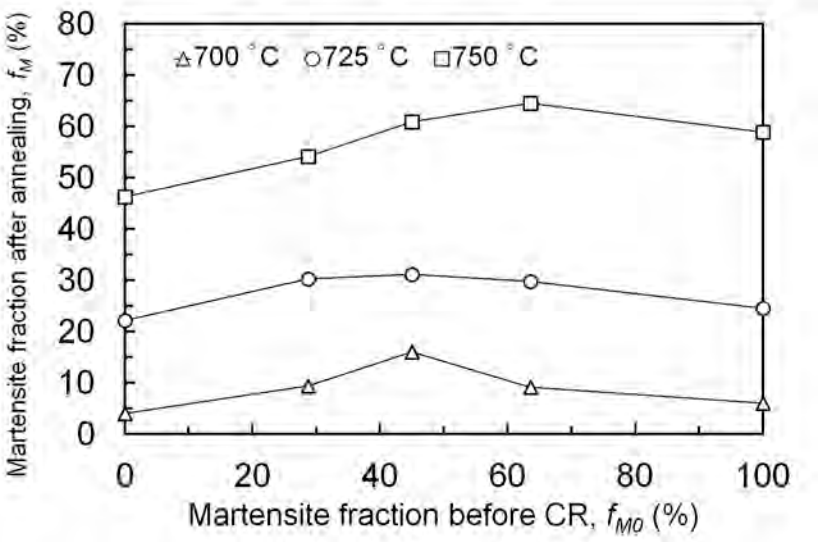

Figure 2.46 Martensite volume fraction in the microstructure after the cold-rolling (CR) and subsequent intercritical annealing, as a function of martensite volume fraction in the starting microstructure before CR. The specimens were cold-rolled to 80% and annealed at various temperatures in intercritical region.

2.3.4 Discussion

First, in order to compare the microstructure formation behaviors in various starting microstructures, the change in hardness during the fabricating process is shown. Vickers hardness of the specimens at each stage of the process was measured. As described in section 2.1.5, the hardness change during the annealing reflects the recrystallization behavior. Figure 2.47 shows the Vickers hardness, H_v, of the specimens A to F before CR, after CR and after annealing at various temperatures. The H_v in the various starting microstructures was different each other, due to the difference in the martensite volume fraction. The H_v in the specimen A was the lowest, and it increased as the martensite volume fraction in the starting microstructures increased up to 100% (the specimens B to E). The H_v in the specimen F was similar to that of the specimen B. By cold-rolling, the H_v significantly increased in all the specimens. The change in H_v during annealing was different each other in those specimens. In the specimens B, C and D having duplex starting microstructures, the H_v gradually decreased as the annealing temperature increased up to 675 °C. This behavior, which has been already observed in this study in the UFG-FC1 steel (Fig. 2.18), suggests that the microstructural formation was not controlled by conventional recrystallization, but by continuous coarsening of very fine regions in the cold-rolled microstructures. On the other hand, in the specimen A (FC starting microstructure), the H_v decreased slightly at annealing temperatures below 650 °C and suddenly dropped when annealed at 675 °C. In the specimen E (fully martensite starting microstructure), the H_v decreased up to 500 °C, kept almost constant up to 650 °C, and then suddenly dropped at 675-700 °C. Although the behavior up to 500 °C was different, it is indicated that the conventional recrystallization occurred around 675 to 700 °C in the specimens A and E. This result corresponds to the microstructural change in the specimens A and E (the appearance of the coarse grains at 675 °C shown in Fig. 2.41).

In order to compare clearly the change in hardness during the annealing at 500 to 700 °C in all the specimens, the measured hardness data were normalized and evaluated. Normalized hardness, H_N, was calculated by

$$H_N = \frac{H - H_0}{H_{500} - H_0} \qquad (2.2)$$

where H is the measured hardness of the specimens annealed at various temperatures, H_{500} is the hardness after annealing at 500 °C, and H_0 is the hardness of fully annealed microstructure of this steel, obtained by annealing of the specimen A at 660 °C for 86.4 ks. This long-time annealing was carried out using an electric furnace with N_2 atmosphere. The microstructure after long-time annealing was FC, and mean ferrite grain size was 7.2 μm.

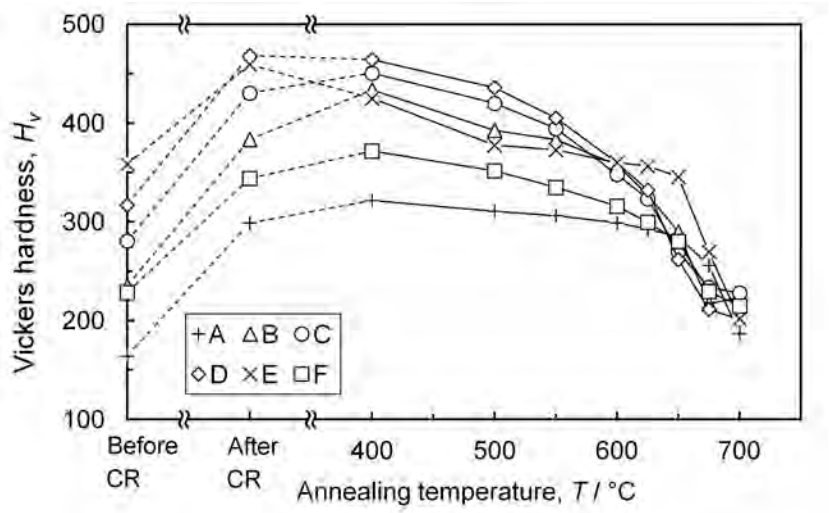

Figure 2.47 Vickers hardness in the specimens A to F before cold-rolling (CR), after CR, and after salt-bath annealing at various temperatures. The martensite volume fraction in the specimens A, B, C, D and E before CR were 0%, 29%, 45%, 64% and 100%, respectively.

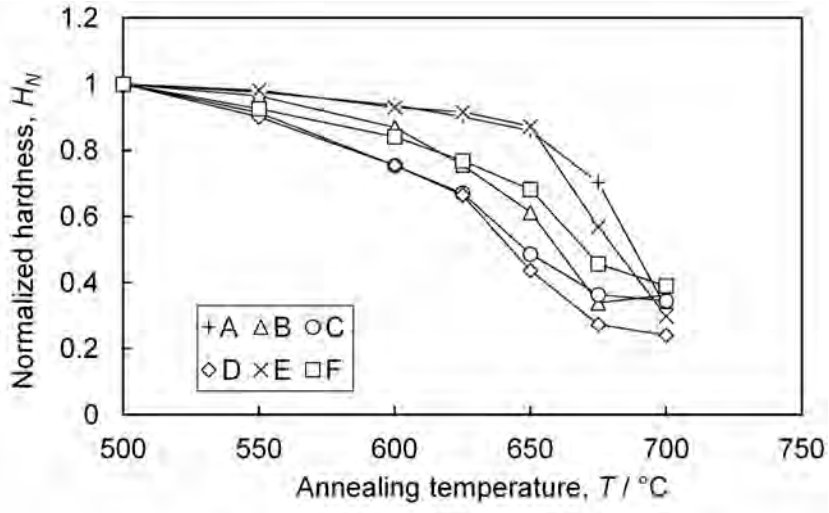

Figure 2.48 Normalized hardness in the specimens A to F as a function of annealing temperature after CR.. The martensite volume fraction in the specimens A, B, C, D and E before CR were 0%, 29%, 45%, 64% and 100%, respectively.

Figure 2.48 shows the change in H_N during the salt-bath annealing. The data shown in Fig. 2.48 were categorized into three groups. The first group included the specimens A and E, of which starting microstructures were FC and full-martensite. In those specimens, the H_N decreased gradually and then suddenly dropped around 675-700 °C. The specimens C and D having duplex starting microstructures belonged to the second group. The hardness continuously decreased up to 675 °C, indicating the occurrence of continuous recovery (continuous coarsening) of the cold-rolled microstructures. The accelerated recovery in the specimens C and D at low temperatures (500 to 600 °C) seemed to be due to the higher volume fractions of martensite in the starting microstructures, which brought higher concentration of plastic strain into the ferrite matrix. The specimens B and F showed intermediate behavior between the first group and the second group. That is, the moderate

decrease in hardness up to 650 °C, and relatively large decrease at 675 °C. Also this behavior corresponded to the microstructural formation shown in Fig. 2.38, 2.41 and 2.42. That is, in the specimens B and F, elongated ferrite grains still remained at 625 °C, indicating that the UFG ferrite formation by recovery was not accelerated very much, and coarse ferrite grains appeared at 675 °C. This result was due to the small amount of martensite in the starting microstructure (in specimen B), and the relatively small difference in hardness between ferrite matrix and tempered martensite (in specimen F).

For further understanding of the UFG ferrite formation behavior, the fraction of equiaxed ferrite region, measured by point-counting method using the SEM microstructures, are plotted as a function of annealing temperature in Fig. 2.49. Similar analysis is generally carried out for investigating the conventional recrystallization. The curves in Fig. 2.49 indicate the formation rate of equiaxed ferrite grains. It is clear that in the specimens B, C and D, the equiaxed ferrite grains appeared at lower temperatures compared with other specimens. The appearance of the equiaxed ferrite grains corresponded to the gradual decrease in the hardness up to 625 °C (Fig. 2.47 and Fig. 2.48). On the other hand, in the specimens A and E, equiaxed ferrite grains (recrystallized ferrite) suddenly appeared at 675 °C, which also corresponds to the sudden decrease in the hardness.

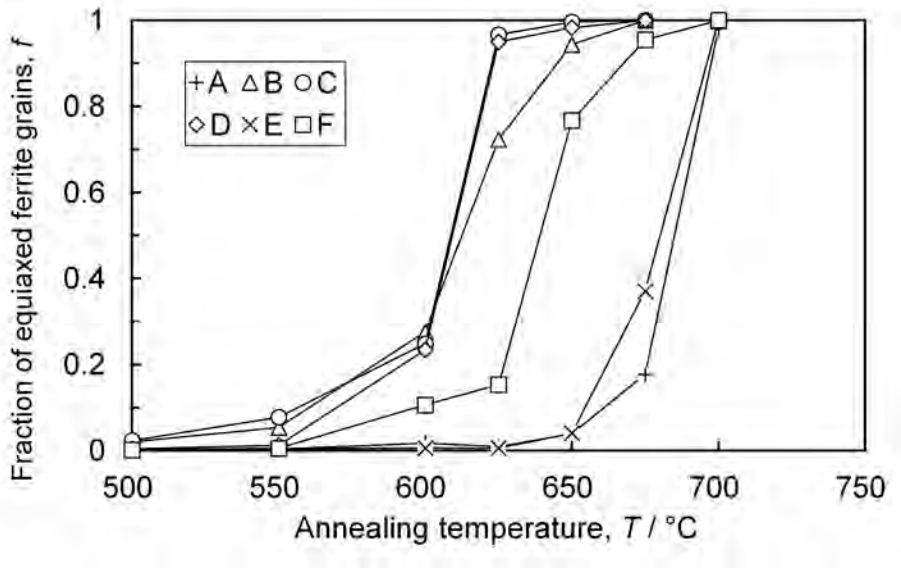

Figure 2.49 Fraction of equiaxed ferrite grains in the specimens A to F cold-rolled and annealed at various temperatures, as a function of annealing temperature.

From the overall results in this section, it is clarified that UFG equiaxed ultrafine ferrite grains appeared at relatively low temperatures during annealing in the specimens when started from duplex microstructures (specimens B, C and D), while normal recrystallization phenomenon was observed in the specimens started from FC and martensite microstructures (specimens A and E). In the specimen F (the starting microstructure of ferrite and tempered martensite), the UFG ferrite formed partially (Fig. 2.38 (f)). This seemed to be owing to the lower hardness of the tempered martensite, which was not enough to concentrate the plastic strain into the ferrite matrix.

Actually, the “equiaxed ferrite grains” included both UFG ferrite and coarse-grained (CG) ferrite. Figure 2.50 shows the fractions of UFG ferrite, CG ferrite and elongated ferrite as a function of annealing temperature in the specimens A and C. The UFG ferrite means the equiaxed ferrite grains having grain diameters of 1 μm or less. The “elongated ferrite” means the large ferrite grains elongated roughly to RD, that were formed by recovery of the cold-rolled microstructure without formation of equiaxed UFG grains, for example, the ferrite matrix shown in Fig. 2.41 (a) and (e) including some boundaries with low contrast in the SEM images. In the specimen A, few amount of equiaxed ferrite grains were observed at annealing temperature of 625 °C, and the amount did not increase at higher temperatures. On the other hand, CG ferrite (recrystallized ferrite) appeared at 675 °C and rapidly increased at higher temperatures. In the specimen C (Fig. 2.50 (b)), UFG ferrite grains formed at 500 to 600 °C, and the amount of the UFG grains increased at 625 °C without formation of CG ferrite, resulting in almost 100% UFG ferrite microstructure. When the annealing temperature increased, CG ferrite appeared and the ratio of UFG ferrite decreased, indicating the growth of the CG ferrite consuming the UFG ferrite.

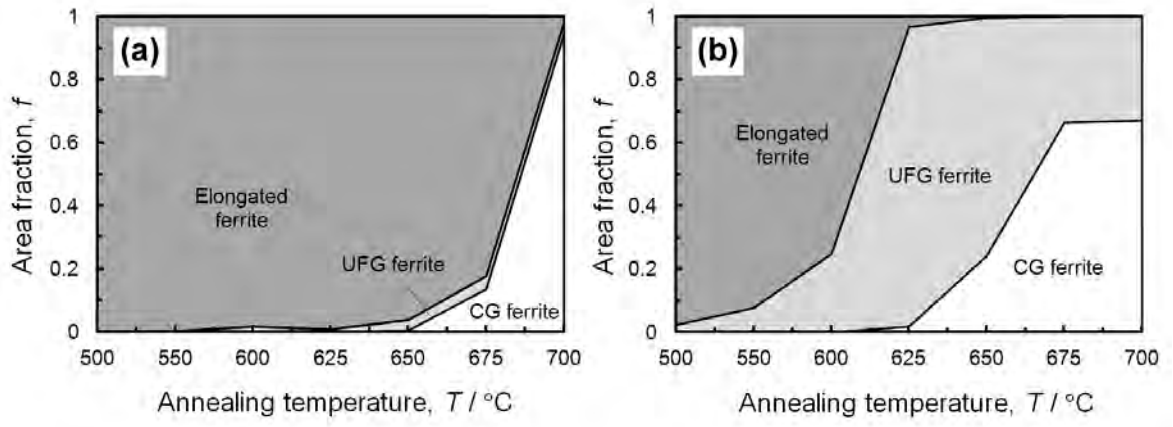

Figure 2.50 Area fractions of elongated ferrite, ultrafine grained (UFG) ferrite and coarse-grained (CG) ferrite in the microstructures after the cold-rolling and subsequent annealing at various temperatures. The martensite volume fractions of the starting microstructures before cold-rolling were (a) 0% (specimen A) and (b) 45% (specimen C).

The optimum martensite volume fraction in the starting microstructure for achieving fully-UFG ferrite microstructure existed. Figure 2.51 shows a contour map drawn according to the area fraction of the UFG ferrite in the microstructures after annealing. The X axis represents the martensite volume fraction in the starting microstructures, and the Y axis represents the annealing temperature after CR of the starting microstructures. The conditions for achieving fully UFG ferrite microstructures were, the martensite fraction in the starting microstructures of 40 to 65 %, and the annealing temperature around 625 °C. In other conditions, the UFG ferrite ratio was smaller. If started from FC or full-martensite microstructures, the fully UFG ferrite could not be obtained under any conditions. If fully UFG ferrite is not required but mostly UFG ferrite microstructure (for example, more than 60% of UFG ferrite) is sufficient, the range of optimum martensite fraction in the starting microstructures was expanded to be between 30 and 70 %

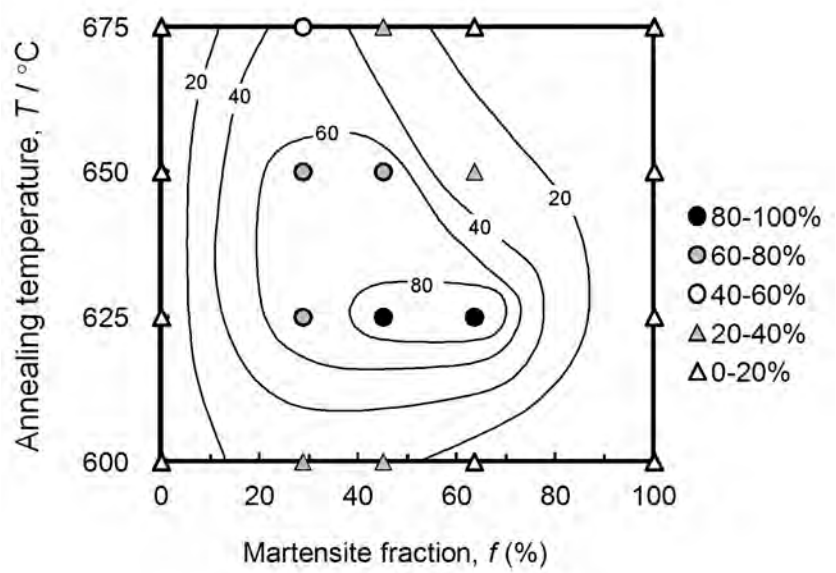

Figure 2.51 Contour map showing area fraction of the ultrafine grained (UFG) ferrite in the microstructures after cold-rolling (CR) and subsequent annealing at various temperatures. The X axis represents the martensite fraction in the starting microstructures before CR, and the Y axis represents the annealing temperature after CR of the starting microstructures. The solid lines in the figure indicate the contour lines for the identical UFG ferrite fraction.

Finally, the behavior during annealing at intercritical region (700 to 750 °C) is discussed. As shown in Fig. 2.46, the amount of martensite in the annealed microstructures was larger when started from the duplex starting microstructures including 29 to 64% martensite. This result suggested that austenite formation was accelerated during intercritical annealing in the specimens started from duplex microstructures, because the UFG ferrite had already formed during annealing at the temperatures below the A_{c1} transformation temperature. The specimens B, C and D annealed below 700 °C (Fig. 2.38 (b, c, d)) and Fig. 2.41 (b, c, d)) contained ultrafine ferrite grains. The ferrite grain boundaries and triple junctions are the most favorable nucleation sites for austenite during intercritical annealing. Therefore, austenite nucleation during annealing at intercritical region seemed to be accelerated in the specimens B, C and D, resulting in the larg amount of martensite in the microstructures after subsequent water-quenching. In addition, it is noteworthy that in the specimens B, C and D, some amount of UFG ferrite grains having grain sizes of 0.5 to 0.6 μm remained in spite of high annealing temperature of 700 °C (Fig. 2.42 (b, c, d)), while coarse grains were dominant in the specimens A and E (Fig. 2.42 (a, e)). It was suggested that the grain growth was suppressed by the higher nucleation density of austenite during intercritical annealing in the present process composed of CR and annealing of duplex microstructures. However, the uniform ultrafine ferrite matrix could not be achieved due to significant growth of some ferrite grains even in the specimens B, C and D. The trials to achieve both uniform UFG ferrite matrix and introduction of hard second phases during intercritical annealing will be done in the next chapter.

2.3.5 Summary

In this section, the effect of martensite volume fraction in the starting microstructures on UFG ferrite formation after cold-rolling and annealing was investigated. By the heat-treatment of hot-rolled sheets of the 0.1C-2Mn-0.3Mo steel at various conditions, martensite volume fraction in the starting microstructure was changed from 0 to 100 %. Then, various starting microstructures were cold-rolled and annealed. The obtained results are summarized below.

(1) After 80% cold-rolling of the duplex starting microstructures containing 29 to 64% martensite, wavy ferrite microstructure elongated roughly to RD and bent along the martensite islands were observed. This seemed to be owing to the existence of hard martensite phase, indicating that complex plastic flow occurred in ferrite. When started from a microstructure composed of ferrite and tempered martensite, similar wavy ferrite was observed but it was not so significant. When started from ferrite-cementite microstructure, such complex flow did not observed at all. Elongated martensite laths were observed when started from full-martensite microstructure.

(2) After annealing at 625 °C, the microstructures were mostly filled with equiaxed UFG ferrite, when started from the duplex microstructures containing 45 to 64 % martensite. When started from the duplex microstructure containing 29 % martensite, both elongated ferrite and equiaxed UFG ferrite were observed. When started from the ferrite-cementite or full-martensite microstructure, elongated ferrite grains containing cementite particles were observed, which seemed to be formed by recovery of the deformed microstructures.

(3) At annealing temperature of 675 °C, coarse recrystallized ferrite grains appeared in the specimens started from the ferrite-cementite, full-martensite and ferrite-tempered martensite microstructures. This result meant that conventional recrystallization where new grains grew into the deformed matrix occurred in those specimens.

(4) The change in hardness during annealing corresponded to the microstructural changes well. In the specimens where fully UFG ferrite microstructure formed, the hardness gradually decreased. On the other hand, in the specimens where conventional recrystallization occurred, sudden drop in hardness was observed at the temperatures where the coarse grains appeared.

(5) The optimum martensite volume fraction in the starting microstructures was clarified. If the fully UFG ferrite microstructure is required, the martensite fraction in the starting microstructures should be between 40 and 65%. If mostly UFG microstructures (more than 60% of UFG ferrite) is sufficient, the required martensite volume fraction in the starting microstructures expanded to be between 30 and 70%.

(6) Tempered martensite as hard second phase had less effect on the UFG ferrite formation after cold-rolling and annealing compared with the case where the second phase was as-quenched martensite. This was because of the relatively smaller difference in hardness between the ferrite matrix and the tempered martensite, leading to insufficient strain concentration in the ferrite matrix.

2.4 Conclusions

In this chapter, a new route to fabricate UFG ferrite microstructures without SPD was introduced. The proposed process consisted of conventional cold-rolling and annealing of duplex microstructures in low-C steel. In the first section, the UFG ferrite formation behavior was investigated using microstructural and textural analyses. Uniform UFG ferrite without dislocation substructures was obtained, and it was suggested that the UFG ferrite formed by continuous coarsening of very fine regions having various orientations in the deformed microstructure. Secondly, the effect of process conditions, cold-rolling reduction and refinement of starting microstructure were investigated. It was clarified that finer ferrite microstructures were obtained when higher cold-rolling reduction and lower annealing temperature were applied. By refining the starting microstructure, the critical cold-rolling reduction and annealing temperature for obtaining UFG microstructure decreased, indicating that the microstructural refinement before cold-rolling was effective to accelerate the UFG ferrite formation. Finally, the effect of martensite volume fraction in the starting microstructures on the UFG ferrite formation was clarified. The optimum condition for achieving fully-UFG ferrite microstructure was the martensite fraction in the starting microstructures of 40 to 65 %, and the annealing temperature around 625 °C.

2.5 References

[1] N. Tsuji, T. Maki, Scripta Mater. 60 (2009) 1044.

[2] N. Tsuji, Adv. Eng. Mater.12 (2010) 707.

[3] R. Ueji, N. Tsuji, Y. Minamino, Y. Koizumi, Acta Mater. 50 (2002) 4177.

[4] R. Ueji, N. Tsuji, Y. Minamino, Y. Koizumi, Y. Saito, in: Y. T. Zhu, T. G. Langdon, R. S. Mishra, S. L. Semiatin, M. J. Saran, T. C. Lowe (Eds.), Ultrafine Grained Materials II, TMS, Seattle, 2002, pp. 399.

[5] A. Ohmori, S. Torizuka, K. Nagai, ISIJ Int. 44 (2004) 1063.

[6] R. Song, D. Ponge, D. Raabe, R. Kaspar, Acta Mater. 53 (2005) 845.

[7] T. Furuhara, T. Mizoguchi, T. Maki, ISIJ Int. 45 (2005) 392.

[8] Y. Okitsu, N. Takata, N. Tsuji, J. Mater. Sci. 43 (2008) 7391.

[9] Y. Okitsu, N. Takata, N. Tsuji, Scripta Mater. 60 (2009) 76.

[10] W. B. Hutchinson, Int. Met. Rev. 29 (1984) 25.

[11] H. Takechi, ISIJ Int. 34 (1994) 1.

[12] R. K. Ray, J. J. Jonas, R. E. Hook, Int. Mater. Rev. 39 (1994) 129.

[13] A. D. Rollett, S. I. Wright, Typical Textures in Metals, in: U. F. Kocks, C. N. Toné, H. -R. Wenk (Eds.), Texture and anisotropy, Cambridge University Press, Cambridge, 1998, pp. 196.

[14] N. Hansen, D.J. Jensen, Phil. Trans. R. Soc. Lond. A357 (1999) 1447.

[15] N. Tsuji, R. Ueji, Y. Minamino, Scripta Mater. 47 (2002) 69.

[16] F. J. Humphreys, M. Hatherly, Recrystallization and Related Annealing Phenomena 2nd edn., Elsevier, Oxford, 2004, pp. 457.

[17] N. Kamikawa, T. Sakai, N. Tsuji, Acta Mater 55 (2007) 5873.

[18] N. Tsuji, Y. Ito, Y. Saito, Y. Minamino, Scripra Mater. 47 (2002) 893.

[19] H. Azizi-Alizamini, M. Militzer, W. J. Poole, Scripta Mater. 57 (2007) 1065.

[20] Y. Wang, M. Chen, F. Zhou, E. Ma, Nature 419 (2002) 912.

[21] Naoya Kamikawa, PhD Thesis, Osaka University, 2005.

[22] K. Sugimoto, A. Kanda, R. Kikuchi, S. Hashimoto, T. Kashima, S. Ikeda, ISIJ Int. 42 (2002) 910.

[23] C. Wang, J. Shi, C. Y. Wang, W. J. Hui, M. Q. Wang, H. Dong, W. Q. Cao, ISIJ Int. 51 (2011) 651.

CHAPTER 3

MECHANICAL PROPERTIES OF ULTRAFINE GRAINED FERRITE MICROSTRUCTURES

3.1 Introduction

It has been shown in the former chapter that bulky ultrafine grained (UFG) ferrite steel sheets with sufficiently large dimensions could be obtained by a simple process composed of conventional rolling and annealing procedures. In this chapter, mechanical properties of the fabricated UFG ferrite steels are shown and discussed.

By the way, when applying the UFG steels to automobile body structures, dynamic deformation properties (mechanical properties at high strain rates around 10^3 s^{-1}) should be considered. This is because the materials deform at such high strain rates and absorb crash energy in cases of car collisions [1, 2]. Due to the increasing demands for the crash worthiness of automobiles, the dynamic deformation properties of materials have become more important [3]. Therefore in this chapter, the dynamic tensile behaviors of the UFG steels are mainly discussed. Generally, different types of testing equipment have been used to obtain stress-strain (s-s) curves at high strain rates. In this study, one of the dynamic test equipment, so-called “load-sensing block type” high-speed testing machine, is applied for obtaining the dynamic tensile properties. As well as the dynamic tensile properties, quasi-static tensile properties (tensile properties at low strain rates around 10^{-3} to 10^{-2} s^{-1}), which are usually used to represent the mechanical properties of materials, are also important. Therefore, the quasi-static tensile properties of the steels are also shown and discussed.

In this chapter, first, the high-speed test equipment used in this study is introduced. Secondly, quasi-static and dynamic tensile properties of conventional sheet steels including high strength steels (HSS) are clarified for comparison. Next, quasi-static and dynamic tensile properties of the UFG ferrite-cementite (FC) steels, fabricated through the new process presented in Chapter 2, are shown. In addition, in order to discuss the effect of grain size on the dynamic tensile properties of ferrite microstructures more clearly, UFG interstitial free (IF) steels fabricated by accumulative roll bonding (ARB) and subsequent annealing, having ferrite single-phase microstructure, are also evaluated. The dynamic tensile properties of the two UFG ferrite microstructures are compared with the conventional HSS and discussed.

3.2 High-speed tensile test methods

Up to now, various kinds of high-speed material test system have been developed [4]. Generally in the high-speed testing, the most important matter in load measurement is to consider the stress wave propagation within load-cell. At the quasi-static strain rate, the load-cell is considered to deform homogeneously, so that the stress can be measured easily using a strain gage mounted on the load-cell. On the other hand, at high strain rates, the time needed to attain the homogeneity of elastic deformation within the load-cell becomes comparable to the testing time of the material. At strain rates higher than about 10 s^{-1}, the signal of the loading force is greatly amplified by multiple passages of stress waves reflected within the load-cell [3, 4]. Therefore, special techniques are required for the load measurement at high strain rates. There are generally two approaches to decrease the effect of the stress wave propagation. One is to use a long bar as the load-cell in order to finish the load measurement before the return of the elastic stress wave reflected at the other end. This approach is a basis for bar-type test equipment such as split Hopkinson pressure bar (SHPB) method [5-7] and one-bar method [8, 9]. Another approach is to use a short load-cell in order to reduce the time needed to homogenize the elastic deformation within the cell. The equipment used in the present study is based on this approach.

First, two major bar-type high-speed test methods are reviewed. The SHPB method was developed by Hopkinson [5] in 1914 and advanced by Davis [6] and Kolsky [7]. A schematic illustration of the SHPB method is shown in Fig. 3.1. The striker bar hits one end of the incident bar, and the stress wave propagates at the speed of sound through the incident bar, the specimen, and the transmitter bar. As a result, the specimen deforms at very high strain rates. Strain gages are attached to the incident bar and transmitter bar as shown in Fig. 3.1. Based on the propagation theory, the stress and strain in the specimen can be calculated by the signal measured by the strain gages.

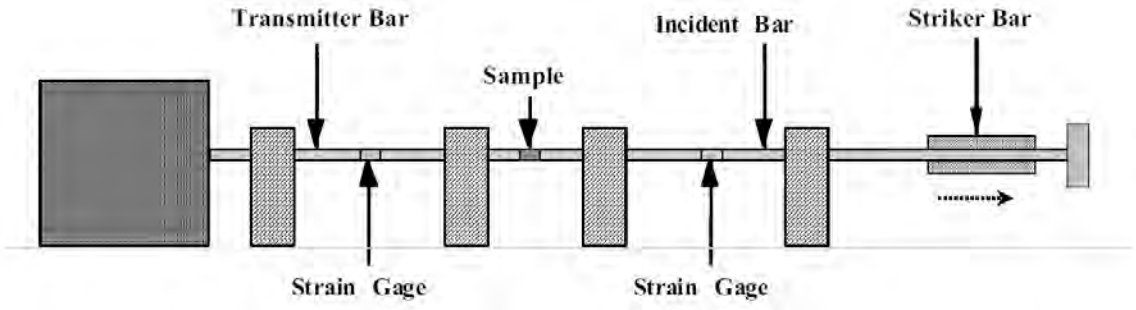

Figure 3.1 Schematic illustration of SHPB (Split Hopkinson Pressure Bar) type high-speed tensile test equipment [3].

The one-bar method is another variation of the bar system developed by Kawada et al. [8, 9] based on the SHPB method. A schematic illustration of the one-bar method is shown in Fig. 3.2. The testing system consists of a hammer, impact block, specimen and output bar. The hammer hits the impact block, and the specimen is deformed in tension. The transmitted stress wave propagates in the output bar, and the stress is measured by a gage mounted at the position C of the output bar. The position of the impact block (position A in Fig. 3.2) is measured using an electro-optical extensometer. An analysis of the propagation of the elastic wave enables to derive the displacement of position B. The elongation of the specimen is thus the difference between the displacements at sections A and B. The strain and strain rate of the specimen are calculated using the elongation and the initial length of the gauge section, L_0 of the specimen.

For these two types of the bar-method, the applicable strain rates of the specimens are limited to relatively high values ranging from 10^2 to 10^4 s^{-1} [4] due to the limitation of the length of the bars. Because the measurement should be finished before the stress wave reflected at the other end of the bar arrives at the gage, the period for the measurement should be short and the strain rates should be relatively high. Therefore, in general the dynamic and quasi-static tensile tests are carried out using different test equipment.

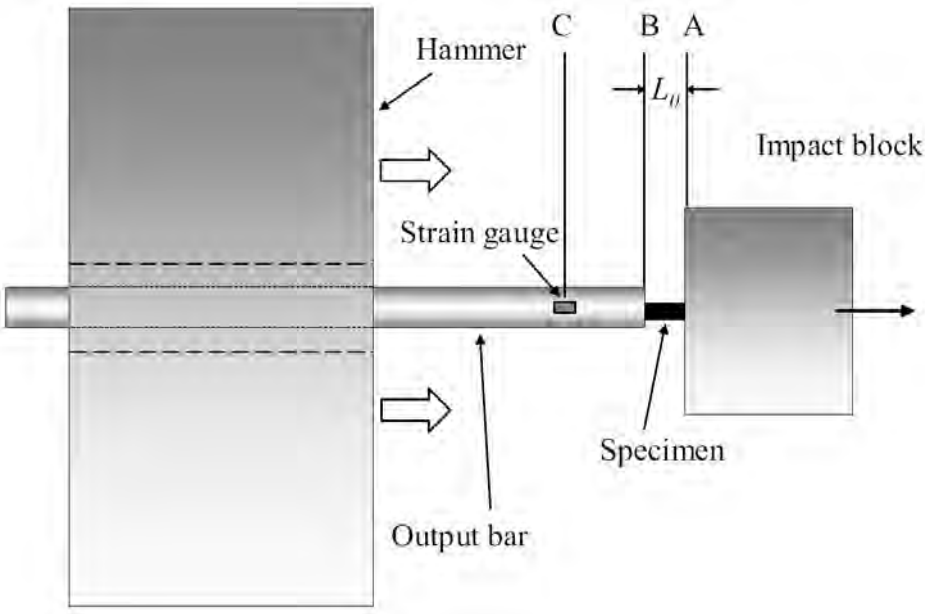

Figure 3.2 Schematic illustration of One-bar type high-speed tensile test equipment [4].

Next, another method for the high-speed tensile testing, which is applied in this study, is explained. This method, which is so-called "load-sensing block method", is based on the second approach to decrease the effect of stress wave propagation described above. That is, to apply a short load-cell. Figure 3.3 shows the schematic illustration of the "load-sensing block method" developed by Tanimura's group [10, 11]. This method was firstly developed for measuring the dynamic load in compression mode. As shown in Fig. 3.3 (a), the load-sensing block consists of a small cylindrical projection (sensing projection)

and a base block having relatively large mass. Figure 3.3 (b) shows the detail of the load-sensing block and the specimen, corresponding to the rectangular area surrounded by broken lines in Fig. 3.3 (a). The cylindrical specimen for compression is set on the top surface of the sensing projection, and the specimen is hit by a loading block that also has large mass. The stress is measured by strain gages mounted at the side surface of the sensing projection. When the specimen is hit by the loading block, shock wave is generated at the contacting surface between the specimen and the loading block, and it travels through the specimen and the sensing projection. The stress wave reflects at the bottom surface of the sensing projection and again reflects at the top surface. Usually the reflected wave disturbs the accurate load measurement, however in this method, the uniform stress state in the projection is achieved after some reflections because the sensing projection is sufficiently small. This means that longer measurement period compared with the bar-methods can be taken, since the measurement is carried out after the uniform stress state in the projection is achieved. The stress wave travels from the sensing projection to the base block, expands with a spherical wave front, and reflects at the free surface of the base block many times. Therefore, the amplitude of the stress wave decreases by repeating the reflections in the base block. Then, the stress wave that comes back into the sensing projection has vanishing magnitude, and hardly affects the stress state in the sensing projection. Therefore, it is possible to measure a dynamic load without the effect of the reflected stress wave.

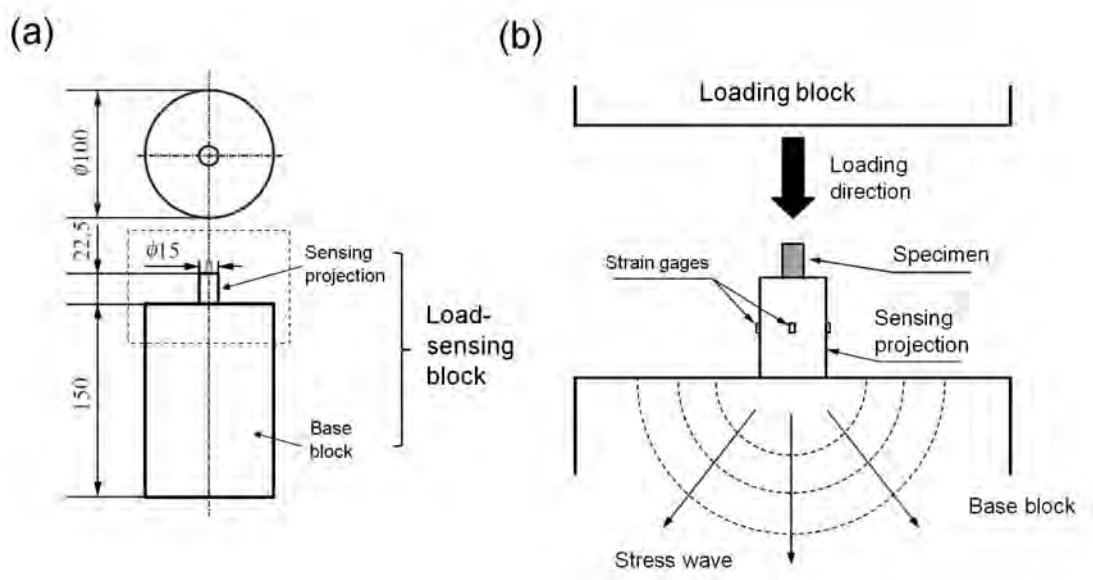

Figure 3.3 Schematic illustration of the load-sensing block method developed for dynamic compression. (a) Dimensions of the load-sensing block composed of base block and sensing projection. (b) Detail of the base block, sensing projection, specimen and loading block. Elastic tress wave propagation in the base block is explained in (b). Reproduced from Fig. 1 in Ref. [10].

The load-sensing block method has been modified for tension mode. In this study, the high-speed tensile test system with the modified load-sensing block is applied. Figure 3.4 (a) shows a schematic illustration of the test equipment, named "high speed material testing system TS-2000" produced by Saginomiya Seisakusyo Inc. The load is applied by the servo-hydraulic actuator set at the top of the equipment. The accumulated hydraulic pressure pushes the loading block, and the load is applied to the specimen attached at the load-sensing block. The details of the load-sensing block and the specimen are shown in Fig. 3.4 (b). The one end of the specimen is attached to the sensing projection of the load-sensing block by a steel pin. The other end is attached to a movable lower jig by also a steel pin. The blades of the loading block hits the lower jig, as shown in Fig. 3.4 (c), and as a result, tension load is applied to the specimen. This system is based on the load-sensing block system for compression shown in Fig. 3.3. Therefore, it is possible to obtain s-s curves with sufficiently high quality at a wide range of strain rates from 10^{-3} to 10^{3} s^{-1}. Figure 3.5 shows photographs of the high-speed tensile test equipment used in this study.

Figure 3.6 shows the schematic drawing of the tensile specimen applied in this study. It has the gauge section 2 mm in width and 6 mm in length, and two shoulder sections with holes at both ends. As described before, the one end is fixed to the load-sensing bock, and the other end is fixed to the lower jig which is hit by the loading block. The displacement of the lower jig is measured by a magnetic reluctant type position sensor. The strain of the specimen is calculated under an assumption that the displacement of the lower jig corresponds to the elongation of the gauge section. Comparing with the bar-methods such as the SHPB and the one-bar methods, this load-sensing block type machine has an advantage in the range of the applicable strain rates. Both quasi-static and dynamic s-s curves can be obtained using the same machine and the same type of specimen.

In this study, the tensile direction of all the specimens was parallel to the rolling direction (RD) of the specimens. Tensile tests were carried out at various strain rates ranging from 10^{-2} s^{-1} to 10^{3} s^{-1} at room temperature. Total elongation of the specimens was measured from the difference in the gauge length before and after the testing.

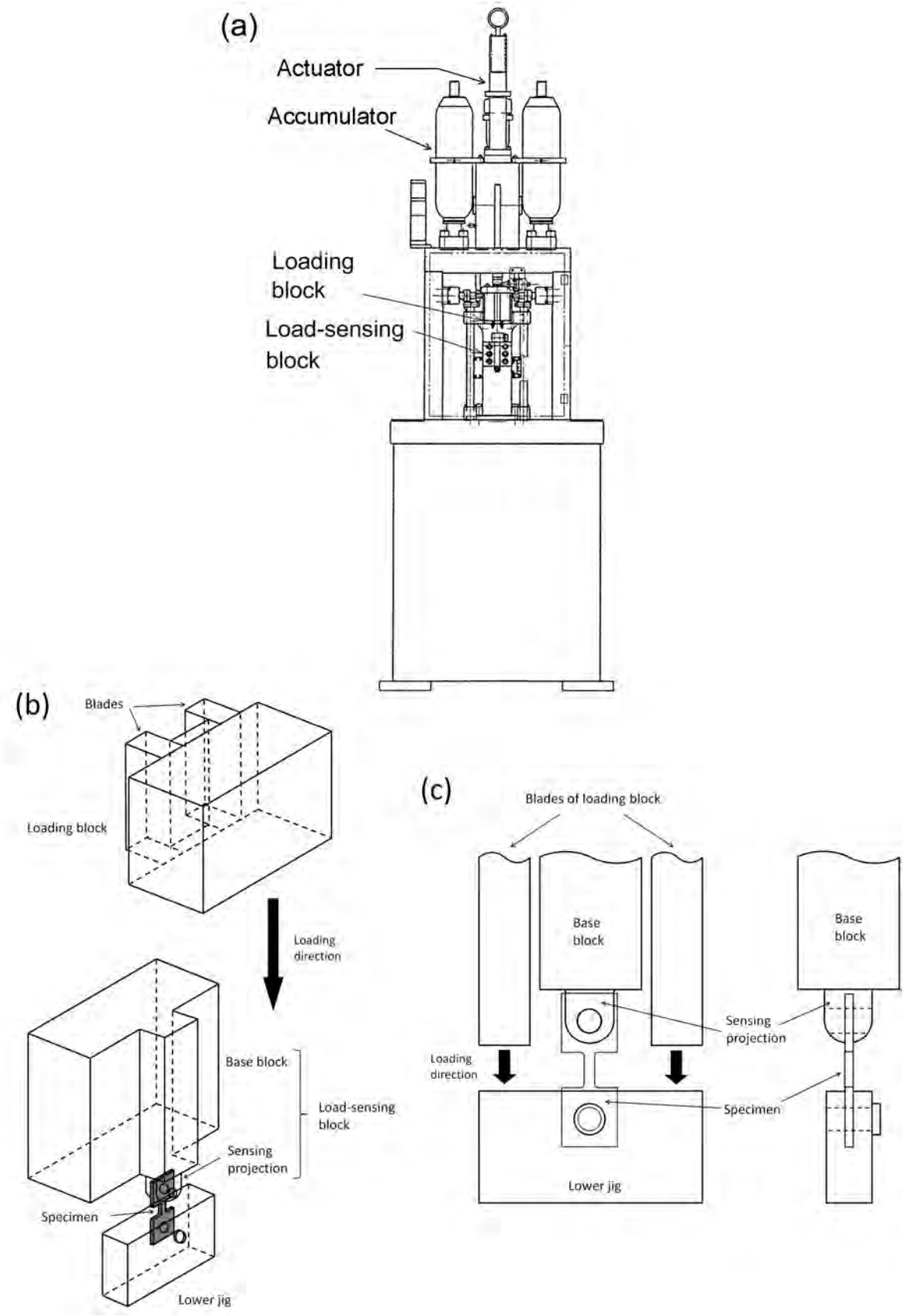

Figure 3.4 (a) Schematic illustration of the dynamic tensile test equipment (TS-2000 produced by Saginomiya Seisakusyo Inc.) used in this study. (b, c) Details of the load-sensing block designed for tension tests attached to the equipment.

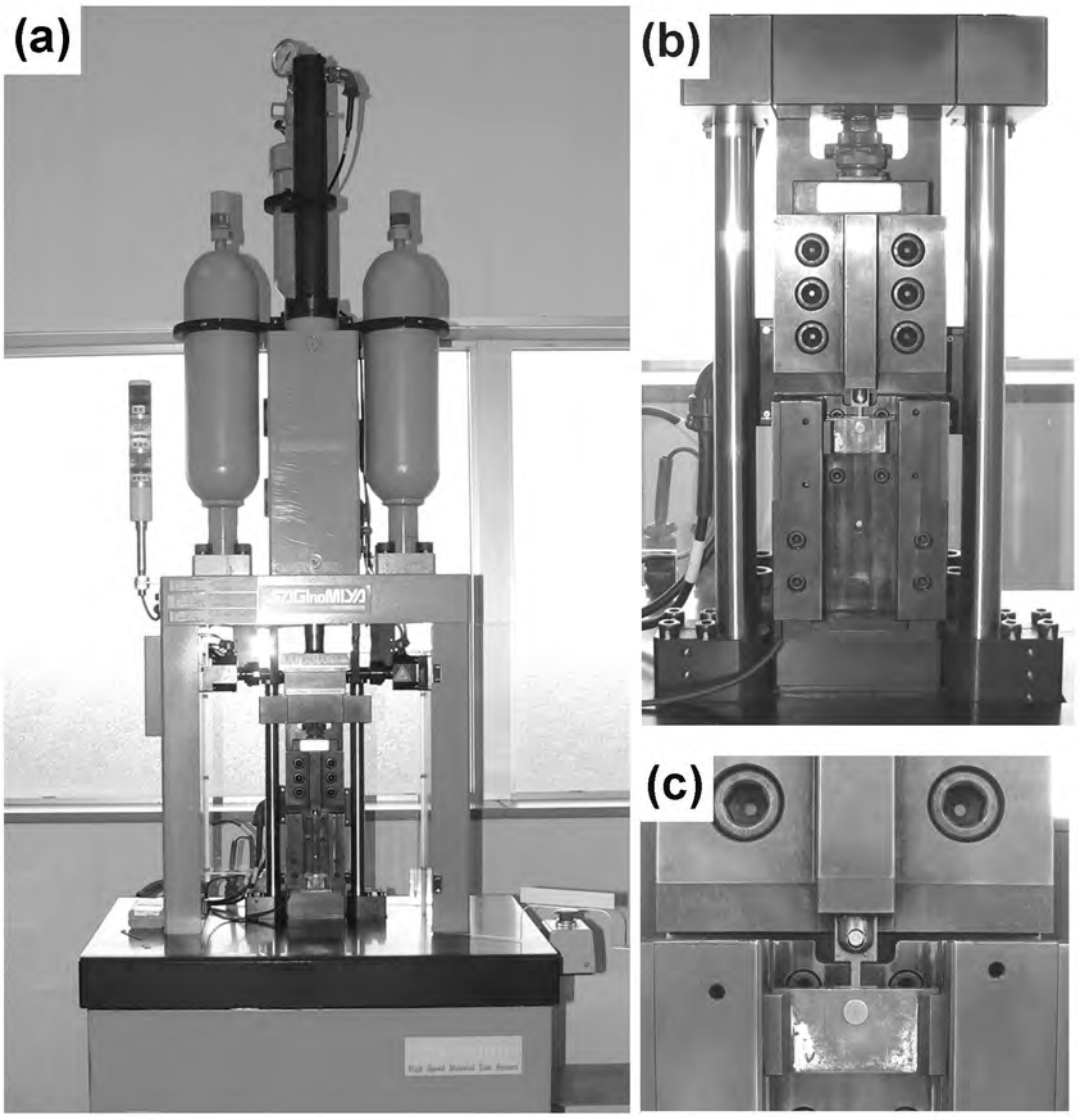

Figure 3.5 Photographs of the high-speed tensile test equipment used in this study. (a) Appearance of the equipment, (b) appearance of the impact block and the load-sensing block and (c) the tensile specimen.

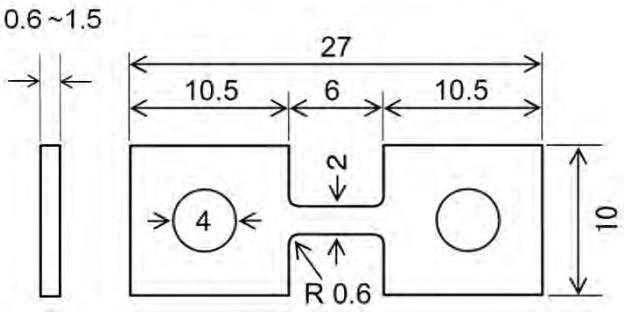

Figure 3.6 Schematic drawing of the tensile specimen used for the load-sensing block type tensile equipment.

3.3 Dynamic tensile properties of conventional sheet steels having various microstructures and strengths

3.3.1 Introduction

As mentioned in section 3.1, the dynamic deformation behaviors of the materials in automobile body structures are very important in order to manage the crash worthiness in case of car collisions. Various sheet steels having various microstructures and strengths have been applied to automobile body structures. Therefore, it is important to clarify the dynamic tensile properties of such commercially available sheet steels. Here in this study, the "dynamic" deformation means the deformation at strain rates around 10^3 s^{-1}. There have been several studies on the dynamic tensile properties of commercial sheet steels including mild steels and high strength steels (HSS) [12-15]. However, in the previous studies [12-15] the variation in microstructures of the tested steels were limited. In addition, there have been few systematic studies on the effects of microstructural factors of the steels [16], such as solute elements, precipitates and second phases, on the dynamic tensile properties. Therefore in this section, various commercial steels having various microstructures and tensile strength (TS) ranging between 270 MPa and 1200 MPa are prepared and their dynamic tensile properties are investigated at wide range of strain rates between 10^{-2} s^{-1} and 10^3 s^{-1}. Additionally the effects of two important microstructural parameters on the dynamic tensile properties are investigated in detail. The first one is volume fraction of hard martensite phase in dual-phase (DP) steels. DP steels having various martensite volume fractions were prepared and investigated. The second one is the state of alloying elements, i.e. in solute or in precipitates. For investigating the effect of this factor, Cu was chosen as an additional alloying element. Fe-0.5 mass% Cu and Fe-1.5 mass% Cu alloys are used for this purpose. In this section, first, the dynamic tensile properties of commercially available sheet steels are shown. Next, the effect of martensite volume fraction in DP steels and the state of Cu in Fe-Cu alloys are shown and discussed.

3.3.2 Dynamic tensile properties of commercially available sheet steels

Commercially available sheet steels including HSS were prepared. For the received steels, microstructural observations were carried out using optical microscopy (OM) or scanning electron microscopy (SEM). The samples for the observations were prepared by etching with a 3% nital. The SEM observations were conducted on Hitachi S-4300E/N SEM operated at 15 kV. All the microstructures were observed on the longitudinal sections perpendicular to the transverse direction (TD) of the sheets (TD section). Quasi-static and dynamic tensile tests were carried out by using the load-sensing block type test equipment described in section 3.2. Tensile tests were carried out using the small tensile test pieces

shown in Fig. 3.6, of which tensile direction was parallel to RD of the sheets. At various strain rates (10^{-2}, 10, 10^2, $5x10^2$ and 10^3 s^{-1}), two or three specimens were tested. From the displacement-load curves, the elastic region was removed and nominal stress-strain curves were generated.

Table 3.1 summarizes the chemical compositions of the received sheet steels. The IF270, IF340 and IF440 steels are IF steels having various strengths. The entire IF steels contained very small amount of interstitial elements (C and N), and also contained strong carbide-formers (Ti and/or Nb). Due to the addition of these elements, C and N are fixed as carbides or nitrides [17, 18]. As a result, the ferrite matrix contains no interstitial atoms. The strengths of the steels were changed depending on the amount of P and Mn. The microstructures of the three kinds of IF steels observed by OM are shown in Fig. 3.7. The entire IF steels exhibited ferrite single-phase microstructure. Table 3.2 summarizes the microstructures and mechanical properties at a strain rate of 10^{-2} s^{-1} of the conventional steels. For example, the TS of the IF440 steel was slightly larger than 440 MPa. Such steel is so-called “440 MPa grade”. The tensile s-s curves of the IF steels at strain rates of 10^{-2} s^{-1} (quasi-static deformation) and 10^3 s^{-1} (dynamic deformation) are shown in Fig. 3.8. At quasi-static deformation (Fig. 3.8 (a)), all the s-s curves showed continuous yielding (without yield drop) followed by work hardening. In the dynamic deformation, the yield strength and flow stress significantly increased compared with the quasi-static deformation. For example, in the IF270 steel, flow stress at 5% strain increased by about 200 MPa. As the strain rate increased, the work hardening significantly decreased in the IF440 steel, and did not observed in the IF270 and IF340 steels. These behaviors were consistent to the results reported in the previous studies [12-15].

Table 3.1 Chemical compositions (mass%) of commercially available sheet steels used for the dynamic tensile tests.

Steel	C	Si	Mn	P	S	Al	Ti	Nb	N	Others
IF270	0.002	0.01	0.17	0.012	0.007	0.033	0.047	0.003	0.003	0.0015B
IF340	0.002	0.02	0.2	0.036	0.012	0.043	0.018	0.013	0.002	
IF440	0.002	0.3	1.53	0.036	0.007	0.035	0.022	0.012	0.003	
FP400	0.093	0.02	1.26	0.012	0.005	0.032	-	-	-	
PP590	0.112	0.09	1.47	0.011	0.004	0.042	0.002	0.042	0.003	
DP780	0.091	0.03	1.98	0.008	0.002	0.043	-	-	-	
DP980	0.157	0.51	2.44	0.009	0.002	0.03	-	-	0.004	
1180	0.151	0.51	2.64	0.007	0.001	0.032	-	-	-	

-: Not measured

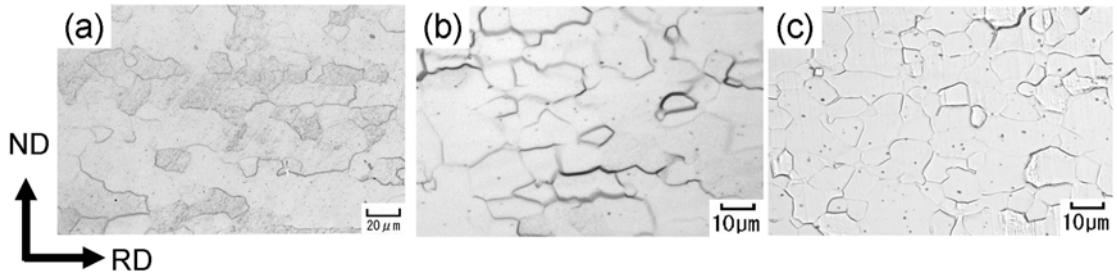

Figure 3.7 Optical micrographs of (a) IF270, (b) IF340 and (c) IF440 steels. Observed from TD.

Table 3.2 Microstructure and quasi-static mechanical properties of the commercial sheet steels, measured using the small tensile specimen shown in Fig. 3.6 of which tensile direction was parallel to RD.

Steel	Micro-structure	Volume fraction of hard phase (%)	Thickness (mm)	0.2% offset stress (MPa)	Tensile strength (MPa)	Total elongation (%)
IF270	F	-	1.0	187	319	50.3
IF340	F	-	0.8	211	370	45.6
IF440	F	-	1.0	300	447	40.2
FP400	F-P	8	1.0	284	421	38.2
PP590	F	-	1.0	468	578	30.2
DP780	F-M	15	1.0	457	785	28.4
DP980	F-M	61	1.0	807	1066	19.0
1180	M(-F)	99	1.2	1030	1206	19.0

F: Ferrite, P: Pearlite, M: Martensite

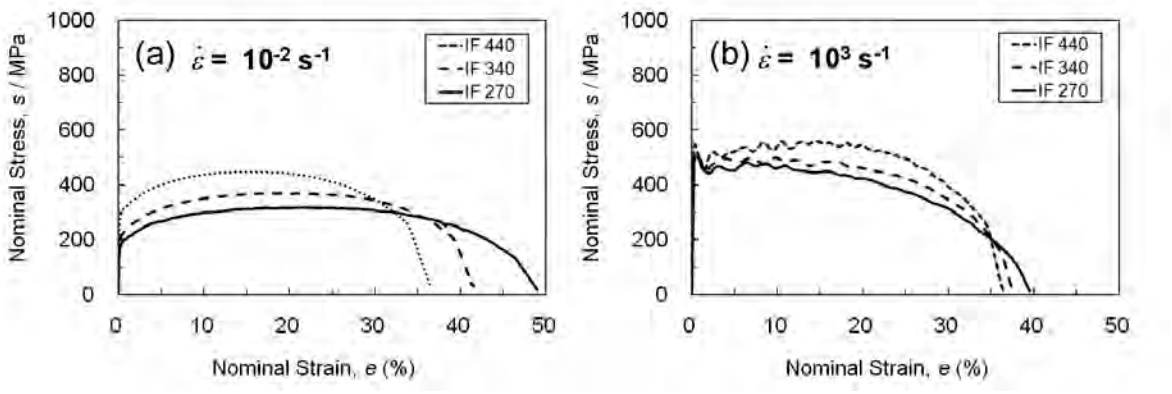

Figure 3.8 Stress-strain curves of the IF270, IF340 and IF440 steels measured at (a) 10^{-2} s^{-1} and (b) 10^{3} s^{-1}.

The FP400, PP590, DP780, DP980 and 1180 steels in Table 3.1 are commercially available HSS. Figure 3.9 shows their SEM microstructures. The FP400 steel is a low-C

ferrite-pearlite steel, and had a TS of 421 MPa (Table 3.2). The PP590 steel is a low-C steel strengthened by precipitation. 0.04 mass% Nb was added to a low-C steel and the hardening was brought by niobium carbides. The SEM observation of the PP590 steel revealed a fine ferrite single-phase microstructure (Fig. 3.9 (b)). The DP780 and DP980 steels are 780 MPa grade and 980 MPa grade DP steels, and their microstructures are ferrite-martensite (Fig. 3.9 (c, d)). The 1180 steel is an 1180 MPa grade steel, and the microstructure is composed of 99% martensite and ferrite. Therefore, the 1180 steel had substantially martensite single-phase microstructure.

The tensile s-s curves of the commercial HSS in quasi-static and dynamic strain rates are shown in Fig. 3.10 (a) and (b), respectively. The s-s curves showed continuous yielding (without yield drop) followed by work hardening in quasi-static deformation (Fig. 3.10 (a)). The work hardening in the 1180 steel was limited within small strain region in the quasi-static deformation. In the dynamic deformation, the yield strength and flow stress increased compared with the quasi-static deformation in all the HSS, however the increase in the yield strength and the flow stress seemed to be smaller than those in the IF270 steel shown in Fig. 3.8. This behavior will be discussed later.

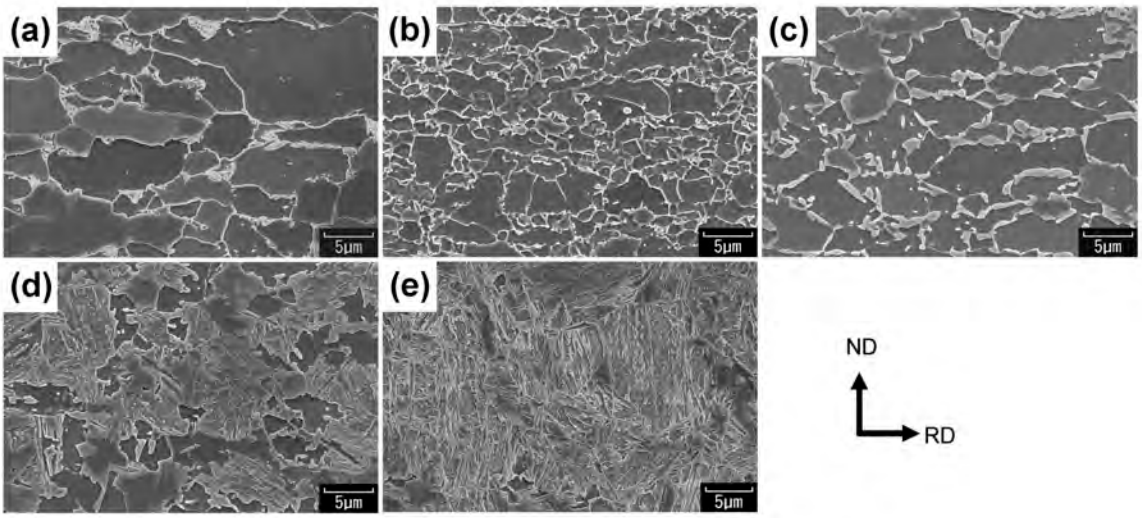

Figure 3.9 SEM microstructures of (a) FP400, (b) PP590, (c) DP780, (d) DP980 and (e) 1180 steels. (a, c, d) Duplex microstructures, (b) ferrite single-phase and (e) 99% martensite. Observed from TD.

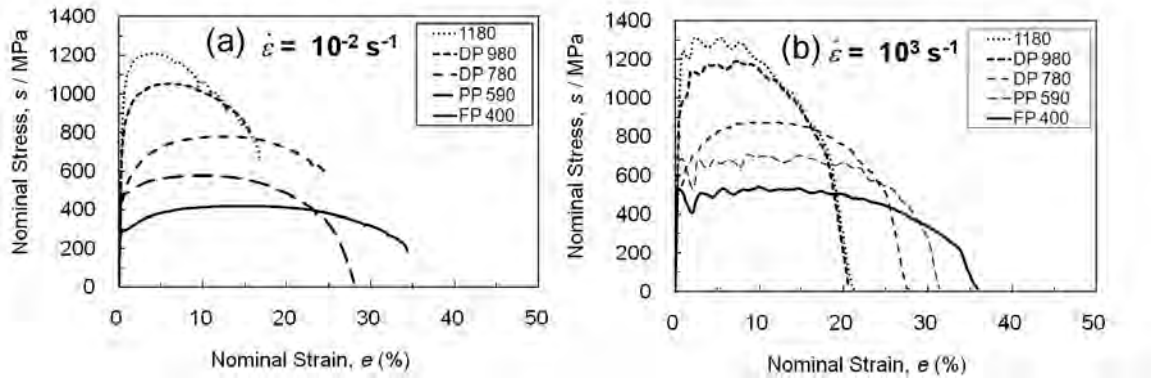

Figure 3.10 Stress-strain curves of FP400, PP590, DP780, DP980 and 1180 steels measured at (a) 10^{-2} s^{-1} and (b) 10^{3} s^{-1}.

3.3.3 Effect of martensite volume fraction on dynamic tensile properties of ferrite-martensite dual phase steels

It is well known that the quasi-static tensile behaviors of DP steels are strongly affected by the volume fraction of martensite in their microstructures [19, 20]. However, the effect of the martensite volume fraction on the dynamic tensile properties of DP steels has not been reported. Therefore, in this section, by using DP microstructures having various martensite volume fractions prepared by intercritical annealing at various temperatures, their dynamic deformation properties are investigated.

Commercially available 590 MPa grade DP steel, of which chemical composition is summarized in Table 3.3, was used. The received sheets were annealed at 750, 800 and 850 °C for 120 s in a salt bath and then water-quenched to room temperature. By this additional annealing, various DP microstructures having various martensite volume fractions were obtained. Table 3.4 summarizes the annealing condition, martensite volume fraction and quasi-static mechanical properties. It is shown that the martensite volume fraction varied from 11% to 95 % depending on the annealing temperature. Figure 3.11 shows SEM microstructures of the as-received 590DP steel and the specimens fabricated by annealing of the DP590 steel. The specimens annealed at 750 °C and 800 °C (Fig 3.11 (b, c)) as well as the as-received DP590 steel (Fig 3.11 (a)) showed duplex microstructures composed of ferrite and martensite, while the specimen annealed at 850 °C (Fig 3.3 (d)) had 95% martensite. The specimen annealed at 850 °C had substantially martensite single-phase microstructure.

The tensile s-s curves of these DP specimens at quasi-static and dynamic strain rates are shown in Fig. 3.12 (a) and (b), respectively. All the s-s curves showed continuous yielding without yield drop, followed by work hardening in quasi-static deformation (Fig. 3.12 (a)). As summarized in Table 3.4, the 0.2% offset stress and tensile strength increased as the volume fraction of martensite increased. The elongation decreased as the annealing temperature increased up to 750 °C, increased at 800 °C annealing, and then decreased again at 850 °C annealing. This behavior is recognized in the s-s curves. The s-s curves in Fig. 3.12 (a) indicate that the specimen annealed at 800 °C had larger local elongation after the peak stress than that in the specimen annealed at 750 °C. Although this is not the main subject in this study, it is noteworthy that the combination of strength and elongation was the best when annealed at 800 °C, indicating that the optimum annealing condition and the martensite volume fraction existed in the DP microstructures. In the specimen annealed at 850 °C, the work hardening was limited within small strain region. This was similar to the behavior in the 1180 steel shown in Fig. 3.10. When the strain rate increased up to 10^3 s^{-1}, the yield strength and flow stress increased. This result will be discussed in detail later.

Table 3.3 Chemical composition (mass%) of commercially available DP590 steel used for preparing the dual-phase structures having various martensite volume fractions.

Steel	C	Si	Mn	P	S	Al	Ti	Nb	Cr
DP590	0.077	0.42	1.84	0.008	0.004	0.026	0.003	0.003	0.038

Table 3.4 Annealing condition, microstructure and quasi-static mechanical properties of the 590DP steels having various martensite volume fractions.

Annealing condition	Micro-structure	Volume fraction of martensite (%)	0.2% offset stress (MPa)	Tensile strength (MPa)	Total elongation (%)
As received	F-M	11	374	652	31.8
750 °C for 120 s	F-M	21	406	774	26.1
800 °C for 120 s	F-M	43	534	896	28
850 °C for 120 s	M (-F)	95	998	1174	24

F: Ferrite, M: Martensite

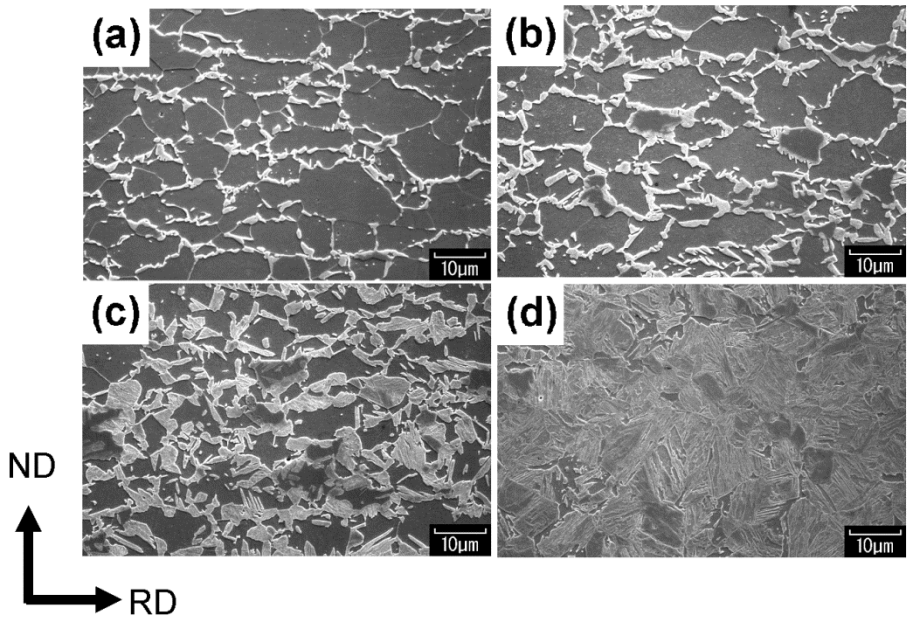

Figure 3.11 SEM microstructures of (a) the as-received DP590 steel, and the specimens after annealing at (b) 750 °C, (c) 800 °C and (d) 850 °C of the DP590 steel. The microstructures in (a, b, c) were dual-phase (DP) ones composed of ferrite and martensite, and the microstructure of (d) was 95% martensite. Observed from TD.

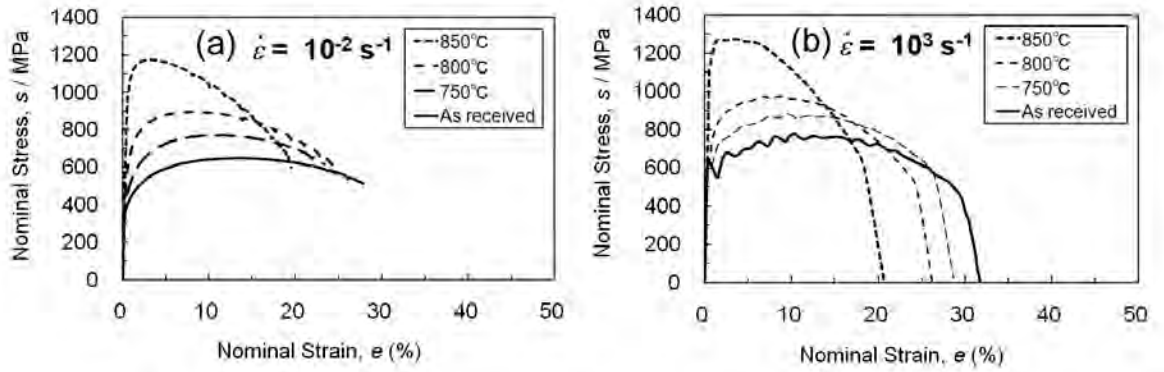

Figure 3.12 Stress-strain curves of the DP590 steel and the dual-phase steels having various martensite volume fractions fabricated by additional annealing at 750, 800 and 850 °C. The strain rates are (a) 10^{-2} s^{-1} and (b) 10^{3} s^{-1}.

3.3.4 Effect of the state of Cu on dynamic tensile properties of Fe-Cu alloys

In order to investigate the effect of state of alloying elements in ferrite microstructures on their dynamic tensile properties, Fe-0.5 mass% Cu and Fe-1.5 mass% Cu alloys are prepared. Using the Fe-Cu alloys, the state of Cu could be changed from solid solution to fine precipitates of Cu with little interaction to other alloying elements in steel, such as C, Mn and Si, etc. Cu_2S might form in the microstructures. However, its effect could be neglected, as the S content was very small.

Table 3.5 summarizes the chemical composition of the Fe-Cu alloys, as well as a pure iron used for comparison. Based on pure iron, 0.5 mass% or 1.5 mass% of Cu were added. Ni was also added depending on the Cu content. The purpose was to avoid the surface cracking during hot-rolling due to Cu enrichment at interface region between surface oxide layer and base metal. The ingots fabricated by vacuum-melting were hot-rolled at austenite region with a finishing temperature (FT) of 850 °C and air-cooled to room temperature. After removing the surface oxide layers by pickling in HCl, the 4 mm thick hot-rolled sheets were cold-rolled to 1 mm in thickness. The cold-rolling reduction in thickness was 75 %.The cold-rolled sheets were annealed at 850 °C for 120 s in a salt bath and cooled by water to room temperature. This annealing was carried out in order to form recrystallized ferrite grains and to resolve Cu in solid solution (solution-treatment). For the Fe-1.5 mass% Cu alloy, some solution-treated sheets were subsequently annealed at 550 °C or 600 °C for various periods (precipitation-treatment of Cu). By this precipitation-treatment, the state of Cu was changed. Only the solution-treatment at 850 °C was applied to the pure iron and Fe-0.5 mass% Cu alloy.

Table 3.5 Chemical compositions (mass%) of pure iron and Fe-Cu alloys used for the dynamic tensile tests.

Steel	C	Si	Mn	P	S	Al	Ni	N	Cu
Pure iron	0.0020	0.01	0.19	0.001	0.002	0.009	0.01	0.0006	0.01
Fe-0.5Cu	0.0027	0.01	0.19	0.001	0.002	0.014	0.30	0.0006	0.49
Fe-1.5Cu	0.0018	0.01	0.19	0.001	0.002	0.015	0.80	0.0004	1.47

Figure 3.13 shows the change in Vickers hardness through the precipitation-treatment at 550 °C and 600 °C of the Fe-1.5 mass% Cu alloy. When annealed at 550 °C, the hardness reached the maximum at the aging time of 1.8 ks. The condition with the maximum hardness is called as “peak strength condition” hereafter. On the other hand, during the annealing at 600 °C, the hardness reached the maximum faster, and then dropped rapidly by increasing the aging time. This condition showing the hardness drop is called as “over-aged condition” hereafter.

The precipitation behavior of Cu in α-Fe has been widely studied [21-28]. At the over-aged condition, fcc-Cu particles are clearly observed by transmission electron

microscopy (TEM) [22]. On the other hand, at the peak strength condition, it is difficult to obtain significant evidence indicating the state of Cu such as image contrast in TEM observation [22]. Many studies on the state of Cu at the peak strength condition by using various analysis methods such as field ion microscopy (FIM) [22-24], small angle neutron scattering [25, 26], and X-ray absorption fine structure (XAFS) [27, 28] have been reported. Based on those studies, it is thought that very small Cu-rich clusters having bcc structure and sizes of 2 to 4 nm exist in the ferrite matrix, contributing to the strengthening of the steel [23-28]. Therefore in this study, two kinds of specimens having different Cu precipitates, annealed at 550 °C for 1.8 ks (peak strength condition), and 600 °C for 3.6 ks (over-aged condition) are used for investigating the tensile properties.

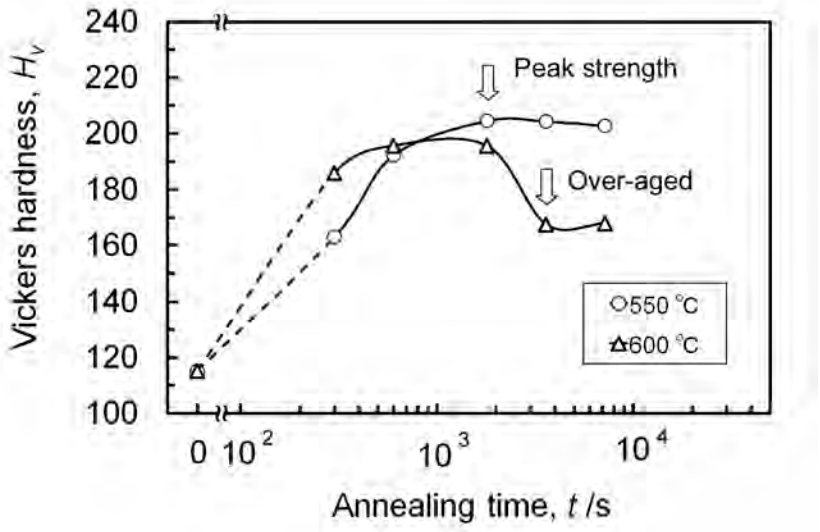

Figure 3.13 Relationship between Vickers hardness and aging time of the Fe-1.5 mass% Cu alloy solution-treated and subsequently precipitation-treated at 550 °C and 600 °C. White arrows indicate the annealing conditions of the specimens used for the tensile tests, the "peak strength condition" (550 °C for 1.8 ks), and the "over-aged condition" (600 °C for 3.6 ks).

Fig. 3.14 shows the microstructures observed by OM of the fabricated specimens of the pure iron, Fe-0.5 mass% Cu alloy and Fe-1.5 mass% Cu alloy heat-treated at various conditions. All the specimens showed ferrite single-phase microstructures, and no significant change in the microstructures were observed after the precipitation-treatments (Fig. 3. 13 (d, e)). Cu precipitates were not observed by OM. However as mentioned before, the hardness of the specimens significantly changed by the precipitation-treatments.

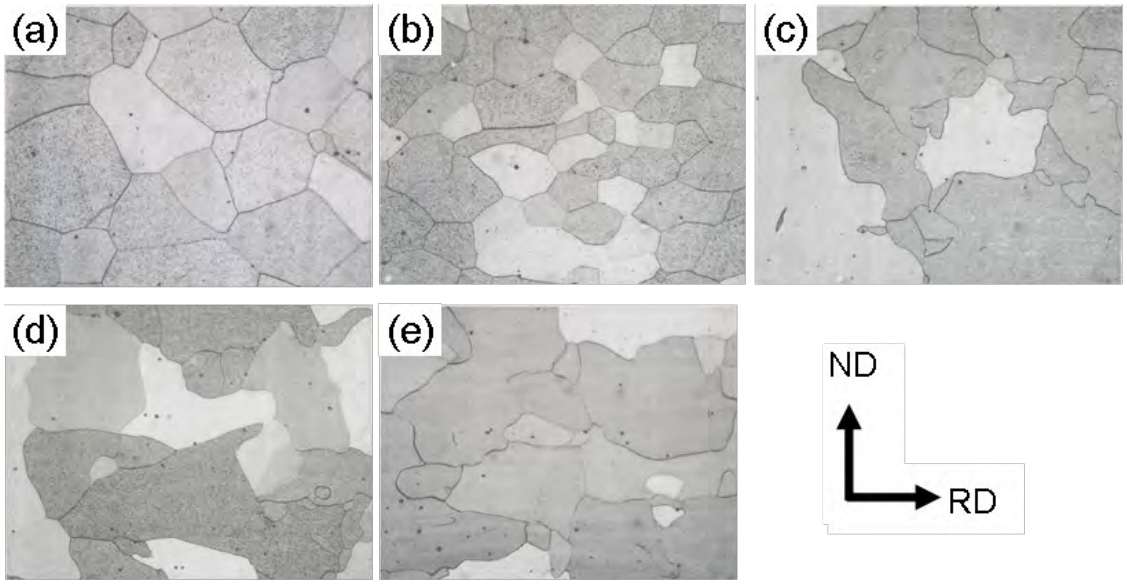

Figure 3.14 Optical micrographs of (a) pure iron, (b) Fe-0.5 mass% Cu (as solution-treated), (c) Fe-1.5 mass% Cu alloy (as solution-treated), (d) Fe-1.5 mass% Cu alloy (peak strength condition: precipitation-treated at 550 °C for 1.8 ks), and (e) Fe-1.5 mass% Cu alloy (over-aged condition: precipitation-treated at 600 °C for 3.6 ks). All the images were observed from TD. In all the optical micrographs, Cu precipitates were not observed.

Table 3.6 summarizes the microstructure and quasi-static tensile properties at 10^{-2} s^{-1} of the pure iron and the Fe-Cu alloys after the solution-treatment and subsequent precipitation-treatment under various conditions. As shown in the optical micrographs in Fig. 3.14, all the specimens had ferrite single-phase microstructure. However, the strength was increased significantly by increasing the solute Cu content up to 1.5 mass%, and by the precipitation-treatments in the Fe-1.5 mass% Cu alloy.

Table 3.6 Microstructure and quasi-static mechanical properties of the pure iron and Fe-Cu alloys.

Steel	Microstructure	0.2% offset stress (MPa)	Tensile strength (MPa)	Total elongation (%)	Note
Pure iron	Ferrite	165	255	53.6	
Fe-0.5Cu	Ferrite	189	300	49.0	solution-treated
Fe-1.5Cu	Ferrite	231	349	44.0	solution-treated
Fe-1.5Cu (peak strength)	Ferrite	492	610	28.8	550 °C for 1.8 ks
Fe-1.5Cu (over-aged)	Ferrite	416	517	29.4	600 °C for 3.6 ks

Figure 3.15 shows the tensile s-s curves of the pure iron and Fe-Cu alloys listed in Table 3.6. At quasi-static strain rate, only the pure iron showed yield drop phenomenon (Fig.

3.15 (a)). This is because the pure iron did not contain carbide/nitride-formers and therefore contained some amount of solute C and N. Other specimens of Fe-Cu alloys did not show the yield drop. The work hardening after the yielding was observed in all the specimens in the quasi-static deformation (Fig. 3.15 (a)). In the dynamic deformation (Fig. 3.15 (b)), the yield strength significantly increased, and the work hardening decreased in all the specimens. The difference in the flow stress between quasi-static and dynamic deformation in the pure iron seemed to be larger than those in other specimens. This behavior will be compared with the IF (270-440) steels and discussed in the later section.

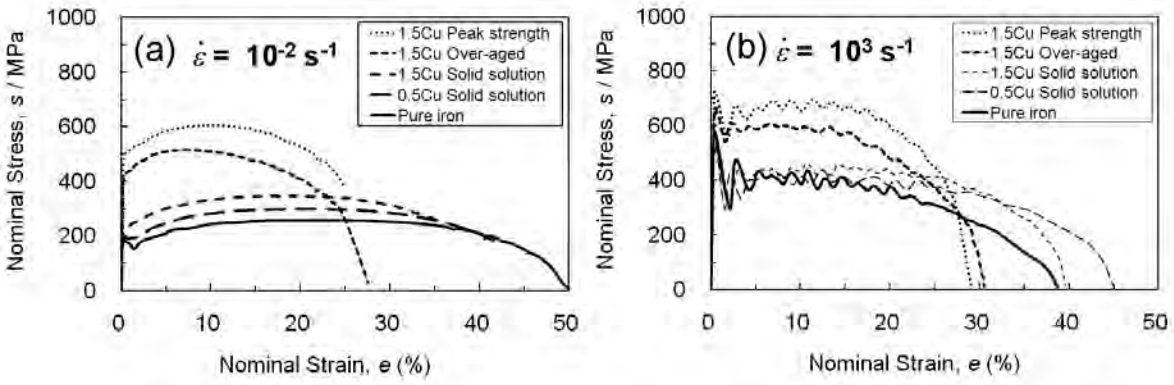

Figure 3.15 Stress-strain curves of the pure iron, Fe-0.5 mass% Cu alloy and Fe-1.5 mass% Cu alloy. For Fe-1.5 mass% Cu alloy, data of the specimens precipitation-treated at the peak-strength condition, and at the over-aged condition are shown. The strain rates are (a) 10^{-2} s^{-1} and (b) 10^{3} s^{-1}.

3.3.5 Discussion

For evaluating the effect of strain rate on strength of materials, there are two indexes generally. One is the strain rate sensitivity, *m*, which is described as:

$$\frac{\sigma_d}{\sigma_s} = \left(\frac{\dot{\varepsilon}_d}{\dot{\varepsilon}_s}\right)^m \tag{3.1}$$

where σ_s and σ_d are flow stresses at quasi-static and dynamic strain rates, respectively; $\dot{\varepsilon}_s$ and $\dot{\varepsilon}_d$ are quasi-static and dynamic strain rates, respectively. High *m*-value means the high strain rate sensitivity. The other is the increase in flow stress, $\Delta\sigma$, described as:

$$\Delta\sigma = \sigma_d - \sigma_s \tag{3.2}$$

The $\Delta\sigma$ directly indicates the difference in flow stress between dynamic and quasi-static strain rates. In automobile body design and management of crash worthiness, the difference in flow stress, $\Delta\sigma$, is more convenient and practical. Therefore in this study, the $\Delta\sigma$ is mainly discussed.

The relationship between flow stress at 5% strain and strain rate of all the specimens investigated in this section are shown in Fig. 3.16. In all the steels, the 5% flow stress continuously increased as the strain rate increased from 10^{-2} s^{-1} to 10^{3} s^{-1}. Figure 3.16

(a) shows the data of the three kinds of IF steels. The slope of the plots was the highest in the IF270 steel. When the quasi-static strength of the steel increased from 270 to 440 MPa, the slope decreased. This is due to the addition of alloying elements (Mn and P), since the those IF steels had similar ferrite single-phase microstructures. Figure 3.16 (b) shows the data of the commercial FP400, PP590, DP 780, DP980 and 1180 steels. In these commercial steels, the slope of the plots were almost the same, and smaller than that in the IF270 steel shown in Fig. 3.16 (a). Figure 3.16 (c) shows the data of the DP steels having various martensite volume fractions shown in section 3.3.3. The slope of the plots was again almost the same although the martensite volume fractions widely changed. Figure 3.16 (d) shows the data of the pure iron and Fe-Cu alloys. It is clearly seen that the slope of the plots in the pure iron was the highest, however it was decreased by Cu addition and by the precipitation-treatment in the Fe-1.5 mass% Cu alloy.

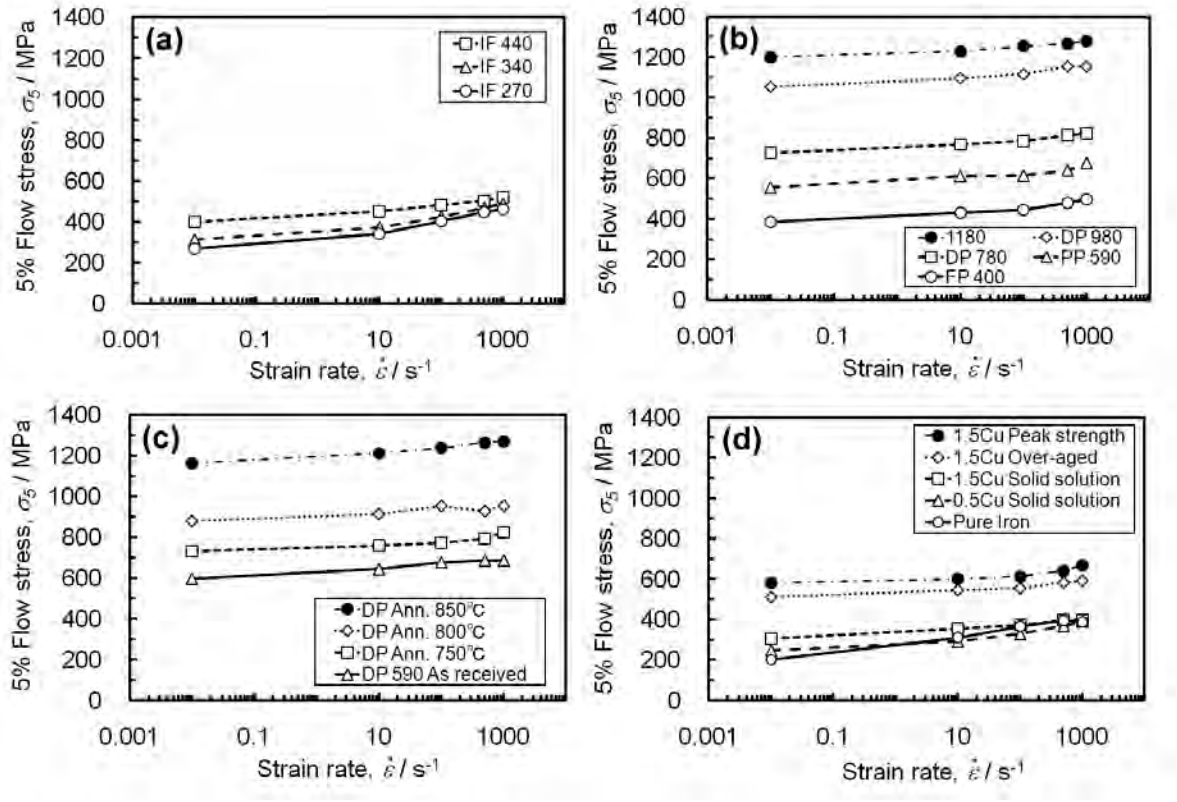

Figure 3.16 Relationship between flow stress at 5% strain and strain rate in the commercial steels. (a) IF270, IF340 and IF440 steels, (b) commercial high strength steels (HSS) having tensile strengths ranging from 400 to 1180 MPa, (c) DP590 steel and additionally annealed specimens, and (d) pure iron and Fe-Cu alloys after various heat treatments.

Figure 3.17 shows relationship between $\Delta\sigma$ and quasi-static flow stress of the commercially available sheet steels (the IF steels and the HSS) listed in Table 3.1. The $\Delta\sigma$ values were calculated as the difference in flow stress at a nominal strain of 5%, between strain rates of 10^{-2} s^{-1} and 10^{3} s^{-1}. It is shown in Fig. 3.17 that the $\Delta\sigma$ decreased significantly as the quasi-static flow stress increased up to about 400 MPa. The $\Delta\sigma$ of the FP (ferrite-pearlite) steel and the IF 440 steel, which have similar quasi-static flow stresses of

about 400 MPa, were almost the same. By further increase in the quasi-static flow stress up to 1200 MPa, the $\Delta\sigma$ did not decrease so much.

Figure 3.18 shows the $\Delta\sigma$ of the DP steels having various martensite volume fractions and the same chemical composition listed in Table 3.4. It is shown that the $\Delta\sigma$ did not change so much when the martensite volume fraction changed. Figure 3.19 shows the $\Delta\sigma$ of the pure iron and Fe-Cu alloys listed in Table 3.5. By the addition of solute Cu to the pure iron, the $\Delta\sigma$ significantly decreased, which was the same as the case in the IF steels shown in Fig. 3.17. When the solute Cu changed to precipitates by the precipitation-treatments in the Fe-1.5 mass% Cu alloy, the $\Delta\sigma$ slightly decreased. However the effect of the solute Cu content on the $\Delta\sigma$ was much larger than the effect of the state of Cu (in solid solution or in precipitates).

In order to compare the $\Delta\sigma$ values in all the steels used in this study, Figure 3.20 shows again the relationship between the $\Delta\sigma$ values at 5% strain and the quasi-static 5% flow stress of all the steels shown in Fig. 3.17 to 3.19. In addition, reference data [13, 15, 29] for commercial sheet steels including mild steels and HSS are plotted in the figure. All the data were plotted in a band indicating a decrease in the $\Delta\sigma$ with the increase in the quasi-static flow stress. The mild steels and the pure iron having quasi-static flow stress around 200 MPa had the highest $\Delta\sigma$, while it significantly decreased by strengthening the steel up to 400 MPa. When the flow stress increased up to 1200 MPa, the $\Delta\sigma$ did not decrease so much. The reference data [13, 15, 29] were plotted within the same band.

By the way, there have been a few reports where the strain rate dependence of the strength of commercial steels was evaluated using the equation (3.1). It has been reported that the ratio of dynamic TS and quasi-static TS, σ_{Bd}/σ_{Bs} in the conventional sheet steels, continuously decreased as the quasi-static TS increased from 300 to 1500 MPa [30]. However, by rearranging the data in this report [30] into the difference between dynamic and quasi-static TS ($\Delta\sigma_B$), the same behavior as the $\Delta\sigma$ in the present result was confirmed. That is, the $\Delta\sigma_B$ did not change so much when the TS was higher than 400 MPa.

Generally speaking, in most metals and alloys the flow stress increases when the strain rate increases [31-35]. A reduced effect of strain rate on the flow stress is often observed when alloying elements are added to the materials [34]. Also in this study, it was revealed that the difference in flow stress, $\Delta\sigma$, decreased by strengthening the steel using alloying elements, precipitates, and second phase. In addition, the $\Delta\sigma$ values in the steels stronger than 400 MPa were almost the same.

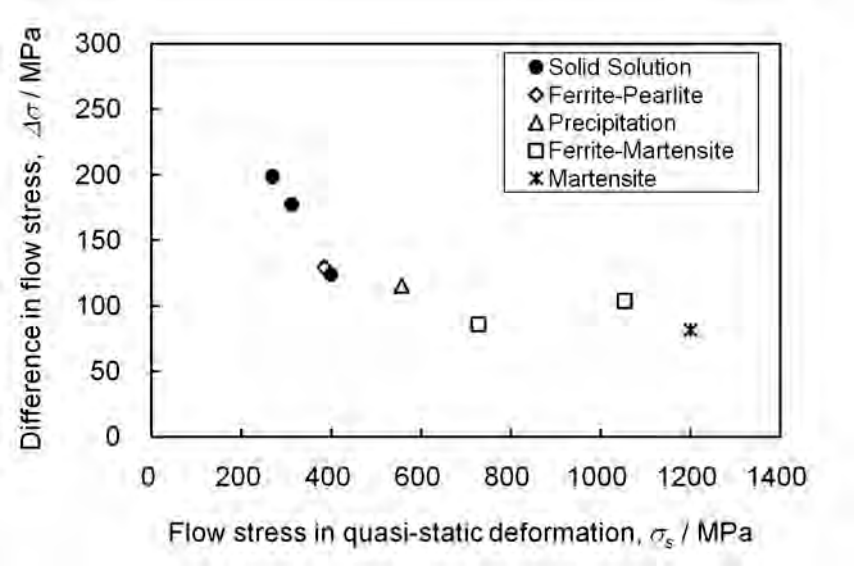

Figure 3.17 Relationship between $\Delta\sigma$ (difference in flow stress between dynamic and quasi-static strain rates) and quasi-static flow stress of the commercial IF steels and HSS strengthened by various ways. The data were taken at a nominal strain of 5%.

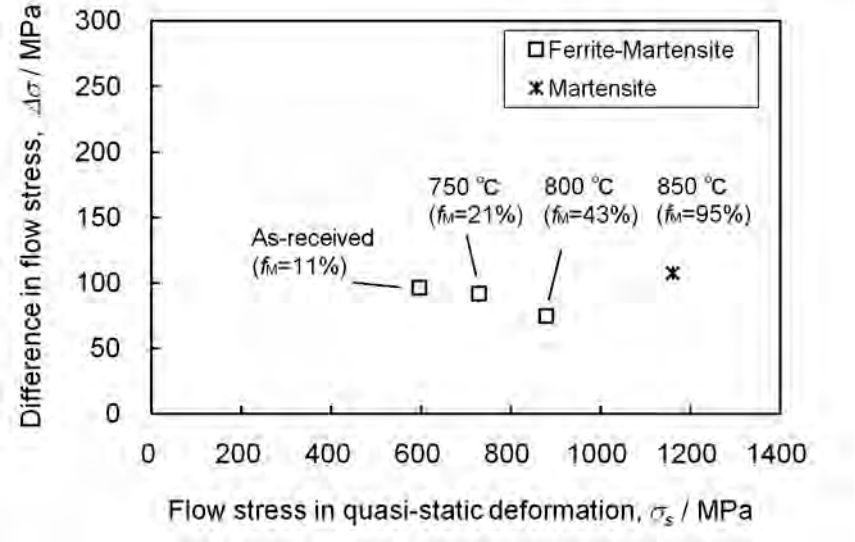

Figure 3.18 Relationship between $\Delta\sigma$ (difference in flow stress between dynamic and quasi-static strain rates) and quasi-static flow stress of the DP590 steel and additionally annealed specimens of the DP590 steel. The annealing temperatures and martensite volume fracrion, f_M, are indicated in the figure. The data were taken at a nominal strain of 5%.

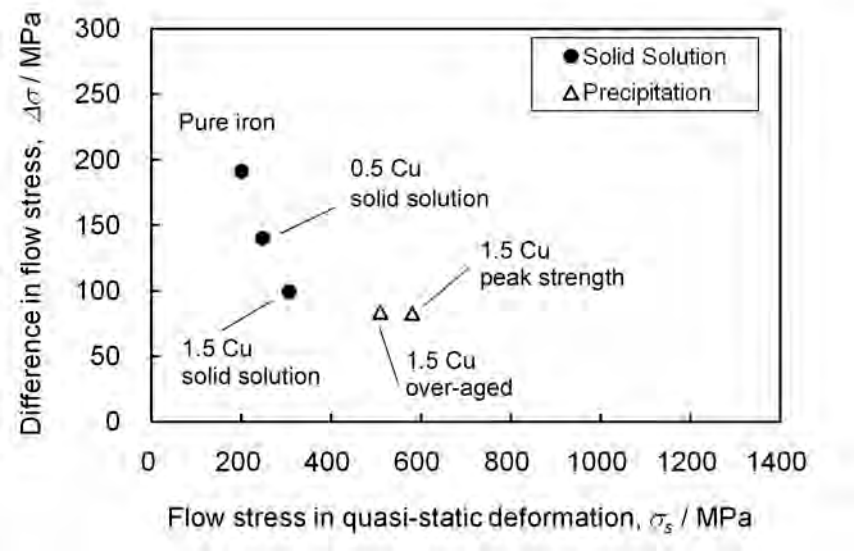

Figure 3.19 Relationship between $\Delta\sigma$ (difference in flow stress between dynamic and quasi-static strain rates) and quasi-static flow stress of the pure iron and Fe-Cu alloys. The data were taken at a nominal strain of 5%.

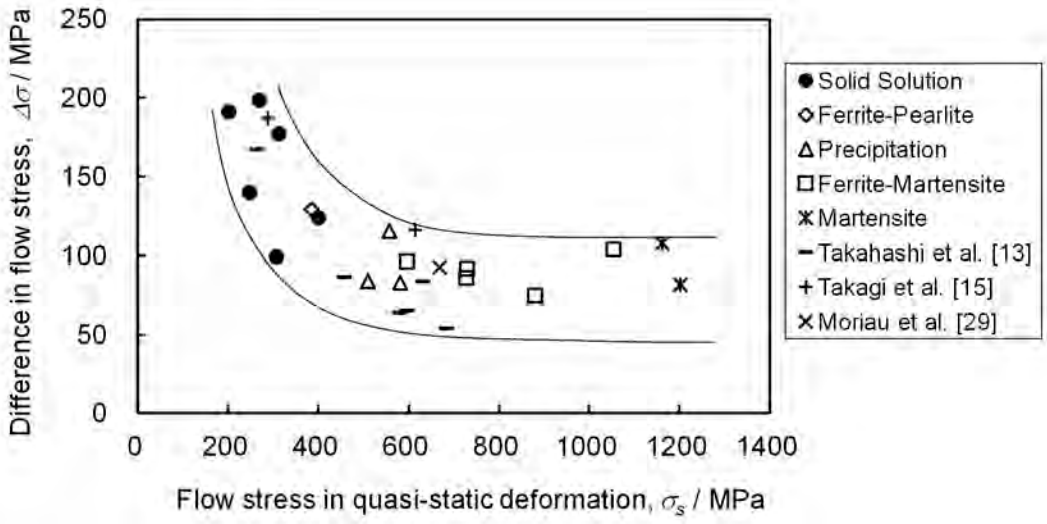

Figure 3.20 Relationship between $\Delta\sigma$ and quasi-static flow stress of the commercial sheet steels used in this sectoin. Data of conventional steels obtained from references [13, 15, 29] are also plotted. For the conventional steels used in this study, the data were taken at a nominal strain of 5%. Reference data were calculated at various nominal strains from 3 to 10 %.

3.3.6 Summary

In this section, dynamic tensile properties of the conventional sheet steels were clarified. In order to evaluate the difference in flow stress, the difference in flow stress between dynamic and quasi-static strain rates, $\Delta\sigma$, at a strain of 5% was discussed. The obtained results are summarized below.

(1) Among the commercially available sheet steels, the IF270 steel had the highest $\Delta\sigma$. As solute elements such as Mn and P were added to the IF270 steel and TS (tensile strength) increased up to 440 MPa by solution hardening, the $\Delta\sigma$ decreased significantly.

(2) When the strength increased up to 1200 MPa in commercially available HSS (high strength steels), further decrease in the $\Delta\sigma$ was not observed. Various microstructures (ferrite, ferrite-pearlite, ferrite-martensite and martensite) had similar low $\Delta\sigma$ values.

(3) The ferrite-martensite DP (dual-phase) microstructures having various martensite volume fractions were fabricated, and their dynamic tensile properties were investigated. Although the TS of the steels were widely changed from 590 to 1200 MPa depending on the martensite volume fraction, the $\Delta\sigma$ was almost constant. The change in martensite volume fraction did not affect the difference in flow stress.

(4) The dynamic tensile properties of the Fe-0.5 mass% Cu and Fe-1.5 mass% Cu alloys heat-treated at various conditions were investigated in order to clarify the effect of the state of Cu on dynamic deformation behavior. The $\Delta\sigma$ of the pure iron was as high as that in the IF270 steel, and it significantly decreased by addition of solute Cu up to 1.5 mass%. As the state of Cu changed from solute to precipitates, the $\Delta\sigma$ decreased slightly.

(5) All the $\Delta\sigma$ values of the various steels obtained in this section were distributed within a band, indicating the decrease in $\Delta\sigma$ by strengthening the steels with various mechanisms (solution hardening, precipitation hardening and introduction of hard phases). In other words, all the strengthening mechanisms decreased the difference in flow stress similarly.

3.4 Quasi-static and dynamic tensile properties of ultrafine grained ferrite steels

3.4.1 Introduction

In the previous section, it was revealed that the difference in flow stress in conventional sheet steels between dynamic and quasi-static strain rates decreased, as the strength of the steels increased by any strengthening mechanisms. However, the effect of grain refinement on dynamic deformation behavior was not investigated in the previous section. It is important to clarify the strain rate dependence of the UFG steels mainly strengthened by

grain refinement. In this section, quasi-static and dynamic tensile properties of the UFG-FC steels fabricated by the new process proposed in this study are investigated.

There have been various studies on the grain size effect on quasi-static mechanical properties of UFG steels. Tsuji et al. [36] have shown the increase in strength and the decrease in elongation by ultra grain refinement of IF steel fabricated by ARB and subsequent annealing, at a quasi-static strain rate. They [36] have revealed the significant drop in uniform elongation by grain refinement down to sub-micrometer, and have pointed out that it was caused by the early plastic instability due to lack of work hardening in the ultrafine single-phase microstructure. The same phenomenon has been reported in previous studies on UFG aluminium [36, 37] and consolidated iron [38].

On the other hand, there have been only a few studies on dynamic deformation properties of UFG iron and steel [39, 40]. Jia et al. [39] have shown dynamic compression properties of a consolidated pure iron. Tsuchida et al. [40] have shown dynamic tensile properties of an UFG bar-steel fabricated by caliber-rolling at warm temperatures (i.e. 450 °C). Dynamic deformation properties in tension mode of UFG sheet steels having fully-annealed ferrite microstructures have not been reported yet. The fully-annealed UFG-FC steels produced by the thermomechanical process shown in Chapter 2 are favorable for the systematic investigation of the grain size effect on the dynamic deformation properties. In addition, in the previous studies [39, 40] dynamic deformation experiments were carried out by using the SHPB type equipment, so that the applied strain rates were limited at around 10^3 to 10^3 s^{-1}. Consequently, dynamic deformation behaviors in the UFG steels at intermediate strain rates between 10^{-1} and 10^2 s^{-1} have not been clarified yet. In this study, by using the load-sensing type high-speed test equipment, tensile properties at a wide range of strain rates could be obtained. In this section, first, quasi-static tensile properties of the UFG-FC steels fabricated in this study are shown and compared with the previous results. Secondly, the dynamic tensile behaviors of the UFG-FC steels at various strain rates are shown and discussed.

By the way, the UFG-FC steels fabricated in this study, as well as the UFG iron and steel in the previous studies [39, 40], contained some amounts of solute C. Therefore, the effect of such interstitial solute elements still could not be neglected. In order to clarify the dynamic deformation behavior of the UFG steels without interstitial solute elements, UFG-IF steels are prepared and their dynamic tensile properties are investigated. By using IF steels, pure effect of grain refinement can be clarified. The ferrite grain sizes are widely changed by ARB and subsequent annealing from ultrafine grain size to conventional one in an IF steel. A systematic investigation of tensile properties at a wide range of grain size and strain rate is carried out.

Finally in this section, the strain rate dependence of the mechanical properties in the UFG-FC and UFG-IF steels are summarized and compared with those in the conventional HSS.

3.4.2 Experimental procedure

The fabricating process and microstructures of the UFG-FC steels have been shown in Chapter 2. The UFG-FC1 and UFG-FC2 steels are used in this section. Table 3.7 summarizes again the chemical compositions of these steels, which have been already shown in Table 2.4 and Table 2.5. The UFG-FC1 and UFG-FC2 steels have substantially the same chemical composition.

Figure 3.21 and 3.22 show the fabricating conditions of the UFG-FC1 and UFG-FC2 steels, respectively. In order to prepare the duplex microstructures before cold-rolling, two different procedures were taken after hot-rolling. The UFG-FC1 steel was air-cooled to intercritical region of ferrite and austenite after hot-rolling, and then water-cooled. On the other hand, in the UFG-FC2 steel, the hot-rolled sheet was reheated at 1000 °C followed by water-quenching and then reheated again at intercritical region of ferrite and austenite followed by water-quenching to room temperature. As shown in section 2.2, the UFG-FC2 steel had finer microstructure than the UFG-FC1 steel before cold-rolling. Cold-rolling was carried out with lubrication at room temperature, and all the cold-rolled sheets were annealed in a salt bath at various temperatures between 575 and 700 °C. In addition, for comparison, coarse-grained (CG) FC specimen was prepared by using the cold-rolled sheets of the UFG-FC1 steel, by applying a long-time annealing at 650 °C for 57.6 ks (16 h) in N_2 atmosphere.

As another UFG ferrite microstructure, UFG-IF steel was fabricated by ARB and subsequent annealing. Table 3.8 summarizes the chemical composition of the commercial IF steel used for the ARB process. The received IF steel with a thickness of 1 mm was cut in a width of 30 mm and a length of 300 mm. Two sheets were stacked, heated at 500 °C for 1.8 ks and then roll-bonded by one pass 50% reduction without lubrication. This ARB process was repeated up to 5 times (5 cycles of ARB). The ARB processed sheets, having the same thickness as the starting material of 1 mm, were annealed at various temperatures between 600 and 700 °C for 1.8 ks in order to change the ferrite grain sizes.

Table 3.7 Chemical compositions (mass%) of the low-C steels for fabricating UFG-FC microstructures.

Steel	C	Si	Mn	P	S	Al	Nb	B	N
UFG-FC1	0.10	0.01	1.98	0.002	0.001	0.018	0.018	0.0015	0.0011
UFG-FC2	0.10	0.01	2.00	0.002	0.001	0.035	0.022	0.0015	0.0007

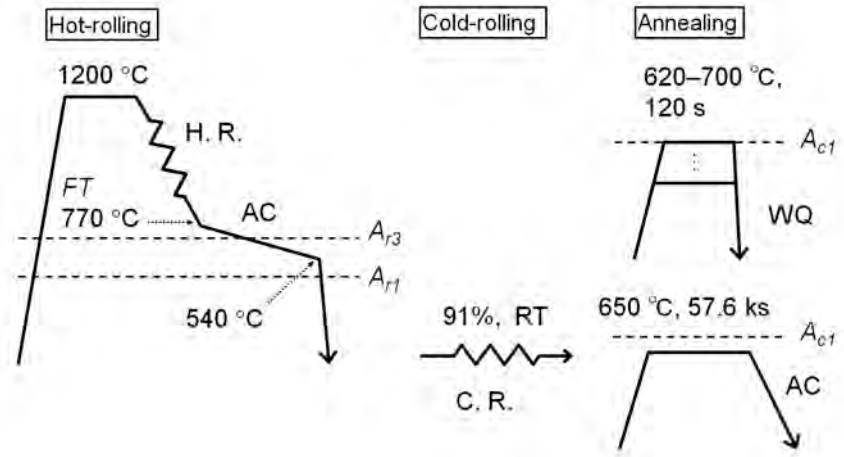

Figure 3.21 Schematic drawing of the process for fabricating the UFG-FC1 steels. A_{r1}, A_{r3}, and A_{c1} mean the transformation temperatures measured by dilatometer. The A_{r1}, A_{r3}, and A_{c1} are 465 °C, 625 °C and 700 °C, respectively.

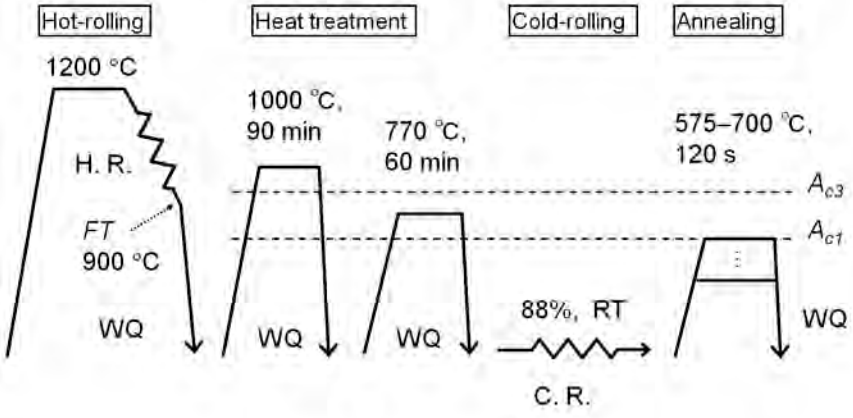

Figure 3.22 Schematic drawing of the process for fabricating the UFG-FC2 steels. A_{c1} and A_{c3} mean the transformation temperatures measured by dilatometer. The A_{c1} and A_{c3} are 699 °C and 832 °C, respectively.

Table 3.8 Chemical composition (mass%) of the IF steel for ARB processing to fabricate UFG microstructures.

Steel	C	Si	Mn	P	S	Al	Ti	N
UFG-IF	0.002	0.01	0.17	0.012	0.007	0.033	0.047	0.003

Microstructures of the specimens were observed by SEM. The samples for SEM were etched with a 3% Nital. SEM observations were conducted on Hitachi S-4300E/N SEM operated at 15 kV. All the specimens were observed on the TD section of the sheets. For the UFG-IF steels, the dislocation substructures were observed using transmission electron microscopy (TEM). The TEM observation was operated for both specimens before and after the tensile test at various strain rates. Thin foils for the deformed specimens, prepared by twin-jet electropolishing, were taken from the un-necked gauge section (1-1.5

mm far from the fractured point) of the tensile specimens after the tensile tests. The TEM observations were also carried out from TD of the sheets. Ferrite grain sizes were measured by mean intersection method using SEM microstructures. In section 2.2, the grain sizes of the same UFG-FC1 specimens calculated in the EBSD analysis were shown, however, in order to unify the measurement method with other UFG-FC specimens which do not have EBSD data, the grain sizes in the UFG-FC1 steels were measured again by the mean intersection method.

The small tensile specimens shown in Fig. 3.6, of which tensile direction was parallel to RD were taken from the fabricated sheets. Quasi-static and dynamic tensile tests were carried out by using the load-sensing block type test equipment shown in Fig. 3.5. At various strain rates (10^{-2}, 10, 10^{2}, $5x10^{2}$ and 10^{3} s^{-1}), two or three specimens were tested. From the displacement-load curves, the elastic region was removed and nominal stress-strain curves were generated.

3.4.3 Quasi-static tensile properties of ultrafine grained ferrite-cementite steels

Quasi-static tensile properties of the UFG-FC steels are shown and discussed. First, representative microstructures are shown again. Figure 3.23 (a, b, c and d) shows the SEM microstructures of the UFG-FC1 steel annealed at 620, 635, 670 and 700 °C, respectively. The specimens annealed at 620 to 670 °C shown in Fig. 3.23 (a-c) had ultrafine FC microstructures, while the specimen annealed at 700 °C (Fig. 3.23 (d)) contained slight amount of martensite (light gray islands) in addition to the FC microstructure. This microstructure is called as FCM (ferrite-cementite-martensite) microstructure hereafter. Figure 3.23 (e) shows the SEM microstructure of the coarse-grained (CG) ferrite specimen, obtained by the log-time annealing at 650 °C for 57.6 ks. This is called as CG-FC microstructure hereafter.

Figure 3.24 shows s-s curves of the UFG-FC1 specimens of which microstructures are shown in Fig. 3.23, at quasi-static strain rate (10^{-2} s^{-1}). Representative curves for each microstructure are shown. In the figure, mean ferrite grain sizes are indicated. By ultra grain refinement down to 0.6 μm, the yield strength increased up to about 1000 MPa, which is about two times higher than that of the CG specimen annealed at 650 °C for 57.6 ks. All the UFG-FC specimens (d < 1.14 μm) showed significant yield drop, but did not show work hardening after yielding. On the other hand, in the CG-FC and the FCM specimen, work hardening was observed after slight yield-drop, resulting in an improvement of uniform elongation. The work hardening was more significant in the FCM specimen. This is due to the introduction of martensite to the FC microstructure.

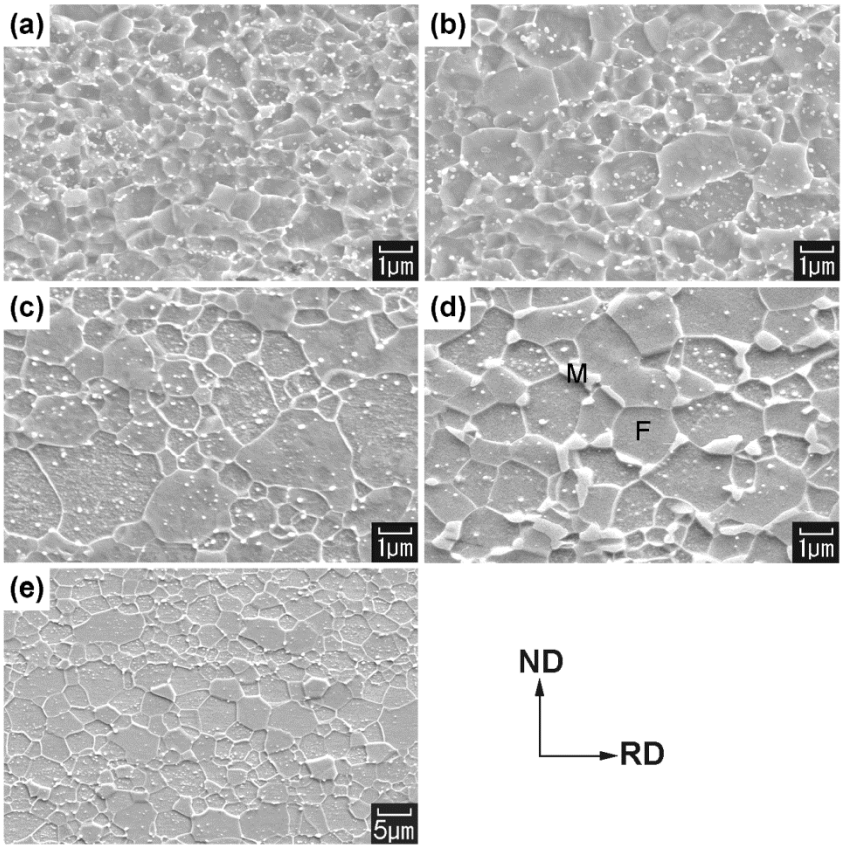

Figure 3.23 SEM microstructures of the UFG-FC1 steel 91% cold-rolled and annealed at (a) 620 °C, (b) 635 °C, (c) 670 °C and (d) 700 °C for 120 s. The letters "F" and "M" in (d) indicate ferrite and martensite, respectively. (e) Coarse-grained FC specimen annealed at 650 °C for 57.6 ks using the same cold-rolled sheet as the UFG-FC1 specimens. All the microstructures were observed from TD.

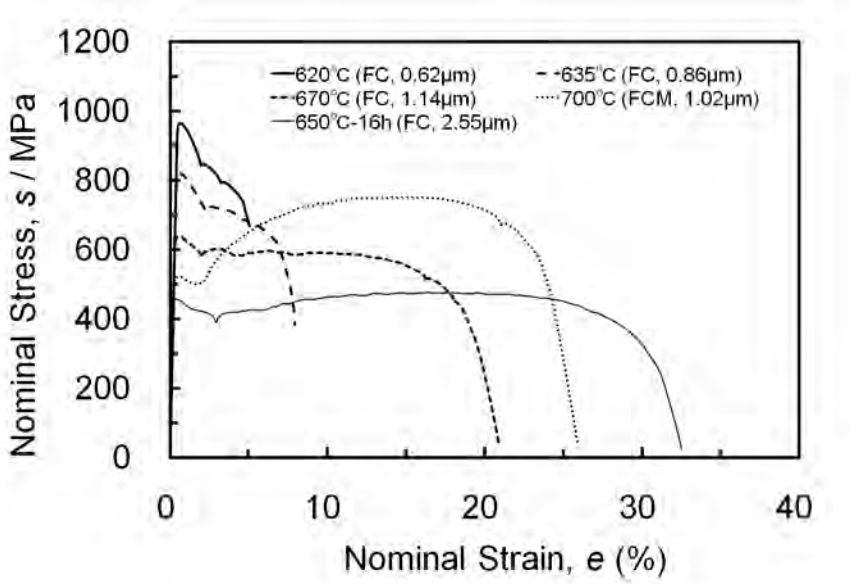

Figure 3.24 Nominal stress-strain curves at a strain rate of 10^{-2} s^{-1} of the UFG-FC1 specimens 91% cold-rolled and annealed at 620 °C, 635 °C, 670 °C, 700 °C for 120 s, and at 650 °C for 57.6 ks (long-time annealing). The mean ferrite grain sizes measured by mean intersection method are indicated in the figure.

Table 3.9 and Table 3.10 summarizes annealing condition, microstructure, mean ferrite grain size and quasi-static mechanical properties of the specimens fabricated from the UFG-FC1 and UFG-FC2 steels, respectively. The total elongation was slightly higher in the UFG-FC2 specimens than that in the UFG-FC1 specimens having the same tensile strength. This is due to the difference in thickness of the specimens. The thickness was 1.0 mm in the UFG-FC2 specimens, which improved the (post-necking) elongation compared with the UFG-FC1 specimens having a thickness of 0.6 mm. In both steels, uniform elongation dropped as the grain size decreased down to about 1 μm. This behavior was the same as that observed in the UFG-IF steel [36] and UFG aluminium [36, 37].

Figure 3.25 shows mean ferrite grain size, 0.2% offset stress and total elongation of the UFG-FC1 and UFG-FC2 steels as a function of annealing temperature. When compared the data at the same annealing temperature, the mean ferrite grain sizes of the UFG-FC2 specimens were slightly larger than those of the UFG-FC1 steel. Therefore, the strength of the UFG-FC2 specimens was slightly lower than those of the UFG-FC1 specimens at the same annealing temperatures. This is because the UFG ferrite grains formed at lower annealing temperature in the UFG-FC2 steel, as described in section 2.2.

Table 3.9 Annealing temperature, microstructure, mean ferrite grain size and mechanical properties of the UFG-FC1 steels annealed under various conditions, at quasi-static strain rate (10^{-2} s^{-1}). The thicknesses of the specimens are 0.6 mm.

Annealing temperature (°C)	Micro-structure	Mean ferrite grain size (μm)	0.2% offset stress (MPa)	Tensile strength (MPa)	Uniform elongation (%)	Total elongation (%)
620	UFG-FC	0.62	966	966	0.6	8.4
635	UFG-FC	0.86	822	825	0.7	10.9
650	UFG-FC	0.96	770	772	0.6	11.7
655	UFG-FC	1.01	663	672	0.8	16.7
670	UFG-FC	1.14	636	640	0.6	22.1
680	UFG-FC	1.18	608	616	15.0	30.9
700	FCM	1.12	520	753	14.2	28.0
650 (57.6ks)	CG-FC	2.55	465	477	15.7	35.1

F: ferrite, C: cementite, M: martensite

Table 3.10 Annealing temperature, mean ferrite grain size and mechanical properties of the UFG-FC2 steels annealed at various conditions, at quasi-static strain rate (10^{-2} s^{-1}). The thicknesses of the specimens are 1.0 mm.

Annealing temperature (°C)	Micro-structure	Mean ferrite grain size (μm)	0.2% offset stress (MPa)	Tensile strength (MPa)	Uniform elongation (%)	Total elongation (%)
575	UFG-FC	0.58	938	940	0.7	12.4
600	UFG-FC	0.80	819	823	0.7	15.0
625	UFG-FC	1.06	666	673	0.7	18.0
650	UFG-FC	1.35	609	609	0.6	25.8
675	UFG-FC	1.79	566	568	15.1	35.3
700	FCM	1.77	514	609	17.1	36.8

F: ferrite, C: cementite, M: martensite

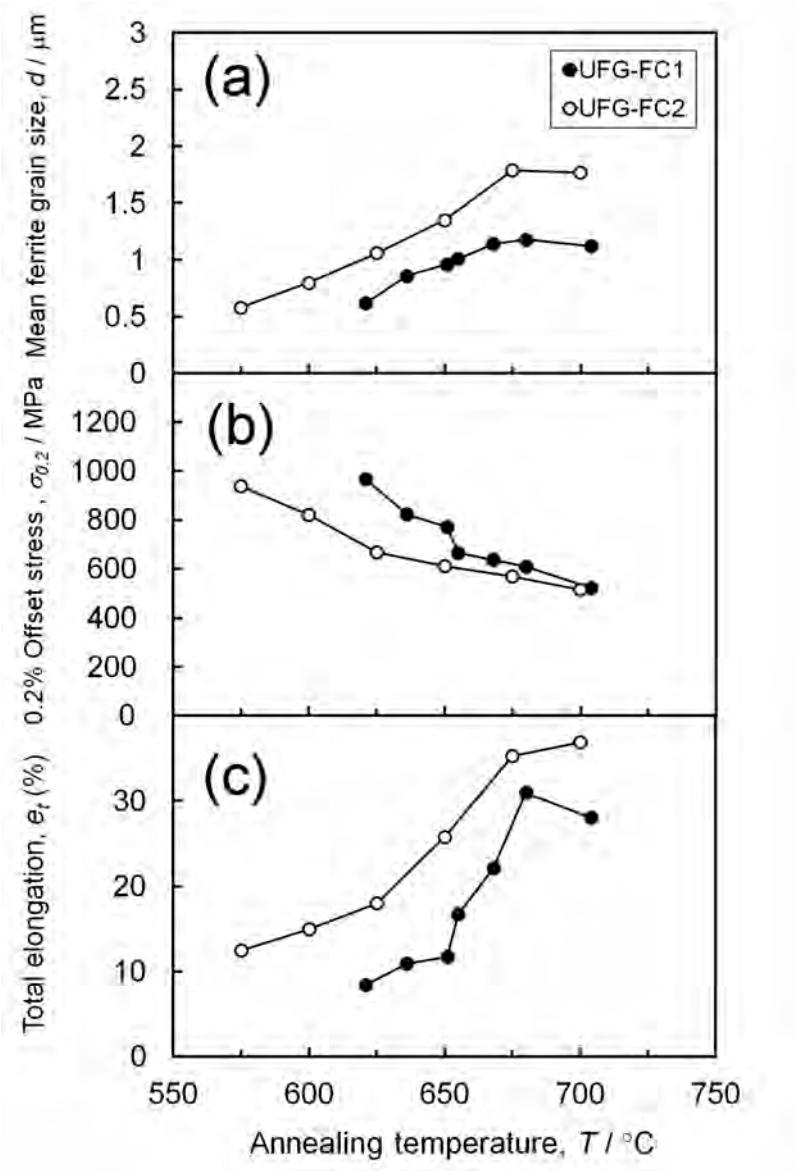

Figure 3.25 (a) Mean ferrite grain size, (b) 0.2% offset stress and (c) total elongation of the UFG-FC1 and UFG-FC2 steels as a function of annealing temperature.

3.4.4 Dynamic tensile properties of ultrafine grained ferrite-cementite steels

Dynamic tensile behaviors of the UFG-FC steels are shown and discussed here. Figure 3.26 shows the s-s curves of the UFG-FC1 steels at various strain rates ranging from 10^{-2} to 10^{3} s^{-1}. Figure 3.26 (a, b, c, d) correspond to the UFG-FC1 steels annealed at 620, 635, 670 and 700 °C, respectively. The microstructures have been shown in Fig. 3.23 (a-d). The oscillations in the s-s curves at high strain rates are caused by remained stress wave generated during the dynamic tensile test, and do not reflect the nature of deformation behaviors of the materials. It is shown that the flow stress significantly increased when the strain rate increased in the UFG-FC microstructures (Fig. 3.26 (a-c)). On the other hand, the increase in flow stress in the FCM specimen (Fig. 3.26 (d)) seemed to be smaller than those in the UFG-FC specimens. In order to clarify this behavior, Figure 3.27 shows the relationship between 5% flow stress and strain rate in the UFG-FC microstructures and FCM microstructure. Examples of the UFG-FC specimens having various ferrite grain sizes were chosen from the UFG-FC1 and UFG-FC2 steels and plotted in Fig. 3.27. The slopes of plots for the UFG-FC specimens were almost the same and close to that for the CG-FC specimen. On the other hand, the slope for the FCM microstructure was smaller than those of the UFG-FC ones. This small strain rate dependence in the FCM microstructure was similar to those of the commercial DP steel shown in section 3.3.

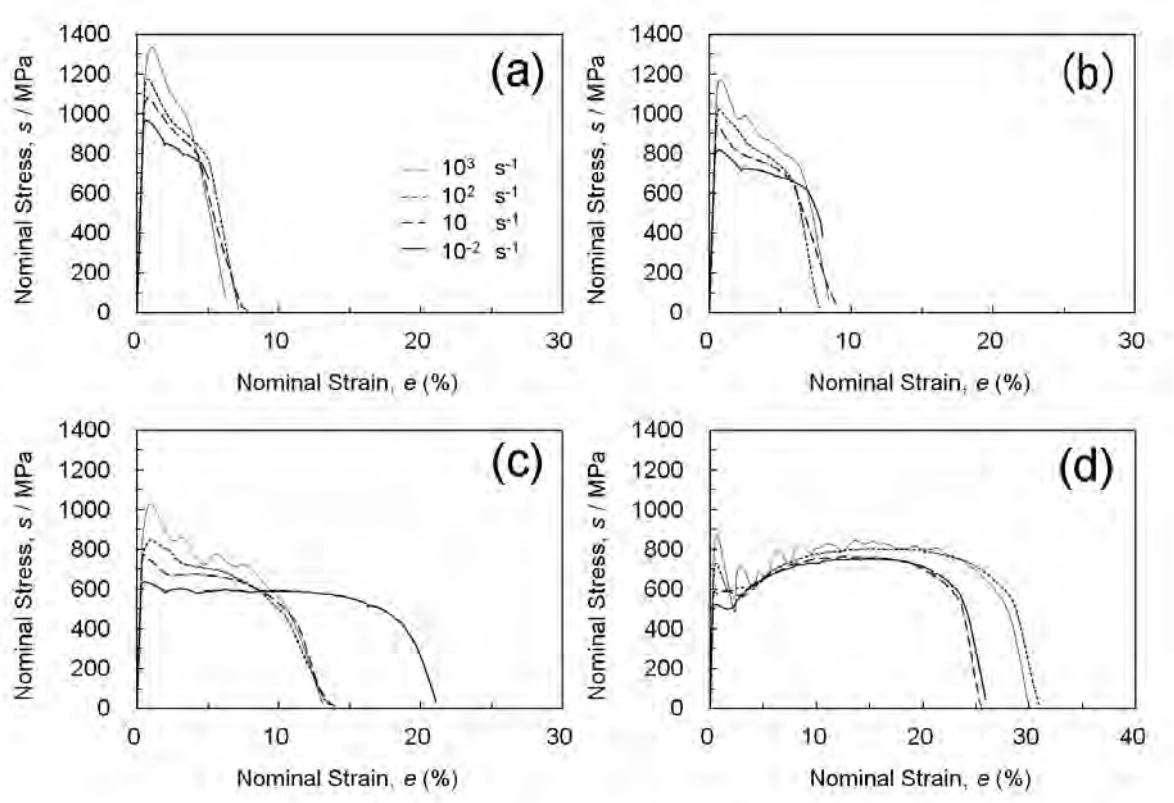

Figure 3.26 Nominal stress-strain curves of the UFG-FC1 steel 91% cold-rolled and annealed at (a) 620 °C, (b) 635 °C and (c) 670 °C. (d) FCM specimen fabricated from the same cold-rolled sheet of the UFG-FC1 specimens by annealing at 700 °C.

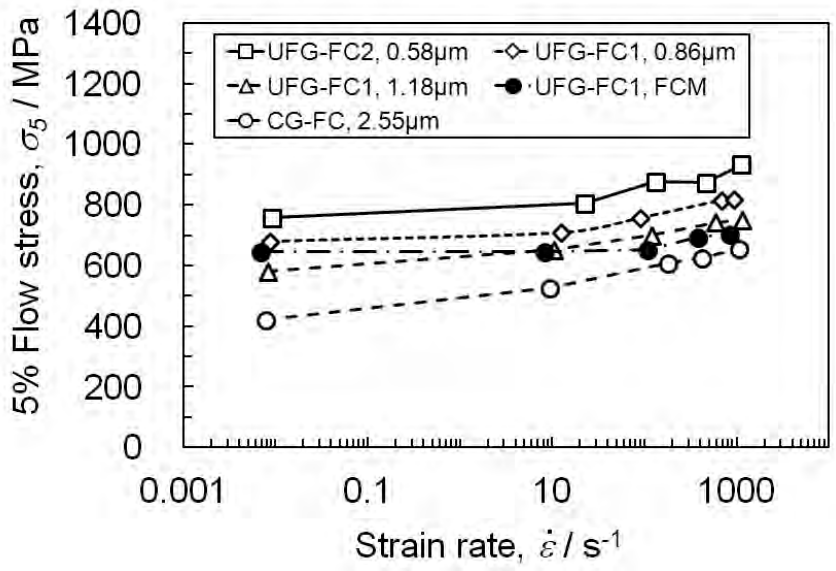

Figure 3.27 Relationship between 5% flow stress and strain rate in the UFG-FC steels having ferrite grain sizes of 0.58 μm, 0.86 μm, and 1.18 μm. In addition, the data of the FCM and CG-FC microstructures fabricated from the same UFG-FC1 steel are shown.

Table 3.11 summarizes 5% flow stress at dynamic and quasi-static strain rates, and calculated $\Delta\sigma$ values in the UFG-FC1 and UFG-FC2 specimens. The UFG-FC microstructures showed high $\Delta\sigma$ values, ranging from 134 to 186 MPa. On the other hand, the $\Delta\sigma$ value in the FCM microstructure was fairly low (26 MPa). It has been shown in Fig. 3.20 that the $\Delta\sigma$ values in the conventional HSS with quasi-static flow stresses larger than 500 MPa were in a range between 54 and 116 MPa.

On the other hand, the previous studies [39, 40] indicated that the UFG iron and steel have high $\Delta\sigma$ (difference in flow stress) in steels. Jia et al. [39] have carried out dynamic and quasi-static compression tests for a consolidated iron having ferrite grain sizes between 270 nm and 20 μm, and have shown that $\Delta\sigma$ was almost constant regardless the grain size, indicating that the grain refinement does not change the difference in flow stress. However, the $\Delta\sigma$ in tension mode has not been clarified in their study [39]. Tsuchida et al. [40] have prepared bar-steel specimens having FC microstructures and various ferrite grain sizes by warm-rolling at various temperatures ranging from 773 to 1043 K and investigated dynamic tensile properties by using the SHPB method. However, the specimens they [40] obtained contained only 60% of high-angle grain boundaries (HAGBs). As shown in Fig. 2.8, the UFG-FC specimens fabricated in this study contained at least 77% of HAGBs, indicating fully annealed microstructure. Therefore, it was clarified in this section that grain refinement of ferrite down to sub-micrometer certainly kept high $\Delta\sigma$ value in low-C steel.

By the way, the UFG-FC steel shown in this section still contained some amount of solute atoms such as C. Therefore, the effect of the solute atoms on the deformation behavior could not be neglected. In the next section, by using the UFG-IF steels which contain no interstitial atoms, the dynamic tensile behaviors of the UFG ferrite microstructures will be discussed in detail.

Table 3.11 Flow stress at 5% strain at quasi-static and dynamic strain rates, and $\Delta\sigma$ of the UFG-FC1 and UFG-FC2 steels fabricated under various conditions.

Steel	Annealing temperature (°C)	Micro-structure	5% flow stress at 10^{-2} s^{-1} (MPa)	5% flow stress at 10^{3} s^{-1} (MPa)	Difference in flow stress, $\Delta\sigma$ (MPa)
UFG-FC1	635	UFG-FC	680	817	137
UFG-FC1	650	UFG-FC	652	838	186
UFG-FC1	655	UFG-FC	627	761	134
UFG-FC1	670	UFG-FC	594	755	161
UFG-FC1	680	UFG-FC	582	753	171
UFG-FC1	700	FCM	649	675	26
UFG-FC1	650 (57.6ks)	CG-FC	420	655	235
UFG-FC2	575	UFG-FC	759	933	174
UFG-FC2	625	UFG-FC	600	767	167
UFG-FC2	650	UFG-FC	565	716	151
UFG-FC2	675	UFG-FC	510	702	192

UFG: ultrafine grained, CG: coarse grained

F: ferrite, C: cementite, M: martensite

3.4.5 Quasi-static and dynamic tensile properties of ultrafine grained interstitial-free steels

The IF specimens after ARB and subsequent annealing showed ferrite single-phase matrix. Figure 3.28 shows SEM microstructures of the fabricated UFG-IF steels. The name of the specimen and annealing condition are indicated in Table 3.12. The specimens after ARB (which is hereafter called as specimen A) and the specimen ARB processed and annealed at 600 °C (specimen B) had elongated ferrite grains including dislocation substructures, while the specimens annealed at 625 °C (specimen C) and 700 °C (specimen D) had equiaxed ferrite grains. The TEM observations have confirmed that the microstructures of the specimens C and D were free from dislocation substructures. For these UFG-IF steels, mean ferrite grain sizes are represented by the mean intersection length of ferrite grains, d_t along the normal direction (ND), measured on the SEM micrographs. This is because some of the UFG-IF specimens showed ferrite grains elongated to RD. The mean ferrite grain sizes, d_t, and quasi-static tensile properties of the UFG-IF steels as well as those in the as-received IF steel are summarized in Table 3.12. It is shown that strength significantly increased but uniform elongation decreased by ultra grain refinement in the IF steel.

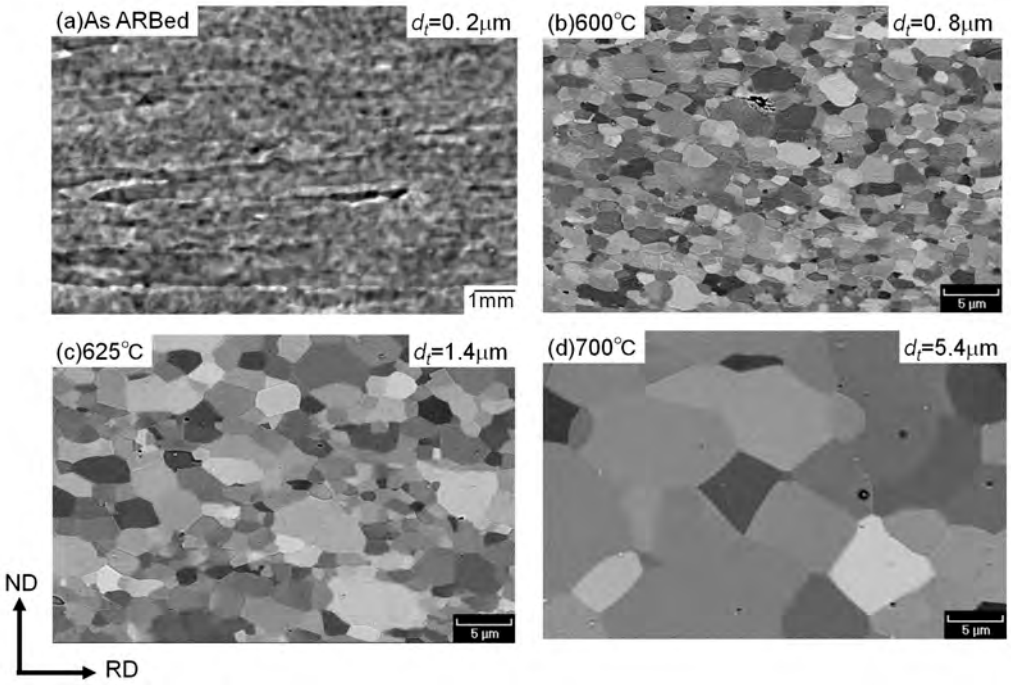

Figure 3.28 SEM microstructures of the fabricated UFG-IF steels. (a) As ARB processed. (b, c, d) ARB processed and then annealed at 600 °C, 625 °C and 700 °C, respectively. Observed from TD.

Table 3.12 Annealing temperature, mean ferrite grain size and mechanical properties at quasi-static strain rate (10^{-2} s^{-1}) of the IF steels ARB processed and subsequently annealed under various conditions. In addition, data of the as-received IF steel are summarized as well. The thicknesses of the specimens are 1.0 mm.

Specimen	Annealing temperature (°C)	Mean ferrite grain size (μm)	0.2% offset stress (MPa)	Tensile strength (MPa)	Uniform elongation (%)	Total elongation (%)
A	As ARBed	0.2	762	830	2.1	10.5
B	600	0.8	541	549	2.2	20.1
C	625	1.4	287	384	16.8	37.5
D	700	5.4	158	307	23.1	46.7
IF steel	-	13	188	319	20.7	50.3

Figure 3.29 shows representative nominal s-s curves of the specimens at various strain rates ranging from 10^{-2} to 10^{3} s^{-1}. The tests were carried out for 2 to 3 times under the identical condition, and typical curves were selected and shown. The flow curves at 10^{3} s^{-1} showed oscillations. The oscillations are caused by the impact wave generated during the dynamic tensile test, and do not reflect the nature of deformation behaviors of the materials. It is shown that the strength of the steel increased and the elongation decreased as the strain rate increased. Only in the specimen A, the total elongation increased as the strain rate increased. However, the reason of the increase in elongation is unclear at this moment.

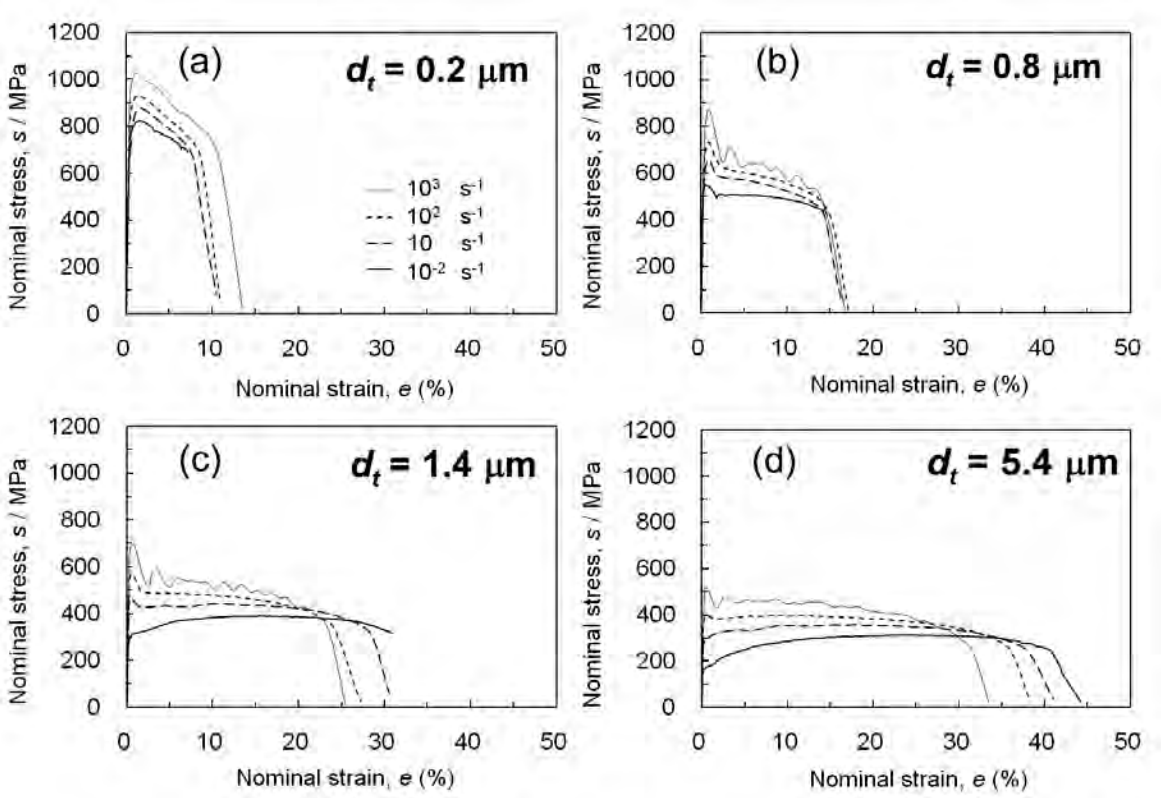

Figure 3.29 Stress-strain curves of the ultrafine grained IF steels. (a) As ARB processed. (b, c, d) ARB processed and annealed at 600 °C, 625 °C and 700 °C, respectively. The mean ferrite grain sizes of the specimens are presented in the figures.

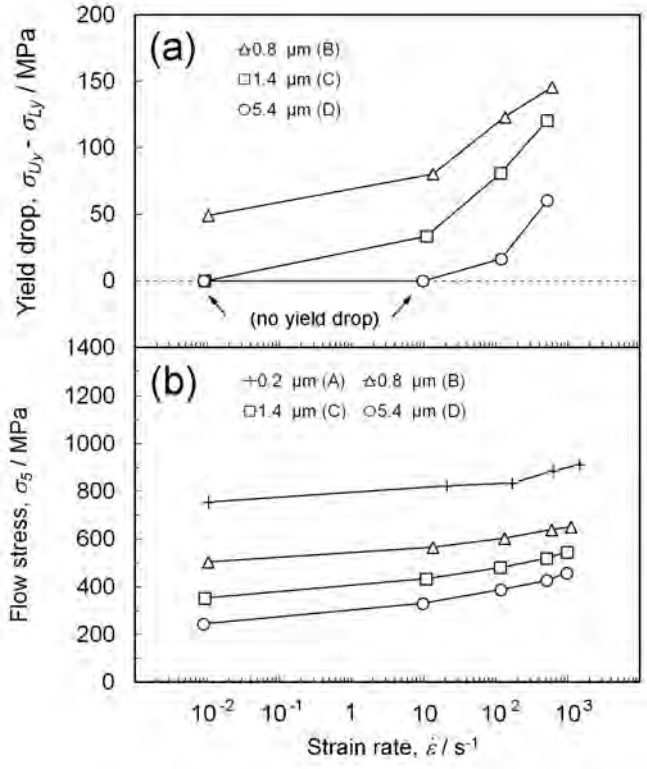

Figure 3.30 (a) Amount of yield drop, and (b) flow stress at 5% tensile strain as a function of strain rate in the ARB processed and subsequently annealed IF steels having various ferrite grain sizes.

First, the yielding behavior of the fabricated IF steels is described. At the quasi-static strain rate (10^{-2} s^{-1}) yield drop phenomenon was observed in the UFG-IF specimens A and B, which had ferrite grain sizes smaller than 1 μm. The effect of strain rate on yielding behavior was slightly different between large and small grain sizes. In the specimens C and D having grain sizes larger than 1 μm, yield drop phenomenon appeared only at higher strain rates (Fig.3.29 (c, d)). On the other hand, in the specimens A and B having grain sizes smaller than 1 μm, yield drop phenomenon was observed at all the strain rates between 10^{-2} s^{-1} and 10^{3} s^{-1} (Fig. 3.29 (a, b)). The amount of yield drop (difference between upper yield stress (σ_{Uy}) and lower yield stress (σ_{Ly})) is plotted as a function of strain rate in Fig.3.30 (a). As upper yield stress, peak stress was taken. The critical strain rate above which yield point phenomenon happened decreased with decreasing the grain size. In all the grain sizes, the yield drop became more significant and the amount of yield drop increased, as strain rate increased.

Next, the effect of strain rate on flow stress during plastic deformation is discussed. Figure 3.30 (b) shows flow stresses at a nominal tensile strain of 5% (σ_5) as a function of strain rate. The flow stress increased as the strain rate increased, which is similar behavior to that in the UFG-FC steels. The difference in the 5% flow stress between strain rates of 10^{-2} s^{-1} and 10^{3} s^{-1}, $\Delta\sigma$, is summarized in Table 3.13. In addition, data of the as-received IF steel is also listed. It is shown that the $\Delta\sigma$ values in the specimens C and D having ferrite grain sizes larger than 1 μm were as high as that in the as-received IF steel. On the other hand, when the ferrite grain sizes were smaller than 1 μm (specimens A and B), slight decrease in the $\Delta\sigma$ compared with the as-received IF steel was observed. However they were still higher than those in the conventional HSS (see Fig. 3. 20), and close to those in the UFG-FC steels having sub-micrometer ferrite grain sizes (see Table 3.11). The mechanism for the high $\Delta\sigma$ will be discussed in detail later.

Table 3.13 Annealing temperature, 5% flow stress at quasi-static and dynamic strain rates, and $\Delta\sigma$ of the ARB processed and subsequently annealed IF steel fabricated at various conditions. In addition, the data of the as-received IF steel without the ARB process are summarized as well.

Specimen	Annealing temperature (°C)	5% flow stress at 10^{-2} s^{-1} (MPa)	5% flow stress at 10^{3} s^{-1} (MPa)	Difference in flow stress, $\Delta\sigma$ (MPa)
A	As ARBed	756	912	157
B	600	504	629	151
C	625	353	515	193
D	700	246	458	214
IF steel	-	269	460	199

3. 4. 6 Discussion

Quasi-static tensile properties

The effect of grain size on the strength of the UFG-FC steels is discussed. It is well known that yield strength of polycrystalline metals depends on the grain size. The yield strength, σ_y is described as

$$\sigma_y = \sigma_0 + kd^{-1/2} \quad (3.3)$$

where σ_0 and k are constants, and d is grain size. This relationship was firstly proposed by Hall [41] and Petch [42], therefore it is well known as "Hall-Petch (H-P) relationship". Figure 3.31 shows the relationship between the yield stress at a quasi-static strain rate and inverse square root of the mean ferrite grain size for the UFG-FC1 and UFG-FC2 steels. Two kinds of yield stress were taken. One is the lower yield stress, σ_{Ly}, and the other is the 0.2% offset stress, $\sigma_{0.2}$, which has been shown in Table 3.9 and Table 3.10. The lower yield stress in the specimens having ferrite grain sizes smaller than 0.8 μm was not clear. In addition, data of lower yield stress from references by Armstrong et al. [43] for a 0.1% C steel, by Morrison [44] for a 0.13% C steel, and that for UFG bar-steels fabricated by warm deformation in caliber-rolling of 0.15% C steel having ferrite grain sizes from 0.47 to 13.6 μm [40] are plotted in Fig. 3.31.

The solid straight line in the figure corresponds to the H-P relationship obtained using the data by Morrison [44]. The lower yield stress (σ_{Ly}) in the UFG-FC steels, as well as the UFG bar-steels reported by Tsuchida et al. [40], were plotted on the line extended from coarse-grain region to ultrafine-grain region of the Morrison's data. However, the $\sigma_{0.2}$ for the present UFG-FC steels having smaller grain sizes than 1 μm were slightly larger than the expected values indicated by the straight line.

Kamikawa et al. have shown similar increase in $\sigma_{0.2}$ compared with the conventional H-P relationship in UFG-IF steel [45] and UFG aluminium [37]. They [37, 45] have shown that the 0.2% offset stress increased from the values expected by the conventional H-P relationship when the grains were refined down to around 1 μm both in pure aluminium and IF steel. In Fig. 3.31, $\sigma_{0.2}$ of the ARB processed and subsequently annealed IF steels (ARB-IF steels) is also plotted. Data obtained in this study, and data from references [36, 45] are included. The dotted line indicates the conventional H-P relationship in IF steels having coarse ferrite grain sizes fabricated by conventional cold-rolling and annealing [45]. It is seen that the $\sigma_{0.2}$ of the UFG-IF steels was higher than that expected from the conventional H-P relationship, when the grain size was smaller than 2 μm. The difference between the actual $\sigma_{0.2}$ and the expected one was larger in the UFG-IF steels compared with that in the UFG-FC steels. These results suggest that other strengthening mechanisms may exist in addition to the grain boundary strengthening described by the H-P relationship. One possible explanation is that the UFG microstructures having such fine grain sizes are strengthened by an additional mechanism caused by impotent dislocation sources due to closely spaced grain boundaries. The additional hardening was smaller in the

UFG-FC steels compared with the UFG-IF steels. The reason is unclear, however the fine cementite particles or solute alloying elements such as C existed in the UFG-FC steels might affect this behavior.

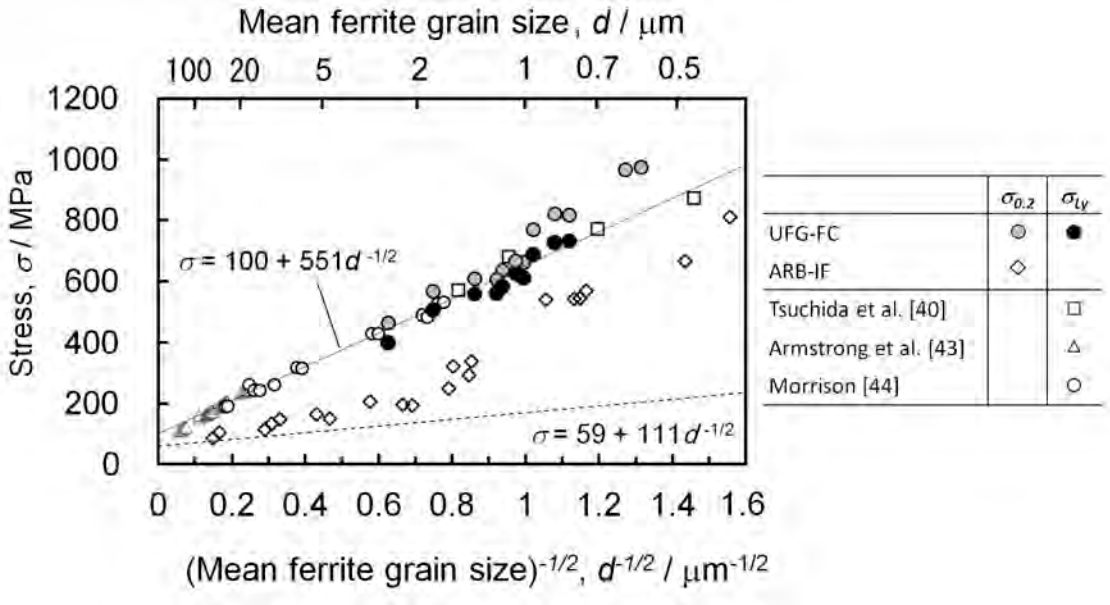

Figure 3.31 Relationship between quasi-static yield stress and inverse square root of mean ferrite grain size (H-P plot) of the low-C UFG-FC steels and the UFG-IF steels ARB processed and subsequently annealed. As the yield stress, either 0.2% offset stress, $\sigma_{0.2}$, or lower yield stress, σ_{Ly}, were taken. Reference data of σ_{Ly} are additionally plotted, and the line indicates the Hall-Petch equation from the data by Morrison [44].

Next, the yield drop phenomenon observed in the UFG-FC and UFG-IF steels are discussed. As shown in the s-s curves in Fig. 3.26 and Fig. 3.29, the yield drop phenomenon was more significant in smaller ferrite grain sizes and higher strain rates. Fig. 3.30 (a) clarified this behavior as well. Yield drop phenomena are commonly observed in quasi-static tensile deformation of C-steels, and it is well known that they are due to the presence of interstitial alloying elements, especially C [46]. In IF steels which do not contain solute C and N [17, 18], yield drop phenomenon is not observed usually in tensile deformation. However in the present UFG-IF steels, the yield drop phenomenon was observed when the grain sizes were smaller than 1 μm, or at high strain rates. Also in aluminium, the occurrence of yield drop when the matrix was refined to sub-micrometer sizes, which is never observed in conventional grain sizes, has been already reported [36, 37, 45]. Although the mechanism of yield drop phenomenon in the UFG metals has not been fully clarified yet, it has been well-known that any types of yield drop phenomena are due to the lack of mobile dislocations [46]. As mentioned above, one possible explanation is that the UFG microstructures having such fine grain sizes are strengthened by an additional mechanism caused by impotent dislocation sources due to closely spaced grain boundaries [37]. The present results seem to be attributed to mobile dislocations as well, though further studies are required to clarify the detailed mechanism.

Finally, the effect of ferrite grain size on elongation is discussed. Figure 3.32 shows relationship between uniform elongation and mean ferrite grain size of the UFG-FC and ARB-IF steels obtained in this study together with the data of ARB-IF steels from references [36, 45]. Uniform elongation in the UFG-FC steels drastically dropped to a few percent when the ferrite grains were refined down to around 1 μm. This behavior was similar to that in the ferrite single-phase microstructure in ARB-IF steel [36, 45] and 1100 aluminium [36, 37], and was due to insufficient work hardening rate in UFG single-phase microstructures [47, 48]. Based on the plastic instability condition in tensile deformation, highly strengthened material requires larger work hardening rate to keep uniform deformation. The Considére criterion [48], which describes plastic instability condition in tensile deformation, is explained as

$$\frac{d\sigma}{d\varepsilon} \leq \sigma \tag{3.4}$$

where σ and ε are true stress and true strain, respectively. The $d\sigma/d\varepsilon$ is work hardening rate. When work hardening rate coincides with the flow stress, plastic instability starts in the tensile deformation, which determines uniform elongation. The work hardening rate in the UFG-FC steels, especially in the specimens having grain sizes smaller than 1μm, seemed insufficient, which resulted in early necking (early plastic instability) in the tensile test. When considering application of the UFG steels to automobile body parts through stamping processes, poor uniform elongation is not favorable and it may prevent expanding the applications of the UFG steels. Therefore, in order to apply the UFG steels widely to automobiles, uniform elongation should be improved. For this purpose, a concept for improving uniform elongation in UFG ferric microstructures is established in this study, and will be shown in Chapter 4.

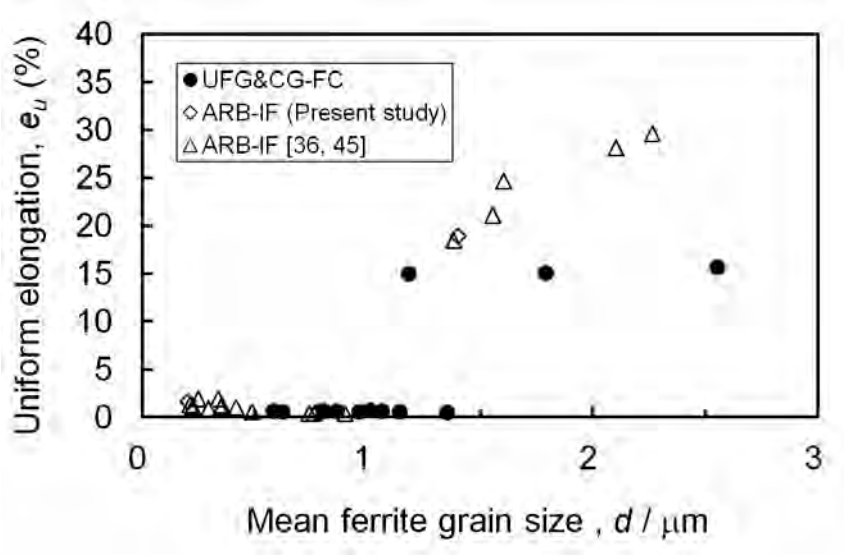

Figure 3.32 Relationship between uniform elongation at quasi-static tensile deformation and mean ferrite grain size in the low-C UFG-FC steels and ARB-IF steels fabricated in this study. Data of ARB-IF steels from Ref. [36, 45] are also plotted.

Dynamic tensile properties

Here, the results for dynamic deformation of the UFG ferrite microstructures are discussed. Generally in dynamic deformation, adiabatic heating should be considered. In this study, a temperature measurement during the dynamic tensile deformation using an infrared thermography system was carried out. The temperature increase until 5% strain was only several degrees, which also agreed with the results previously reported by other researchers [49, 50]. Therefore the effect of adiabatic heating can be neglected when the mechanical behaviour till 5% strain is discussed.

The difference in flow stress between dynamic and quasi-static strain rates, $\Delta\sigma$, in the UFG-FC and UFG-IF steels was investigated in this section. It was revealed that the both UFG microstructures showed higher $\Delta\sigma$ than that of conventional HSS. Figure 3.33 shows the relationship between $\Delta\sigma$ and quasi-static flow stress, both at 5% strain. Data of the fabricated UFG steels and conventional steels obtained from section 3.3 and references [13, 15, 29] are plotted. For the ARB-IF steels, data of the UFG microstructures having grain sizes smaller than 1 μm are shown in solid circles (indicated as ARB-IF (UFG)), while data of the specimens having grain sizes larger than 1 μm are shown in open circles (indicated as ARB-IF (FG)). Data of the UFG bar-steel fabricated by caliber-rolling reported by Tsuchida et al. [40] are plotted as well. The $\Delta\sigma$ in the UFG-FC and ARB-IF (UFG) steels were similar. The $\Delta\sigma$ values reported by Tsuchida et al. [40] were close to those of the present UFG-FC and IF steels.

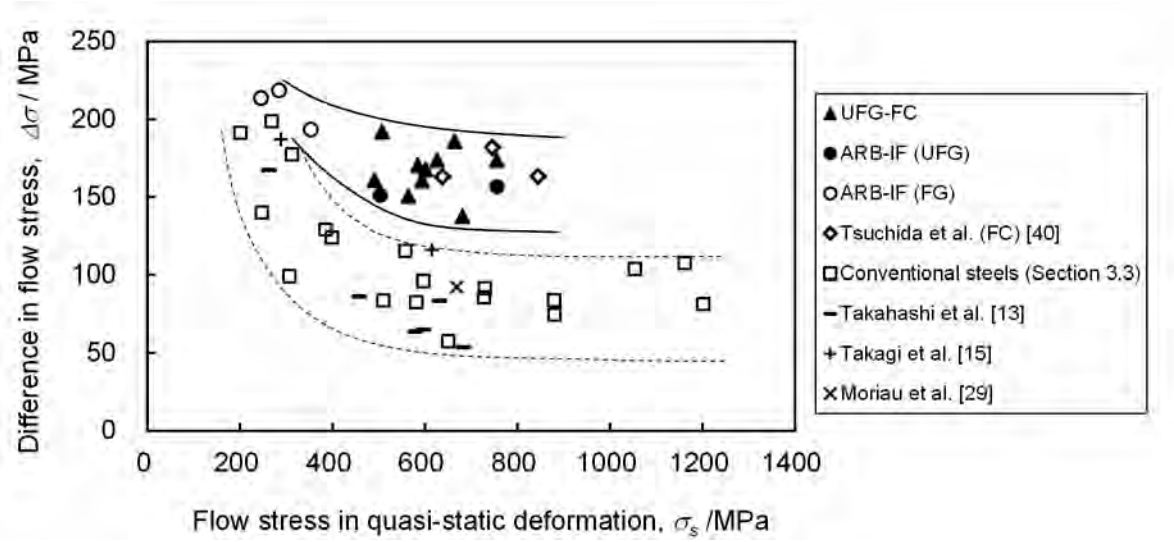

Figure 3.33 Relationship between $\Delta\sigma$ (difference in flow stress between dynamic flow stress and quasi-static strain rates) and quasi-static flow stress, σ_s. Data of the conventional steels obtained from section 3.3 (Fig. 3.20) and references [13, 15, 29] are additionally plotted. The data of the UFG-IF and the UFG-FC steels are shown in solid symbols. The data of the UFG-FC and ARB-IF steels were calculated at a nominal strain of 5%. Reference data were calculated at various nominal strains ranging from 3 to 10 %.

Two features are recognized in Fig. 3.33. The $\Delta\sigma$ in the FC and IF steels slightly decreased when the ferrite grain size was refined from micrometer to sub-micrometer dimensions. However, the $\Delta\sigma$ values in the UFG-FC and IF steels were still higher than those in the conventional HSS. Here, these two features are discussed.

First, the high $\Delta\sigma$ in the UFG steels compared with the conventional HSS is discussed. It is widely known that the flow stress increases when strain rate increases in iron and ferritic steels having bcc structure [31-35]. This is due to the high temperature (or strain rate) dependence of Peierls stress for screw dislocations in bcc metals. However, the deformation mechanism changes when ferrite grain size is decreased down to sub-micrometer or nanometer regions. According to previous reports [51, 52], polycrystalline materials can be classified into three groups having different deformation mechanisms as follows.

(I) Coarse grained polycrystalline materials (grain size d > 300 nm ~ 1 μm):
The deformation is controlled by lattice dislocation slip in large grain interiors. The dislocations are generated mostly by dislocation sources (i.e. Frank-Read sources) located at grain interiors. Grain boundaries serve as obstacles for movement of lattice dislocations. During plastic deformation, the lattice dislocations are stored in the form of dislocation cells/sub-grains at grain interiors.

(II) Ultrafine grained materials and nanocrystalline materials with relatively larger grain size (10~30 nm < d < several-hundred nanometers):
Lattice dislocation slip is still dominant, but the action is controlled by grain boundaries that act as sources and sinks of lattice dislocations. The level of flow stress is affected by grain boundaries. The lattice dislocations are not stored at grain interiors.

(III) Nanocrystalline materials with the finest grains (d < 10~30 nm):
The volume fraction occupied by grain boundaries is extremely large in these materials, therefore the lattice dislocation slip is suppressed and alternative deformation mechanisms by grain boundaries, such as grain-boundary sliding and other mechanisms are dominant. In this case, flow stress is much higher than those in the lattice dislocation slip mechanism in conventional coarse-grained and ultrafine grained materials.

It should be emphasized that grain size ranges used in this classification scheme are approximate and depend on the materials. For example, the grain size between the groups (I) and (II) has been indicated as a wide band ranging from 500 nm to 1 μm in the report by Cheng et al. [52]. Therefore, the UFG-FC and UFG-IF steels shown in Table 3.9, 3.10, and 3.12, having grain sizes between 200 nm and 1 μm, could show both features of the group (I) and (II).

The high $\Delta\sigma$ values in the present UFG ferrite steels suggested that the nature of bcc iron (high strain rate sensitivity) was still maintained when the ferrite grains were refined to “ultrafine” region. This result is reasonable if supposing that the motion of lattice dislocation in grain interiors having high strain rate dependence is still the dominant process in plastic deformation of these materials. In this assumption, the grain boundaries served as

obstacles for the dislocation motion and affected the level of flow stress, although the behavior of grain boundaries might change from that in coarse grained materials. Figure 3.34 (a, b) shows a schematic illustrations explaining the high $\Delta\sigma$ in the UFG ferritic steels. Figure 3.34 (a) and (b) correspond to low strain rate and high strain rate deformations, respectively. The solid curves indicate Peierls stress, which significantly increases when the strain rate increases. In Fig. 3.44 (a, b), the stress increase by grain refinement is explained as "bottom-up" of the stress level that is independent of strain rate. This figure was drawn under an assumption that the grain boundaries are a kind of "long-range obstacles", which is commonly considered in case of coarse grained materials [53]. As a result, ultrafine grained iron keeps high $\Delta\sigma$.

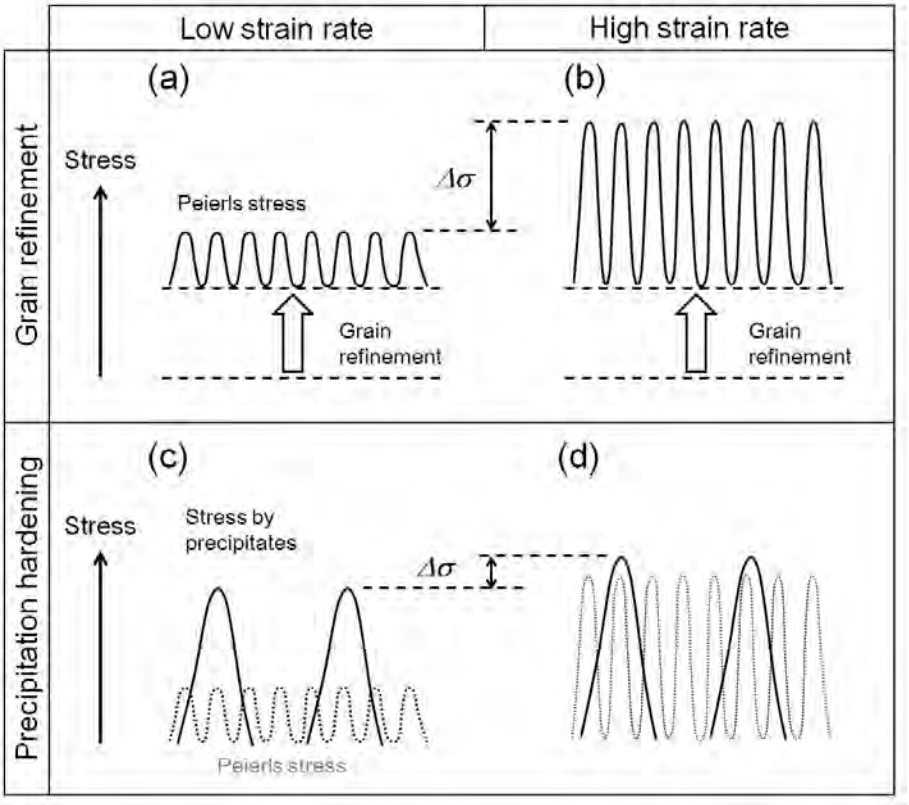

Figure 3.34 Schematic illustrations describing the flow stress of iron strengthened by different ways. (a, b) Iron strengthened by grain refinement, and (c, d) iron strengthened by introduction of fine precipitates. (a, c) At low strain rate, and (b, d) at high strain rate.

Similar trends in the $\Delta\sigma$ have been reported in dynamic compression of consolidated iron having grain sizes between 270 nm to 20 μm [39], and dynamic tensile deformation of UFG bar-steel having FC microstructure and grain sizes between 470 nm to 13.6 μm [40]. Those results coincide well with the present data. Jia et al. [39] have tested other specimens having finer grain sizes of 80 nm and 138 nm as well, and suggested a change in deformation mechanism at such small grain sizes, resulting in early fracture and slightly smaller $\Delta\sigma$ values compared with those in the materials having grain sizes larger than 270 nm. If the grain size is refined and become close to those in the group (III), the strain rate dependence of flow stress may change because the dominant deformation

mechanism changes. However, dynamic tensile behavior of the nanocrystalline metals has not been clarified yet, due to the difficulty of dynamic tensile tests for such materials. In addition, nanocrystalline materials generally show brittle behaviors [51]. Further study is required to clarify the strain rate dependence of flow stress in ferritic steels at a wide range of grain sizes including nanocrystalline region.

Next, as a conventional strengthening way, precipitation-hardening of coarse-grained ferrite is considered. Figure 3.34 (c, d) shows schematic illustrations of the stress in iron strengthened by precipitates. It is considered that the stress required to overcome the precipitates, which is much larger than Peierls stress, controls the flow stress at low strain rate. Under an assumption that the stress for overcoming the precipitates has a strain-rate dependence smaller than that for Peierls stress, $\Delta\sigma$, of the precipitation-hardened iron becomes smaller than that of the ultrafine grained iron. Consequently, it is concluded that grain refinement is a strengthening way which does not decrease the difference in flow stress between dynamic and quasi-static strain rates, $\Delta\sigma$, in ferritic steels.

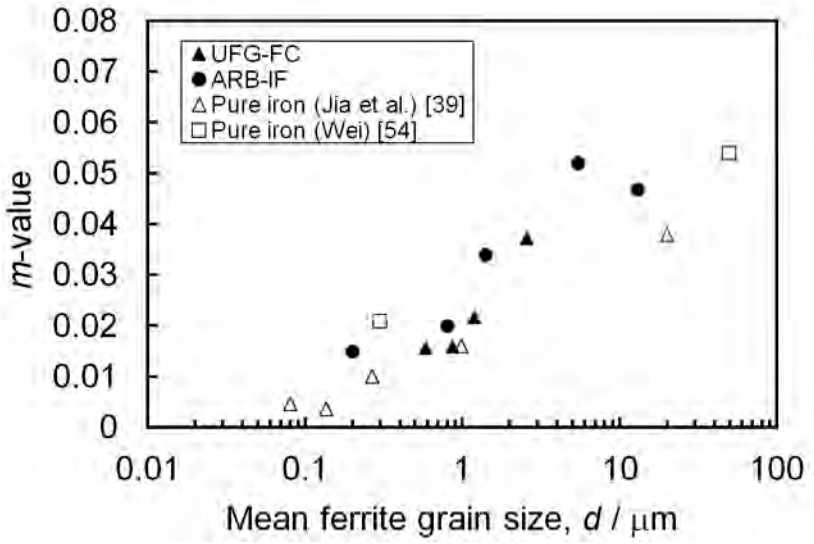

Figure 3.35 Strain rate sensitivity, *m*, at a strain rate range between 10^{-2} s^{-1} and 10^{3} s^{-1} evaluated by 5% flow stress as a function of mean ferrite grain size in the UFG-FC and ARB-IF steels. Reference data of consolidated and annealed iron evaluated by 4% flow stress [39], and of ECAE processed iron evaluated by 10% flow stress [54] are additionally plotted. The coarse-grained (d=50 μm) iron in reference [54] was fabricated by annealing without ECAE. The *m* in references [39, 54] were evaluated at a strain rate range between 10^{-4} s^{-1} and 10^{4} s^{-1}

By the way, as described in section 3.3, another evaluating parameter of the strain rate dependence of flow stress is also commonly used. For further understanding, the strain rate sensitivity, *m*, described in the equation (3.1) was also evaluated for the UFG-FC and ARB-IF steels. The *m*-values were calculated as the gradient of log-log plot of 5% flow stress and strain rate, at a strain rate range between 10^{-2} s^{-1} and 10^{3} s^{-1}. Figure 3.35 shows the *m*-values of the UFG-FC steels shown in Fig 3.27 and those of the IF steels listed in Table 3.13, as a function of mean ferrite grain size. The mean thickness of ferrite, d_t, represents the ferrite grain size in the ARB-IF steels. Reference data of pure iron fabricated

by consolidation and annealing [39] and by ECAE (equal channel angular extrusion) [54] are also plotted in Fig. 3.35. The *m*-values in the previous studies, at a strain rate range between 10^{-4} s^{-1} and 10^{4} s^{-1}, were evaluated by 4% flow stress in Ref. [39] and by 10% flow stress in Ref. [54], respectively. It was confirmed that the *m*-value decreased by grain refinement in the present UFG-FC and ARB-IF steels as well as in the pure iron previously reported [39, 54]. By grain refinement, the flow stress increases and the $\Delta\sigma$ becomes less dominant in the whole flow stress, because $\Delta\sigma$ is almost independent of ferrite grain size. Therefore, the decrease in the *m*-value by grain refinement is reasonably understood.

As has been mentioned, the UFG-FC and UFG-IF steels showed similar $\Delta\sigma$ values. The UFG-FC steels did not have 100% ferrite single-phase, but contained slight amount of cementite particles in the microstructures. However, the existence of the cementite particles did not decrease the $\Delta\sigma$ values. It is suggested that overcoming of the cementite particles by dislocations was not a rate-controlling process for the dislocation motion in the present UFG-FC steel because the amount of cementite was very small (a few volume %).

Next, the slight decrease in $\Delta\sigma$ when the ferrite grain size is refined to sub-micrometer one is discussed. A slight decrease in the $\Delta\sigma$ in the UFG-IF and ARB-FC (UFG) steels was observed when the ferrite grains were refined down to sub-micrometer sizes (Fig. 3.33). Here, this behavior is discussed using the data of the ARB-IF steels. The mechanism for the high $\Delta\sigma$ discussed before did not include the change in dislocation substructures by the change in strain rate. In fact, however, it was confirmed that dislocation substructures changed as the strain rate changed in the ARB-IF specimen C (d_t = 1.4 μm). Figure 3.36 (a, b, c) shows TEM microstructures of the specimen C before deformation, after deformation at 10^{-2} s^{-1} and after deformation at 10^{3} s^{-1}, respectively. By measuring the area of the test pieces before and after deformation, the area reduction near the observed regions were estimated to be 29% in quasi-static deformation (Fig. 3.36 (b)), and 16% in dynamic deformation (Fig. 3.36 (c)). Note that grain boundaries with sharp contrast are observed in the TEM images before and after deformation. As shown in Fig. 3.36 (a), few dislocations were observed before deformation. After the tensile deformation at quasi-static strain rate (Fig. 3.36 (b)), dislocation cells were seen. The dislocation density inside the cells was fairly low. On the other hand, as shown in Fig. 3.36 (c), the dislocation cells were not clear but randomly distributed dislocations were observed after dynamic deformation.

Figure 3.36 (d-f) shows microstructures of the specimen A (as-ARB processed, having mean ferrite grain size of 0.2 μm) before deformation, after deformation at 10^{-2} s^{-1} and after deformation at 10^{3} s^{-1}, respectively. The area reductions of the observed regions were estimated to be 7% in quasi-static deformation (Fig. 3.36 (e)), and 9% in dynamic deformation (Fig. 3.36 (f)). Before deformation (Fig. 3.36 (d)), slight amount of dislocations introduced by ARB process remained in the elongated ferrite grains. After the deformation at quasi-static strain rate (Fig. 3.36 (e)), the dislocation substructure was significantly different from that in the specimen C deformed at quasi-static strain rate. That is, dislocation cell structure was not observed in the UFG ferrite grains but randomly distributed dislocations were observed. When deformed at dynamic strain rate (Fig. 3.36 (f)), the dislocation substructure obtained was similar to that in the quasi-static deformation, that is, randomly dispersed dislocations.

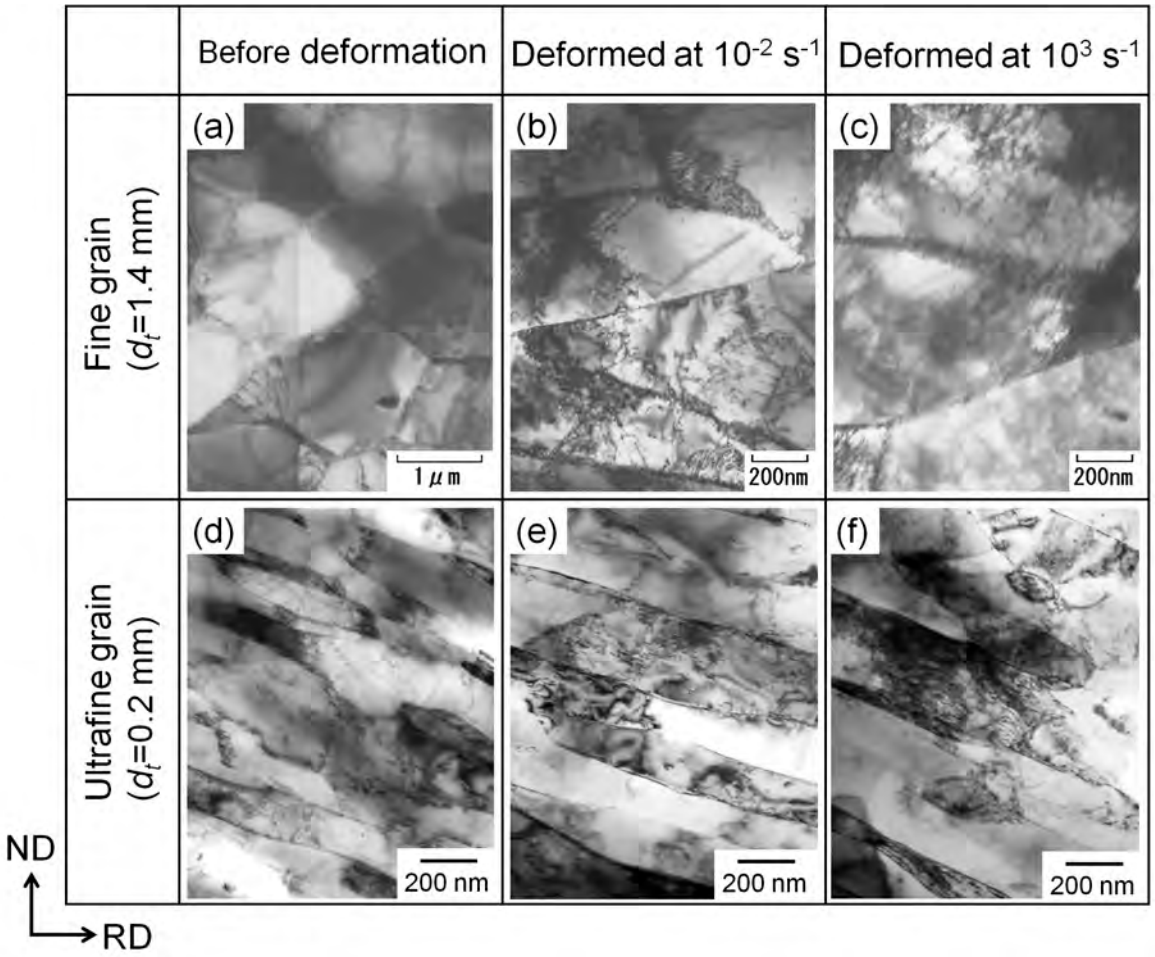

Figure 3.36 TEM microstructures of the UFG-IF specimens before and after tensile deformation. (a, b, c) Specimen C (ARB processed and annealed at 625 °C, d_t=1.4 μm) and (d, e, f) specimen A (as-ARB processed, d_t=0.2 μm). (a, d) Before the tensile deformation, (b, e) deformed at 10^{-2} s^{-1} and (c, f) deformed at 10^{3} s^{-1}. The area reductions of the tensile specimens near the observed regions were estimated to be (b) 29%, (c) 16%, (e) 7%, and (f) 9%. All microstructures were observed from TD.

There have been reported other examples showing similar dislocation substructures in steels [12, 55] and aluminium [35, 56]. Miura et al. [12] have reported that dislocation cells were observed after quasi-static deformation, whereas they were not observed after dynamic deformation in a mild steel containing 0.003 mass% C and having grain size of 10 to 20 μm. Kojima [55] has reported similar dislocation substructure in a mild steel containing 0.002 mass% C and having coarse grained ferrite microstructure. We have reported dislocation substructures in the deformed 1100 aluminium fabricated by ARB and subsequent annealing [56]. Figure 3.37 shows TEM microstructures of the deformed 1100 aluminium having coarse and ultrafine grain sizes [54]. The area reductions of the specimens near the observed regions shown in Fig. 3.37 (a, b, c, d) were estimated to be 23%, 34%, 15% and 13%, respectively. In the coarse-grained specimen having grain size of 9.9 μm, dislocation cell structures were observed after deformation at quasi-static strain rate (Fig. 3.37 (a)), while randomly dispersed dislocations were observed at dynamic strain rate

(Fig. 3.37 (b)). On the other hand, the UFG specimen having grain size of 0.2 μm (Fig. 3.37 (c, d)) showed random distribution of dislocations at both quasi-static and dynamic strain rates.

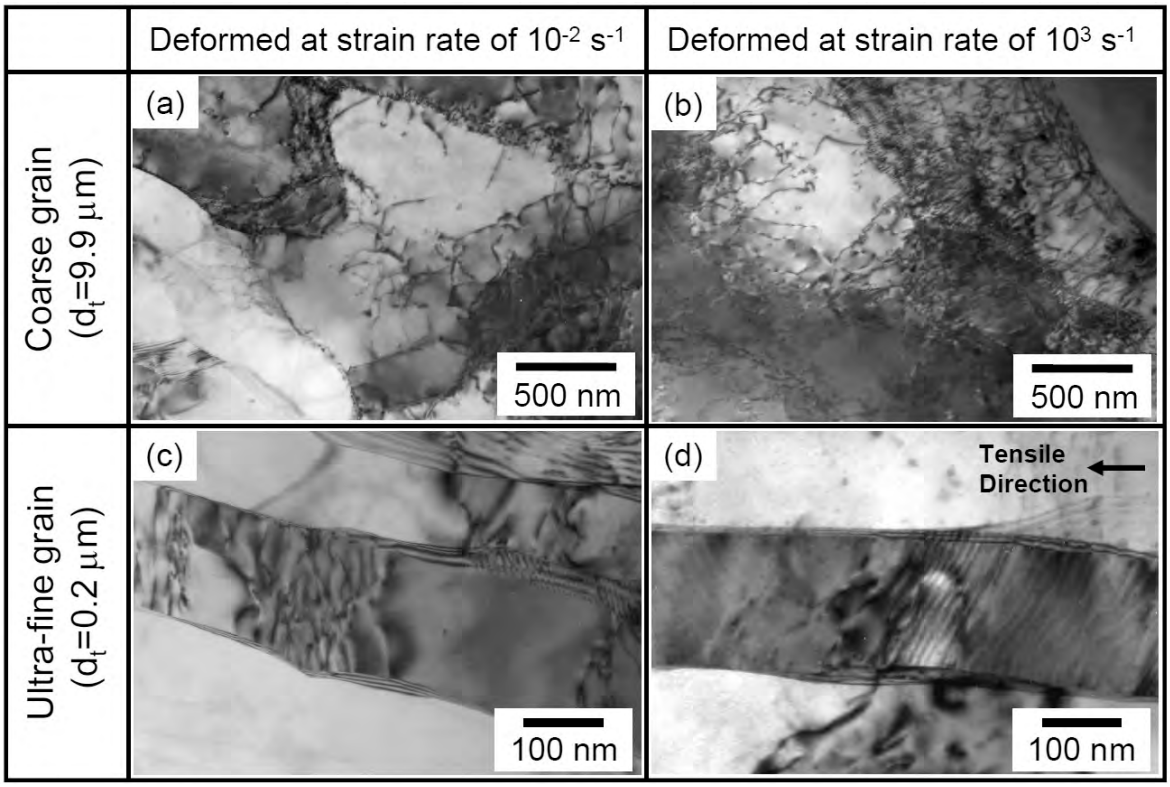

Figure 3.37 TEM microstructures showing dislocation substructures in the deformed 1100 aluminium specimens having coarse and ultrafine grain sizes [56]. (a, b) Coarse-grained microstructure, and (c, d) ultrafine grained microstructure. The strain rates are (a, c) 10^{-2} s^{-1} and (b, d) 10^{3} s^{-1}. Observed from TD. The area reductions of the tensile specimens near the observed regions were estimated to be (a) 23%, (b) 34%, (c) 15%, and (d) 13%. All microstructures were observed from TD.

For low-C UFG steels, a few studies have been reported on the microstructures deformed at quasi-static strain rate [57, 58]. Wang et al. [58] have been investigated deformed microstructure of a UFG-FC steel containing 0.13 mass% C and having mean ferrite grain size of about 0.6 μm [58], fabricated by the process developed in this study and shown in Chapter 2. Figure 3.38 shows a TEM microstructure of the tensile specimen after quasi-static deformation at a strain rate of 10^{-3} s^{-1} [58]. The applied strain was supposed to be around 20% since the observation was carried out at the uniformly deformed section. In the relatively coarse ferrite grains having grain sizes of 1.2 to 1.6 μm at the center of the TEM image, planar-type dislocation configuration was observed instead of dislocation cells. This behavior is similar to that observed in the UFG-IF specimen (Fig. 3.36 (e)).

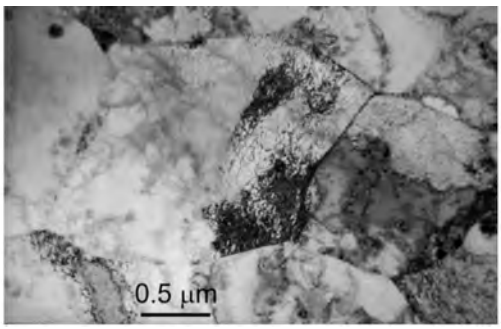

Figure 3.38 TEM microstructure showing dislocation substructures in a 0.13 mass%-C ferrite-cementite steel having mean ferrite grain size of 0.6 μm deformed at quasi-static strain rate [58]. Relatively coarse ferrite grains existed in the microstructure are shown in this image.

In plastic deformation of metals having high stacking fault energy, the dislocation cell structures form through dynamic recovery that rearranges the accumulated dislocations [56]. The quasi-static deformation allows time for dislocations to be rearranged into more stable configurations. However, as seen in Fig. 3.36 and Fig. 3.37, annihilation and rearrangement of dislocations seem to be difficult when the strain rate is very high. When the grains are refined down to sub-micrometer sizes, dislocation cell structures are also difficult to form during deformation even at quasi-static strain rate because of the limited space. According to the detailed measurement of dislocation cell sizes in the deformed coarse-grained low-C steel [17], the cell size was around 1 μm at 10% strain. It means that the dislocation cell size and the ferrite grain size are comparable in the UFG ferrite microstructures. Therefore, it would be difficult to form dislocation cells inside the ferrite grain, and the dislocations tend to distribute randomly within the UFG ferrite grains.

Considering the present results of dislocation substructures as well as the results in the previous studies, the reason of the slight decrease in $\Delta\sigma$ of the UFG microstructures is described below. The change in the dislocation substructure from dislocation cells to random distribution in coarse-grained (d_t > 1 μm) microstructures probably gives an additional hardening. Therefore, in the coarse-grained microstructures, the effect of the change in dislocation configurations was included in the observed $\Delta\sigma$ values. On the other hand, in the UFG-IF specimens the $\Delta\sigma$ values simply reflected strain rate dependence of Peierls stress, because dislocation substructures did not change even when the strain rate changed.

Finally, the dynamic tensile behaviors of various ferritic steels clarified in this chapter are summarized. Figure 3.39 (a-c) shows quasi-static and dynamic s-s curves experimentally obtained for the fine-grained ferrite single-phase microstructure represented by the ARB-IF specimen C, UFG ferrite single-phase microstructure (the ARB-IF specimen B), and the conventional PP590 steel (section 3.3), respectively. In the fine-grained ferrite (Fig. 3.39 (a)), the $\Delta\sigma$ was the highest among three microstructures, because it reflected both high strain rate dependence of Peierls stress and the change in dislocation configurations. In the UFG ferrite (Fig. 3.39 (b)), the $\Delta\sigma$ was slightly smaller than that in the fine-grained ferrite because dislocation configuration did not change. However the $\Delta\sigma$ was

still larger than that in the PP590 steel (Fig. 3.39 (c)) . The PP590 steel had the smallest $\Delta\sigma$ due to small strain rate dependence of the stress required to overcome the precipitates, as discussed in this section.

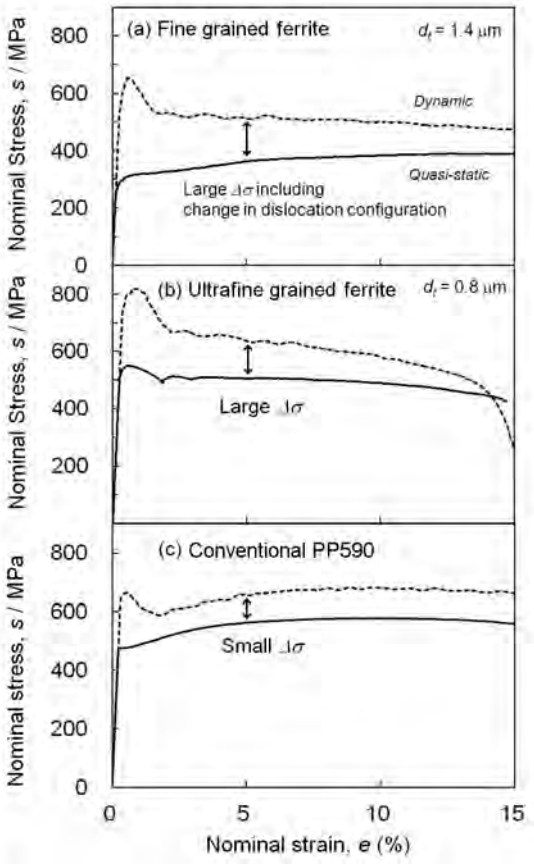

Figure 3.39 Stress-strain curves of various ferrite microstructures. describing the difference in flow stress, $\Delta\sigma$. (a) Fine-grained ferrite, (b) ultrafine grained ferrite and (c) conventional precipitation-hardened ferrite. The solid lines indicate s-s curves at quasi-static deformation (at a strain rate of 10^{-2} s^{-1}) and the broken lines indicate s-s curves at dynamic deformation (at a strain rate of $5x10^{2}$ s^{-1}).

3.4.7 Summary

In this section, quasi-static and dynamic tensile properties of the UFG-FC steels fabricated by cold-rolling and annealing of duplex starting microstructures, and the UFG-IF steels fabricated by ARB and subsequent annealing were shown and discussed. The obtained results are summarized below.

(1) Lower yield stress of the UFG-FC steels having various ferrite grain sizes roughly held the same Hall-Petch relationship as that of the coarse-grained low-C steels previously reported. However, 0.2% offset stress in the UFG-FC steels having grain sizes smaller than 1 μm was slightly higher than that expected from the Hall-Petch relationship in the coarse-grained low-C steels. This behavior was similar to that in the UFG aluminium

and IF steels previously reported, and seemed to be caused by impotent dislocation sources due to closely spaced grain boundaries.

(2) The difference in flow stress between dynamic and quasi-static strain rates, $\Delta\sigma$, of the UFG-FC steels was slightly smaller than that of mild steels, however it was still higher than that of the conventional HSS. When martensite was introduced to the UFG-FC microstructures, the $\Delta\sigma$ significantly decreased to the similar value to that in the conventional HSS. This is due to the change in strengthening way of the steels from grain refinement of matrix to introduction of hard second phase. It was indicated that ultrafine grain refinement is a good way to strengthen steels without decrease in $\Delta\sigma$.

(3) The slight decrease in $\Delta\sigma$ in the UFG-FC and UFG-IF steels when the ferrite grain size was refined from micrometer size to sub-micrometer one was described by the change in dislocation substructures, based on the results of TEM observation of the deformed microstructures. It was suggested that the change in dislocation substructures also contributed to $\Delta\sigma$.

3.5 Conclusions

In this chapter, quasi-static and dynamic tensile properties of the fabricated UFG-FC and UFG-IF steels as well as the conventional sheet steels were shown and discussed. The conventional strengthening ways by solid solution, precipitation, and introduction of hard phases significantly decreased the difference in flow stress, $\Delta\sigma$, in the steels. On the other hand, the UFG-FC and UFG-IF steels showed higher $\Delta\sigma$ compared with the conventional HSS. It was indicated that grain refinement of ferrite is a good way to strengthen ferritic steels without decrease in $\Delta\sigma$. Therefore, it is expected that the UFG-FC steels show good performance if applied to automobile body structures and are deformed at high strain rates, i.e. in case of car collisions. The dynamic collapse properties of the UFG-FC steels will be shown and discussed in Chapter 5.

On the other hand, the UFG-FC steels showed poor uniform elongation. This is due to the lack of work hardening in the sub-micrometer ferrite single-phase microstructure. If considering their application to automobile body parts by stamping, adequate uniform elongation is required. Therefore, improvement of uniform elongation in the UFG steels is a very important issue. The attempt to improve uniform elongation by improving work hardening rate in the UFG ferrite microstructures are introduced in Chapter 4.

3.6 References

[1] A. Otubushin, Int. J. Impact Eng. 21 (1998) 349.

[2] S. Simunovic, P. Kumar, V. Nukala, J. Fekete, D. Meuleman, M. Milititsky, SAE Technical Paper, 2003-01-1383, SAE International, Warrendale, 2003.

[3] B. Yan, Y. Kuriyama, A. Uenishi, D. Cornette, M. Borsutzki, C. Wong, SAE Technical Paper 2006-01-0120, SAE International, Warrendale, 2006.
[4] Int. Iron Steel Inst, Recommendations for dynamic tensile testing of sheet steels, 2005, available at: www.worldautosteel.org [Accessed 14 October 2011].
[5] B. Hopkinson, Phil. Trans. A 213 (1914) 437.
[6] R. M. Davis, Phil. Trans. A 240 (1948) 375.
[7] H. Kolsky, Proc. Royal Soc. B 62 (1949) 676.
[8] K. Kawata, S. Hashimoto, N. Takeda, S. Sekino, in: J. R. Vinson, M. Taya (Eds.), Recent advances in composites in the United States and Japan, ASTM STP864, Am. Soc. For Testing and Materials, Philadelphia, 1985, pp. 701-711.
[9] K. Kawata, J. Soc. Mater. Sci, Japan 36 (1987) 12.
[10] S. Tanimura, T. Umeda, W. Zhu, K. Mimura, Impact Eng. Appl. (2001) 77.
[11] S. Tanimura, K. Mimura, T. Umeda, J. Phys. IV 110 (2003) 385.
[12] K. Miura, S. Takagi, T. Hira, O. Furukimi, S. Tanimura, SAE Technical Paper 980952, SAE International, Warrendale, 1998.
[13] M. Takahashi, A. Uenishi, H. Yoshida, Y. Kuriyama, SAE Technical Paper 2003-01-2765, SAE International, Warrendale, 2003.
[14] D. M. Bruce, D. K. Matlock. J. G. Speer, A. K. De, SAE Technical Paper 2004-01-0507, SAE International, Warrendale, 2004.
[15] S. Takagi, Y. Tokita, K. Sato, T. Shimizu, K. Hashiguchi, K. Ogawa, K. Mimura, S. Tanimura, SAE Technical Paper 2005-01-0494, SAE International, Warrendale, 2005.
[16] R. Rana, S. B. Singh, W. Bleck, O. N. Mohanty, Mater. Trans. A 40 (2009) 856.
[17] G. Krauss, STEELS Processing, Structure, and Performance, ASM International, Materials Park, 2005, pp. 226.
[18] H. Takechi, ISIJ Int. 34 (1994) 1.
[19] Z. Zhang, Z. Guan, J. Lian, Mater. Sci. Eng. A 190 (1995) 55.
[20] P. H. Chang, A. G. Preban, Acta Metall. 33 (1985) 897.
[21] E. Hornbogen, R. C. Glenn, Trans. Metall. AIME 218 (1960) 1064.
[22] N. Maruyama, M. Sugiyama, T. Hara, H. Tanehiro, Mater. Trans. JIM 40 (1999) 268.
[23] S. R. Goodman, S. S. Brenner, J. R. Low, Jr, Metall. Trans. 4 (1973) 2363.
[24] S. R. Goodman, S. S. Brenner, J. R. Low, Jr, Metall. Trans. 4 (1973) 2371.
[25] K. Osamura, H. Okuda, M. Takashima, K. Asano, M. Furusaka, Mater. Trans. JIM 34 (1993) 305.
[26] K. Osamura, H. Okuda, K. Asano, M. Furusaka, K. Kishida, F. Kurosawa, ISIJ Int. 34 (1994) 359.
[27] M. Imafuku, T. Mizutani, Y. Takagi, Y. Okitsu, Proc. of Int. Conf. on Microstructures and Functions of Materials, Tokyo, 1996, pp. 25.
[28] H. Yaguchi, M. Nomura, T. Watabe, Tetsu-to-Hagené 94 (2008) 14 (in Japanese).
[29] O. Moriau, L. Tosal-Martinez, P. Verieysen, J. Degrieck, Int. Conf. on TRIP-Aided High Strength Ferrous Alloys, Aachen, 2002, pp. 247.
[30] X. M. Chen, M. F. Shi, G. Chen, M. Kamura, K. Watanabe, Y. Omiya, SAE Technical Paper 2005-01-0354, SAE International, Warrendale, 2005.
[31] J. Harding, Acta Metall. 17 (1969) 949.

[32] J. D. Campbell, W. G. Ferguson, Phil. Mag. 21 (1970) 63.
[33] J. Harding, J. Mater. Tech. 4 (1977) 6.
[34] J. Harding, The effect of high strain rate on material properties. in: T. Z. Blazynski (Ed.), Materials at high strain rates, ELSEVIER, London, 1987, pp. 133.
[35] M. A. Meyers, Dynamic behavior of materials, John Wiley & Sons, Inc., New York, 1994, pp. 340.
[36] N. Tsuji, Y. Ito, Y. Saito, Y. Minamino, Scripra Mater. 47 (2002) 893.
[37] N. Kamikawa, X, Huang, N. Tsuji, N. Hansen, Acta Mater. 57 (2009) 4198.
[38] S. Takaki, K. Kawasaki, Y. Kimura, in: R. S. Mishra, S. L. Semiatin, C. Suryanarayana, N. N. Thadhani, T. C. Lowe (Eds.), Ultrafine Grained Materials, TMS, Warrendale, 2000, pp. 247.
[39] D. Jia, K.T. Ramesh, E. Ma, Acta Mater. 51 (2003) 3495.
[40] N. Tsuchida, H. Masuda, Y. Harada, K. Fukaura, Y. Tomota, K. Nagai, Mater. Sci. Eng. A 488 (2007) 446.
[41] E. O. Hall, Proc. Phys. Soc. B64 (1951) 747.
[42] N. J. Petch, J. Iron Steel Inst. 174 (1953) 25.
[43] R. Armstrong, I. Godd, R. M. Douthwaite, N. J. Petch, Phyl. Mag. 7 (1962) 45.
[44] W. B. Morrison, Trans. ASM 50 (1966) 824.
[45] Naoya Kamikawa, PhD Thesis, Osaka University, 2005.
[46] E. O. Hall, Yield Point Phenomena in Metals and Alloys, Plenum Press, New York, 1970, pp. 65.
[47] Y. M. Wang, E. Ma, Acta Mater. 52 (2004) 1699.
[48] N. Tsuji, Fabrication of bulk nanostructured materials by accumulative roll bonding (ARB), in: M. J. Zehetbauer, Y. T. Zhu (Eds.) Bulk nanostructured materials, WILEY-VCH, Weinheim, 2009, pp. 246.
[49] R. Kapoor, S. Nemat-Nasser, Mech. Mater. 27 (1981) 1.
[50] T. M. Link, B. M. Hance, SAE Technical Paper 2003-01-0516, SAE International, Warrendale, 2003.
[51] C. C. Kock, I. A. Ovid'ko, S. Seal, S. Veprek, Structural Nanocrystalline Materials, Chambridge Universtiy Press, Cambridge, 2007, pp. 292.
[52] S. Cheng, J. A. Spencer, W. W. Milligan, Acta Mater. 51 (2003) 4505.
[53] M. Kato, Introduction to the theory of dislocations, Shokabo, Tokyo, 1999, pp.102.
[54] Q. Wei, J. Mater. Sci. 42 (2007) 1709.
[55] N. Kojima, The final report of research group on high-speed deformation of steel for automotive use, ISIJ, Tokyo, 2001, pp. 171.
[56] N. Takata, Y. Oktisu, N. Tsuji, J. Mater. Sci. 43 (2008) 7385.
[57] D. H. Shin, B. D. Ahn, H. S. Cho, K. T. Park, in: Y. T. Zhu, T. G. Langdon, R. Z. Valiev, S. L. Semiatin, D. H. Shin, T. C. Lowe (Eds.), Ultrafine Grained Materials III, TMS, Warrendale, 2004, pp. 421.
[58] T. S. Wang, Z. Li, B. Zhang, X. J. Zhang, J. M. Deng, F. C. Zhang, Mater. Sci. Eng. A 527 (2010) 2798.

CHAPTER 4

IMPROVEMENT OF DUCTILITY IN ULTRAFINE GRAINED FERRITE MICROSTRUCTURES BY INTRODUCING HARD PHASES

4.1 Introduction

In Chapter 3, it was shown that ultra grain refinement of ferrite increased strength significantly keeping large high $\Delta\sigma$ (difference in flow stress between dynamic and quasi-static strain rates) in low-C steels. On the other hand, the ultra grain refinement decreased uniform elongation of the steel. This is due to insufficient work hardening rate in the ultrafine grained (UFG) single-phase microstructures [1, 2]. As discussed in section 3.4.6, based on the plastic instability condition in tensile deformation, highly strengthened material requires larger work hardening rate to maintain uniform elongation. The work hardening rate of the present UFG-FC steels shown in Chapter 3 seemed insufficient, which resulted in early necking (early plastic instability) in tensile deformation. Considering the stamping process of automobile body parts, adequate uniform elongation is required in steels. Therefore, in order to apply UFG steels widely to automobile body parts, uniform elongation should be improved.

To satisfy this demand, the most effective way is an introduction of hard second phases to the UFG microstructure [3]. Generally in conventional steels, duplex microstructures composed of soft and hard phases, i.e. dual-phase (DP) or multi-phase (MP) microstructures, show improved uniform elongation by enhanced work hardening rate. Also in case of fine grained steels, it has been shown in previous studies, i.e. in a calculation using “secant method” [4], that significant improvement of uniform elongation is expected by an introduction of hard second phases.

In this chapter, first, a concept for improving uniform elongation in the UFG ferrite microstructures by introducing hard second phases is proposed. UFG-MP steels composed of UFG ferrite and hard phases are fabricated, and their microstructures and mechanical properties are investigated. Secondly, various UFG-MP steels containing retained austenite are fabricated, and TRIP (transformation induced plasticity) effect on mechanical properties is investigated. The TRIP effect means the improvement of elongation by transformation of retained austenite to martensite during deformation. The appearance of hard martensite during deformation improves work hardening rate of the steel, resulting in large uniform elongation. The TRIP effect has been applied to low-C sheet steels, and those steels are so-called “TRIP-steels” or “TRIP-aided steels”. Next, the effect of grain refinement in MP

microstructures on tensile properties is shown. The MP microstructures having the same chemical composition and different ferrite grain sizes are fabricated, and the microstructures and mechanical properties are shown and discussed. The combination of strength and ductility is compared between the UFG and FG (fine-grained) MP microstructures.

4.2 Fabrication of ultrafine grained multi-phase steels having high strength and high ductility

4.2.1 Introduction

In order to improve work hardening rate and uniform elongation of UFG ferrite microstructures, an introduction of hard phases has been studied [5-9]. Table 4.1 summarizes carbon content in the steels, fabricating conditions, and obtained microstructures in the previous studies [5-9] aiming for the improvement of work hardening rate of the UFG ferrite. First, the increase of cementite particles in UFG-FC microstructures was considered [5-7]. It has been shown that work hardening rate of the UFG-FC microstructures certainly increased by increasing cementite particles [5-7]. However, the change in work hardening rate was slight. This is because the amount of cementite was limited in low-C steels.

Recently a few studies on introduction of martensite into the UFG/FG ferrite microstructures have been reported [8, 9]. It has been shown that UFG-DP microstructure composed of ferrite and martensite showed improved tensile strength (TS) without decrease in uniform elongation, compared with coarse grained DP steels. However, in the previous studies [8, 9] the grain sizes of the ferrite matrix were relatively larger (0.8 to 1.8 μm). This is because grain growth of ferrite during intercritical annealing at two-phase region of ferrite and austenite, which is required for obtaining DP or MP microstructures, could not be avoided. Due to the high intercritical annealing temperatures, grain growth of ferrite was accelerated in the previous studies [8, 9].

Also in the UFG-FC steels shown in section 2.3 and section 3.4, it has been shown that ferrite grain growth could not be avoided when annealing temperature increased up to intercritical region for introducing martensite into the microstructure. Therefore, TS of the obtained DP microstructures was limited to about 750 MPa (see Table 3.9). Consequently, the introduction of large amount of hard second phases (martensite, bainite and retained austenite) into the UFG ferrite matrix keeping ultrafine grain sizes (smaller than 0.8 μm) has not been achieved yet.

Due to the increasing demands for improving crash worthiness of automobile body structures, UHSS (ultra high strength steels) having higher tensile strengths than 1000 MPa have been developed and have started to be applied [10, 11]. One of the potential competitors for the UFG steels is modern UHSS. Therefore, the target in mechanical properties of the UFG steels as new generation of AHSS (advanced high strength steels) are

the TS over 1000 MPa with adequate uniform elongation. In this section, attempts to introduce hard second phases to the UFG ferrite microstructures with maintaining ultrafine ferrite matrix are made. In order to avoid grain growth, transformation temperature of the steel was decreased by addition of alloying elements, Mn in this study. The annealing temperature required for obtaining MP microstructure can be decreased, which is expected to contribute to keeping of ultrafine ferrite matrix. In this section, low-C steels containing various amounts of Mn are prepared, and their microstructures and mechanical properties are shown and discussed.

Table 4.1 Carbon content, fabricating conditions, and obtained microstructures in the previous studies aiming for the improvement of work hardening rate of FC/UFG ferrite microstructures.

Carbon content (mass%)	Starting micro-structure	Deformation method and temperature	Final heat- treatment condition	Obtained micro-structure	Obtained ferrite grain size (μm)	Ref. No.
0.13	M	CR	500 °C, 1.8 ks	FC	0.18	[5]
0.1~0.3	TM	WR, 500 °C	500~550 °C, 3.6 ks	FC	0.6	[6]
0.17~0.31	F-P	PC, 550 °C	550 °C, 7.2 ks	FC	1.1~1.4	[7]
0.15	F-P	ECAE	730 °C, 600 sec	DP	0.8~1.2	[8]
0.17	F-P	PC, 550 °C	730 °C, 60 sec	DP	1.6~1.8	[9]

F: Ferrite, P: Pearlite, TM: Tempered Martensite, FC: ferrite-cementite, DP: dual-phase

WR: Warm-rolling, PC: Plane strain compression, ECAE: equal channel angular extrusion

4.2.2 Experimental procedure

Table 4.2 summarizes the chemical compositions of the steels prepared in this section, 2Mn, 3Mn and 5Mn steels. The 2Mn steel is the same as the UFG-FC2 steel shown in section 2.2. Based on the 2Mn steel, Mn content was increased in other steels. The fabricating process is shown in Fig. 4.1. The ingots were hot-rolled to a thickness of 6 mm at a finishing temperature (FT: the temperature after the final pass in the hot-rolling) of 900 °C in austenite region, and immediately cooled to room temperature by water. The hot-rolled sheets were heat-treated at 1000°C for 90 minutes and water-quenched to room temperature in order to obtain uniform full-martensite microstructures. Next, the sheets were again reheated to intercritical region of ferrite and austenite for 60 minutes, and water-quenched to room temperature. The heat-treatment temperatures, T_A for the hot-rolled sheets of 2Mn, 3Mn and 5Mn steels were set to be 770, 740 and 715 °C, respectively. Table 4.3 summarizes the transformation temperatures of the steels measured by dilatometer. The measurements were carried out at heating and cooling rate of 2 °C s^{-1}. The A_{c1} transformation temperatures, which are important for deciding intercritical annealing temperature, of the 3Mn and 5Mn steels were 680 and 648 °C respectively, while that of the 2Mn steel was about 700 °C. Therefore, all the T_A for three steels were within the intercritical region of ferrite and

austenite. Table 4.4 summarizes the heat-treatment temperatures, T_A, and microstructural parameters of the hot-rolled and subsequently heat-treated sheets before cold-rolling (CR). The heat-treated sheets were mechanically grinded to a thickness of 5 mm and cold-rolled by a reduction of 80 % in thickness with lubrication. The final thickness was 1 mm. The cold-rolled sheets were annealed at various temperatures ranging from 600 to 750 °C for 120 sec in a salt bath and water-quenched to room temperature.

Microstructural observations were carried out for the specimens at each stage of the process. All the specimens were observed from the transverse direction (TD) of the sheets. The samples for optical microscopy (OM) or scanning electron microscopy (SEM) were etched with a 3% nital. The SEM observations were conducted on Hitachi S-4300E/N SEM operated at 15 kV. An electron backscatter diffraction (EBSD) analysis was also carried out by using Hitachi S-4300E/N SEM equipped with TSL OIM system operated at 15 kV. The EBSD scanning was carried out at the thickness center on the longitudinal section perpendicular to TD (TD section). The mapping was carried out on a hexagonal grid at a step size of 0.03 or 0.05 μm, depending on the ferrite grain sizes. Mean grain sizes of ferrite and second phases were measured on the SEM micrographs by using mean intersection method. Several lines were drawn on the SEM micrographs along RD and ND, and intersection lengths of each phase were measured. The average of the intersection lengths along RD and ND were used as the mean grain size.

The volume fraction of austenite was evaluated by X-ray diffractometry using Co-K_α radiation. The specimens were chemically polished to the 75% thickness of the initial specimens on the rolling planes before the X-ray measurements. The austenite volume fraction was calculated using the integrated intensities of (110)α, (200)α, (211)α, (111)γ, (200)γ and (220)γ diffraction peaks.

Vickers hardness was measured on the TD sections of the specimens at each stage of the process. At a load of 1 kgf, hardness was measured at least three times for each specimen, and the data were averaged. The small tensile specimens shown in Fig. 3.6, of which tensile direction was parallel to RD were taken from the fabricated sheets. Quasi-static and dynamic tensile tests were carried out by using the load-sensing block type test equipment described in section 3.2. At various strain rates (10^{-2}, 10, 10^2, $5x10^2$ and 10^3 s^{-1}), two or three specimens were tested. From the displacement-load curves, the elastic region was removed and nominal stress-strain curves were generated. Total elongation of the specimens was measured from the difference in the gauge length before and after the testing.

Table 4.2 Chemical compositions (mass%) of the steels aiming for ultrafine grained multi-phase microstructures.

Steel	C	Si	Mn	P	S	Al	Nb	B	N
2Mn	0.100	0.01	2.00	0.002	0.0013	0.035	0.022	0.0015	0.0007
3Mn	0.103	0.02	3.13	0.002	0.0018	0.036	0.021	0.0015	0.0007
5Mn	0.098	0.02	4.93	0.002	0.0023	0.031	0.019	0.0014	0.0009

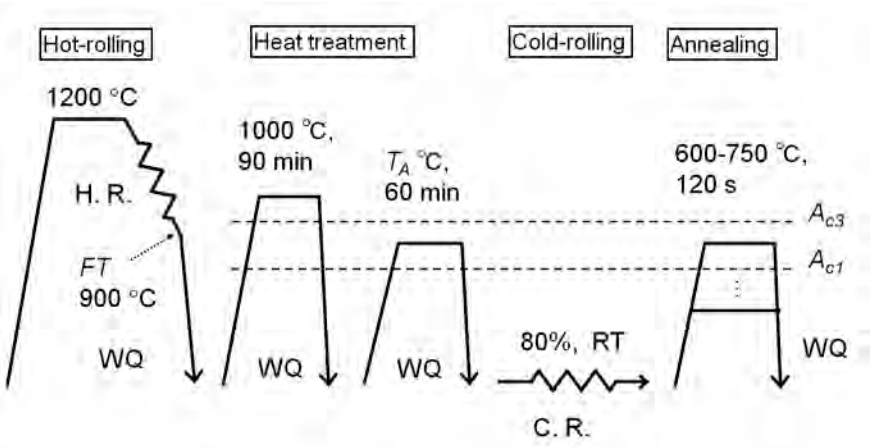

Figure 4.1 Schematic drawing of the process for fabricating UFG multi-phase microstructures by cold-rolling and annealing of a duplex microstructure. A_{c1} and A_{c3} mean the transformation temperatures measured by dilatometer.

Table 4.3 Transformation temperatures of the prepared steels measured by dilatometer. The data were measured at heating and cooling rate of 2 °C s^{-1}.

Steel	A_{c1}	A_{c3}	A_{r1}	A_{r3}
2Mn	699	832	423	618
3Mn	680	803	250	418
5Mn	648	755	173	338

Table 4.4 Fabricating conditions and microstructural parameters of the hot-rolled and subsequently heat-treated sheets (before cold-rolling) of the 2Mn, 3Mn and 5Mn steels.

Steel	Heat-treatment temperature, T_A (°C)	Mean intersection length of ferrite along ND (μm)	Volume fraction of martensite (%)
2Mn	770	1.79	50
3Mn	740	0.62	65
5Mn	715	0.66	65

4.2.3 Microstructures of ultrafine grained multi-phase steels

Figure 4.2 shows again the A_{c1} and A_{c3} transformation temperatures during heating at 2 °C s^{-1} in the 0.1% C steels listed in Table 4.2 as a function of Mn content. It is indicated that temperature of two-phase region of ferrite and austenite significantly decreased by Mn addition up to 5 mass%. In other words, intercritical annealing temperatures in order to obtain multi-phase microstructures were decreased significantly by Mn addition.

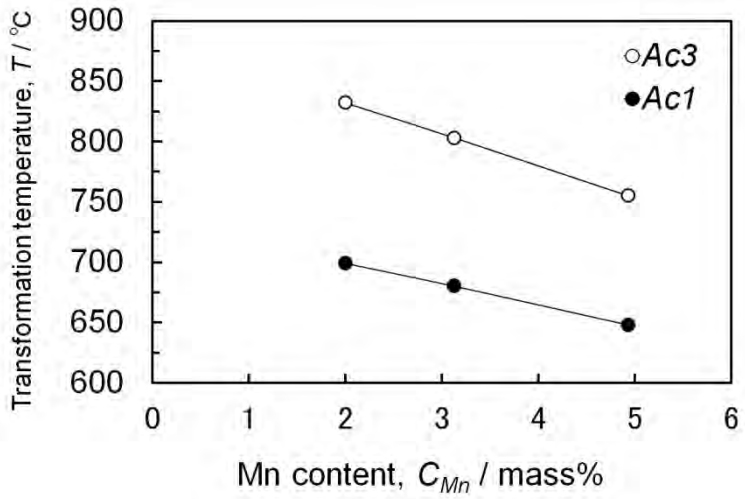

Figure 4.2 Effect of Mn content on the transformation temperatures in the 0.1 mass% C-steels. The chemical compositions of the steels are summarized in Table 4.2.

Figure 4.3 shows optical micrographs of the hot-rolled and heat-treated sheets (before CR) of the 2Mn, 3Mn and 5Mn steels. Fine duplex microstructures composed of ferrite (dark gray regions) and martensite (light gray regions) were observed in all the steels. The mean intersection lengths along ND in the ferrite region, and martensite volume fraction, measured using the optical micrographs shown in Fig. 4.3, are summarized in Table 4.4. The mean intersection length of ferrite and the martensite volume fraction in the 2Mn steel were almost the same as those in the UFG-FC2 steel in section 2.2, having substantially the same chemical composition and heat-treatment condition. By Mn addition, the mean intersection length of ferrite decreased significantly. The martensite volume fractions of three steels were in a range between 50 and 65 %.

Figure 4.4 shows SEM microstructures of three steels after CR to a reduction of 80%. It was shown that the ferrite grains (dark gray regions) were elongated and had wavy shapes, which meant that large and complex plastic strain was introduced into the ferrite. The martensite regions (light gray regions) were also deformed to some extent, and elongated roughly to RD. The features are the same as those in the cold-rolled microstructures of the UFG-FC1 and UFG-FC2 steels shown in Chapter 2.

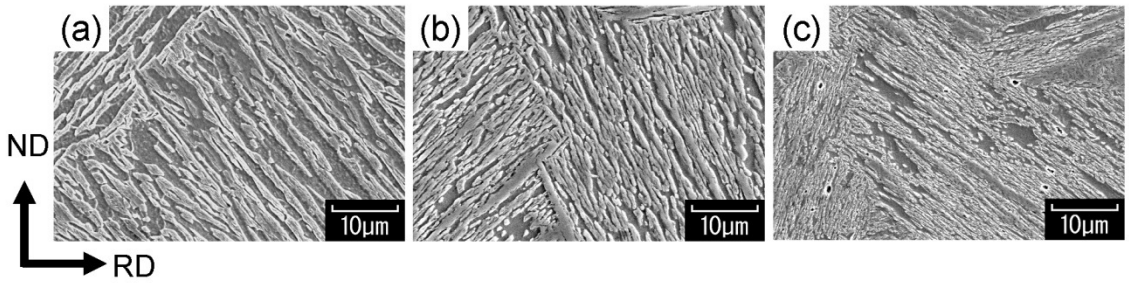

Figure 4.3 SEM microstructures of the hot-rolled and subsequently heat-treated sheets as starting microstructures. (a) 2Mn steel, (b) 3Mn steel and (c) 5Mn steel. Observed from TD.

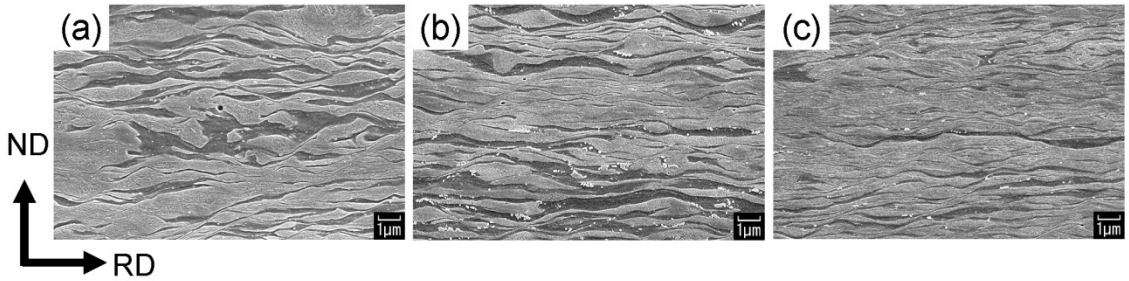

Figure 4.4 SEM microstructures of the specimens cold-rolled by 80% reduction in (a) 2Mn steel, (b) 3Mn steel and (c) 5Mn steel. Starting microstructures are shown in Fig. 4.3. Observed from TD.

Figure 4.5 shows SEM microstructures after final annealing of the cold-rolled sheets of the 2Mn steel. The microstructure composed of ultrafine ferrite and cementite was obtained at annealing temperature of 600 °C. When the annealing temperature increased up to 680 °C, significant grain growth was observed. The measured mean ferrite grain sizes are described later. When annealed at 700 °C, small amount of martensite islands were observed at ferrite grain boundaries or triple junctions. This is because the annealing temperature reached to the A_{c1} transformation temperature (approximately 700 °C), austenite phase formed during annealing and transformed to martensite during water-cooling. This behavior is the same as that in the UFG-FC1 steel shown in Chapter 2.

Figure 4.6 shows SEM microstructures after final annealing of the cold-rolled sheets of the 3Mn steel. An UFG-FC microstructure was obtained at 600 °C. In contrast to the 2Mn steel, the second phases (light gray regions in the SEM images) appeared at annealing temperature of 680 °C. This is because the A_{c1} transformation temperature was about 680 °C in the 3Mn steel. The ferrite grain sizes in the 3Mn specimens seemed smaller than those in the 2Mn steels.

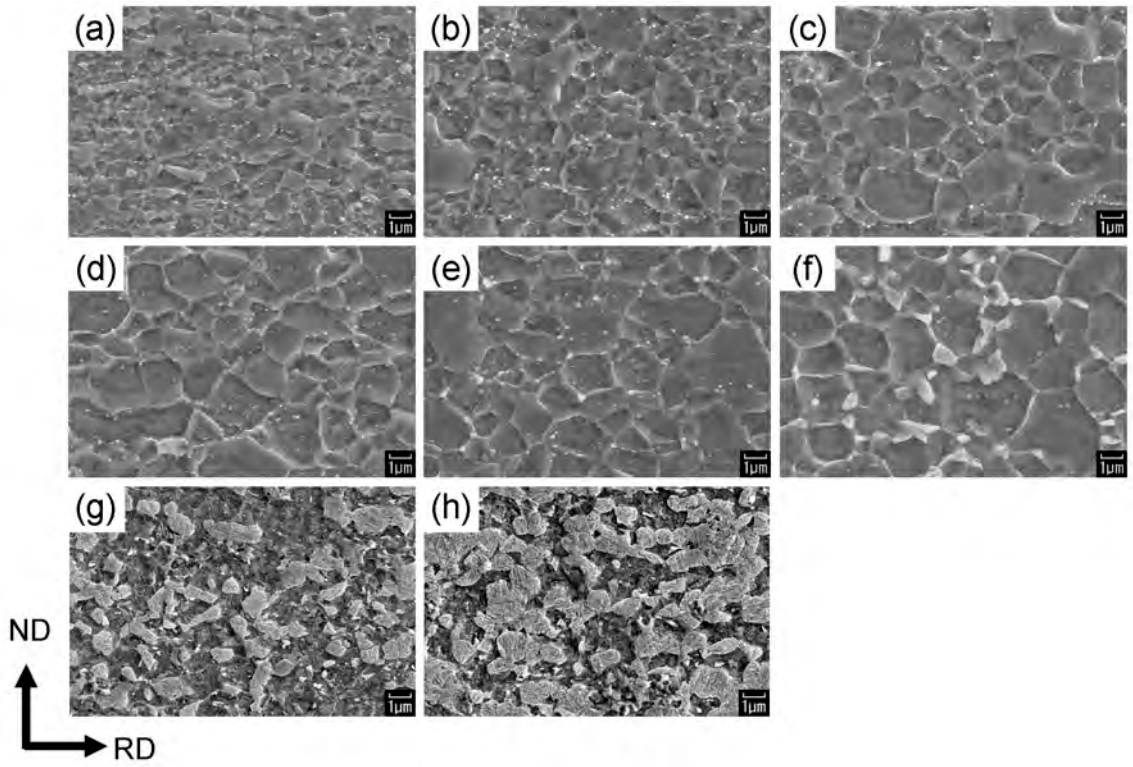

Figure 4.5 SEM microstructures of the 2Mn steel cold-rolled by 80% reduction and annealed at (a) 600 °C, (b) 620 °C, (c) 640 °C, (d) 660 °C, (e) 680 °C, (f) 700 °C, (g) 725 °C and (h) 750 °C for 120 s and then water-quenched to room temperature. Observed from TD.

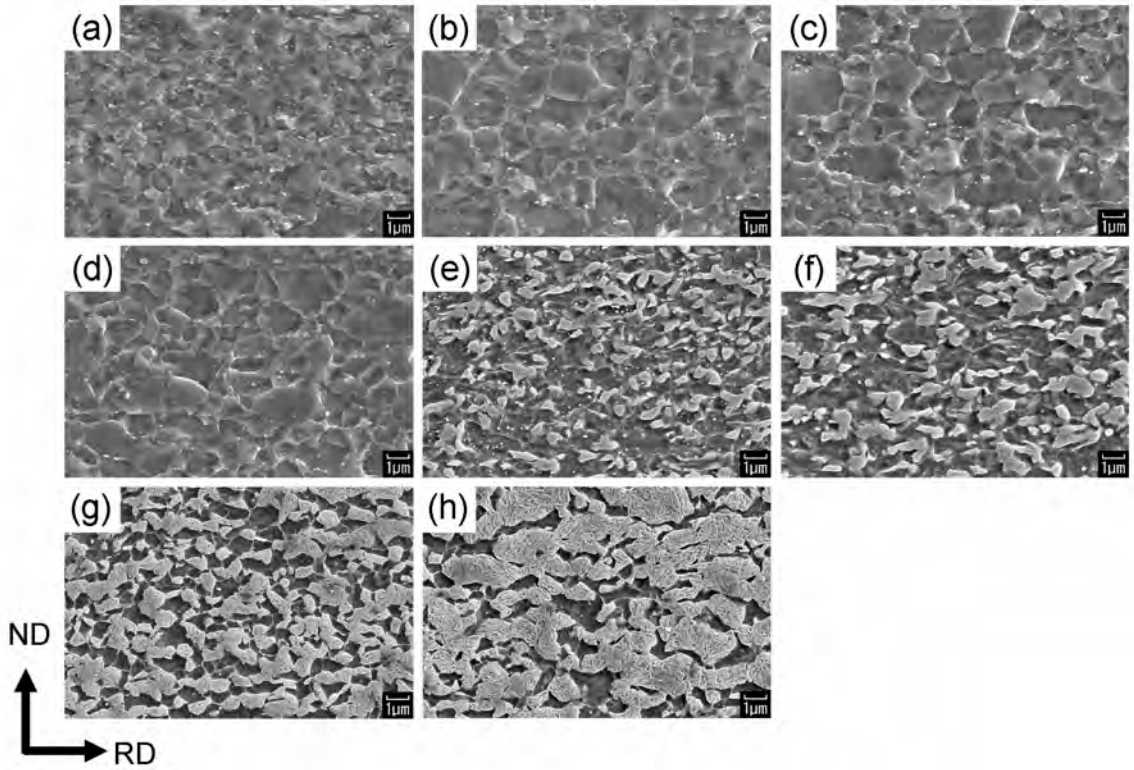

Figure 4.6 SEM microstructures of the 3Mn steel cold-rolled by 80% reduction and annealed at (a) 600 °C, (b) 620 °C, (c) 640 °C, (d) 660 °C, (e) 680 °C (f) 700 °C, (g) 725 °C and (h) 750 °C for 120 s and then water-quenched to room temperature. Observed from TD.

Figure 4.7 shows SEM microstructures after final annealing of the cold-rolled sheets of the 5Mn steel. The microstructures annealed at 600 to 700 °C are shown. In contrast to the 2Mn and 3Mn steels, ferrite grains were refined further, and kept sub-micrometer sizes at all the annealing temperatures. The second phases (relatively lighter regions showing substructures within the grains) were observed in the specimens annealed at 660 to 700 °C (Fig. 4.7 (d-f)). As will be shown in the EBSD results, the specimens annealed at 600 to 640 °C actually contained slight amount of retained austenite. However, the second phase was not observed clearly in the SEM microstructures of the specimens annealed at 600 to 640 °C.

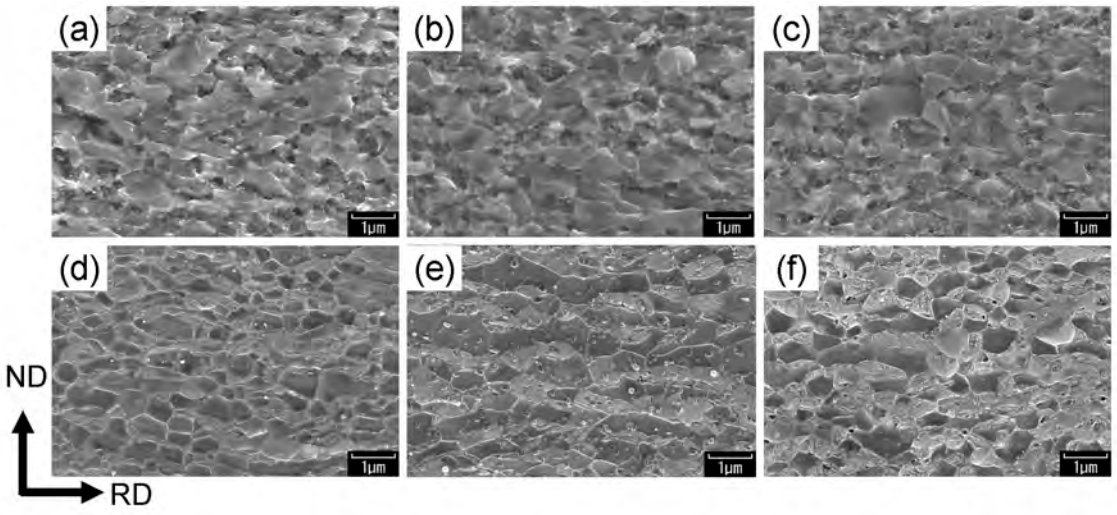

Figure 4.7 SEM microstructures of the 5Mn steel cold-rolled by 80% reduction and annealed at (a) 600 °C, (b) 620 °C, (c) 640 °C, (d) 660 °C, (e) 680 °C and (f) 700 °C for 120 s and then water-quenched to room temperature. Observed from TD.

As shown in the SEM microstructures in Fig. 4.5 to 4.7, grain growth of ferrite seemed to be suppressed by Mn addition. Figure 4.8 shows the relationship between mean ferrite grain size and annealing temperature in the 2Mn, 3Mn and 5Mn steels. In the 2Mn steel, the mean ferrite grain size at 600 °C was 0.69 μm. It significantly increased as annealing temperature increased, and reached above 1 μm at 660 °C. In the 3Mn steel, the mean ferrite grain size at 600 °C was 0.54 μm, which was smaller than that in the 2Mn steel. The ferrite grain size increased up to 625 °C, but did not increase so much at annealing temperatures higher than 625 °C in the 3Mn steel. In the 5Mn steel, the mean ferrite grain size at 600 °C was 0.34 μm, which was much smaller than those in other steels. The grain size did not increase so much when the annealing temperature increased in the 5Mn steel. It was only 0.48 μm at the annealing temperature of 700 °C. Ferrite grain growth was significantly suppressed at all annealing temperatures in the 5Mn steel.

Two factors preventing grain growth of ferrite matrix is discussed here. One is the increased amount of solute Mn. The specimens annealed at 600 °C, showing FC microstructures without hard second phases, were certainly refined by Mn addition. The microstructures before CR were also refined by Mn addition (Fig. 4.3). According to the results shown in section 2.2, the microstructural refinement before CR seemed to accelerate

the UFG ferrite formation. Another important factor is the appearance of austenite in intercritical annealing. Especially at higher annealing temperatures at 660 to 700 °C, this factor seemed to be more effective. During intercritical annealing, austenite seemed to form mainly at ferrite grain boundaries or triple junctions. If considerable amount of newly formed austenite existed at ferrite grain boundaries, it seems difficult for the ferrite grains to grow beyond those new austenite grains. As described below, retained austenite was observed by EBSD analysis in the 5Mn specimens annealed at 600 to 640 °C. Therefore it is reasonable to assume that the new austenite grains formed at ferrite grain boundaries suppressed grain growth of ferrite at 600 to 700 °C in the 5Mn steel.

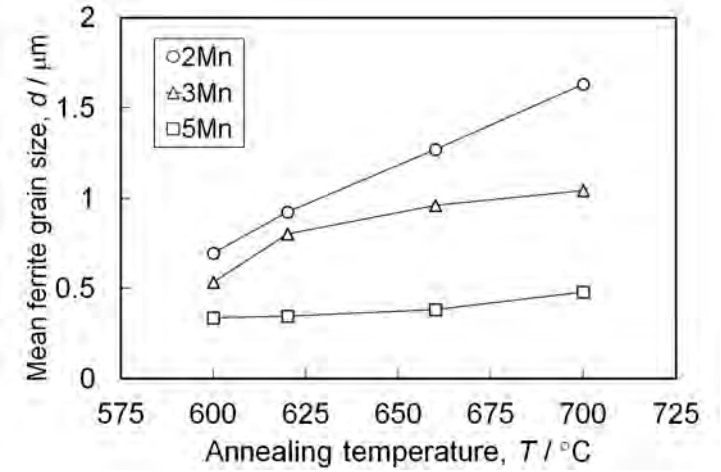

Figure 4.8 Relationship between mean ferrite grain size and annealing temperature in the 2Mn, 3Mn and 5Mn steels.

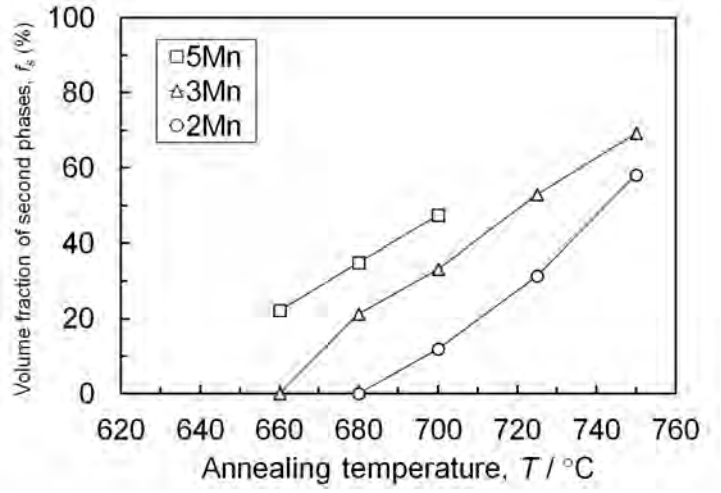

Figure 4.9 Volume fraction of second phases after annealing as a function of annealing temperature in the 2Mn, 3Mn and 5Mn steels.

The volume fraction of the second phases in the annealed microstructures in the 2Mn, 3Mn and 5Mn steels are shown in Fig. 4.9 as a function of annealing temperature. Here, the “second phases” include martensite, bainite and austenite indicated as light gray islands in SEM images, and those phases are hard to be distinguished in SEM microstructures due to their very small sizes. It is shown in Fig. 4.9 that the second phases

appeared at lower temperatures as the Mn content increased up to 5 mass%.

In order to clarify the microstructures of the 5Mn steel, EBSD analysis was carried out. Figure 4.10 shows image quality (IQ) maps of the 5Mn specimens annealed at 600 to 700 °C. The austenite regions are displayed in red. Equiaxed ferrite grains having grain sizes much smaller than 1 μm were clearly observed. In addition, it is noteworthy that slight amount of austenite was observed in the specimens annealed at 600 to 640 °C, which were not distinguished clearly in the SEM microstructures in Fig. 4.7. These annealing temperatures were much lower than the A_{c1} transformation temperature listed in Table 4.3. However, this A_{c1} transformation temperature was measured during continuous heating, so that it is possible that austenite appeared during holding at 600 °C. An analysis for the transformation temperature has shown that the equilibrium A_1 transformation temperature in low-C 5%-Mn steels was lower than 600 °C [12], and the present result agrees with it.

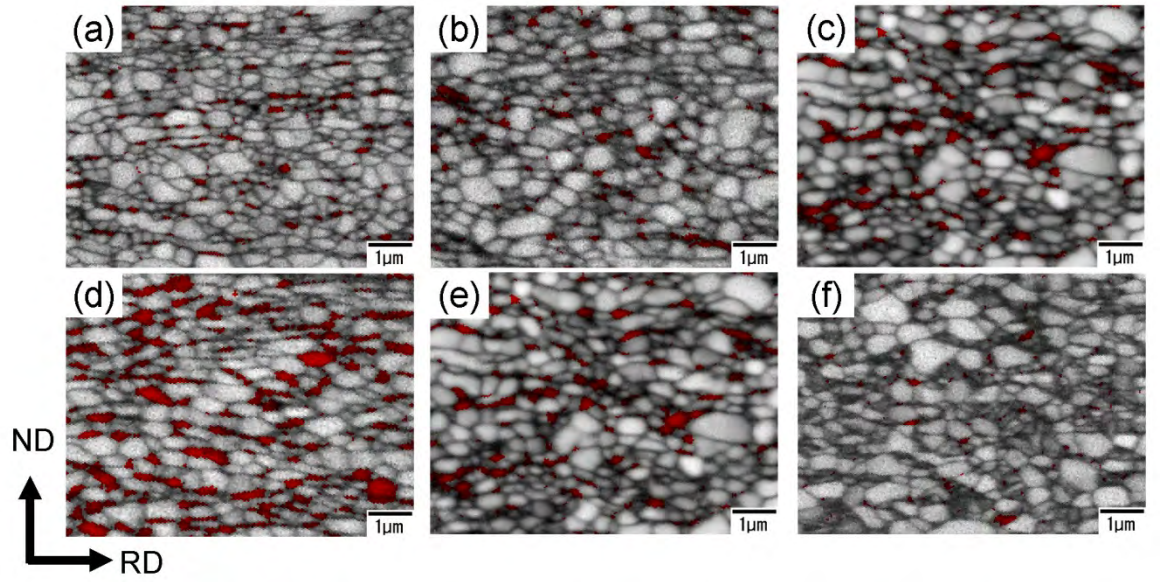

Figure 4.10 Image quality (IQ) maps obtained by EBSD analysis of the 5Mn steel cold-rolled by 80% reduction and annealed at (a) 600 °C, (b) 620 °C, (c) 640 °C, (d) 660 °C, (e) 680 °C and (f) 700 °C for 120s and then water-quenched to room temperature. The regions colored in red are austenite. Observed from TD.

Table 4.5 summarizes austenite fraction of the 3Mn and 5Mn steels annealed at various temperatures measured by two different methods, X-ray diffractometry and EBSD analysis. The EBSD analysis was carried out only for the 5Mn steels. It was shown that the optimum annealing temperature for obtaining the maximum retained austenite fraction existed. According to the X-ray diffractometry measurement, austenite fraction was the maximum at 700 °C in the 3Mn steel, and 680 °C in the 5Mn steel. According to the EBSD data in the 5Mn steel, annealing temperature of 660 °C gave the maximum austenite fraction. The EBSD analysis was carried out at vary small area compared with X-ray diffractometry, therefore the data of austenite fraction analyzed by the EBSD contained some errors. However, the IQ maps in Fig. 4.10 revealed an important feature. That is, retained austenite exited mostly in a blocky-shape. In the conventional TRIP-steels, many of retained austenite exist at lath boundaries in bainite as a film-like shape [13]. This feature in the conventional

TRIP-steels is different from the result in the present 5Mn UFG-MP steel. Another example of blocky-shaped retained austenite has been shown in a FG TRIP-steel having mean ferrite grain size of 2 μm [14]. The change in the shape of austenite from film-like to blocky may be a characteristic feature in FG/UFG-MP microstructures.

Table 4.5 Volume fraction of retained austenite measured by X-ray diffractometry and EBSD analysis of the steel B and C annealed at various temperatures.

Steel	Annealing temperature (°C)	Austenite fraction (X-ray) (%)	Austenite fraction (EBSD) (%)
3Mn	680	4.6	-
3Mn	700	14.6	-
3Mn	725	10.9	-
5Mn	600	7.2	4.5
5Mn	620	10.7	4.8
5Mn	640	15.5	14.7
5Mn	660	21.5	20.9
5Mn	680	26.5	14
5Mn	700	4.7	1.7

-: not measured.

When the annealing temperature increased above the "optimum temperatures", austenite fraction decreased in the 5Mn steel. The austenite fraction during annealing at higher temperatures should be also higher, however all the austenite regions did not remain at room temperature and seemed to transform to other phases, i.e. martensite. At higher temperature in intercritical region, austenite fraction is large, but C content in austenite is small. The small C content decreases thermal stability of austenite, and austenite with small amount of C tends to transform to martensite during cooling. Due to this reason, austenite fraction decreased at higher annealing temperatures in the 3Mn and 5Mn steels. On the other hand, the increase of martensite was observed in the IQ map (dark gray bcc region in Fig. 4.10 (f)). In conventional TRIP-steels, the same behavior has been reported. That is, decrease in retained austenite fraction by increasing intercritical annealing temperature [15].

Figure 4.11 shows ND orientation color maps corresponding to the IQ maps shown in Fig. 4.10, indicating crystal orientations of bcc phase. The ferrite grains showed various orientations, which indicated that the ultrafine ferrite grains involved large amount of high angle grain boundaries (HAGBs). In the orientation color maps, blue and red grains seems to be dominant, indicating that the microstructures contained large amount of grains having <111> or <100> directions parallel to ND. ODF (orientation distribution function) analysis was carried out to investigate the texture more quantitatively. Figure 4.12 shows ODFs (in Bunge notation) at various φ_2 values between 0 and 90 degrees, which were constructed by the EBSD data of the 5Mn steel annealed at 600 °C. The ODFs showed similar features to those in the UFG-FC steels shown in Fig. 2.16 and Fig. 2.40. That is, strong α-fiber and γ-fiber components. They were clearly observed in the φ_2=45° section in the ODFs and are

the typical texture components in cold-rolling texture of low-C steels [16]. This result means that the UFG ferrite in the 5Mn steel were formed by the same mechanism as that in the 2Mn UFG steels discussed in Chapter 2, that is, continuous coarsening of very fine regions in the cold-rolled microstructures.

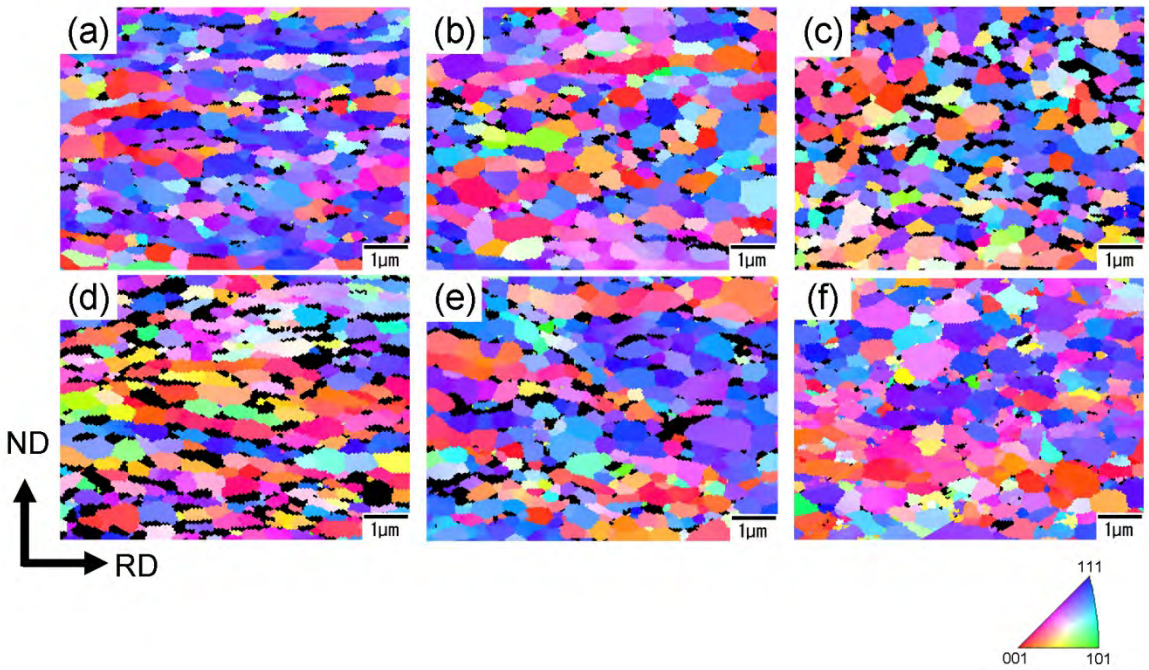

Figure 4.11 ND orientation color maps indicating crystal orientations of ferrite, corresponding to the IQ maps shown in Fig. 4.10. Obtained by EBSD analysis of the 5Mn steel cold-rolled by 80% reduction and annealed at (a) 600 °C, (b) 620 °C, (c) 640 °C, (d) 660 °C, (e) 680 °C and (f) 700 °C for 120s and then water-quenched to room temperature. Observed from TD. The colors indicate the crystal orientation of ferrite grains parallel to ND. Austenite regions are not displayed (colored in black).

Finally, Vickers hardness of three steels at each stage in the fabricating process is shown in Fig. 4.13. In all steels, the hardness continuously decreased from 500 °C to around 650 °C. These are the same behaviors as that observed in other UFG steels containing 2% Mn which have been shown in Chapter 2, and different from the behaviors in conventional recrystallization of steels [17]. The continuous decrease in hardness supports the mechanism of UFG ferrite formation described before. As annealing temperature increased from 650 to 750 °C, hardness increased in all steels. This is due to the appearance of hard second phases in the microstructures, as annealing temperatures reached intercritical regions. The hardness started to increase at lower temperatures when the Mn content in the steel increased.

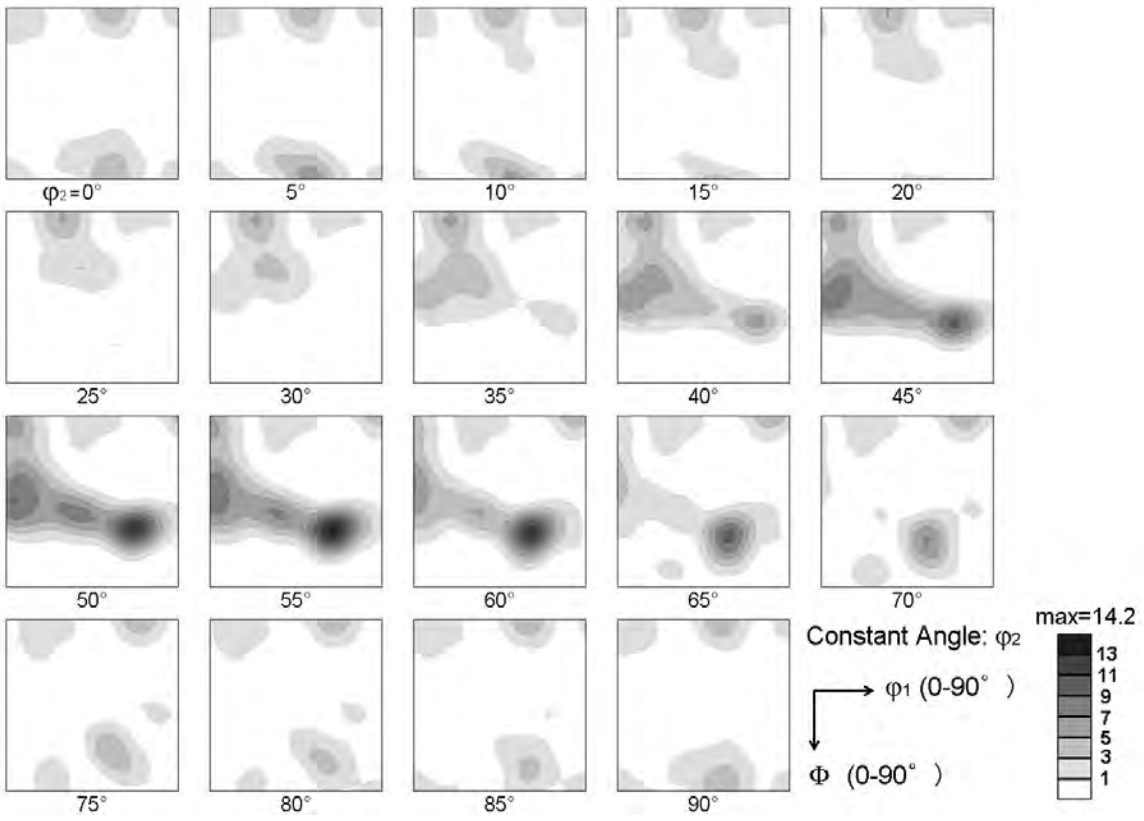

Figure 4.12 ODFs (in Bunge notation) of the 5Mn steel cold-rolled by 80% reduction and annealed at 600 °C.

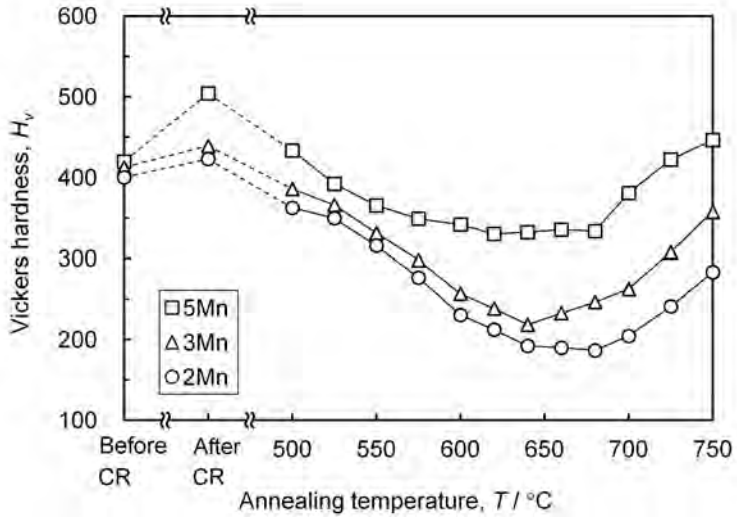

Figure 4.13 Vickers hardness of the 2Mn, 3Mn and 5Mn steels before cold-rolling (CR), after CR, and after salt-bath annealing at various temperatures.

4.2.4 Tensile properties of ultrafine grained multi-phase steels

First, the effect of annealing temperature on quasi-static tensile properties of the fabricated UFG-MP steels are shown and discussed. Figure 4.14 shows stress-strain (s-s) curves of the 2Mn steel annealed at various temperatures, at a strain rate of 10^{-2} s^{-1}. Figure 4.15 shows tensile strength (TS), 0.2% offset stress (YS), total elongation (t-El) and uniform elongation (u-El) of the 2Mn steel as a function of annealing temperature. The 2Mn steel is substantially the same as the UFG-FC2 steel shown in Chapter 2 and Chapter 3. Therefore, this is the base steel for investigating the effect of Mn. As expected, the effect of annealing temperature was very close to that in the UFG-FC2 steel. Uniform elongation was not observed in the specimens annealed at 600 to 660 °C, while significant work hardening and uniform elongation were observed in the specimens annealed at 700 to 750 °C. This was due to the introduction of martensite to the ferrite-cementite matrix.

Figure 4.16 shows the appearance of the tensile specimens of the 2Mn steel after the tensile tests at quasi-static strain rate. It is shown clearly that the deformation was localized to the region near shoulder section, at annealing temperatures of 600 and 620 °C (Fig 4.16 (a, b)). At higher annealing temperatures, the gauge section deformed uniformly and fracture occurred at the center of the gauge section (Fig 4.16 (e-h)). This result corresponded to the change in the s-s curves in Fig. 4.14. In the specimens having uniform elongation in the s-s curves, uniform deformation through the gauge section of the tensile specimens was observed.

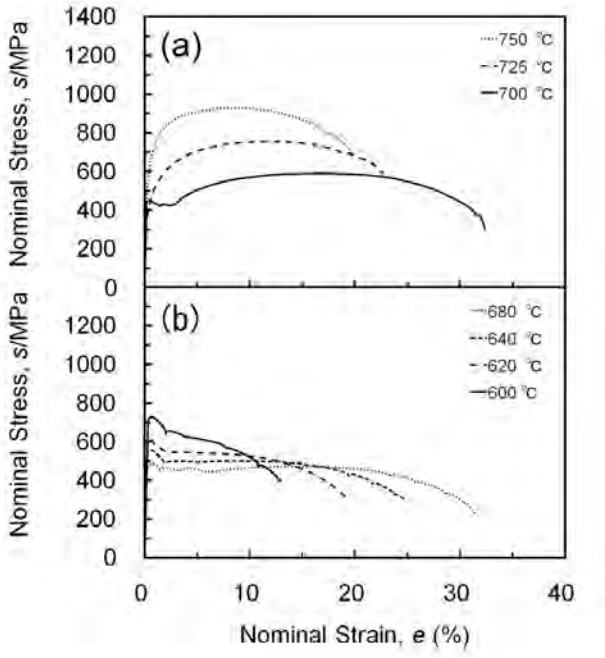

Figure 4.14 Nominal stress-strain curves of the 2Mn steel cold-rolled by 80% reduction and annealed at various temperatures.

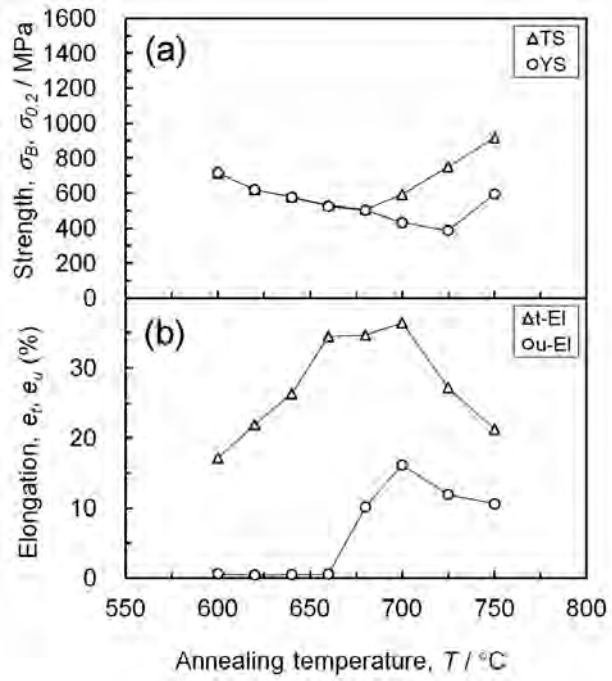

Figure 4.15 (a) Tensile strength (TS) and 0.2% offset stress (YS), (b) total elongation (t-El) and uniform elongation (u-El) of the 2Mn steel as a function of annealing temperature.

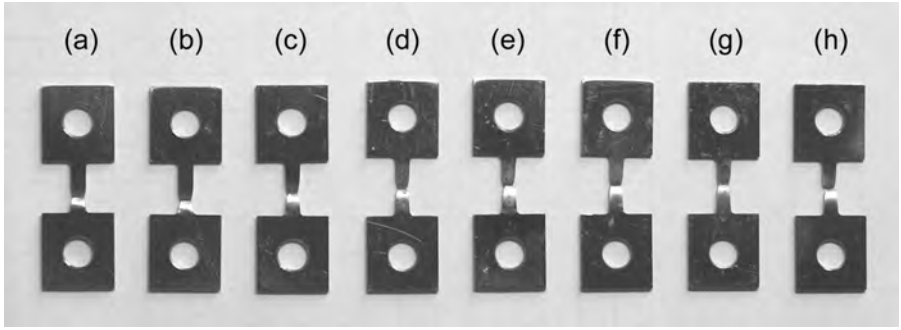

Figure 4.16 Appearance of the tensile specimens after the quasi-static tensile tests. The specimens were taken from the sheets of the 2Mn steel annealed at (a) 600 °C, (b) 620 °C, (c) 640 °C, (d) 660 °C, (e) 680 °C, (f) 700 °C, (g) 725 °C and (h) 750 °C.

Figure 4.17 shows s-s curves at a strain rate of 10^{-2} s^{-1} of the 3Mn steel annealed at various temperatures. Figure 4.18 shows TS, YS, t-El and u-El of the 3Mn steel as a function of annealing temperature. Uniform elongation was not observed in the specimens annealed at 600 to 640 °C. Work hardening and uniform elongation appeared clearly at annealing temperature of 680 °C. This temperature was the same as that where the second phases clearly appeared in the microstructures shown in Fig. 4.6. The specimens annealed at 700 to 750 °C showed typical s-s curves commonly observed in DP steels, composed of low yield strength and high work hardening rate. When annealing temperature increased up to 750 °C, both yield strength and tensile strength increased. Generally in conventional DP steels, yield strength linearly increases as martensite volume fraction increases [18]. The behavior of the present 3Mn steel at annealing temperature range between 700 and 750 °C was the same as that of the conventional DP steels. Figure 4.19 shows the appearance of the

tensile specimens of the 3Mn steel after tensile test at a quasi-static strain rate. It is shown that deformation was localized at the region near shoulder section at annealing temperatures of 600 to 640 °C (Fig 4.19 (a-c)). At annealing temperatures of 680 to 750 °C uniform deformation in the gauge section was clearly observed (Fig. 4.19 (e-h)). This result corresponded to the change in the s-s curves in Fig. 4.17.

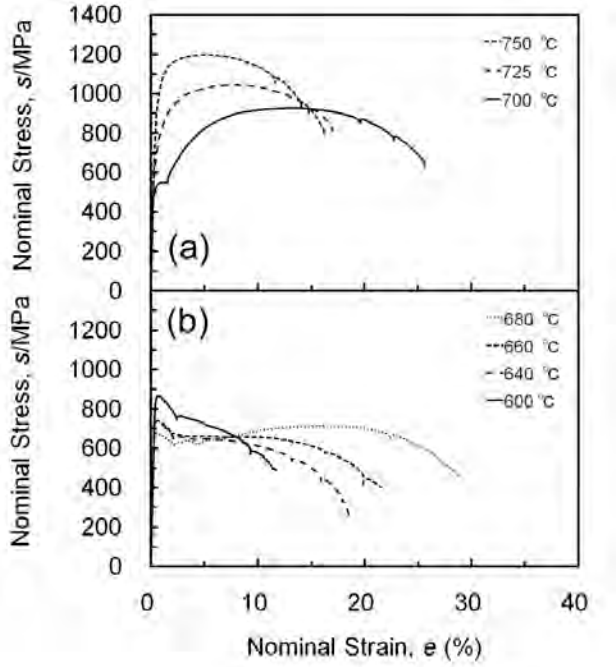

Figure 4.17 Nominal stress-strain curves of the 3Mn steel cold-rolled by 80% reduction and annealed at various temperatures.

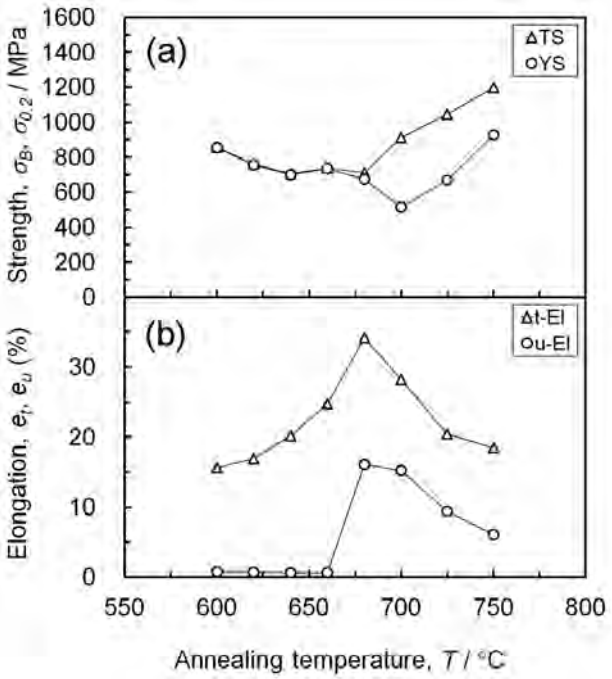

Figure 4.18 (a) Tensile strength (TS) and 0.2% offset stress (YS), (b) total elongation (t-El) and uniform elongation (u-El) of the 3Mn steel as a function of annealing temperature.

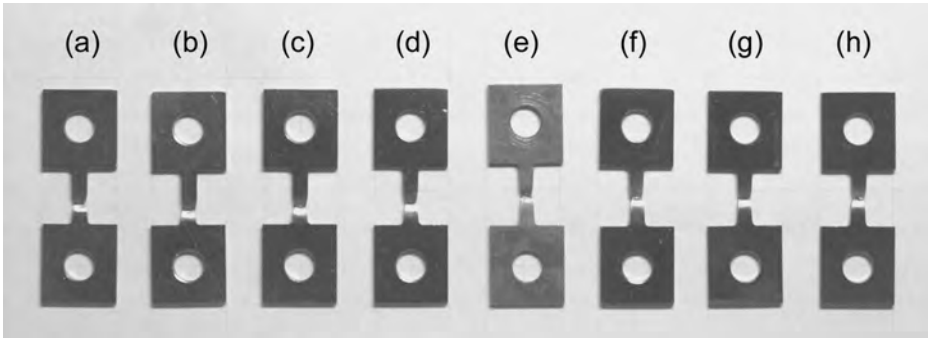

Figure 4.19 Appearance of the tensile specimens after quasi-static tensile test. The specimens were taken from the sheets of the 3Mn steel annealed at (a) 600 °C, (b) 620 °C, (c) 640 °C, (d) 660 °C, (e) 680 °C, (f) 700 °C, (g) 725 °C and (h) 750 °C.

Figure 4.20 shows s-s curves of the 5Mn steel annealed at various temperatures, at a strain rate of 10^{-2} s^{-1}. Figure 4.21 shows TS, YS, t-El and u-El of the 5Mn steel as a function of annealing temperature. Also in Fig. 4.21, retained austenite fractions in the microstructures measured by X-ray diffractometry and EBSD analysis, which have been summarized in Table 4.5, are shown again. No uniform elongation was observed at annealing temperatures between 600 and 640 °C (Fig. 4.21 (b)). As annealing temperature increased up to 660 °C, yield strength did not change so much but work hardening appeared (Fig. 4.20 (b)). This was due to the increased amount of hard second phases. Here, as shown in Fig. 4.21, the 5Mn specimens annealed at 600 to 640 °C contained some amount of retained austenite. However, in the s-s curves of these specimens in Fig. 4.20 did not show work hardening. This result indicates that austenite fraction up to 15% was not sufficient in order to show significant work hardening. This seems to be owing to the fact that yield strength of the material was very high (1000 to 1100 MPa in the 5Mn specimens annealed at 600 to 640 °C). Considering the plastic instability condition in the equation (3.4), when the material strength is very high, also high work hardening rate is required for keeping uniform elongation. In the 5Mn steel having ultrafine ferrite grains and therefore high yield strength, large amount of second phases was necessary.

Figure 4.22 shows the appearance of the tensile specimens of the 5Mn steel after tensile deformation at a quasi-static strain rate. Uniform deformation in the gauge section was observed in the specimens annealed at 660 to 700 °C (Fig. 4.22 (d-f)). This result also corresponded to the appearance of the s-s curves in Fig. 4.20. From these experiments of the 2Mn, 3Mn and 5Mn steels, it was shown that introduction of hard second phases was effective to improve work hardening and therefore to maintain uniform elongation even in UFG ferrite microstructures having very high strength.

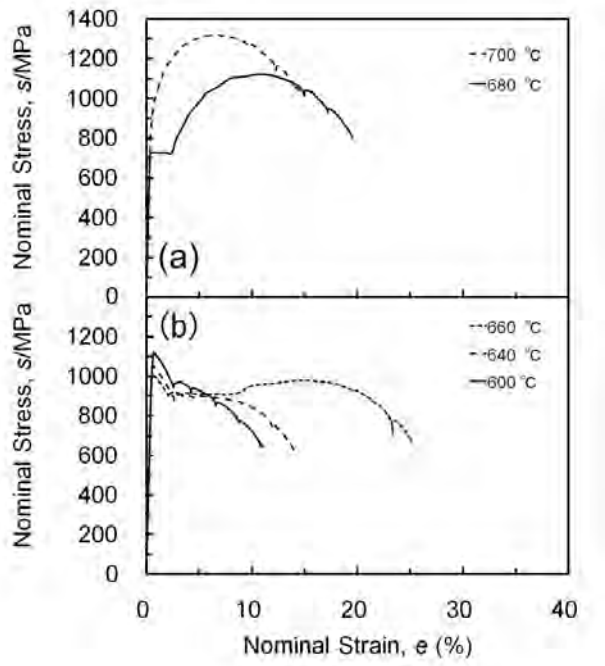

Figure 4.20 Nominal stress-strain curves of the 5Mn steel cold-rolled by 80% reduction and annealed at various temperatures.

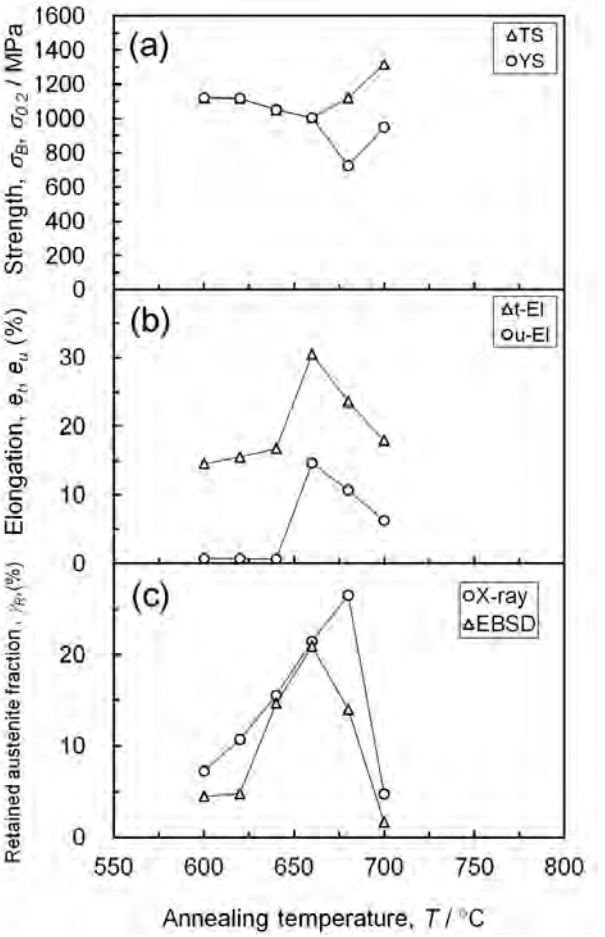

Figure 4.21 (a) Tensile strength (TS) and 0.2% offset stress (YS), (b) total elongation (t-El) and uniform elongation (u-El), and (c) retained austenite fraction of the 5Mn steel as a function of annealing temperature. The retained austenite fraction was evaluated by two methods, X-ray diffractometry and EBSD analysis.

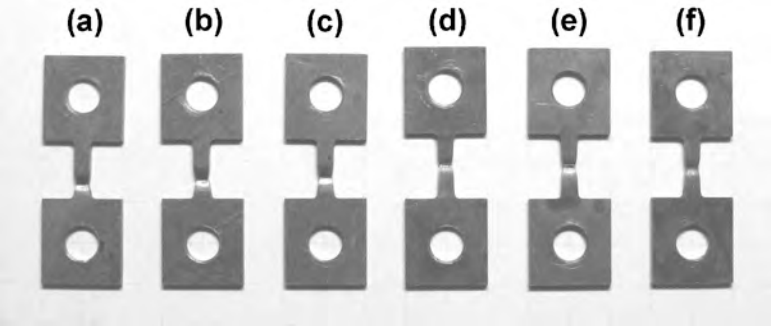

Figure 4.22 Appearance of the tensile specimens after quasi-static tensile test. The specimens were taken from the sheets of the 5Mn steel annealed at (a) 600 °C, (b) 620 °C, (c) 640 °C, (d) 660 °C, (e) 680 °C and (f) 700 °C.

Next, strength-ductility balances of the 2Mn, 3Mn and 5Mn steels are compared. Figure 4.23 shows the relationship between t-El and the TS of three steels. Three dotted curves mean that the product of TS and t-El ((TS) x (t-El)) are 15000, 20000 and 25000 (MPa%), respectively. Figure 4.23 (a) shows the data of the specimens which did not show u-El in tensile tests, while Fig. 4.23 (b) shows the data with u-El. Therefore, the t-El in Fig. 4.23 (a) was contributed mainly by local (post-necking) elongation. The balance of TS and t-El shown in Fig. 4.23 (a) was not different so much in three steels. On the other hand, it is clearly shown in Fig. 4.23 (b) that the 5Mn steel had the best balance of TS and t-El.

Figure 4.24 shows the relationship between TS and u-El of three steels. In this figure, it is also clearly shown that the 5Mn steel had the best strength-ductility balance. This result means that the Mn addition contributed mainly to the improvement of u-El. In the 5Mn steel, u-El was kept high in spite of high TS over 1000 MPa, resulting in improved strength-ductility balance.

The improvement of u-El in the 5Mn steel seemed to be related to martensite transformation of retained austenite. The retained austenite seemed to improve work hardening rate through TRIP effect. Figure 4.25 shows relationship between work hardening rate, $d\sigma/d\varepsilon$ and retained austenite fraction measured by X-ray diffractometry in the 3Mn and 5Mn steels. The work hardening rate during tensile deformation, $d\sigma/d\varepsilon$, was calculated using the stress-strain data in tensile tests and a formula described as

$$d\sigma/d\varepsilon = (\sigma_{0.1} - \sigma_{0.05})/0.05 \qquad (4.1)$$

where $\sigma_{0.1}$ and $\sigma_{0.05}$ are the true stress at true strains of 0.10 and 0.05, respectively. It is shown in Fig. 4.25 that work hardening rate was improved by increase of retained austenite fraction. However, in the 5Mn steel, higher amount of retained austenite was required to improve work hardening rate, compared with the 3Mn steel. This is because ferrite matrix in the 5Mn steel was very hard due to its very small grain size, therefore higher amount of retained austenite was required to show significant work hardening.

Figure 4.26 shows the product of TS and u-El ((TS) x (u-El)) as a function of work

hardening rate in the 2Mn, 3Mn and 5Mn steels. It is shown that the product of TS and t-El showed good correlation to work hardening rate. This result indicates that improvement of work hardening rate was effective in order to improve strength-ductility balance of the UFG steels.

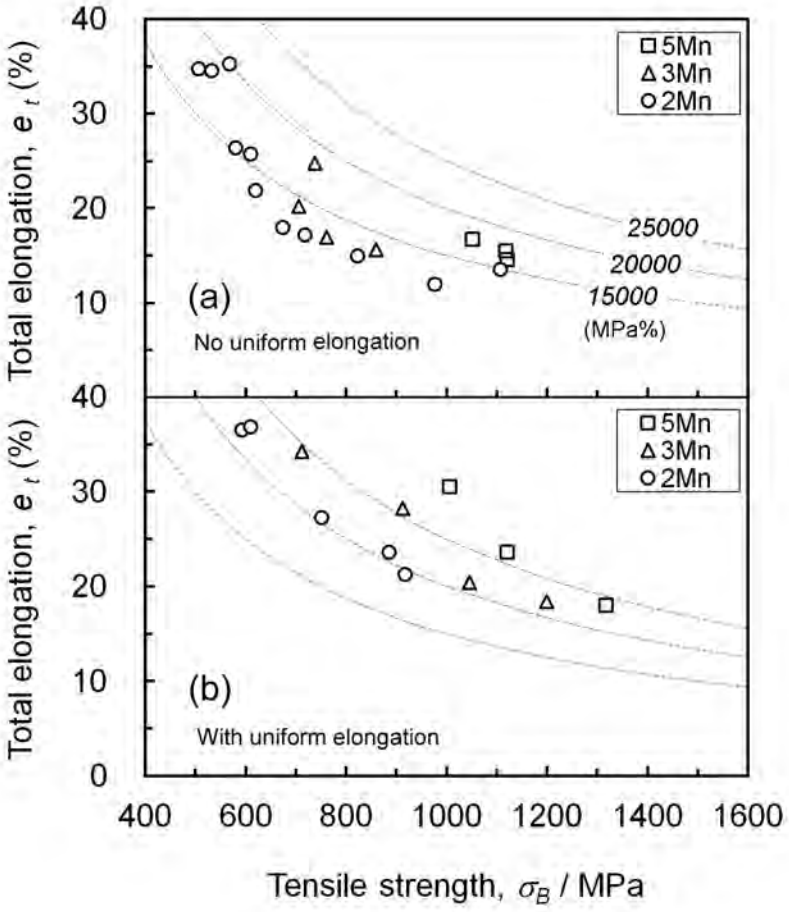

Figure 4.23 Relationship between tensile strength and total elongation of the 2Mn, 3Mn and 5Mn steels annealed at various temperatures. (a) The specimens showing no uniform elongation and (b) the specimens with uniform elongation.

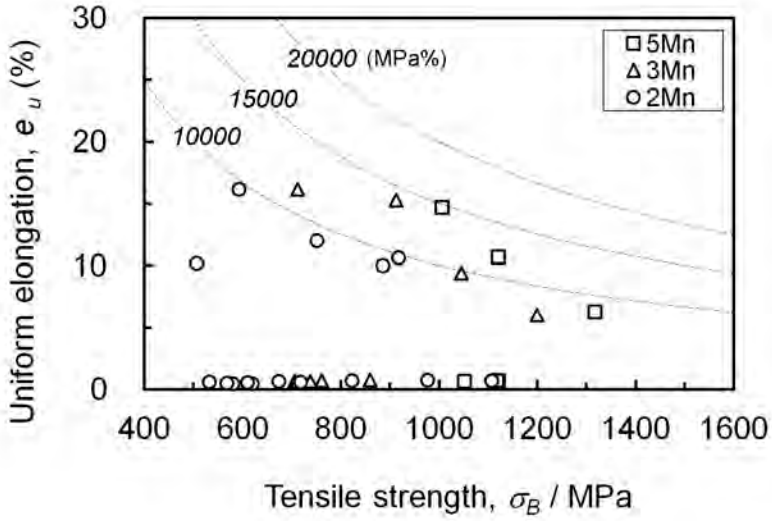

Figure 4.24 Relationship between tensile strength and uniform elongation in the 2Mn, 3Mn and 5Mn steels annealed at various temperatures.

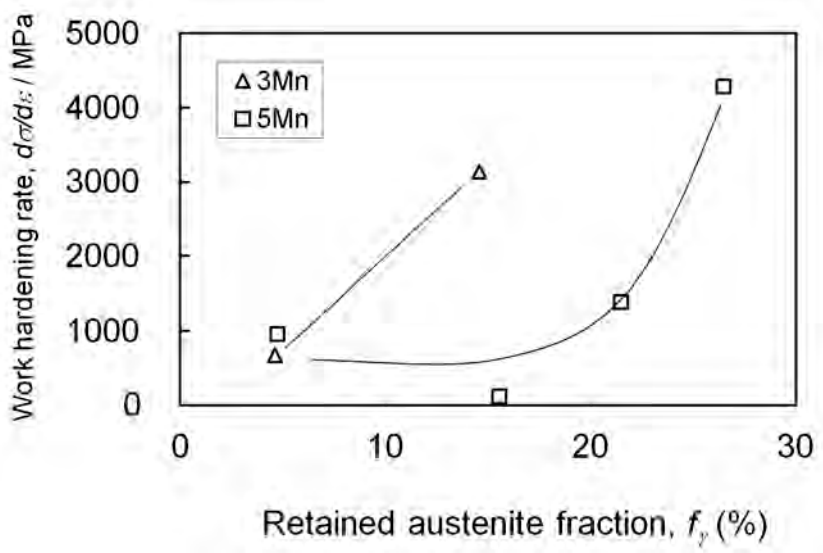

Figure 4.25 Relationship between retained austenite fraction and work hardening rate in quasi-static tensile deformation of the 3Mn and 5Mn steels annealed at various temperatures.

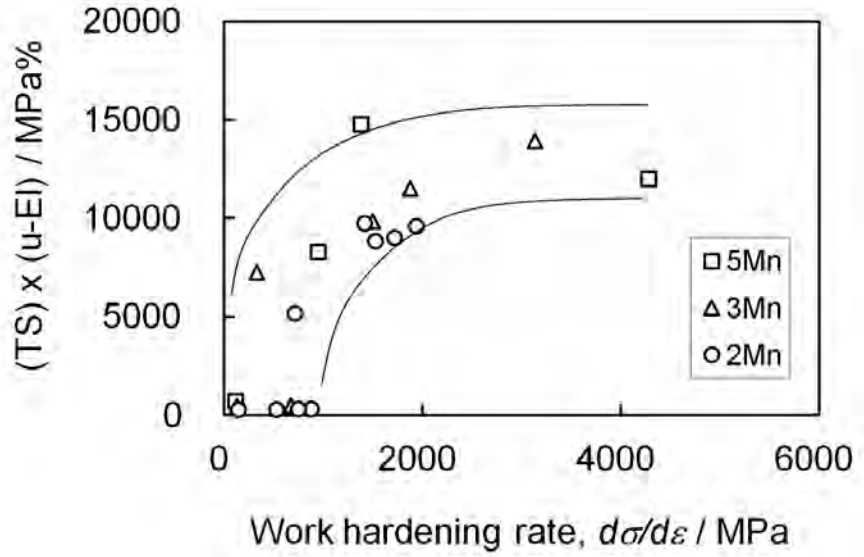

Figure 4.26 Relationship between (TS) x (u-El) and work hardening rate at a strain range between 0.05 and 0.10 in quasi-static tensile deformation of the 2Mn, 3Mn and 5Mn steels annealed at various temperatures.

Next, dynamic tensile properties of the 2Mn, 3Mn and 5Mn steel are shown. Here, as shown in Chapter 3, the difference in 5% flow stress between quasi-static and dynamic strain rates, $\Delta\sigma$, is focused. The $\Delta\sigma$ was calculated in the same way described in section 3.3 using the quasi-static (ε=10^{-2} s^{-1}) and dynamic (ε=10^{3} s^{-1}) s-s curves. Figure 4.27 shows the $\Delta\sigma$ as a function of the quasi-static 5% flow stress in the 2Mn, 3Mn and 5Mn steels. In Fig. 4.27, the data of the conventional sheet steels from references [19-21] that have been shown in Fig. 3.33 are plotted. Also for comparison, the data of the low-C bar-steel having UFG-FC microstructure reported by Tsuchida et al. [22] are plotted. The 2Mn specimens having FC microstructures had higher $\Delta\sigma$ value compared with the HSS having the same

quasi-static flow stress. The $\Delta\sigma$ decreased and become close to those in the conventional HSS when the microstructure changed to DP (indicated in solid circles). This behavior is consistent to the result shown in Chapter 3.

By increasing Mn content up to 5 mass% in the UFG-FC microstructures, the $\Delta\sigma$ slightly decreased while quasi-static flow stress increased significantly. This is supposed to be because solute Mn, which decreased the strain rate dependence of flow stress. In the 5Mn steel, when the microstructure changed from FC to MP, the $\Delta\sigma$ significantly decreased (an open square). This seems to be due to the introduction of second phases into the ferrite matrix.

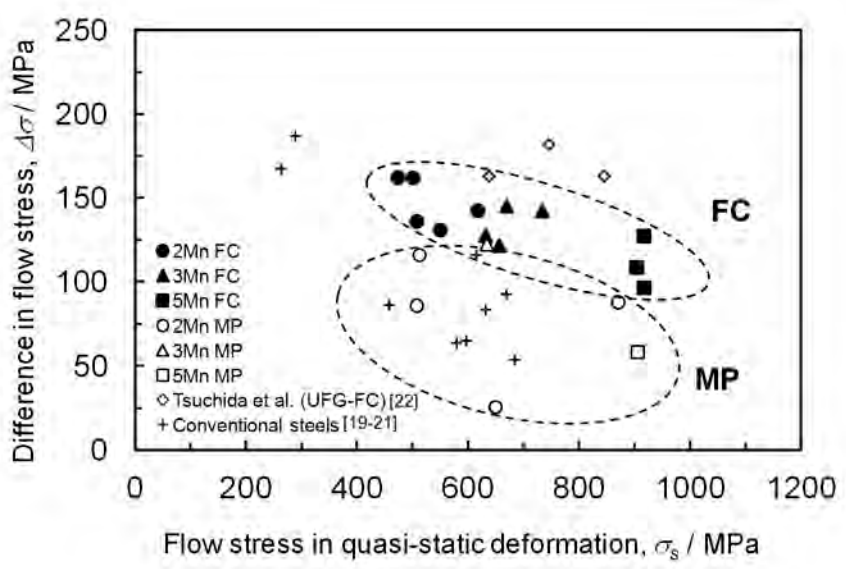

Figure 4.27 Relationship between $\Delta\sigma$ (difference in flow stress between dynamic and quasi-static strain rates) and quasi-static flow stress, σ_s, of the 2Mn, 3Mn and 5Mn steels cold-rolled by 80% reduction and annealed at various temperatures. The solid symbols indicate UFG-FC microstructures, and the open symbols indicate multi-phase (MP) microstructures. Reference data of conventional steels [19-21] and UFG bar-steel [22] are also plotted. The data were calculated at a nominal strain of 5%. Reference data were calculated at various nominal strains form 5 to 10 %.

Here, only one of the 3Mn specimens annealed at 680°C having MP microstructure (open triangle) had relatively high $\Delta\sigma$ value among MP specimens. In order to clarify this behavior, the s-s curves at various strain rates of the 3Mn specimen annealed at 680 °C are shown in Fig. 4.28. As shown in the s-s curves of the UFG-FC and DP microstructures (Fig. 3.26 (c, d)), features of the FC microstructure are yield drop and no work hardening, while those for the DP microstructure are low yield strength and high work hardening rate. It can be considered that the 3Mn specimen annealed at 680 °C had intermediate features between the FC and DP microstructures. Relatively high yield strength with yield drop, and relatively high work hardening were observed simultaneously in this 3Mn specimen. As a result, the $\Delta\sigma$ at 5% strain was also intermediate (higher than those in the conventional HSS but lower than those in the UFG-FC steels). This result suggests that the deformation behavior of this 3Mn specimen especially at small strains was rather close to that of the FC microstructure, although the mechanism was not clarified in this study. However, it was suggested that

better combination of strain rate dependence of flow stress and work hardening rate could be obtained by controlling annealing conditions and microstructure in the UFG-MP steels.

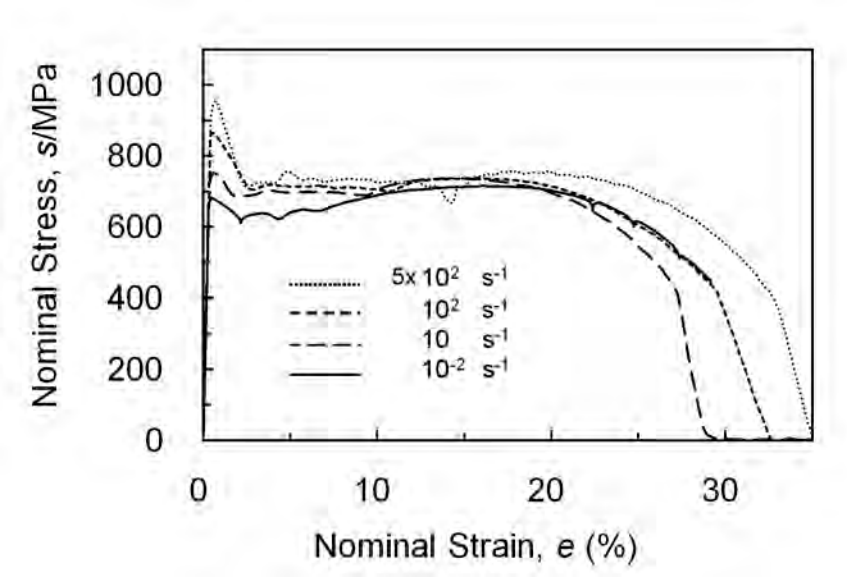

Figure 4.28 Nominal stress-strain curves of the 3Mn steel 80% cold-rolled and annealed at 680 °C at various strain rates ranging from 10^{-2} to $5x10^{2}$ s^{-1}.

4.2.5 Summary

In this section, attempts to improve ductility by introducing hard second phases to the UFG ferrite microstructure have been made. In order to achieve both multi-phase (MP) microstructure and ultrafine ferrite matrix, grain growth of ferrite matrix should be suppressed. For this purpose, decrease of intercritical annealing temperature was considered. Based on the concept, three low-C steels containing various amounts of Mn were prepared. The low-C steels containing 2 to 5 % Mn were hot-rolled and heat-treated to obtain duplex microstructures, and then cold-rolled and annealed at intercritical regions. This process was based on the new route for fabricating UFG ferrite microstructures without severe plastic deformation (SPD) shown in Chapter 2. The microstructures and mechanical properties including dynamic tensile properties were shown and discussed. The obtained results are summarized below.

(1) The transformation temperatures significantly decreased by Mn addition, which made it possible to decrease intercritical annealing temperatures. UFG-MP microstructures were successfully obtained in the 3Mn and 5Mn steels.

(2) The grain growth of ferrite matrix was significantly suppressed in the 3Mn and 5Mn steels. This was considered to be because new austenite grains appeared at grain boundaries of ferrite matrix during intercritical annealing prevented grain growth of ferrite.

(3) The second phases in the annealed microstructures included retained austenite, and its amount changed depending on intercritical annealing temperature.

(4) In tensile deformation of the UFG-MP microstructures, significant work hardening was observed, resulting in improved uniform elongation compared with the FC microstructures.
(5) The strength-ductility balance of the UFG-MP microstructures was better when Mn content was higher. This was because uniform elongation did not decrease in spite of high tensile strength. Large uniform elongation in the 3Mn and 5Mn UFG-MP steels were achieved by the improvement of work hardening rate.
(6) The difference in 5% flow stress between dynamic and quasi-static strain rates, $\Delta\sigma$, decreased depending on Mn content in the UFG-FC microstructures, however it was still higher than that in the conventional HSS. When hard second phases ware introduced, the $\Delta\sigma$ significantly decreased in all steels. It was concluded that introduction of second phases decreases the strain rate dependence also in the UFG ferrite microstructures.

4.3 Transformation induced plasticity effect in the ultrafine grained multi-phase steels

4.3.1 Introduction

In the former section, microstructures and mechanical properties of the UFG-MP steels were shown. Uniform elongation was significantly increased by introducing hard second phases. The microstructures of the UFG-MP steels contained large amount of retained austenite, and it was suggested that transformation of austenite to martensite during the deformation contributed to the improvement of work hardening rate and uniform elongation. As has been mentioned, this is so-called “transformation induced plasticity (TRIP)” effect [10]. The TRIP effect was originally observed in a Fe-Cr-Ni metastable austenite steel [23], and it has been applied to low-C steels since 1980's [24, 25]. Nowadays, the low-C TRIP-steels, which have MP microstructures composed of ferrite, bainite and retained austenite and show good formability in stamping process, are widely applied to automobile body structures.

It is well known that mechanical properties of TRIP-steels are strongly affected by transformation behavior of retained austenite [26, 27]. Strength and elongation of the TRIP-steels are improved when retained austenite has high mechanical stability against straining. In this section, various UFG-MP steels having various chemical compositions are prepared, and TRIP effect in those steels is shown. The microstructures and mechanical properties are shown and discussed in terms of work hardening rate and transformation of retained austenite.

By the way, ferrite matrix in commercial TRIP-steels has grain sizes of several micrometers [13]. The UFG-MP steels shown in the former section had sub-micrometer ferrite grain sizes. The strain-induced transformation behavior of austenite in the UFG

ferrite matrix, which has not been reported, is also investigated in this section. In order to clarify the effect of microstructural refinement, two kinds of MP microstructures, having UFG and FG ferrite grain sizes are prepared in the same steel. The mechanical properties of both MP microstructures are shown and compared.

4.3.2 Experimental procedure

Three kinds of TRIP-aided UFG-MP steels were fabricated. Table 4.6 summarizes the chemical compositions of the steels. C content was varied from 0.15 to 0.4 mass%, and Mn content was varied from 1.6 to 4 mass%. Figure 4.29 shows a schematic illustration describing the fabricating process and conditions. Table 4.7 summarizes the fabricating conditions for the UFG-MP steels. Ingots prepared through vacuum-melting and casting were austenitized at 1200 °C for 1 h, hot-rolled to a thickness of 5 mm at a FT of 800 °C in austenite region, and then air-cooled to room temperature. After mechanical grinding to a thickness of 3.5 mm, the hot-rolled sheets were warm-rolled or cold-rolled. Warm-rolling (WR) means the following process. The hot-rolled sheets were reheated at 500 °C for 1 hour in order to reduce the hardness, and rolled without additional reheating to a thickness of 1.0 mm. The WR was applied to the UFG-MP1 steel containing 0.4 mass% C, because of high hardness after hot-rolling. The hot-rolled sheets of the UFG-MP2 and UFG-MP3 steels were cold-rolled at room temperature to a thickness of 1.2 mm with lubrication. The total reductions in WR and CR were 71% and 66%, respectively. The warm-rolled or cold-rolled sheets were annealed at various temperatures between 695 and 735 °C corresponding to intercritical regions of ferrite and austenite. For the UFG-MP1 and UFG-MP2 steels, subsequent heat-treatment (over-aging: OA) at 400 °C for 5 minutes were applied after intercritical annealing. The purpose of this OA treatment was to accelerate partitioning of C atoms into non-transformed austenite, and to retain large amount of austenite at room temperature. Two salt baths, of which temperatures were set at intercritical annealing temperature and OA temperature (400 °C), were used. After the annealing at intercritical region for 120 s, the sheets were moved to another bath for the OA treatment, kept for 300 s and then air-cooled to room temperature. For the UFG-MP3 steel, the sheets were directly water-quenched to room temperature after intercritical annealing.

Table 4.6 Chemical compositions (mass%) of the UFG TRIP-aided multi-phase steels.

Steel	C	Si	Mn	P	S	Al	Nb	Ni	B	N
UFG-MP1	0.393	1.47	1.59	0.001	0.0005	0.021	0.022	2.0	-	0.0017
UFG-MP2	0.152	0.55	3.96	0.001	0.0011	0.024	0.047	-	-	0.0019
UFG-MP3	0.198	0.02	2.98	0.001	0.001	0.018	0.051	-	-	0.0017

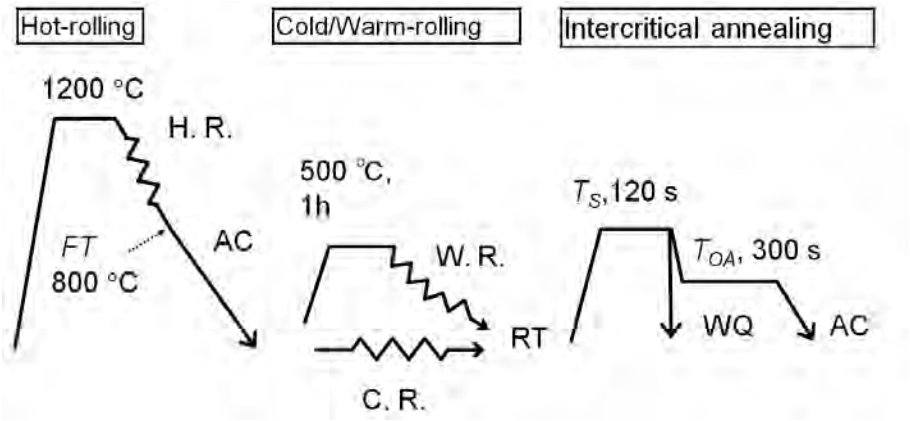

Figure 4.29 Schematic illustration of the process for fabricating the UFG TRIP-aided multi-phase steels.

Table 4.7 Fabricating conditions of the UFG TRIP-aided multi-phase steels.

Steel	CR/WR	Thickness after CR/WR (mm)	CR/WR reduction (%)	T_S (°C)	T_{OA} (°C)
UFG-MP1	WR	1.0	71	735	400
UFG-MP2	CR	1.2	66	695	400
UFG-MP3	CR	1.2	66	700	-

CR: cold-rolling, WR: warm-rolling,

T_S: intercritical annealing temperature, T_{OA}: over-aging temperature

Next, the procedures for fabricating MP microstructures having different ferrite grain sizes are explained. The UFG-MP2 steel was chosen as the base steel. The chemical composition of the prepared steel, summarized in Table 4.8, was substantially the same as the UFG-MP2 steel shown in Table 4.6. Figure 4.30 shows the fabricating process. Ingots prepared through vacuum-melting and casting were austenitized at 1230 °C for 1 h, hot-rolled at a FT of 860 °C in austenite region to a thickness of 5 mm, and then air-cooled to room temperature. After mechanical grinding to 3.5 mm in thickness, the hot-rolled sheets were cold-rolled at room temperature to a thickness of 1.2 mm with lubrication. The total reduction in CR was 66%. The cold-rolled sheets were heat-treated through different two routes. The one is shown as “FG route” in Fig. 4.30. A long-time heat-treatment at 620 °C for 10.8 ks in ferrite-cementite region, in order to coarsening ferrite grains, was applied at first. This heat-treatment was carried out in an electric furnace with air. The heat-treated sheets were annealed at intercritical region of ferrite and austenite followed by OA treatment, in order to fabricate MP microstructure. The methods used for intercritical annealing and following OA treatment were the same as those described before. The other route indicated as “UFG route” in Fig. 4.30 is the route for fabricating UFG-MP microstructures. The cold-rolled sheets were directly annealed at intercritical region followed by OA treatment. The intercritical annealing temperatures varied between 675 and 750 °C, and OA condition

was fixed at 400 °C for 300 s for the both routes. Table 4.9 summarizes the fabricating conditions for the UFG and FG routes.

Table 4.8 Chemical composition (mass%) of the TRIP-aided multi-phase steel used for fabricating UFG and FG microstructures.

C	Si	Mn	P	S	Al	Nb	N
0.151	0.54	4.05	0.002	0.001	0.024	0.052	0.001

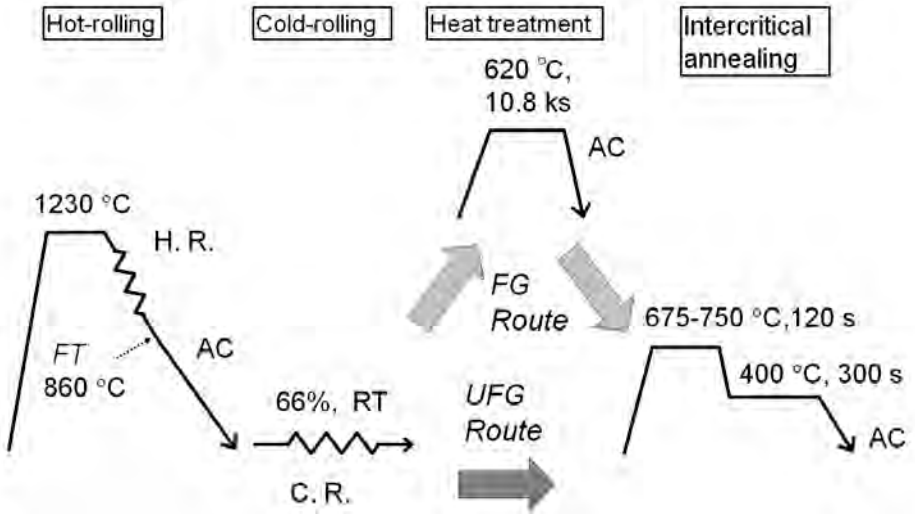

Figure 4.30 Schematic drawing of the process for fabricating UFG and FG MP microstructures in the TRIP-aided multi-phase steel.

Table 4.9 Fabricating conditions of the UFG and FG TRIP-aided MP steels.

Route	Heat-treatment condition	Intercritical annealing condition
UFG	-	675-700 °C, 120 s and 400 °C, 300 s
FG	620 °C, 10.8 ks	675-750 °C, 120 s and 400 °C, 300 s

The microstructures of the fabricated steel sheets were observed by SEM at the thickness center on the TD section. The SEM observations were conducted on Hitachi S-4300E/N SEM operated at 15 kV. Mean grain sizes of ferrite and second phases were measured on the SEM micrographs by using mean intersection method. Several lines were drawn on the SEM micrographs along RD and ND, and intersection lengths of each phase were measured. The average of the intersection lengths along RD and ND were used as the mean grain size. The area fractions of ferrite and second phases were measured by point counting method using SEM micrographs. Here, the “second phases” means austenite, bainite and martensite, which appeared as light gray islands in SEM micrographs. These phases could not be distinguished clearly in SEM micrographs due to their very small sizes.

The volume fraction of austenite was estimated by X-ray diffractometry using Co-Kα radiation. The specimens were chemically polished to 75% thickness of the initial

specimens, and diffraction was carried out on the rolling planes. The austenite fraction, $f_{\gamma,}$ was calculated using integrated intensities of (110)α, (200)α, (211)α, (111)γ, (200)γ and (220)γ diffraction peaks. The C content in austenite was calculated by using the lattice parameter and following equation proposed by Dyson and Holmes [28].

$$a_\gamma = 0.3578 + 0.0033C + 0.000095Mn - 0.00002Ni + 0.0022N + 0.00056Al + 0.00051Nb \quad (4.2)$$

where a_γ is the lattice parameter of austenite (nm), *C*, *Mn*, *Ni*, *N*, *Al* and *Nb* are the content of each element in mass%. Therefore, the C content in austenite, C_γ, is calculated as

$$C_\gamma = (a_\gamma - 0.3578 - 0.000095Mn + 0.00002Ni - 0.0022N - 0.00056Al - 0.00051Nb)/0.0033 \quad (4.3)$$

For the a_γ, average value of the calculated lattice parameters of austenite using three diffraction peaks in X-ray measurement was used. Here, for the contents of other alloying elements except for C, the average contents in the steel (the chemical compositions listed in Table 4. 6 and Table 4.8) were used. This is because the contents of alloying elements such as Mn or Ni in retained austenite were difficult to be measured. If using other equations which do not consider other alloying elements except for C [29], the C_γ values were over-estimated, and sometimes the product of C_γ and f_γ exceeded the total amount of C. Therefore in this study, the equations (4.2) and (4.3) were applied, considering they were relatively accurate.

In order to investigate the change in retained austenite fraction during deformation, austenite content of the deformed tensile specimens were measured. JIS No. 5 tensile specimens having a gauge length of 50 mm and gauge width of 25 mm were taken from the fabricated sheets. The tensile direction was parallel to RD. The tensile specimens were strained to 5%, 10%, and 15% in nominal strain at a strain rate of 3.3 x 10^{-3}, and diffraction was conducted at the center of the gauge section by X-ray diffractometry.

For investigating tensile properties, the small tensile specimen shown in section 3.2 was used. The tensile direction was parallel to RD. Quasi-static tensile tests were carried out by using the load-sensing block type test equipment and small test pieces described in section 3.2 at a strain rate of 10^{-2} s^{-1}. Two or three specimens were tested for each sheet.

4.3.3 Transformation induced plasticity (TRIP) effect in various ultrafine grained multi-phase steels having various chemical compositions

Figure 4.31 shows SEM microstructures of the fabricated UFG-MP1, UFG-MP2 and UFG-MP3 steels after final salt-bath annealing. All the steels showed MP microstructures composed of ultrafine ferrite (dark gray region) and second phases (light gray region). The mean ferrite grain size, volume fraction of second phases and volume fraction of retained austenite are summarized in Table. 4.10. It is shown that all the steels have sub-micrometer sized ferrite matrix, and volume fractions of the second phases were similar. However, the

volume fraction of retained austenite in the UFG-MP3 steel was smaller than other two steels. This is because OA treatment for stabilizing austenite was replaced by direct water-cooling in fabricating process for the UFG-MP3 steel. Therefore, the rest of the second phase in the UFG-MP3 steel seemed to be martensite. In Table 4.10, the C content in retained austenite is also shown. The C content in austenite strongly depended on the C content of the steel. The UFG-MP1 steel showed the highest C content. This was because total C content in the UFG-MP1 steel was the highest among the steels.

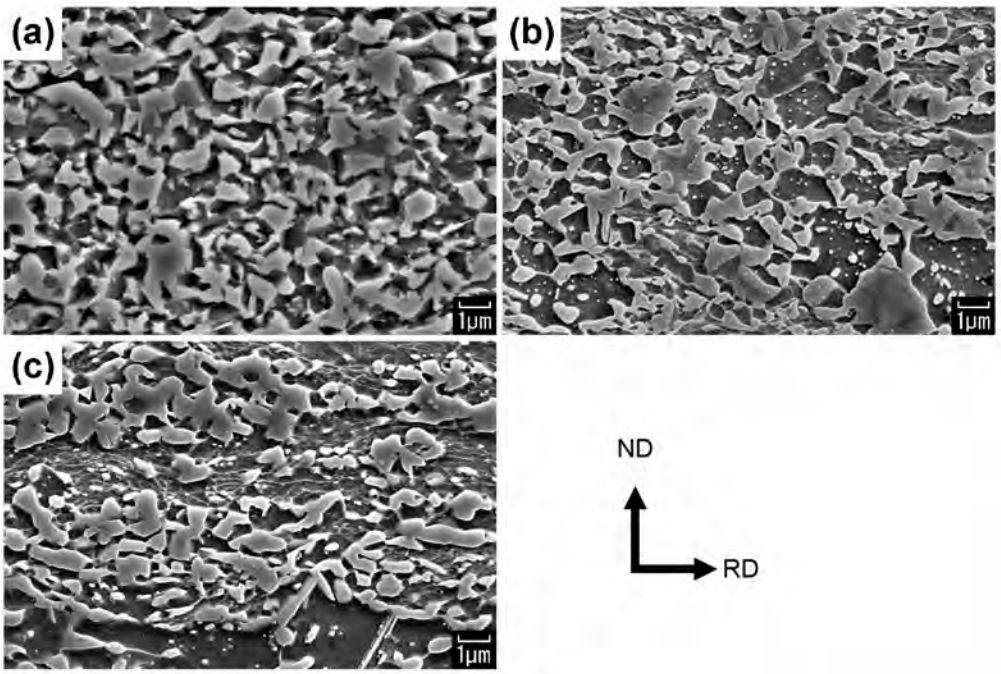

Figure 4.31 SEM microstructures of the fabricated UFG TRIP-aided MP steels. (a) UFG-MP1 steel, (b) UFG-MP2 steel and (c) UFG-MP3 steel. Observed from TD.

Table 4.10 Mean ferrite grain sizes, volume fraction of second phases and volume fraction of retained austenite in the UFG TRIP-aided MP steels.

Steel	d_f (μm)	f_s (%)	f_γ (%)	C_γ (mass %)
UFG-MP1	0.54	43	28.3	0.75
UFG-MP2	0.64	47	23.7	0.34
UFG-MP3	0.70	42	16.1	0.50

d_f : mean ferrite grain size, f_s : volume fraction of second phases,
f_γ : volume fraction of austenite, C_γ : C content in retained austenite

Next, mechanical properties and transformation behavior of retained austenite through deformation are shown. Table 4.11 summarizes 0.2% offset stress and nominal flow stress at 15% strain of three steels. All the steels showed flow stresses at 15% strain higher than 980 MPa. In Fig. 4.32 (a), true stress-true strain curves of three steels are shown. The UFG-MP1 and UFG-MP2 steels showed Lüders deformation after yielding, while the UFG-MP3 steel showed continuous yielding. Among three steels, the UFG-MP1 steel showed the highest flow stress at 15% strain. This seemed to be due to the high work

hardening rate of the steel. Figure 4.32 (b) shows work hardening rate, $d\varepsilon/d\sigma$ of three steels as a function of true strain. The work hardening rate was calculated based on the equation (4.1), but the strain range was set to be 0.001. The plotted values in Fig. 4.32 (b) are the average of $d\varepsilon/d\sigma$ at a strain range of 0.01. It is shown that $d\varepsilon/d\sigma$ of the UFG-MP2 and UFG-MP3 steels decreased significantly by straining, especially at low strains. On the other hand, the UFG-MP1 steel showed different behavior. The work hardening rate decreased gradually as strain increased, however it was still larger than those in other steels at high strains around 0.1 to 0.15. This is the reason why the UFG-MP1 steel showed the highest 15% flow stress.

Table 4.11 0.2% offset stress and flow stress at 15% strain of the UFG TRIP-aided MP steels. JIS No.5 tensile specimens having tensile direction along RD were used.

Steel	0.2% offset stress (MPa)	Nominal stress at 15% strain (MPa)
UFG-MP1	845	1291
UFG-MP2	788	1181
UFG-MP3	460	985

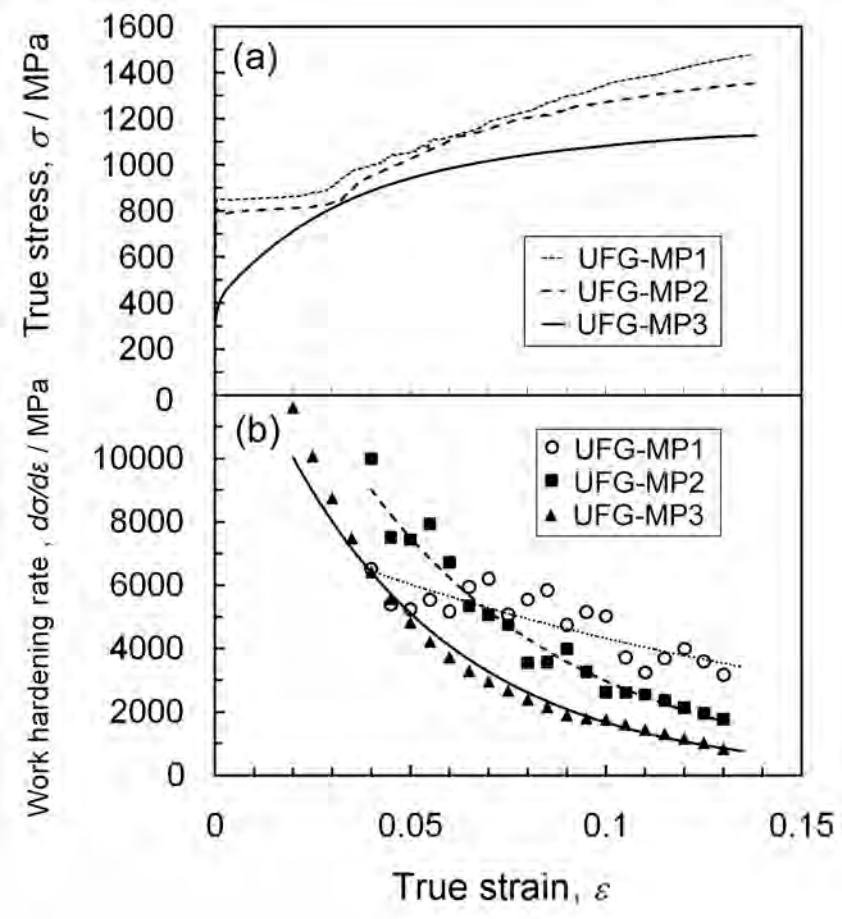

Figure 4.32 (a) True stress-true strain curves and (b) relationship between work hardening rate and true strain in the UFG TRIP-aided multi-phase steels. Tensile tests were carried out using JIS No.5 specimens having tensile direction along RD.

Work hardening behavior in the UFG-MP steels seems to be closely related to the deformation induced martensitic transformation of retained austenite. Table 4.12 summarizes austenite volume fraction at various nominal strains applied. Figure 4.33 shows the relationship between austenite volume fraction and true strain. The austenite volume fraction decreased as strain increased in all steels. This is an evidence of the occurrence of deformation induced martensitic transformation of retained austenite during deformation.

Table 4.12 Applied nominal strain and austenite volume fraction in the UFG TRIP-aided MP steels.

Steel	Volume fraction of retained austenite at various strains (%)		
	5%	10%	15%
UFG-MP1	17.0	13.1	9.8
UFG-MP2	7.5	3.6	3.1
UFG-MP3	3.7	1.5	1.0

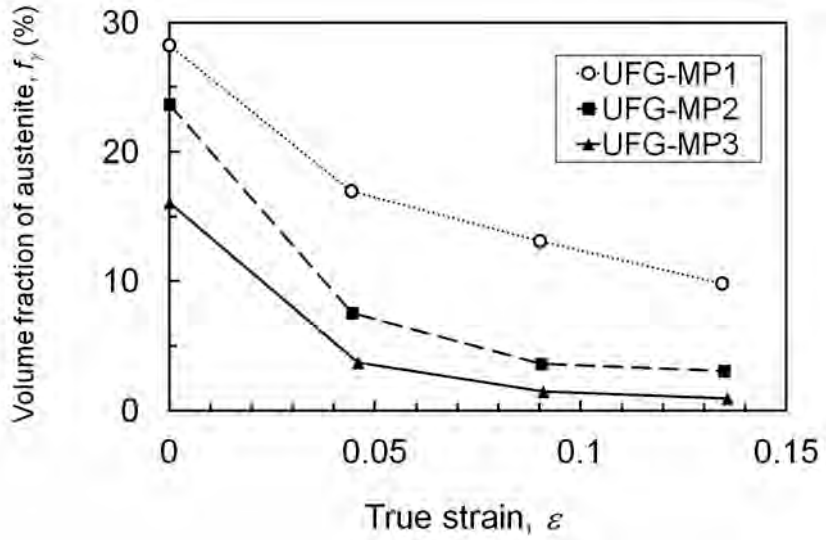

Figure 4.33 Relationship between volume fraction of retained austenite and true strain applied in the UFG TRIP-aided multi-phase steels. Tensile tests were carried out using JIS No.5 specimens having tensile direction along RD. Austenite volume fraction was measured by X-ray diffraction.

Direct observation of deformation induced martensitic transformation in the UFG-MP1 steel was carried out using neutron diffraction [30]. *In-situ* neutron diffraction during tensile deformation was performed using an engineering diffractometer “TAKUMI” [31] at J-PARC (Japan Proton Accelerator Research Complex). A tensile tester was set at 45 degrees with respect to the incident neutron beam. Tensile load that was applied to the specimen was increased in a step by step manner and neutron diffraction profiles in the axial and transverse directions were collected by two detectors simultaneously. Spacing of each lattice plane was calculated by using neutron diffraction profiles, and lattice strains were calculated for each lattice plane by using the plane spacing, assuming the spacing before loading as “stress-free” state. A double-peak fitting was applied to the overlapped diffraction profiles of martensite and ferrite, and information for these phases were separated.

Figure 4.34 shows the lattice strains of three kinds of planes in the constituent phases as a function of applied stress. The increase in lattice strains indicates elastic deformation, while the decrease indicates the start of plastic deformation of the phase. In Fig. 4.34 (b), it is shown that austenite grains oriented to <111> and <220> along the tensile direction (axial direction) showed a decrease in the lattice strain after the lower yield strength (LYS), indicating plastic deformation of austenite. On the other hand, the lattice strain of <200> grains continuously increased. The ferrite lattice strains were plotted in Fig. 4.34 (a). The lattice strains for ferrite did not show clear decrease after LYS, indicating that plastic deformation of ferrite was smaller than that of austenite after the LYS. This is because the ferrite grains were extremely fine in the UFG-MP1 steel. The strength of ferrite seemed to become comparable with that of C-enriched austenite. These results of the UFG-MP1 steel were quite different from those of conventional TRIP-steels. A study on the deformation behavior of conventional TRIP-steels with coarse grain size using *in-situ* neutron diffraction [31] has revealed that ferrite grains preferentially deformed plastically before the plastic deformation of austenite, indicating that C-enriched austenite is stronger than the ferrite matrix in conventional TRIP- steels..

The role of deformation induced martensite must be crucial in the UFG-MP1 steel. Fig. 4.34 (c) shows the lattice strain of martensite as a function of applied stress. The plane spacing of the martensite before loading was estimated by C content in the austenite before loading, assuming that the C content did not change during the deformation induced martensitic transformation. It is shown in Fig. 4.34 (c) that the lattice strain of martensite increased rapidly after the LYS, indicating that martensite beard higher stress than other phases.

It should be noted that the lattice strain of ferrite in transverse direction decreased just after the LYS (see Fig. 4.34 (a)). After the LYS, martensitic transformation accompanying with expansion of the volume took place in austenite grains. Hence, the compressive strain along the tensile direction and tensile strain along the transverse direction must be yielded in neighboring ferrite grains, leading to the change in the transverse strain of ferrite observed in Fig. 4.34 (a).

In order to discuss the macroscopic stress-strain behavior of multi-phase microstructures, stress partitioning is useful [30]. As shown in Fig. 4.34 (c), the martensite was the strongest and hard to deform plastically. It is supposed that internal stress existed in

the specimen during tensile deformation, caused by stress partitioning among constituent phases, and it contributed to the high work hardening rate of the UFG-MP1 steel. In order to clarify this mechanism, Fig. 4.35 shows residual strains in ferrite, austenite and martensite, represented by the lattice strains in axial direction at unloaded state after loading by 1250 MPa. Compressive strain remained in ferrite and austenite, while tensile strain in martensite. Generally in duplex or complex microstructures, compressive stress should be remained in softer phases after tensile deformation. It was clarified that the order in strength of constituent phases was martensite, ferrite, and austenite. The stress partitioning between the soft and hard phases seemed to contribute to the high work hardening rate of the UFG-MP1 steel.

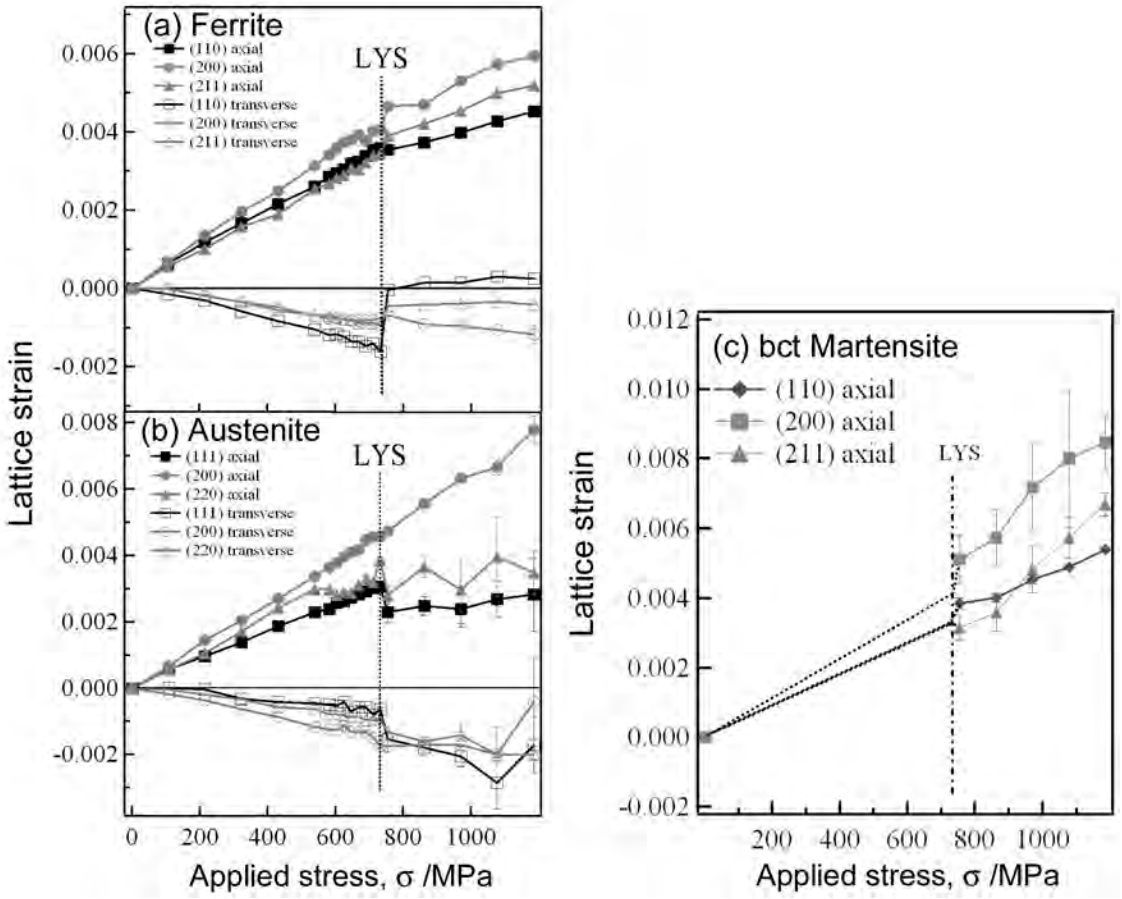

Figure 4.34 Change in lattice strains in (a) ferrite, (b) austenite, and (c) martensite as a function of applied stress in *in-situ* neutron diffraction for the UFG-MP1 steel.

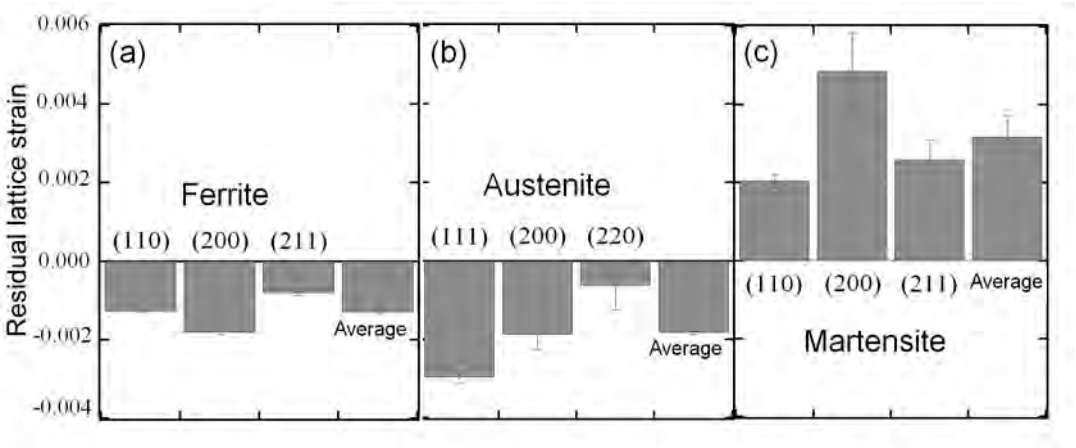

Figure 4.35 Residual strains after unloading in (a) ferrite, (b) austenite and (c) martensite in the UFG-MP1 steel measured by *in-situ* neutron diffraction.

By the way, as shown in Fig. 4.33, the decrease in austenite volume fraction during plastic deformation seemed to be smaller in the UFG-MP1 steel compared with other steels. From this result, it is indicated that larger work hardening rate in high strain region in the UFG-MP1 steel was caused by the relatively higher stability of austenite against straining. In order to evaluate the stability of retained austenite against straining, several methods have been proposed [27, 32, 33]. In this study, a simple equation proposed by Sugimoto et al. [32] is applied. The equation is described as

$$log\, f_\gamma = log f_{\gamma 0} - k\varepsilon \qquad (4.4)$$

where f_γ is austenite fraction at given applied strains, $f_{\gamma 0}$ is initial austenite fraction, k is an index representing the stability of austenite, and ε is the applied plastic stain, respectively. Low k-value means high stability of retained austenite. Figure 4.36 shows the relationship between log (f_γ) and true strain in the present three TRIP-aided UFG-MP steels. The gradient of the plots gives the k-value. Table 4.13 summarizes the measured k-values of three steels. The UFG-MP1 steel showed the lowest k-value, indicating the highest mechanical stability of austenite against straining. The UFG-MP3 steel had the lowest stability of retained austenite.

It has been well known that austenite stability strongly depends on C content in austenite [26, 27, 29, 32, 33]. As shown in Table 4.10, the C content in retained austenite, C_γ , was highest in the UFG-MP1 steel. It seems that the high C content in retained austenite brought high austenite stability. On the other hand, the UFG-MP2 steel had lower k-value (higher austenite stability) than the UFG-MP3 steel, in spite that the C_γ in the UFG-MP2 steel was slightly lower than that in the UFG-MP3 steel. Therefore, another factor should be considered. The UFG-MP2 steel contained higher amount of Mn than the UFG-MP3 steel, which meant retained austenite in the UFG-MP2 steel contained more Mn than that in the UFG-MP3 steel. In addition, Mn seemed to be concentrated in retained austenite in the present UFG steels. Recently, Lee et al. [34] have investigated Mn partitioning between ferrite matrix and austenite in a 6 mass% Mn-containing multi-phase steel, and shown that

Mn was concentrated in austenite in spite of short-time intercritical annealing. They [34] concluded that the partitioning of Mn and very fine austenite grain size were the main contributions to austenite stability. Therefore, it is supposed that retained austenite in the UFG-MP2 steel, containing higher amount of Mn than that in the UFG-MP3 steel, consequently showed higher stability against straining.

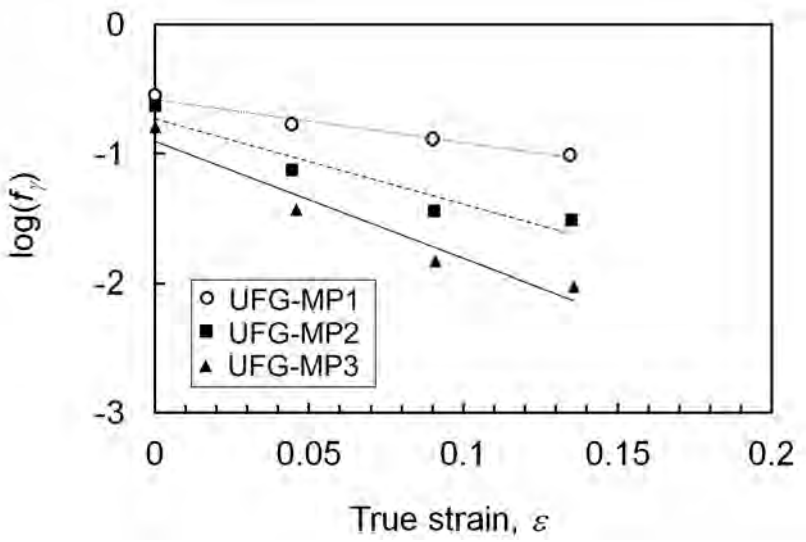

Figure 4.36 Relationship between log (f_γ) and true strain applied in the UFG TRIP-aided MP steels. Tensile tests were carried out using JIS No.5 specimens having tensile direction along RD. Austenite volume fraction was measured by X-ray diffraction.

Table 4.13 Calculated k-values in the UFG TRIP-aided MP steels calculated using the data in Fig. 4.36.

Steel	*k*-value
UFG-MP1	3.32
UFG-MP2	6.61
UFG-MP3	9.04

4.3.4 Effect of ferrite grain size on mechanical properties of ultrafine grained multi-phase steels

It has been described in the former section that in the TRIP-aided UFG-MP steels the high work hardening rate which contributed to large uniform elongations was brought by high stability of retained austenite against straining [26, 27, 32]. The stability of retained austenite was strongly affected by C content in austenite [26, 27, 29, 32, 33]. In addition, the morphology of retained austenite is also an important factor affecting the mechanical stability of austenite [26]. It has been pointed out that the stability of retained austenite improves when the grain size of austenite is small [26, 35], and when retained austenite exists at lath boundaries in bainite as a film-like shape [27, 36]. However, an opposite result showing higher stability of isolated blocky-shaped retained austenite has been reported [14]. Therefore, the effects of morphology of retained austenite on its stability have not been clarified yet. In this section, the effect of microstructural refinement of the MP microstructure containing retained austenite is focused. Effect of grain size of ferrite matrix seems to be an important factor affecting mechanical properties of TRIP-steels, however systematic study of the effect of grain refinement of matrix on mechanical properties has not been carried out. In this section, using two kinds of TRIP-aided MP steels having ultrafine and conventional ferrite grain sizes, their mechanical properties are compared and discussed.

First, MP microstructures having ultrafine ferrite grain sizes are shown. Figure 4.37 shows SEM microstructures of the UFG-MP2 steel fabricated through “UFG route” in Fig. 4.30. The microstructures of four specimens obtained from different intercritical annealing temperatures between 675 and 700 °C are shown. As annealing temperature increased, volume fraction of second phases (light gray regions in SEM microstructures) increased. Table 4.14 summarizes d_f (mean grain size of ferrite), d_s (mean grain size of second phases), f_s (volume fraction of second phases) and f_γ (volume fraction of austenite) of the fabricated microstructures. All the UFG specimens had ultrafine ferrite matrix and second phases. The f_s increased as annealing temperature increased.

Figure 4.38 shows SEM microstructures fabricated through “FG route”, having ferrite grain sizes between 1 μm and 2.2 μm. These microstructures are named “FG-MP” microstructures hereafter. The microstructures of four specimens having different intercritical annealing temperatures between 675 and 750 °C are shown. As the annealing temperature increased, the volume fraction of second phases (light gray regions in SEM microstructures) increased. The microstructural parameters in the FG-MP steel are also summarized in Table 4.14. Figure 4.39 shows relationship between second phase fraction and annealing temperature in the UFG-MP and FG-MP steels. The second phase fraction at given annealing temperature in the UFG microstructures was much higher than that in the FG microstructures. This seemed to be due to the ultrafine grain refinement of ferrite matrix. In UFG ferrite matrix, there were many nucleation sites for austenite, such as grain boundaries or triple junctions, during intercritical annealing. Therefore, nucleation of austenite seemed to be accelerated in the UFG microstructures, resulting in the higher

volume fraction of austenite. The retained austenite fractions of some specimens, measured by X-ray diffractometry, are summarized in Table 4.14. The retained austenite fraction showed the maximum at annealing temperature around 690-700 °C in both microstructures.

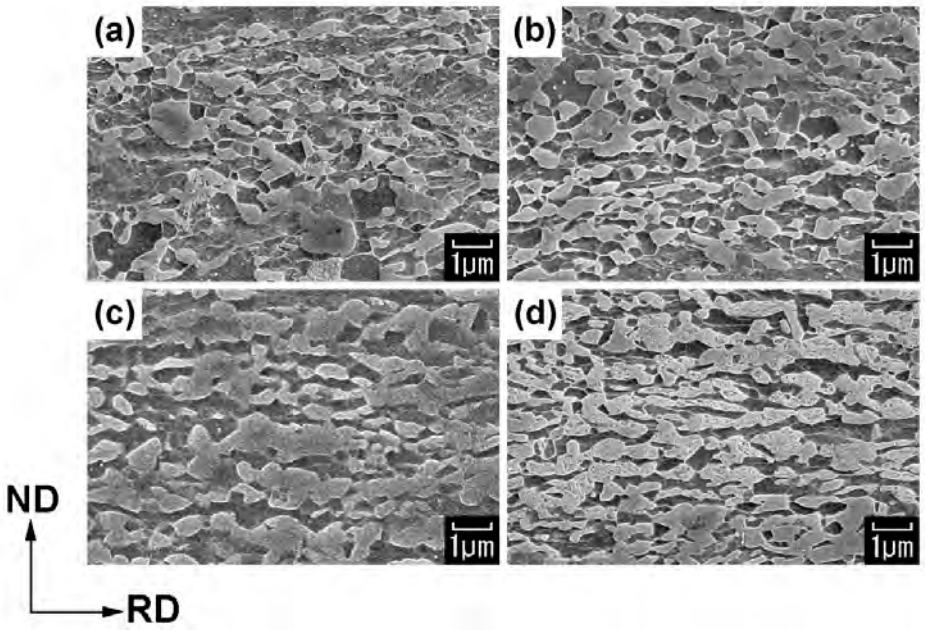

Figure 4.37 SEM microstructure of the 0.15C-0.5Si-4Mn steel having ultrafine grained (UFG) multi-phase microstructures. The specimens were cold-rolled by 66 % reduction and annealed at (a) 675 °C, (b) 685 °C, (c) 690 °C and (d) 700 °C for 120 s followed by OA treatment at 400 °C for 300 s. Observed from TD.

Table 4.14 Intercritical annealing temperature, mean grain size of ferrite and second phases, volume fraction of second phase, and volume fraction of retained austenite in the 0.15C-0.5Si-4Mn steel having UFG and FG multi-phase microstructures.

Route	Intercritical annealing temperature (°C)	d_f (μm)	d_s (μm)	f_s (%)	f_γ (%)
UFG	675	0.53	0.37	33	16.5
UFG	685	0.47	0.39	45	19.3
UFG	690	0.48	0.50	53	24.9
UFG	700	0.37	0.53	61	-
FG	675	1.71	0.59	18	-
FG	700	1.69	0.81	34	24.0
FG	725	2.20	1.15	43	8.9
FG	750	1.08	0.98	53	-

d_f : mean ferrite grain size, d_s : mean grain size of second phases

f_s : volume fraction of second phases, f_γ : volume fraction of austenite

-: not measured

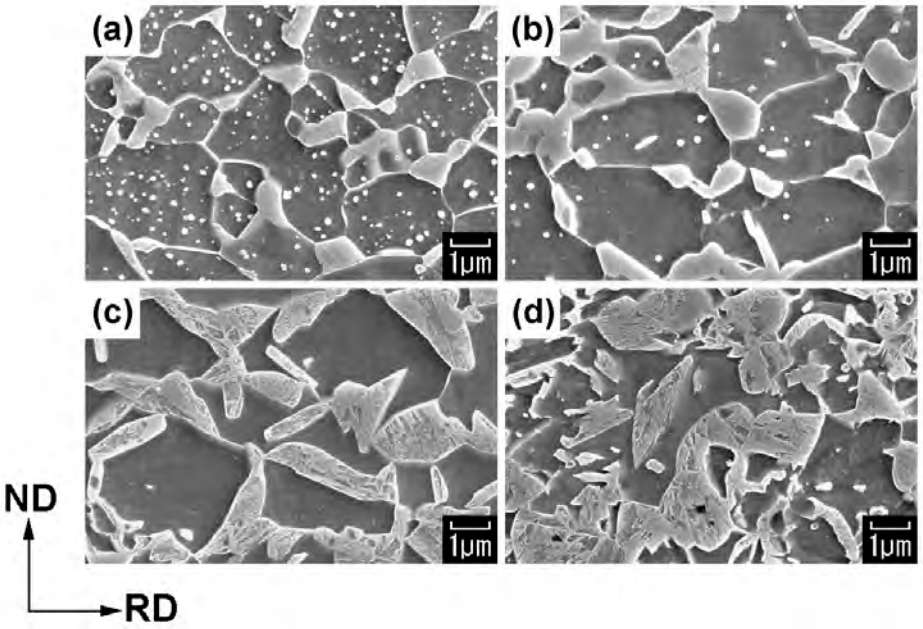

Figure 4.38 SEM microstructure of the 0.15C-0.5Si-4Mn steel having fine-grained (FG) multi-phase microstructures. The specimens were cold-rolled by 66 % reduction, annealed at 620 °C for 5.4 ks, and then intercritically annealed at (a) 675 °C, (b) 700 °C, (c) 725 °C and (d) 750 °C for 120 s followed by OA treatment at 400 °C for 300 s. Observed from TD.

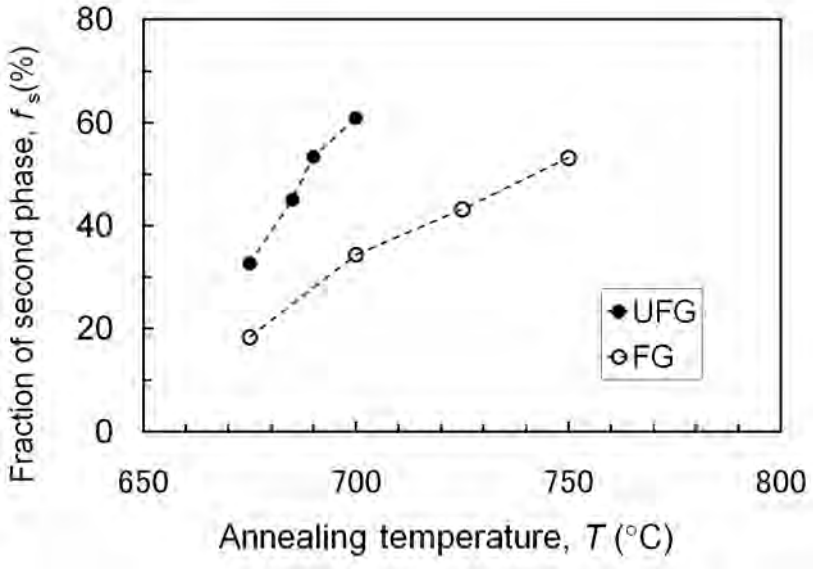

Figure 4.39 Relationship between second phase fraction and annealing temperature in the 0.15C-0.5Si-4Mn steel having ultrafine grained (UFG) and fine-grained (FG) microstructures.

Table 4.15 summarizes quasi-static mechanical properties of all the UFG and FG MP microstructures shown in Fig. 4.37 and Fig. 4.38, at a strain rate of $10^{-2}s^{-1}$. Figure 4.40 shows nominal s-s curves of all the microstructures. In both UFG and FG microstructures, TS increased as annealing temperature increased. In order to compare the strength-ductility

balance between the UFG and FG microstructures, the relationship between t-El and TS is shown in Fig. 4.41. The dotted curves mean that the product of TS and t-El ((TS) x (t-El)) are 20000, 25000 and 30000 (MPa%), respectively. It is clearly shown that the strength-ductility balance in the UFG microstructures was better than that in the FG microstructures especially at tensile strengths between 1200 and 1500 MPa.

Table 4.15 Quasi-static tensile properties of the 0.15C-0.5Si-4Mn steel having UFG and FG MP microstructures. Small tensile specimen shown in Fig. 3.6 was used.

Route	Intercritical annealing temperature (°C)	0.2% offset stress (MPa)	Tensile strength (MPa)	Uniform elongation (%)	Total elongation (%)
UFG	675	1106	1187	13.3	27.2
UFG	685	984	1281	11.3	24.5
UFG	690	635	1393	10.9	21.3
UFG	700	608	1528	8.7	16.9
FG	675	557	766	17.2	36.2
FG	700	349	950	15.4	28.4
FG	725	769	1306	7.5	17.7
FG	750	868	1390	6.2	17.7

The difference in the strength-ductility balance between the present UFG and FG MP microstructures seemed to be related to work hardening behaviors of the steels. Figure 4.42 shows relationship between work hardening rate at a true strain range between 0.05 and 0.10 and retained austenite volume fraction of the UFG and FG MP steels. The work hardening rate was calculated using the equation (4.1). The UFG-MP microstructures showed higher work hardening rate than the FG-MP microstructures having the same retained austenite fractions. As described before, it has been pointed out that stability of retained austenite increases when the grain size of austenite is small [26, 35]. The sizes of the second phases in the UFG-MP microstructure summarized in Table 4.14 were slightly smaller than those in the FG-MP microstructures, suggesting that the mean grain size of retained austenite was also smaller. This fact probably contributed to the improvement of mechanical stability of retained austenite in the UFG-MP microstructure. However, the difference in austenite grain sizes was not so large. In this case, it seems that refinement of ferrite matrix should be additionally considered. In the studies on UFG-DP microstructures composed of ultrafine ferrite and martensite without retained austenite, it has been shown that work hardening rate improved by ultrafine grain refinement of ferrite matrix [8, 9]. In DP steels without retained austenite, the TRIP effect is not necessary to be considered. According to the previous result in the UFG-DP microstructures containing no retained austenite [8, 9] it is assumed that the ultrafine grain refinement of ferrite matrix also contributed to the improvement of work hardening rate in the UFG-MP microstructure.

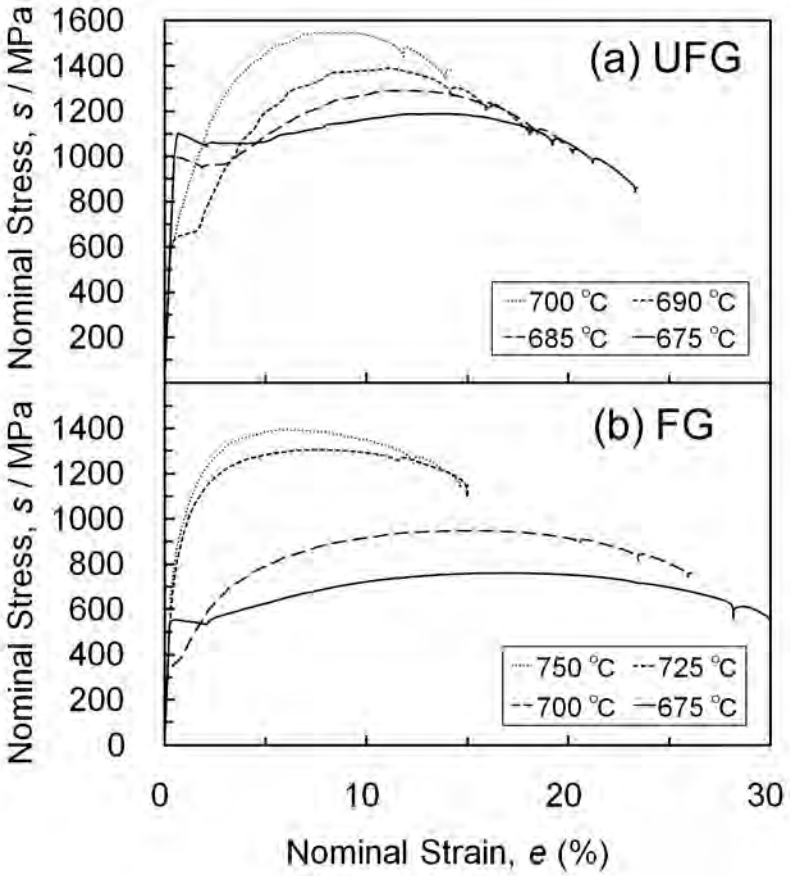

Figure 4.40 Nominal stress-strain curves of the 0.15C-0.5Si-4Mn steel cold-rolled by 66 % reduction and annealed. (a) Ultrafine grained (UFG) specimens, fabricated through "UFG" route in Fig. 4.30. (b) Fine grained (FG) specimens fabricated through "FG route".

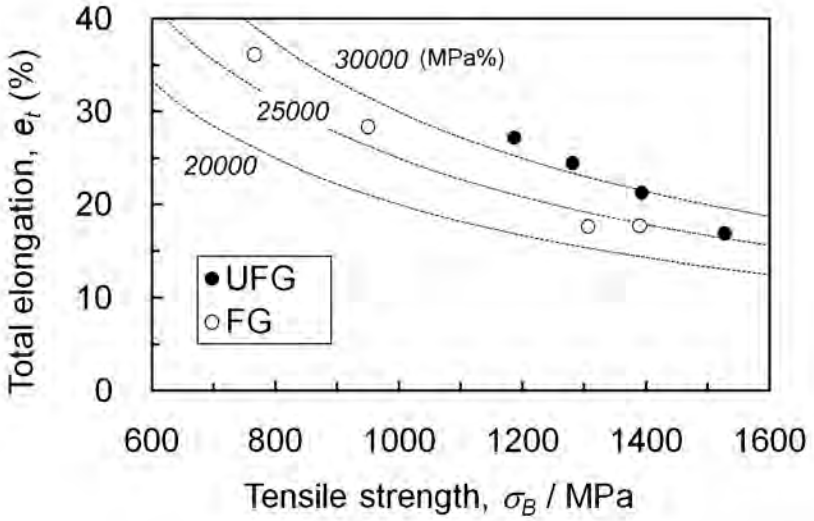

Figure 4.41 Relationship between tensile strength and total elongation of the 0.15C-0.5Si-4Mn steel having UFG and FG MP microstructures.

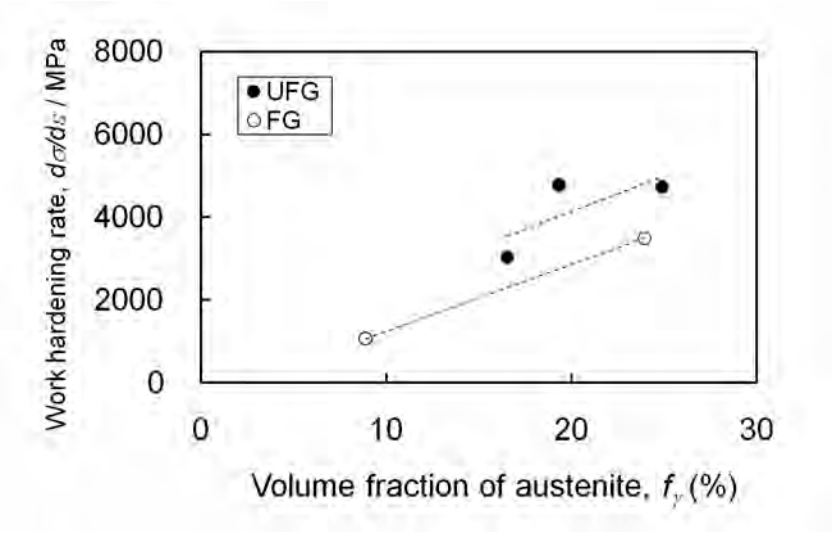

Figure 4.42 Relationship between work hardening rate and retained austenite volume fraction of the 0.15C-0.5Si-4Mn steel having ultrafine grained (UFG) and fine grained (FG) microstructures. The work hardening rate on the true s-s curve at a strain range between 0.05 and 0.10 was calculated using the equation (4.1).

4.3.5 Summary

In this section, first, TRIP effect in the UFG-MP steels was investigated. Three UFG-MP steels having various chemical compositions (0.15 to 0.4 mass% C, and 1.6 to 4 mass% Mn) were fabricated, and the microstructures and mechanical properties were investigated. The obtained results are summarized below.

(1) The retained austenite fraction in microstructures significantly decreased through plastic deformation in all the UFG-MP steels, indicating that austenite transformed to martensite during deformation. The TRIP effect occurred in the UFG-MP steels and it contributed to the improvement of work hardening rate.

(2) Work hardening rate varied among three UFG-MP steels. The UFG-MP1 steel containing 0.4% C showed the highest work hardening rate especially at high strain. This result was caused by high stability of retained austenite against straining.

(3) The stability of retained austenite was evaluated by using *k*-value. The UFG-MP1 steel containing 0.4 mass% C had the lowest *k*-value, indicating the highest mechanical stability of retained austenite. This result was due to the highest C content in austenite in the UFG-MP1 steel. It was shown that C content in retained austenite improved mechanical stability of retained austenite and work hardening rate of the UFG ferrite microstructures.

In the second part of this section, the effect of microstructural refinement on mechanical properties of the MP microstructures was shown. Based on the same steel, UFG and FG MP microstructures were fabricated, and their mechanical properties were investigated. The obtained results are summarized below.

(1) Formation of second phases during intercritical annealing was accelerated in the UFG ferrite matrix. This result seemed to be due to increase in nucleation sites for austenite in intercritical annealing.
(2) The UFG-MP microstructures showed better combination of strength and ductility, especially at tensile strengths between 1200 and 1500 MPa. This result was brought by high work hardening rate in the UFG-MP microstructures.
(3) At the same retained austenite fraction, the UFG-MP microstructures showed higher work hardening rate than the FG-MP microstructures. The small austenite grain size in the UFG-MP microstructures seemed to contribute to the improvement of work hardening rate. In addition, it was suggested that ultrafine grain refinement of ferrite matrix might contribute to it as well. As a result, it was shown that better strength-ductility balance was obtained in UFG-MP steels than in the FG-MP steels.

4.4 Comparison of mechanical properties between the ultrafine grained multi-phase steels and conventional steels

In this section, mechanical properties of the UFG-MP steels are compared with those of conventional sheet steels. Figure 4.43 shows the relationship between t-El and TS of the UFG-MP steels and conventional sheet steels. As the UFG-MP steels, data of the UFG-MP1, UFG-MP2 and UFG-MP3 steels shown in sections 4.2 and 4.3 are plotted. As the conventional steels, data of HSS shown in Chapter 3 are used. All the tensile tests were carried out using the small tensile specimen shown in Fig. 3.6 at a strain rate of 10^{-2} s^{-1}. It is clearly shown in Fig. 4.43 that the strength-ductility balance in the UFG-MP steels is better than that in the conventional steels. Two areas surrounded by dotted ellipses are shown in the figure. The one indicates mechanical properties of high-Mn TWIP (twinning induced plasticity) steels [11]. The other one indicates expected mechanical properties in “third generation AHSS” [11]. The goal of the “third generation AHSS” is an improved elongation, corresponding to stamping performance, with less alloying elements than TWIP steels. The ultrafine grain refinement is thought to be one of the candidates that could contribute to the third generation AHSS [37]. The data of the UFG-MP steels in Fig. 4.43 existed within the area for the third generation AHSS. Therefore, it is indicated that the UFG-MP microstructure is one of the important candidates for the next generation of AHSS.

By the way, several studies on low-C steels containing relatively high Mn content (5 to 7%) have been reported by several research groups [12, 38-41]. The mechanical properties of Mn-containing steels in the previous studies are mentioned here. For comparing with the UFG-MP steel in this study, low-C steels containing 5 mass% Mn are chosen from the previous studies and shown. Table 4.16 summarizes the alloy content in mass%, hot-rolling (HR) condition, CR condition and annealing conditions for various

5%Mn-steels in the previous studies [12, 38-41]. Additionally fabricating conditions for the UFG-MP2 steel in this study are listed. The procedures in the previous studies were composed of HR, CR and subsequent intercritical annealing. In reference [40, 41], CR was not applied. The intercritical annealing in references [38-41] was long-time annealing simulating "batch annealing" in actual manufacturing process of sheet steels, and that in reference [12] was short-time annealing considering continuous annealing (CA). The steel in reference [12] contained 1 to 3 mass% Aluminium.

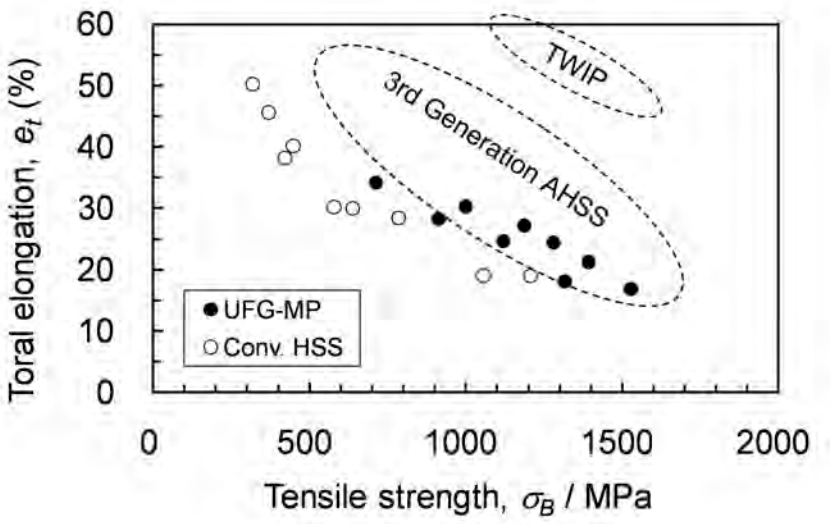

Figure 4.43 Relationship between total elongation and tensile strength of the UFG-MP steels and the conventional sheet steels. The UFG-MP steels are those shown in section 4.2 and section 4.3. The conventional steels are those shown in Chapter 3. The areas surrounded by dotted ellipses indicate the recent research target so-called "third generation AHSS" [11], and high-Mn TWIP steels [11], respectively.

Table 4.16 Alloy content in mass%, hot-rolling (HR) condition, cold-rolling (CR) condition and annealing conditions for 5%Mn-steels in previous studies and present UFG-MP2 steel.

Alloy content	HR condition	CR condition	Annealing condition	Reference
0.1C, 5Mn	FT=925°C, FC	67%, RT	590-730 °C, 65 ks	[39]
0.12C, 5Mn	FT=900 °C, AC	-	650 °C, 10.8 ks	[40]
0.12C, 5Mn, 1-3Al	FT>800 °C, AC	78%, RT	660 to 840 °C, 120 sec	[12]
UFG-MP2 (0.15C, 4Mn)	FT=860 °C, AC	66%, RT	675 to 700 °C, 120 sec	Present study

FT: finishing temperature in hot-rolling, HR: hot-rolling, CR: cold-rolling,

FC: furnace-cooling AC: air-cooling, RT: room temperature

The strength-ductility balance in the 5%Mn-steels in the previous studies is discussed. Actually, the types of tensile specimens in each study were different, which may affect tensile elongation, especially local elongation in tensile tests. Therefore, to increase accuracy in the comparison of ductility, u-El is evaluated here. Figure 4.44 shows the

relationship between TS and u-El in various 5% Mn-steels, and UFG-MP2 steel in this study. In addition, u-El of conventional sheet steels shown in Fig. 4.43 is plotted. The 5%Mn steels in references [39, 40] showed superior strength-u-El balance compared with the conventional steels, in the TS range lower than 1000 MPa. However, u-El decreased and became close to those in the conventional steels when TS increased up to 1200 MPa. In the Al-added 5%Mn-steels [12], the balance was better than the conventional steels even in TS range higher than 1000 MPa. On the other hand, the UFG-MP2 steel showed the best balance at UHSS region (TS > 1000 MPa). This result seems to be attributed to the difference in the fabricating conditions. The long-time annealing in references [39, 40] allowed grain growth of ferrite. The ferrite grain size of the specimen in reference [40] was 1 to 2 μm, actually. In reference [12], an equiaxed MP microstructure composed of sub-micrometer ferrite and second phases has been obtained. This microstructure had the same strength-u-El balance as the UFG-MP2 steel. (i. e. 1200 MPa in TS and 13% in u-El). However at TS range between 1200 and 1500 MPa, the UFG-MP2 steel had better balance than that in reference [12]. In addition, less Mn and Al contents in the present UFG-MP2 steel are advantageous in productivity as well as alloy cost when considering actual production.

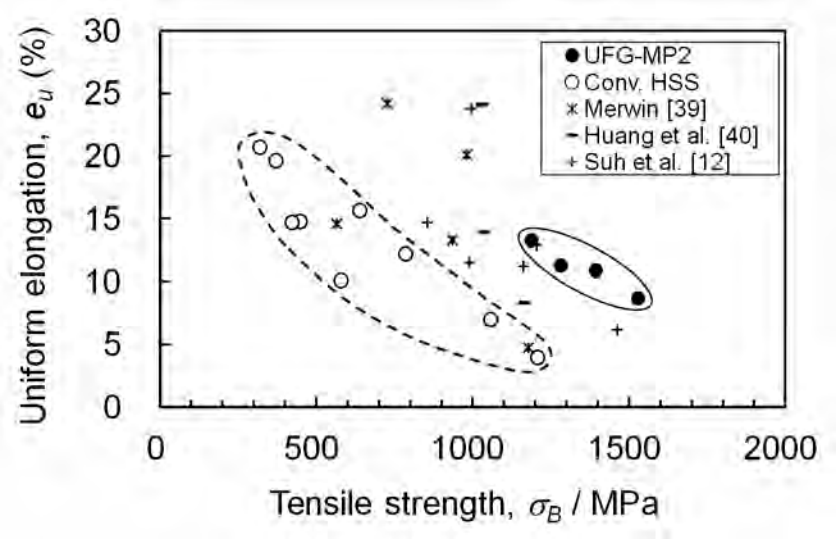

Figure 4.44 Relationship between uniform elongation and tensile strength of the 5%Mn-steels in references, UFG-MP2 steel in this study, and conventional sheet steels.

The strength-ductility balance shown above is a common way for evaluating performance of the steels. In addition to that, work hardening rate is considered in this study. Work hardening rate is represented by *n*-value, which is calculated in a following way. It is assumed that the s-s curves at a strain range between 0.05 and 0.1 can be explained by the equation

$$\sigma = K\varepsilon^n \tag{4.5}$$

where σ, K and n are true stress, a constant and work hardening component (*n*-value), respectively. Therefore, the *n*-values of the fabricated steels are calculated by

$$n = \ln\left(\frac{\sigma_2}{\sigma_1}\right) / \ln\left(\frac{\varepsilon_2}{\varepsilon_1}\right) \quad (4.6)$$

where σ_2 and σ_1 are true stress at certain true strains of ε_2 and ε_1, respectively. Here, as the true strains, 0.10 and 0.05 were used. Figure 4.45 shows the relationship between *n*-value calculated at the strain range between 0.05 and 0.10, and TS of the UFG-MP and conventional sheet steels. The conventional steels are the same as those shown in Fig. 4.43. It is noteworthy that the *n*-values of the UFG-MP steels are much higher than those in the conventional steels, and some of them are as high as those in mild-steels having TS around 300 MPa. Considering practical applications to automobile body structures, high *n*-value should improve formability, especially deep-drawability and stretch formability in stamping process. The conventional UHSS (steels having higher tensile strengths than 1000 MPa) [11] are not adaptive to deep-drawing processes because of their poor formability. The improved formability of the UFG-MP steels will be shown in Chapter 5. In addition, it was found in this study that high *n*-value improves crash performance of body frame parts, when the UFG-MP steels are applied. The crash worthiness of the UFG-MP steels will be focused and described in detail in Chapter 5.

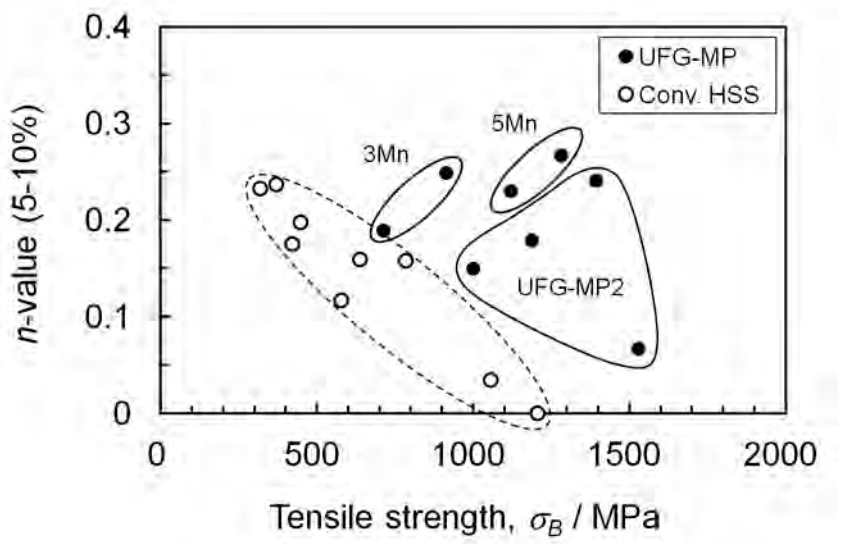

Figure 4.45 Relationship between n-value and tensile strength of the UFG-MP steels and conventional sheet steels. The UFG-MP steels are those shown in section 4.2 and section 4.3. The conventional steels are those shown in Chapter 3. The *n*-value was calculated in a true strain range between 0.05 and 0.10.

4.5 Conclusions

In this chapter, experiments were carried out aiming for the improvement of ductility in the UFG ferrite microstructures. For suppressing grain growth of ferrite, transformation temperatures of the steels were decreased by Mn addition, which made low-temperature intercritical annealing possible. Based on this concept, the UFG-MP microstructures, having both ultrafine ferrite matrix and hard second phases, were successfully obtained during

conventional process composed of cold-rolling and short-time annealing.

The fabricated UFG-MP steels showed superior strength-ductility balance, which was brought by the high work hardening rate of the microstructures. The high work hardening rate was brought by deformation induced martensitic transformation of retained austenite in the microstructures. When the stability of retained austenite was high, work hardening rate was kept high up to large tensile strains. The stability of retained austenite depended on carbon content in austenite.

The effect of microstructural refinement in the MP steels containing retained austenite was investigated. It was shown that the UFG-MP microstructures had higher work hardening rate compared with the FG-MP microstructures having micrometer-sized ferrite matrix. This result seemed to be attributed to the finer austenite grain sizes, which increased the stability of austenite against straining. In addition, it was suggested that ultrafine grain refinement of ferrite matrix contributed to the improvement of work hardening rate as well.

The strength-ductility balance of the UFG-MP steels was better than that of conventional HSS, and it existed within the target performance for the next generation of AHSS. Therefore, the UFG-MP microstructure could be one of the important candidates for the next generation of AHSS. In addition, it is expected that the UFG-MP steels have good performance in the application to automobile body structures, for example, stamping performance, and crash worthiness.

4.6 References

[1] Y. M. Wang, E. Ma, Acta Mater. 52 (2004) 1699.

[2] N. Tsuji, Fabrication of bulk nanostructured materials by accumulative roll bonding (ARB), in: M. J. Zehetbauer, Y. T. Zhu (Eds.) Bulk nanostructured materials, WILEY-VCH, Weinheim, 2009, pp. 246.

[3] Y. Tomota, A, Narui, N. Tsuchida, ISIJ Int. 48 (2008) 1107.

[4] N Tsuchida, Y. Tomota, K. Nagai, Tetsu-to-Hagané 89 (2003) 1170.

[5] N. Tsuji, R. Ueji, Y. Minamino, Scripta Mater. 47 (2002) 69.

[6] A. Ohmori, S. Torizuka, K. Nagai, ISIJ Int. 44 (2004) 1063.

[7] R. Song, D. Ponge, D. Raabe, Scripta Mater. 52 (2005) 1075.

[8] Y. I. Son, Y. K. Lee, K. T. Park, C. S. Lee, D. H. Shin, Acta Mater. 53 (2005) 3125.

[9] M. Calcagnotto, D. Ponge, D. Raabe, ISIJ Int. 48 (2008) 1096.

[10] H. Takechi, JOM, 60 No.12 (2008) 22.

[11] World Steel Association, Advanced High Strength Steel (AHSS) Application Guidelines Version 4.1, Available from: http://www.worldautosteel.org [Accessed 14 October 2011].

[12] D-W. Suh, S-J. Park, T-H. Lee, C-S. Oh, S-J. Kim, Mater. Trans. A 41 (2010) 397.

[13] S. Zaefferer, J. Ohlert, W. Bleck , Acta Mater. 52 (2004) 2765.

[14] Y. Tomota, H. Tokuda, Y. Adachi, M. Wakita, N. Minakawa, A. Moriai, Y. Mori, Acta Mater. 52 (2004) 5737.

[15] O. Matsumura, Y. Sakuma, H. Takechi, Trans. ISIJ 27 (1987) 571.
[16] R. K. Ray, J. J. Jonas, R. E. Hook, Int. Mater. Rev. 39 (1994) 129.
[17] H. Takechi, ISIJ Int. 34 (1994) 1.
[18] Y. Tomota, G. Kuroki, I. Tamura, Tetsu-toHagané, 61 (1975) 108.
[19] M. Takahashi, A. Uenishi, H. Yoshida, Y. Kuriyama, SAE Technical Paper 2003-01-2765, SAE International, Warrendale, 2003.
[20] S. Takagi, Y. Tokita, K. Sato, T. Shimizu, K. Hashiguchi, K. Ogawa, K. Mimura, S. Tanimura, SAE Technical Paper 2005-01-0494, SAE International, Warrendale, 2005.
[21] O. Moriau, L. Tosal-Martinez, P. Verieysen, J. Degrieck, Int. Conf. on TRIP-Aided High Strength Ferrous Alloys, Aachen, 2002, pp. 247.
[22] N. Tsuchida, H. Masuda, Y. Harada, K. Fukaura, Y. Tomota, K. Nagai, Mater. Sci. Eng. A 488 (2007) 446.
[23] V. F. Zackay, E. R. Parker, D. Fahr, R. Bush, Trans. ASM 60 (1967) 252.
[24] O. Matsumura, Y. Sakuma, H. Takechi, Trans. ISIJ 27 (1987) 579.
[25] K. Sugimoto, N. Usui, M. Kobayashi, S. Hashimoto, ISIJ Int. 32 (1992) 1311.
[26] B. C. De Cooman, D. Krizan, in: S. Hashimoto, S. Jansto, H. Mohrbacher, F. Siciliano (Eds.), International Symposium on Niobium Microalloyed Sheet Steel for Automotive Applications. TMS, Warrendale, 2006, pp. 303.
[27] P. J. Jacques, J. Ladrière, F. Delannay, Mater. Trans. A 32 (2001) 2759.
[28] D. J. Dyson, B. Holmes, J. Iron Steel Inst. 208 (1970) 469.
[29] B. C. De Cooman, Curr. Opinion in Solid State and Mater. Sci. 8 (2004) 285.
[30] K. Asoo, Y. Tomota, S. Harjo, Y. Okitsu, ISIJ Int. 51 (2011) 145.
[31] S. Harjo, K. Aizawa, T. Ito, H. Arima, J. Abe, A. Moriai, K. Sakaki, T. Nakamura, T. Nakatani, T Iwahashi, T. Kamiyama, Mater. Sci. Forum 652 (2010) 99.
[32] K. Sugimoto, M. Kobayashi, S. Hashimoto, Metal. Mater. Trans. A 23 (1992) 3085.
[33] A. Itami, M. Takahashi, K. Ushioda, ISIJ Int. 35 (1995) 1121.
[34] S. Lee, S-J. Lee, B. C. De Cooman, Scripta Mater. 65 (2011) 225.
[35] J. Wang, S. Van Der Zwaag, Metal. Mater. Trans. A 32 (2001) 1527.
[36] K. Sugimoto, M. Misu, M. Kobayashi, H. Shirasawa, ISIJ Int. 33 (1993) 775.
[37] D. K. Matlock, J. G. Speer. Third generation of AHSS: microstructure design concepts. in: A. Haldar, S. Suwas, D. Bhattacharjee (Eds.), Microstructure and Texture in Steels and Other materials, Springer, London, 2009. pp. 185.
[38] R. L. Miller, Met. Trans. 3 (1972) 905.
[39] M. J. Merwin, SAE Technical Paper 2007-01-0336, SAE International, Warrendale, 2007.
[40] H. Huang, O. Matsumura, T. Furukawa, Mat. Sci. Tech. 10 (1994) 621.
[41] T. Furukawa, H. Huang, O. Matsumura, Mat. Sci. Tech. 10 (1994) 964.

CHAPTER 5

APPLICATION OF ULTRAFINE GRAINED STEELS TO AUTOMOBILE BODY STRUCTURES

5.1 Introduction

In this chapter, performances of the fabricated UFG-FC (ultrafine grained ferrite-cementite) and UFG-MP (ultrafine grained multi-phase) steels as parts for automobile body structures are shown and discussed. Recently, high strength steels (HSS) are widely applied to automobile body structures [1, 2] in order to improve crash worthiness of body structures. By applying HSS to body frame parts, the crash worthiness of body structures has been improved without large weight increase. If the crash worthiness is improved furthermore by applying new HSS, the body weight could be decreased keeping the crash performance. Therefore in this chapter, the crash worthiness of the fabricated UFG steels in this study as body frame parts is focused. Generally, the parts in automobile body structures are categorized roughly into two groups having different functions. Figure 5.1 shows an example of automobile body structure for a sedan-type passenger car, indicating these groups. The first group contains the parts in passengers' cabin indicated in red. These parts deform little and protect the passengers from injury in car collisions, as seen in the picture for the flat-barrier frontal collision test [3] shown in Fig. 5.2. Recently ultra-high strength steels (UHSS, steels having tensile strengths higher than 1000 MPa) were developed [4, 5] and applied mainly to pillars and rails in the cabin. In addition, the "hot-stamping" [6] has been applied to several cars that require very high strength in such parts. As mentioned in Chapter 1, the hot-stamping is a new technology composed of stamping at high temperatures of austenite region and subsequent cooling in s stamping die, and it supplies very high strength, i. e. 1500 MPa. However, the productivity of hot-stamping is rather poorer than that in conventional stamping process at room temperature, due to its long processing period. Therefore, UHSS suitable for conventional stamping applications are still required because of the demands for high productivity.

The other group of the body parts includes the parts in crushable zones, i.e. front and rear frame sections which deform heavily in car collisions and absorb impact energy. They are indicated in blue in Fig. 5.1. The front and rear frames are usually designed as square or rectangular tubes, and are required to absorb impact energy by deforming along axial direction of the parts. Nowadays HSS having tensile strengths of 440 to 600 MPa are widely applied to the front and rear frames [7-9]. However, the HSS having TS higher than

600 MPa (practically 780, 980 and 1180 MPa class) have not been applied to front or rear frames.

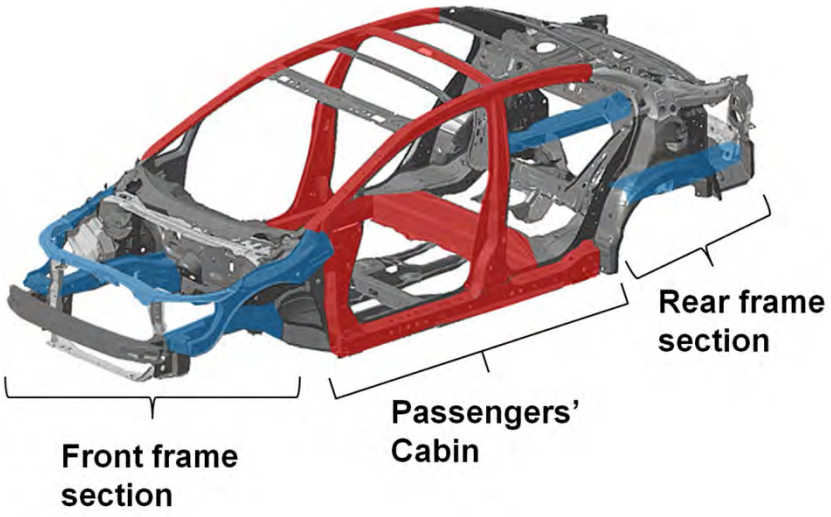

Figure 5.1 An example of automobile body structure for a sedan-type passenger car. The parts colored in blue are those in front and rear frame sections (crushable zones), and the parts colored in red are those in passengers' cabin.

Figure 5.2 A picture showing full-lap frontal collision test according to J-NCAP (Japan New Car Assessment Program) for a passenger car (1800cc class sedan) [1].

The factors which prevent expansion of application of UHSS are generally summarized as below.

(1) Poor elongation in UHSS which decreases the formability in stamping
(2) Poor spot-weldability due to high alloying elements
(3) Occurrence of fracture in car collisions due to poor "residual ductility" in UHSS after stamping process
(4) Occurrence of unstable deformation in axial collapse, which decreases energy absorption efficiency

The factors (1) and (2) are the subjects that have been generally concerned in the application of HSS. The factors (3) (4), which are focused in this study, are the problems which prevent

the UHSS to be applied to the crushable zones in body structures.

In this study, two types of UFG ferrite steels, the UFG-FC and UFG-MP steels, have been developed. In this chapter, the potential of the fabricated UFG steels to give solutions to such problems is discussed. First, it is shown that the UFG-FC steels have better crash worthiness than the conventional steels having the equivalent quasi-static strength, because of their high $\Delta\sigma$ (difference in flow stress between dynamic and quasi-static strain rates).

However, in the UFG-FC steels, obtained tensile strength (TS) was limited. For the parts which require very high strength (>980 MPa) such as those in the UHSS, the UFG-MP steels are suitable. In the attempt to apply the UHSS to the crushable zones, the factors (3) and (4) mentioned above are very important. In the second part of this chapter, it is shown that the UFG-MP steels contribute to solve such problems by improved elongation and work hardening rate. In addition, numerical simulations for dynamic deformation of body frame parts are carried out in order to clarify the effect of mechanical properties of materials on deformation behavior of the parts.

Of course, the high elongation and high work hardening rate in the UFG-MP steels are expected to improve formability in stamping processes. In addition, weldability, which is important in the manufacturing of automobile bodies, should be considered. In the final part of this section, as the other important properties besides crash worthiness, stamping and welding performances of the UFG-MP steels are shown.

5.2 Improvement of crash worthiness of hat columns by applying ultrafine grained ferrite-cementite steels

5.2.1 Introduction

In this section, improvement of energy absorption in the frame parts by applying the UFG-FC steels are shown and discussed. The key factor is the high difference in flow stress between dynamic and quasi-static strain rates, $\Delta\sigma$, of the UFG-FC steels. Generally in cases of car collisions, the material deforms at very high strain rates. For example, in dynamic axial collapse of a steel tube, the strain rates of the material reach to that higher than 10^2 s^{-1} [10, 11]. Therefore, dynamic deformation property of the material is important for those parts. As shown in Chapter 3, the UFG-FC steels, of which microstructures were composed of ultrafine ferrite and finely dispersed cementite, showed higher $\Delta\sigma$ than that of conventional HSS (high strength steels). Therefore, it is expected that the UFG-FC steels having high dynamic strength show good crash worthiness when applied to body frame parts. It means that the steels applied to the body part can be replaced by the UFG-FC steels having the same quasi-static strength and reduced thickness.

In this section, two UFG-FC steels having different ferrite grain sizes, and a fine-grained (FG) dual-phase (DP) steel having ferrite-martensite microstructure are fabricated from the same steel ingot. This is for evaluating the effect of the microstructure and ferrite grain size on crash worthiness clearly. For evaluating crash worthiness of materials, hollow tubes representing body frame parts are generally used in laboratory experiments [8, 12-15]. Various cross sections such as circle, square and rectangular are employed depending on the shapes of the considered parts. In this study, a hollow column so-called “hat column” is prepared using the fabricated UFG-FC and FG-DP steels, and the crash worthiness was evaluated through a “dynamic collapse test”. The obtained results are shown and discussed.

5.2.2 Fabrication of the materials

Three different microstructures fabricated using the same steel ingot were prepared. Table 5.1 summarizes the chemical composition of the steel. This Nb-added low-C steel is the same as the “UFG-FC2” steel shown in Table 2.5. In order to fabricate various microstructures from the same steel, two different fabricating routes and conditions were applied. Figure 5.3 shows schematic illustrations for two fabricating routes.

First, two UFG-FC steels having different ferrite grain sizes were fabricated. The route A was employed for fabricating two microstructures, named “UFG-FC-a” and “UFG-FC-b” steels. The ingots of the steel were hot-rolled to thicknesses of 10 or 6 mm at a FT (finishing temperature) of 900 °C in austenite region and immediately cooled to room temperature by water. The hot-rolled sheets were annealed at 1000 °C for 90 minutes and water-quenched to room temperature in order to form uniform martensite microstructure. Next, the sheets were again reheated to 770°C corresponding to intercritical region of ferrite and austenite for 90 minutes, and water-quenched to room temperature. Finally, the hot-rolled sheets showed fine duplex microstructure composed of ferrite and martensite, which were similar to that shown in Fig. 2.28. Table 5.2 summarizes fabricating route, thickness before CR and martensite volume fraction before CR. All the hot-rolled and heat-treated sheets contained about 50% of martensite. The hot-rolled and heat-treated sheets were mechanically grinded and then cold-rolled to a thickness of 1 mm using a four-high rolling mill with lubrication. Table 5.3 summarizes the conditions of CR and annealing. The CR reductions for the UFG-FC-a and UFG-FC-b steels were 88% and 80%, respectively. Higher reduction was applied for the UFG-FC-a steel in order to fabricate finer ferrite microstructure. Using a salt bath, the cold-rolled sheets were annealed at 575 °C for the UFG-FC-a steel, and 640 °C for the UFG-FC-b steel for 120 sec followed by water-cooling.

From the same ingot as the UFG-FC steels, a DP microstructure was also fabricated. It is called as “FG-DP” steel hereafter. The route B in Fig. 5.3 was applied to fabricate the FG-DP microstructure. An ingot was hot-rolled to a thickness of 10 mm at a FT of 770 °C in austenite region, air-cooled to 540 °C corresponding to intercritical region of ferrite and austenite and water-cooled to room temperature. A duplex microstructure composed of

relatively coarse ferrite and martensite, which was similar to the microstructure after hot-rolling of the UFG-FC1 steel shown in Fig. 2.2, was obtained. Fabricating conditions are summarized in Table 5.2 and Table 5.3. After mechanical grinding to a thickness of 8 mm, the hot-rolled sheets were cold-rolled at room temperature to a thickness of 1 mm. The CR reduction was 88 %. The cold-rolled sheets were annealed at 725 °C for 120 sec in a salt bath and then water-quenched to room temperature.

Microstructures of the fabricated specimens were observed by using scanning electron microscopy (SEM). All the specimens were observed from the transverse direction (TD) of the sheets. The specimens were etched with a 3% nital, and SEM observations were conducted on Hitachi S-4300E/N SEM operated at 15 kV. Mean grain sizes of ferrite and second phases were represented by the mean intersection lengths along ND and RD measured on the SEM micrographs, as described in the former sections.

Table 5.1 Chemical composition (mass%) of the UFG-FC steel used for dynamic collapse tests.

C	Si	Mn	P	S	Al	Nb	B	N
0.10	0.01	2.00	0.002	0.001	0.035	0.022	0.0015	0.0007

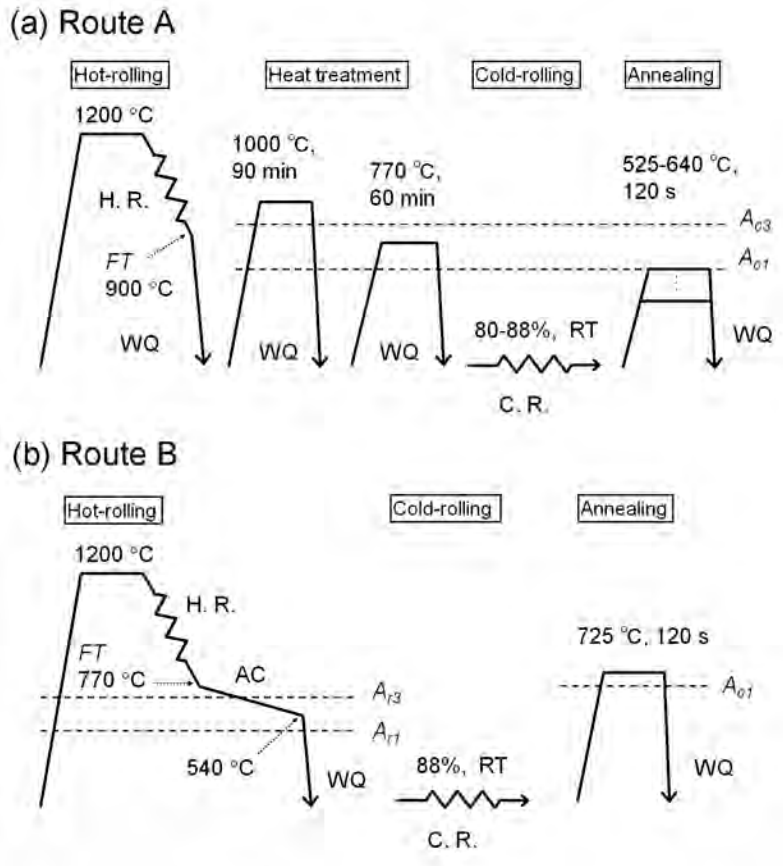

Figure 5.3 Schematic drawing of the processes for fabricating the UFG-FC and FG-DP steels for dynamic collapse tests. (a) Fabrication route A for the UFG-FC steels, and (b) route B for the FG-DP steel. A_{r1}, A_{r3}, A_{c1} and A_{c3} mean the transformation temperatures of the steel measured by dilatometer.

Table 5.2 Fabricating route, thickness and martensite volume fraction in hot-rolled sheet of the UFG-FC and FG-DP steels used for dynamic collapse tests.

Steel	Fabrication route	Thickness before CR (mm)	Martensite volume fraction before CR (%)
UFG-FC-a	A	8	49
UFG-FC-b	A	5	47
FG-DP	B	8	51

CR: cold-rolling

Table 5.3 Cold-rolling reduction and annealing conditions for the UFG-FC and FG-DP steel sheets used for dynamic collapse tests.

Steel	CR reduction (%)	Thickness after CR (mm)	Annealing condition
UFG-FC-a	88	1	575 °C for 120 s, WQ
UFG-FC-b	80	1	640 °C for 120 s, WQ
FG-DP	88	1	725 °C for 120 s, WQ

WQ: water-quenching, CR: cold-rolling

Table 5.4 Chemical compositions (mass%) of commercially available sheet steels used for dynamic collapse tests.

Steel	C	Si	Mn	P	S	Al	Ti	Nb	N	Others
FP400	0.093	0.02	1.26	0.012	0.005	0.032	-	-	-	
PP590	0.112	0.09	1.47	0.011	0.004	0.042	0.002	0.042	0.003	
DP590	0.087	0.79	1.77	0.009	0.002	0.026	-	-	-	
DP780	0.091	0.03	1.98	0.008	0.002	0.043	-	-	-	
DP980	0.157	0.51	2.44	0.009	0.002	0.03	-	-	0.004	
1180	0.151	0.51	2.64	0.007	0.001	0.032	-	-	-	

-: Not measured

Tensile tests were carried out in order to clarify tensile properties of the steels at dynamic strain rate as well as at quasi-static strain rate. The tensile specimens shown in Fig. 3.6 were prepared from each steel sheet. The tensile direction was parallel to the rolling direction (RD) of the fabricated sheets. Tensile tests were carried out by the use of the load-sensing block type test equipment described in section 3.2. Two or three specimens were tested at each strain rate between 10^{-2} and 10^{3} s^{-1}. From the obtained load-displacement curves, absorbed energy (AE) was calculated as the integrated area up to a displacement corresponding to a given strain on the curves.

For comparison, commercially available high strength steel (HSS) sheets were also

prepared. The chemical compositions of the prepared HSS are summarized in Table 5.4. The same steels as those in Chapter 3 were used, and the DP590 steel was additionally prepared in this chapter.

5.2.3 Dynamic axial collapse experiments

In order to evaluate crash worthiness of automobile body parts, dynamic collapse tests [8, 12-15] are widely applied. Also in this study, dynamic collapse tests were carried out using model parts. Figure 5.4 (a) shows the appearance of the specimen for dynamic collapse tests, named “hat column”. Figure 5.4 (b) shows the cross section of the specimen. The hat columns are composed of two parts made of the material for evaluation, the hat section part and the flat back plate. The hat section part, which was prepared by bending of the steel sheet by a corner radius of 5 mm, was set with a back plate and then spot-welded at the center of the flanges. In spot-welding, Cu electrodes having a diameter of 8 mm were used. The hat section part and back plate were clamped at the flange, and spot-welded. The welding conditions were: a force of 5 kN applied to the electrodes, a welding current of 10 kA, and a welding period of 0.6 sec. In order to minimize the effect of strength of spot-welds, relatively large weld-nuggets having diameters around 6 mm were formed by applying high welding current. The same material was used for the hat section part and back plate, and the pitch of spot-welding was 40 mm. The length of the hat column was 230 mm. The hat column was set vertically on a 5 mm thick steel plate and fixed by CO_2 arc-welding. Finally, another steel plate was fixed at the top end of the column also by arc-welding.

Figure 5.4 (c) shows a picture of the hat column with steel plates set on a dynamic collapse test equipment, describing the dynamic axial collapse test. A free-fall type collapse test machine was employed. A 110 kg weight was dropped from 11 m height, the column was hit by the weight at the top end. The experimental conditions are summarized in Table 5.5. Displacement of the weight was measured by a laser-type displacement sensor, and deformation load was measured by a load-cell set under the hat column. Two steel pipes were set beside the hat column in order to stop the falling weight at a collapse displacement of 160 mm. The deformation behavior was observed by high-speed camera with a frequency of 2000 frames a second.

In addition, for comparison with the dynamic collapse, quasi-static axial compression test was also carried out. The same hat columns as shown in Fig. 5.4 were used. Using a servo-hydraulic type compression equipment, the columns were deformed along the axial direction at a cross-head speed of 0.17 mms^{-1} to a displacement of 160 mm. The cross-head displacement and deformation load were measured. The AE of the column was calculated as the integrated area up to a given displacement on the load-displacement curves.

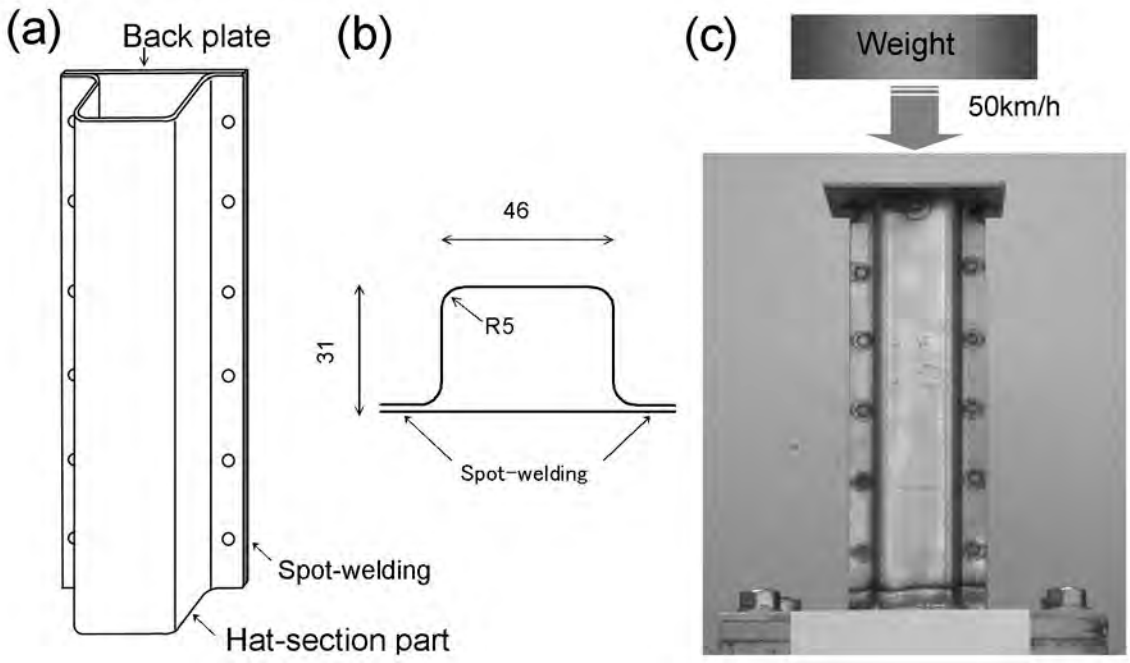

Figure 5.4 (a) Appearance of "hat column" used in dynamic axial collapse tests, (b) cross section of the hat column, and (c) a picture of the hat column with steel plates set on a dynamic collapse test equipment.

Table 5.5 Test conditions of dynamic collapse test.

Mass of weight (kg)	Initial height of weight (m)	Impact velocity (kmh^{-1})
190	11	52

5.2.4 Results and discussion

Figure 5.5 shows SEM microstructures of the fabricated UFG-FC-a, UFG-FC-b and FG-DP steels. The microstructure and mean ferrite grain size in the fabricated steels are summarized in Table 5.6. UFG ferrite microstructures including fine cementite particles were obtained in the UFG-FC steels, and the mean ferrite grain sizes were 0.39 μm in the UFG-FC-a and 0.86 μm in the UFG-FC-b steels. The ferrite grain size was changed significantly within sub-micrometer region. On the other hand, the FG-DP steel annealed at 725 °C showed fine ferrite-martensite microstructure. The ferrite grain size of the FG-DP steel was about 1.2 μm. The quasi-static mechanical properties at a strain rate of 10^{-2} s^{-1} of three steels are also summarized in Table 5.6. As the ferrite grain size decreased in the UFG-FC steels, the 0.2% offset stress significantly increased from 537 to 938 MPa. The two UFG-FC steels did not show uniform elongation. On the other hand, the FG-DP steel showed relatively low 0.2% offset stress and large uniform elongation,

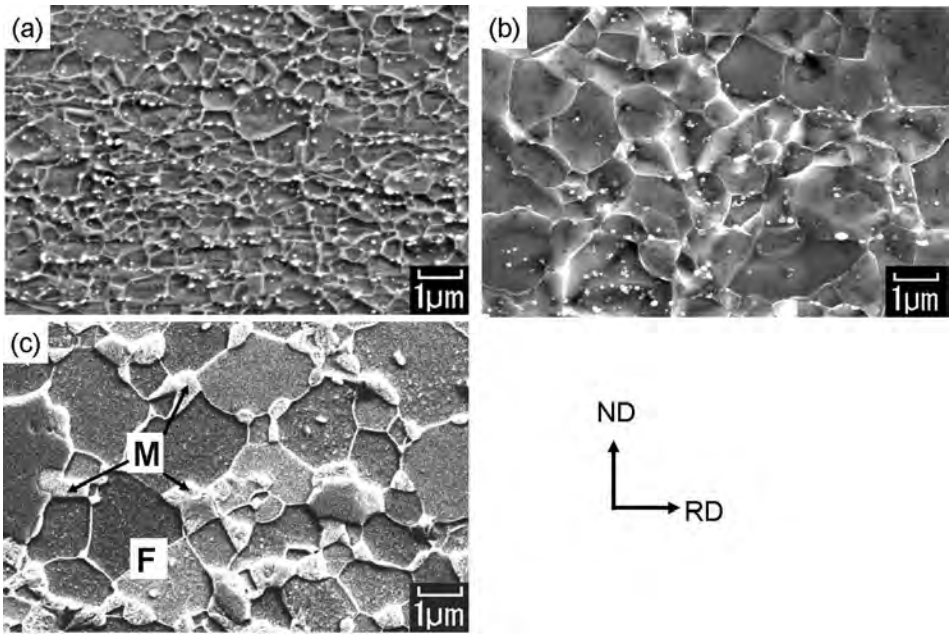

Figure 5.5 SEM microstructures of the steels used for dynamic collapse tests. (a) UFG-FC-a steel, (b) UFG-FC-b steel and (c) FG-DP steel. Observed from TD.

Table 5.6 Mean ferrite grain size and mechanical properties at quasi-static strain rate (10^{-2} s^{-1}) of the UFG-FC and FG-DP steels used for dynamic collapse tests. They had the same chemical composition and were fabricated under various conditions.

Steel	Micro-structure	Mean ferrite grain size (μm)	0.2% offset stress (MPa)	Tensile strength (MPa)	Uniform elongation (%)	Total elongation (%)
UFG-FC-a	F-C	0.39	938	940	0.7	12.4
UFG-FC-b	F-C	0.86	537	540	0.5	31.2
FG-DP	F-M	1.17	551	916	9.8	23.6

F: ferrite, C: cementite, M: martensite

Figure 5.6 shows nominal stress-strain (s-s) curves of three steels at various strain rates ranging from 10^{-2} s^{-1} to 10^{3} s^{-1}. The UFG-FC-a and UFG-FC-b steels showed yield drop phenomenon, while it was not observed in the FG-DP steel. The FG-DP steel showed work hardening after yielding, resulting in large uniform elongation as was summarized in Table 5.6. When the strain rate increased, the flow stress significantly increased in the UFG-FC-a and UFG-FC-b steels. On the other hand, the flow stress in the FG-DP steel did not increase so much as the strain rate increased. Table 5.7 summarizes the difference in flow stress as described in section 3.3, $\Delta\sigma$, of three steels. It is shown that the UFG-FC steels had significantly higher $\Delta\sigma$ than the FG-DP steel. These results were the same as that shown in the dynamic tensile tests of the UFG-FC steel shown in section 3.3 and 3.4. Table 5.8 summarizes microstructural parameters and quasi-static mechanical properties of the commercial HSS used for comparison. The TS varied from 420 to 1200 MPa.

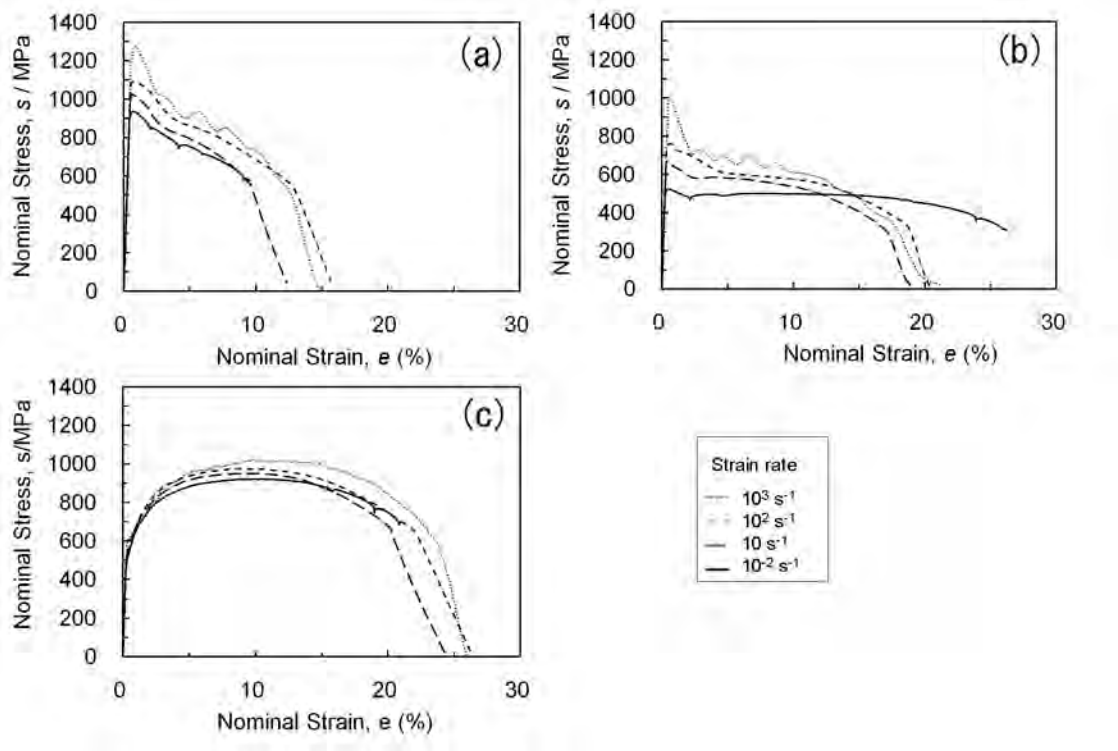

Figure 5.6 Nominal stress-strain curves of the steels used for dynamic collapse tests. (a) UFG-FC-a, (b) UFG-FC-b, and (c) FG-DP steels. Strain rate was varied from 10^{-2} s^{-1} to 10^{3} s^{-1}.

Table 5.7 Difference in 5% flow stress between dynamic and quasi-static strain rates, $\Delta\sigma$, of the UFG-FC and FG-DP steels used for dynamic collapse tests. They had the same chemical composition and were fabricated under various conditions.

Steel	Difference in 5% flow stress, $\Delta\sigma$ (MPa)
UFG-FC-a	165
UFG-FC-b	169
FG-DP	85

Table 5.8 Microstructures and mechanical properties of the commercial steels used for the dynamic tensile tests. Measurement was done using the small tensile specimen shown in Fig. 3.6 of which tensile direction was parallel to RD.

Steel	Micro-structure	Volume fraction of second phase (%)	Thickness (mm)	0.2% offset stress (MPa)	Tensile strength (MPa)	Total elongation (%)
FP400	F-P	8	1.0	284	421	38.2
PP590	F	-	1.0	468	578	30.2
DP590	F-M	11	1.0	459	637	34.2
DP780	F-M	15	1.0	457	785	28.4
DP980	F-M	61	1.0	807	1066	19.0
1180	M(-F)	99	1.2	1030	1206	19.0

F: Ferrite, P: Pearlite, M: Martensite

Next, the result of dynamic collapse tests are shown and discussed. Figure 5.7 shows the appearance of the hat columns made of three steels after the dynamic axial collapse tests. The columns exhibited continuous progression of folds in the axial deformation. This shape is so-called “compact-mode” [16,17]. No fracture was observed in all the steels. It is noteworthy that even in the column of the UFG-FC-a steel having only 12% of total elongation in tensile test, no fracture occurred. This seems to be due to the fact that the column was deformed in the uniform compact mode. The deformation mode in the axial collapse and its effect on crash worthiness is described in detail in next section.

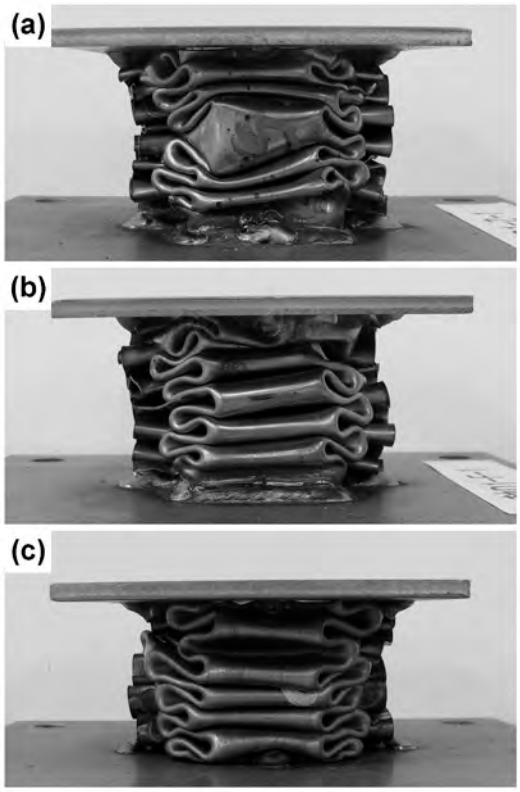

Figure 5.7 Appearance of the hat columns showing continuous progression of folds after dynamic collapse tests. (a) UFG-FC-a steel, (b) UFG-FC-b steel and (c) FG-DP steel.

Load-displacement curves and AE-displacement curves are shown and discussed. First, the curves in quasi-static compression tests of hat columns made of the UFG-FC-a steel and the FG-DP steel are shown in Figure 5.8. Table 5.9 summarizes the peak load, average load during the deformation and AE in quasi-static compression tests for the UFG-FC-a and FG-DP steels. The average load and AE during the quasi-static compression were slightly higher in the UFG-FC-a steel than that in the FG-DP steel. Next, the load-displacement curves and AE-displacement curves in dynamic collapse tests are shown in Figure 5.9. The load and AE data of the UFG-FC-a and FG-DP steels are summarized in Table 5.12. In addition, the data of the UFG-FC-b steel having lower strength are summarized. In the dynamic axial collapse, the load and AE of the UFG-FC-a steel were significantly higher than those in the FG-DP steel. The better crash worthiness of the UFG-FC-a steel seemed to be brought by its high dynamic strength.

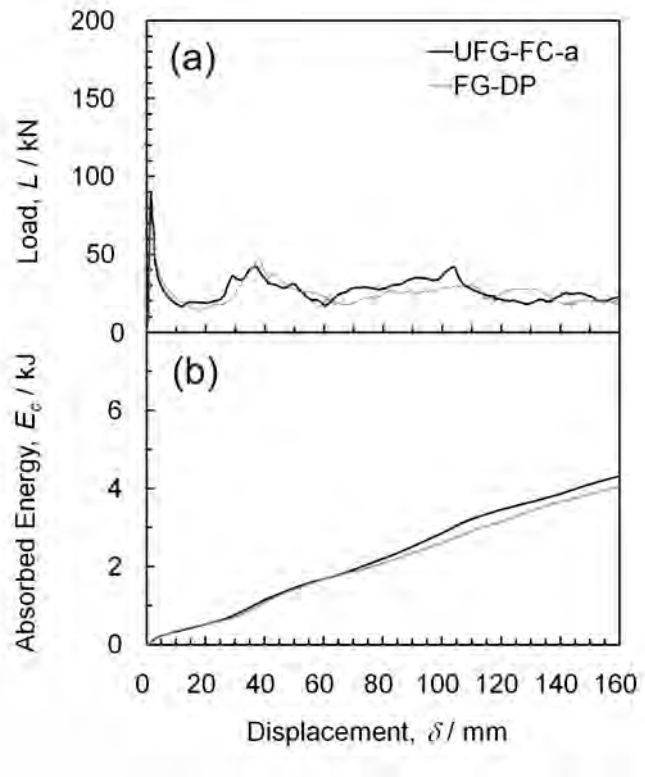

Figure 5.8 (a) Load-displacement curves and (b) absorbed energy-displacement curves in quasi-static axial compression of the hat columns made of the UFG-FC-a steel and the FG-DP steel.

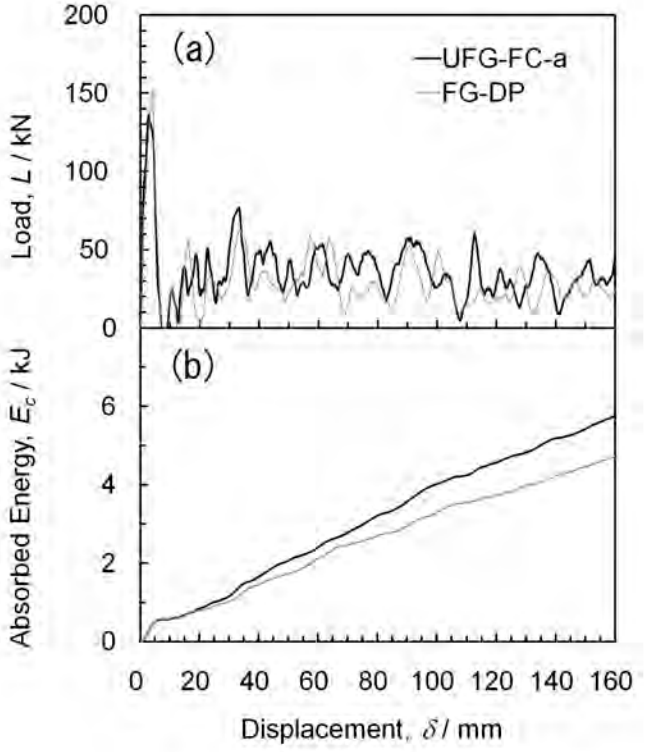

Figure 5.9 (a) Load-displacement curves and (b) absorbed energy-displacement curves in dynamic collapse of the hat columns made of the UFG-FC-a steel and the FG-DP steel.

Table 5.9 Maximum load, average load and absorbed energy obtained in quasi-static compression tests of the UFG-FC-a and FG-DP steels.

Steel	Maximum load (kN)	Average load (10-150 mm) (kN)	Absorbed Energy, E_c (0-150 mm) (kJ)
UFG-FC-a	89	26.8	4.11
FG-DP	72	24.9	3.85

Table 5.10 Maximum load, average load and absorbed energy obtained in dynamic collapse tests of the UFG-FC and FG-DP steels.

Steel	Maximum load (kN)	Average load (10-150 mm) (kN)	Absorbed Energy, E_c (0-150 mm) (kJ)
UFG-FC-a	136	35.6	5.43
UFG-FC-b	119	27.1	4.18
FG-DP	145	30.0	4.72

It is thought that AE of hat columns strongly depends on the strength of the materials in tensile tests at small strain. Takahashi et al. [18] showed that the absorbed energy of hat columns depended on the mean flow stress between 3 and 10% of nominal strain in dynamic tensile tests. Sato et al. [12] showed using numerical simulation for axial collapse of hat column that the strain in the deformed region of the column was only 5-9% when the deformation load reached the maximum. According to these results, the difference in the dynamic AE of the columns having different microstructures in this study can be discussed in terms of the tensile flow stress at small strain. However the shape of the s-s curves at small strain was significantly different between the UFG-FC steels and FG-DP steel, therefore the flow stress value at a certain strain did not give a good correlation with AE of the columns. The AE of the tensile specimens in tensile tests, representing the amount of plastic work of the materials, seems to be more reasonable for evaluating AE of the hat columns. Fist, AE up to 7% strain (E_t) of the UFG-FC-a, UFG-FC-b and FG-DP steels, obtained in the quasi-static and dynamic tensile tests are plotted as a function of strain rate in Fig. 5.10. The E_t was calculated as the area of load-displacement curves up to the displacement corresponding to a nominal strain of 0.07, divided by the volume of gauge section. It is clearly shown in Fig. 5.10 that the strain rate dependence of AE of the UFG-FC steels is higher than that of the FG-DP steel. At a strain rate of 10^3 s^{-1}, the E_t value of the UFG-FC-a steel was higher than that of the FG-DP steel, although their E_t values were almost the same at 10^{-2} s^{-1}. From this result, it is expected that the UFG-FC-a steel has high AE in dynamic axial collapse of the columns.

Figure 5.11 shows the relationship between AE of the hat columns evaluated by dynamic axial collapse, E_c, and E_t of the fabricated steels. Data of commercial DP590 and DP780 steels, obtained in the same dynamic collapse tests are additionally plotted. The data

of the FG-DP steel and conventional DP steels are indicated as “DP”. Figure 5.11 (a) shows the E_c as a function of E_t evaluated by quasi-static tensile tests, E_{ts}. The E_c of the UFG-FC steels are significantly higher than those of the conventional DP steels. It means that the E_c could not be decided by the E_{ts}. Figure 5.11 (b) shows the E_c as a function of E_t evaluated by dynamic tensile tests, E_{td}. The E_c had good correlation with the E_{td}. This result is reasonable because the strain rates of the materials both in dynamic collapse of the columns and dynamic tensile test were in the same order. It was confirmed in the data analysis that the AE in dynamic tensile test gave a good correlation with the AE of the column evaluated by the dynamic collapse test. Consequently, it was clarified that the UFG-FC steels have higher AE evaluated by the dynamic collapse than conventional HSS having the equivalent quasi-static strength, due to the high $\Delta\sigma$ of the UFG-FC steels.

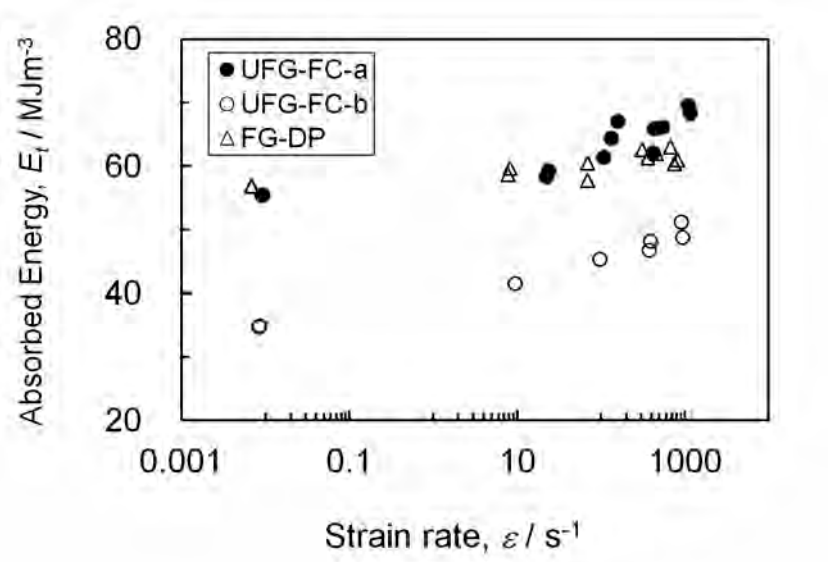

Figure 5.10 Relationship between absorbed energy up to a nominal strain of 7%, E_t, and strain rate in tensile tests of the UFG-FC and FG-DP steels. The steels had different microstructures while the same chemical composition.

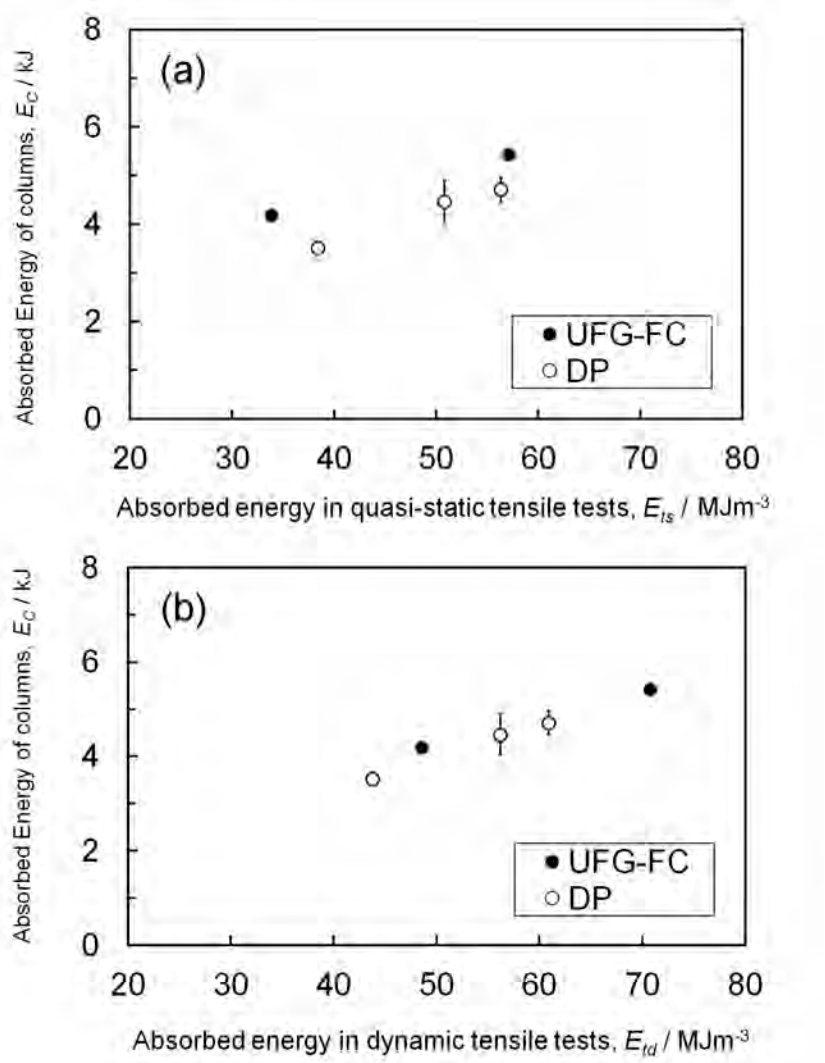

Figure 5.11 Relationship between absorbed energy of hat columns evaluated by dynamic axial collapse tests, E_c, and absorbed energy evaluated by (a) quasi-static tensile tests at a strain rate of 10^{-2} s^{-1} and (b) dynamic tensile tests at a strain rate of 10^{3} s^{-1}.

5.2.5 Summary

In this section, dynamic collapse experiments using hat columns were carried out in order to evaluate crash worthiness of the UFG-FC steels. Three microstructures, UFG-FC-a steel having ferrite grain size of 0.39 μm, UFG-FC-b steel having ferrite grain size of 0.86 μm, and FG-DP steel, were fabricated in the same steel and evaluated. The obtained results are summarized below.

(1) The hat columns made of the UFG-FC steels deformed in “compact-mode” showing continuous progressive folds in axial collapse, and did not show any fractures.

(2) The absorbed energy in the dynamic collapse of the UFG-FC steels was higher than that of the conventional high strength steels having the equivalent quasi-static strength.

(3) It was revealed that the absorbed energy of the hat columns evaluated by dynamic axial

collapse had good correlation with the absorbed energy evaluated by dynamic tensile test.

(4) It was shown that the columns made of the UFG-FC steels had high absorbed energy because of its high $\Delta\sigma$ (difference in flow stress between dynamic and quasi-static strain rates). Therefore, the UFG-FC steels are expected to improve the crash worthiness of automobile body frame parts, and contribute to further weight reduction of automobile body structures.

5.3 Improvement of crash worthiness of hat columns by applying ultrafine grained multi-phase steels

5.3.1 Introduction

In this section, improvement of energy absorption by controlling deformation shapes in axial collapse is shown and discussed. This technology is targeted to the parts that require very high strength such as that in UHSS, i.e., higher than 980 MPa. Up to now, the improvement of automobile steels has been discussed in terms of formability in stamping. However, as mentioned in the introduction of this chapter, other features must be preferentially considered if UHSS are applied to the parts in the crushable zones, aiming for further weight reduction. The one is the occurrence of fracture in car collisions due to poor "residual ductility" in UHSS after stamping process. The other is the occurrence of unstable deformation in axial collapse, which decreases the efficiency of energy absorption. When UHSS are applied to the crushable parts, their deformation mode tends to become unstable. The ideal deformation shape in axial collapse for impact energy absorption is a stable deformation through the formation of a series of continuous folds like accordion, which is called as "compact section" [16] or "compact-behavior" [17]. The examples of the deformation shapes have been shown in Fig. 1.10 in Chapter 1. On the other hand, "Non-compact" [16, 17] means an unstable deformation through the formation of a series of folds separated by remaining straight regions in the column walls. Sometimes falling down of the column or fracture in the hat wall occurs when the column deforms in "non-compact" mode. The change in deformation mode from compact to non-compact, which reduces the efficiency of energy absorption, is thought to be caused by the decreased work hardening rate of the material highly strengthened [19]. Commercially available UHSS generally have low work hardening rate (*n*-value) [9]. Uenishi et al. [19] showed by using FEM simulation that the desirable "compact-mode" deformation of hat columns in axial collapse could be promoted by improving work hardening rate of the material. However, this concept has not been confirmed yet, because such UHSS having high work hardening rate have not been obtained yet.

The UFG-MP steels fabricated in this study showed improved uniform elongation

as well as high TS. Due to the improved work hardening rate by introducing hard second phases to the UFG ferrite microstructures, the UFG-MP steels showed better strength-ductility balance than conventional UHSS. It seems that the improved work hardening rate contributes to the improvement of deformation shape during the axial collapse. In this chapter, results of dynamic collapse tests using hat columns made of the UFG-MP steels are introduced. The improvement of deformation shape in axial collapse is shown and discussed.

5.3.2 Fabrication of the materials

The chemical compositions of the UFG-MP steels used for dynamic collapse tests in this section are listed in Table 5.11. The UFG-MP2 and UFG-MP3 steels are the same steels as those shown in section 4.3. The UFG-MP4 steel is a high-Si version (1.4 mass%) of the UFG-MP2 steel, while the UFG-MP5 steel is a high-Mn version (5 mass%) of the UFG-MP2 steel.

Table 5.11 Chemical compositions of the UFG-MP steels (mass%) used for axial collapse tests.

Steel	C	Si	Mn	P	S	Al	Nb	N
UFG-MP2	0.155	0.50	4.0	0.001	0.001	0.021	0.054	0.0022
UFG-MP3	0.202	0.02	3.0	0.002	0.001	0.020	0.049	0.0015
UFG-MP4	0.150	1.42	4.0	0.001	0.001	0.026	0.054	0.0021
UFG-MP5	0.149	0.47	4.9	0.002	0.002	0.015	0.055	0.0023

Figure 5.12 shows a schematic drawing of the fabricating process, and Table 5.12 summarizes the fabricating conditions of the various UFG-MP steels for dynamic collapse tests. Two or three variations of specimens were fabricated from the UFG-MP2, UFG-MP3 and UFG-MP4 steels by applying different fabricating conditions. The ingots of the steels prepared by vacuum-melting were hot-rolled to thicknesses of 5 to 6 mm at various FT in austenite region. The cooling condition after hot-rolling was chosen from three patterns. The one is air-cooling to room temperature, which was applied to the UFG-MP2-a, UFG-MP4-a, UFG-MP4-b, and UFG-MP5 steels. The second is water-cooling to room temperature after air-cooling to 460 °C, which corresponds to two-phase region of ferrite and austenite. This pattern was applied to the UFG-MP3 steel. The third pattern consisted of air-cooling to 550 °C, keeping at 550 °C for 1h in an electric furnace and cooling to room temperature in the furnace. This pattern was applied to the UFG-MP2-b and UFG-MP2-c steels, in order to simulate the coiling procedure in actual hot-rolling process. Basically, all the hot-rolled sheets showed complex microstructures composed of ferrite and hard phases.

The hot-rolled sheets having thicknesses of 5 or 6 mm were mechanically grinded to 3.5 or 5 mm, respectively. Then, the hot-rolled sheets were warm-rolled or cold-rolled.

Warm-rolling (WR) is the following process. The hot-rolled sheets are reheated at 500 °C for 1 hour in order to reduce the hardness, and rolled to the aiming thickness without additional reheating. The purpose of WR is to reduce the hardness of the hot-rolled sheet and to reduce the load in rolling of the hot-rolled sheet. The WR was applied to the UFG-MP2-a, UFG-MP4-a and UFG-MP4-b steels. CR with lubrication at room temperature was applied to the UFG-MP2-b, UFG-MP2-c, UFG-MP3 and UFG-MP5 steels. The final thickness and the rolling reduction in WR and CR are summarized in Table 5.12. The sheets after WR/CR were annealed at various temperatures between 685 and 700 °C corresponding to intercritical regions of ferrite and austenite. The conditions after intercritical annealing for each steel was chosen from three patterns, air-cooling to room temperature (AC), water-cooling to room temperature (WQ), and subsequent annealing at 400 °C for 300 sec (over-aging: OA). The purpose of this OA treatment was to accelerate partitioning of C atoms into non-transformed austenite, and to retain large amount of austenite at room temperature. Two salt baths of which temperatures were set at each intercritical temperature and OA temperature (400 °C) were used. After the annealing at intercritical region for 120 s, the sheets were moved to another bath for OA treatment, kept for 300 s and then air-cooled to room temperature.

Microstructures of the fabricated specimens were observed by using scanning electron microscopy (SEM). All specimens were observed from the transverse direction (TD) of the sheets. The specimens were etched with a 3% nital, and the SEM observations were conducted on Hitachi S-4300E/N SEM operated at 15 kV.

Tensile tests were carried out in order to clarify the tensile properties of the steels at high strain rate as well as at quasi-static strain rate. The tensile specimens shown in Fig. 3.6 were prepared from each steel sheet. The tensile direction was parallel to RD of the fabricated sheets. Tensile tests were carried out by the use of the load-sensing block type test equipment described in section 3.2. At strain rates of 10^{-2} and 10^{3} s^{-1}, two or three specimens were tested. From the obtained load-displacement curves, absorbed energy (AE) was calculated as the integrated area up to a displacement corresponding to a given strain on the curves.

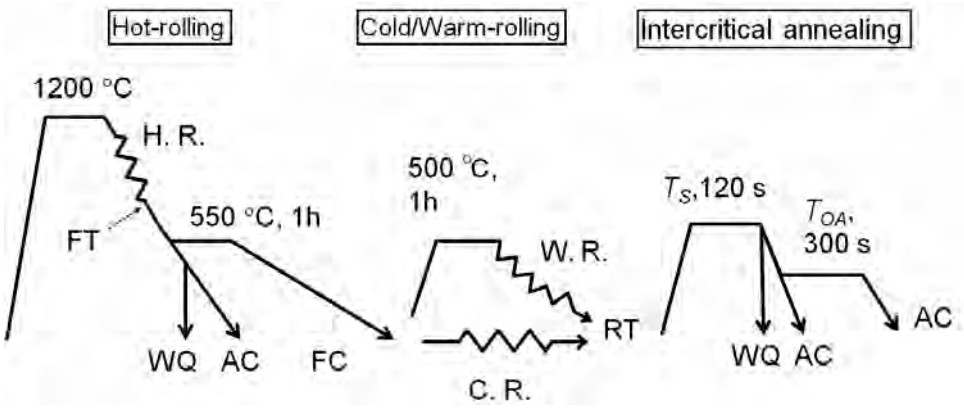

Figure 5.12 Schematic drawing of the process for fabricating the UFG-MP steels for dynamic collapse tests.

Table 5.12 Fabricating conditions of the UFG-MP steels used for dynamic collapse tests.

Steel	FT (°C)	Cooling after HR	CR/ WR	t (mm)	R (%)	T_S (°C)	T_{OA} (°C)
UFG-MP2-a	860	AC	WR	1.2	66	685	400
UFG-MP2-b	770	FC from 550 °C	CR	1.2	66	690	400
UFG-MP2-c	850	FC from 550 °C	CR	1.2	66	690	400
UFG-MP3	770	WQ from 460 °C	CR	1.0	71	700	(AC)
UFG-MP4-a	840	AC	WR	1.2	66	685	400
UFG-MP4-b	850	AC	WR	1.2	66	690	400
UFG-MP5	770	AC	CR	1.0	80	675	(WQ)

FT: Finishing temperature in hot-rolling,

HR: Hot-rolling, CR: cold-rolling, WR: warm-rolling,

AC: Air-cooling, FC: Furnace-cooling, WQ: Water-cooling,

t: Thickness after cold/warm-rolling, R: Reduction in cold/warm-rolling,

T_S: intercritical annealing temperature, T_{OA}: over-aging temperature

5.3.3 Dynamic axial collapse experiments

The hat columns shown in Fig. 5.4 were prepared using the UFG-MP steels listed in Table 5.12. The hat section part and back plate were welded at a force of 5kN applied to the electrodes. The welding current and period were optimized for each material. Two or three columns were prepared for each steel, and they were dynamically deformed in axial collapse. The the conditions of dynamic axial collapse tests have been described in section 5.2.3. In the data analysis, some data showing irregularities, such as fracture at the interface between the arc-welding beads and the lower plate, were removed.

5.3.4 Experimental results

Figure 5.13 shows typical SEM microstructures of the fabricated UFG-MP steels. The UMP2-a, UFG-MP3, UFG-MP4-a and UFG-MP5 steels are shown. All the specimens in Fig. 5.13 showed complex microstructures composed of sub-micrometer ferrite matrix and second phases. Table 5.13 summarizes quasi-static mechanical properties of all the fabricated UFG-MP steels. TS varied from 990 to 1350 MPa. Here, the n-values, which represent work hardening rate of the steels, were calculated applying the equations (4.5) and (4.6). In the calculation of n-values, the plastic tensile strains (true strain) of 0.05 and 0.1 were chosen. The UFG-MP steels had fairly higher n-values than the conventional HSS (see Fig. 4.45).

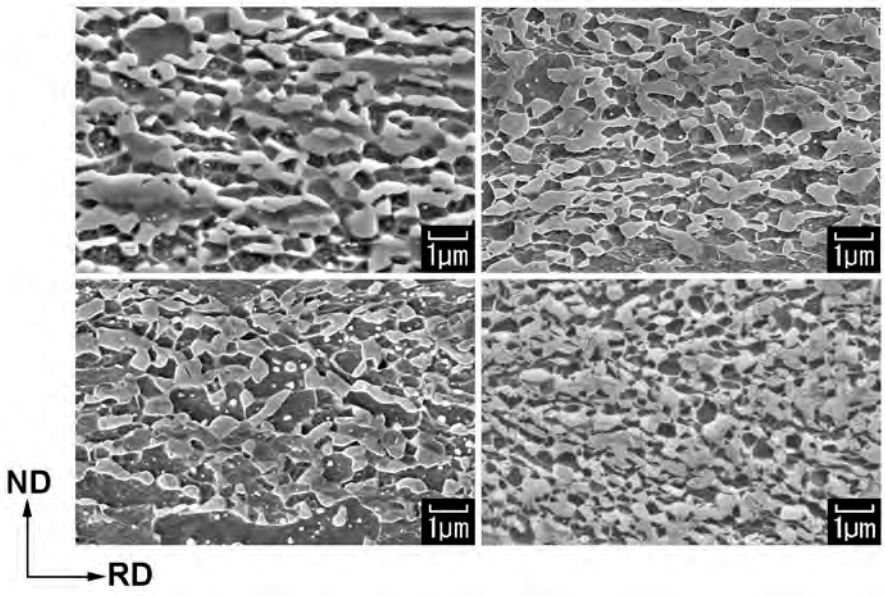

Figure 5.13 Typical SEM microstructures of the UFG-MP steels used for dynamic collapse tests. (a) UFG-MP2-a steel, (b) UFG-MP3 steel, (c) UFG-MP4-a steel and (d) UFG-MP5 steel. Observed from TD.

Table 5.13 Mechanical properties at quasi-static strain rate (10^{-2} s^{-1}) of the UFG-MP steels used for dynamic axial collapse tests. Small tensile specimen shown in Fig. 3.6 was used.

Steel	0.2% offset stress (MPa)	Tensile strength (MPa)	Uniform elongation (%)	n-value at 5-10%
UFG-MP2-a	1022	1253	12	0.259
UFG-MP2-b	911	1010	18	0.160
UFG-MP2-c	913	1227	13	0.296
UFG-MP3	607	991	14	0.296
UFG-MP4-a	978	1133	14	0.226
UFG-MP4-b	800	1001	16	0.239
UFG-MP5	1044	1345	10	0.156

Next, typical s-s curves of the UFG-MP steels are shown. Figure 5.14 shows nominal s-s curves of the UFG-MP4-a and UFG-MP3 steels at a strain rate of 10^{-2} s^{-1}. The microstructures of these steels have been shown in Fig. 5.13 (b, c), and dynamic collapse behaviors of these steels are described in detail later. For comparison, s-s curve of the conventional DP980 steel is also shown in Fig. 5.14. Significant work hardening at tensile strains up to 10% was confirmed in the UFG-MP steels. Figure 5.15 shows dynamic s-s curves of the same steels at a strain rate of 10^{3} s^{-1}. The oscillations seen in the s-s curves were caused by the impact wave generated during dynamic tensile test, and do not reflect the nature of deformation behaviors of the materials. The UFG-MP steels kept high work hardening rate at high strain rate, which is in contrast to the DP980 steel.

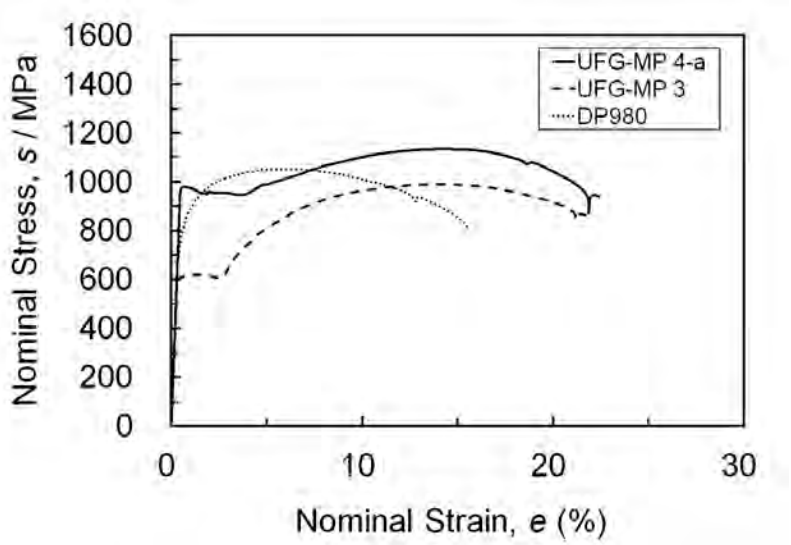

Figure 5.14 Nominal stress-strain curves at a strain rate of 10^{-2} s^{-1} of the UFG-MP4-a steel and UFG-MP3 steel, as well as the DP980 steel for comparison. Small tensile specimen shown in Fig. 3.6 was used.

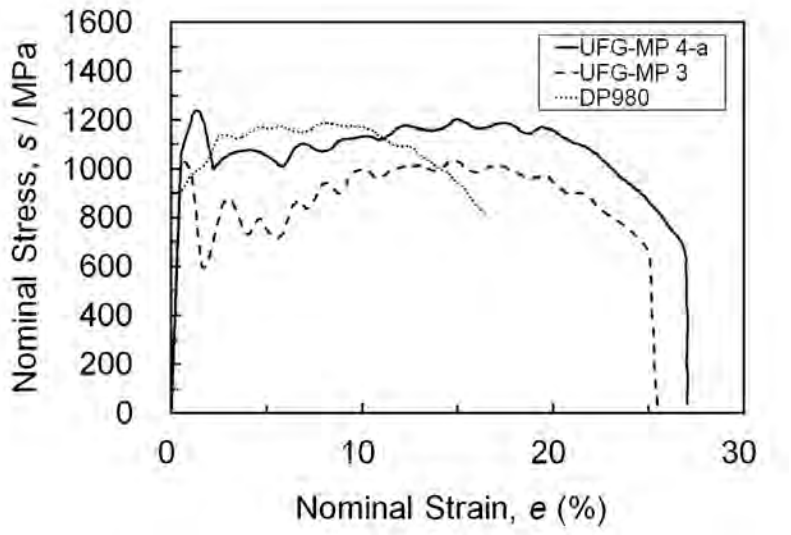

Figure 5.15 Nominal stress-strain curves at a strain rate of 10^{3} s^{-1} of the UFG-MP4-a steel and UFG-MP3 steel, as well as the DP980 steel for comparison. Small tensile specimen shown in Fig. 3.6 was used.

Next, the result of dynamic collapse tests are shown and discussed. Figure 5.16 shows the appearance of the hat columns having a thickness of 1.2 mm that were made by the UFG-MP4-a and DP980 steels. The UFG-MP4-a column showed “compact-mode” deformation (Fig. 5.16 (a, b)) [16, 17] with a series of continuous folds like accordion. This is an ideal deformation shape for optimizing the efficiency of impact energy absorption in axial collapse. For the DP980 steel, two examples showing different features are shown. Fig. 5.16 (c, d) shows a typical “non-compact” deformation shape with remaining straight regions accompanied with falling down of the column. Some folds near the top end of the

column were also observed. Actually, the fracture in the hat part was simultaneously observed in this column. The other column shown in Fig. 5.16 (e, f) had also a remaining straight regions and showed falling down of the column, but the fractures at the hat wall and spot-welds were more significant. The column shown in Fig. 5.16 (c, d) is categorized to "non-compact mode". However, such column with significant fracture as shown in Fig. 5.16 (e, f) is called as "fracture mode" or "deformation with fracture" hereafter.

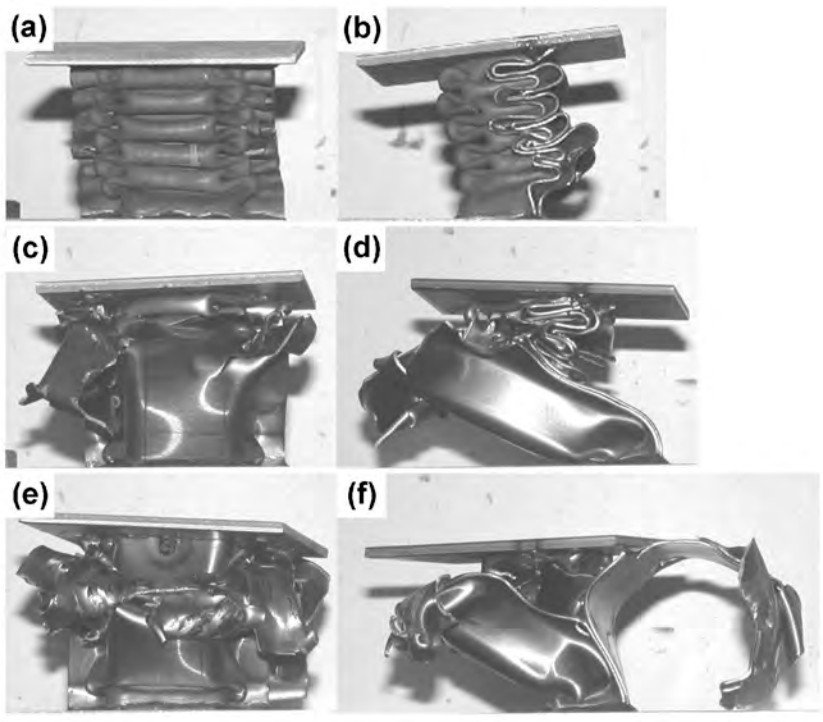

Figure 5.16 Appearances of the hat columns with a thickness of 1.2 mm showing various deformation shapes after dynamic collapse tests. (a, b) The UFG-MP4-a steel deformed in compact-mode, (c, d) DP980 column deformed in non-compact mode, (e, f) Another DP980 column showing significant fracture in both hat part and back plate. The pictures (a, c, e) were taken from the front of the columns and (b, d, f) from the right hand side of the columns.

Figure 5.17 shows images captured from high-speed movies during collapse progression for three columns shown in Fig. 5.16. The images at displacements (deformation lengths) between 40 and 140 mm are shown. Figure 5.17 (a, b) clearly shows continuous formation of folds with no fracture in the UFG-MP4-a steel. In the column made of the DP980 steel shown in Fig. 5.17 (c, d), compact folds formed at early stage of the collapse. However new folds did not form at 80 mm displacement, and a straight region remained resulting in falling down of the column after the displacement of 100 mm. In another DP980 column shown in Fig. 5.17 (e, f), the fracture near the top end of hat part occurred at 60 mm, and falling down of the column occurred at 100 mm.

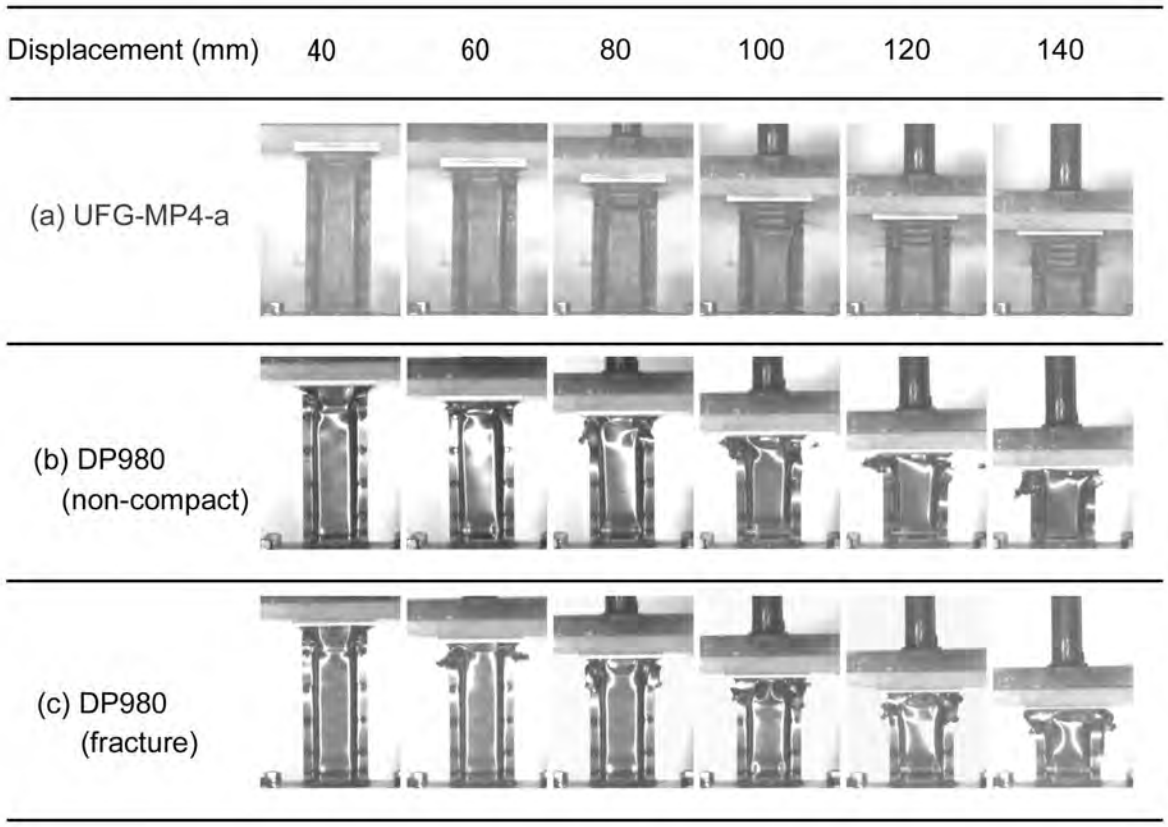

Figure 5.17 Captured images of the movies during collapse progression in the columns made of (a) UFG-MP4-a column deformed in compact-mode, (b) The DP980 column deformed in non-compact mode with fracture. (c) Another DP980 column showing significant fracture in both hat part and back plate. The appearances of three columns after the collapse tests are shown in Fig. 5. 16.

The features in deformation shapes clearly affected the deformation load and AE. Figure 5.18 (a) shows load-displacement curves, and Figure 5.18 (b) shows AE-displacement curves of three hat columns made of the UFG-MP4-a, and DP980 steels deformed in different modes. The appearances of these hat columns are shown in Fig. 5.16 and Fig. 5.17. The UFG-MP4-a steel showed the ideal axial deformation behavior for energy absorption without significant load drop and with continuous increase in AE up to high displacement. In the UFG-MP4-a column and the DP980 column deformed in non-compact mode, the deformation loads and AE were almost the same up to the displacement of 100 mm. However, in the DP980 column (non-compact), deformation load dropped after 100 mm displacement resulting in a saturation in AE after displacement about 100 mm. This is because of the occurrence of falling down of the column at 100 mm, as shown in Fig. 5.17 (b). It means that falling down of column requires smaller load than that in continuous fold formation. In other words, when falling down of column occurs, the efficiency in energy absorption by the column decreases. In the DP980 column deformed with fracture, slight drop in deformation load was observed at about 50 to 60 mm displacements (Fig. 5.18 (a)). This load drop corresponded to the occurrence of fracture at the hat section part, which was observed at displacement of 60 mm (Fig. 5.17 (c)). It was

also indicated that fracture at the hat section decreased deformation load. Therefore, the AE of the DP980 column (fracture) saturated once at 50 to 60 mm and increased again due to progression of deformation at another places.

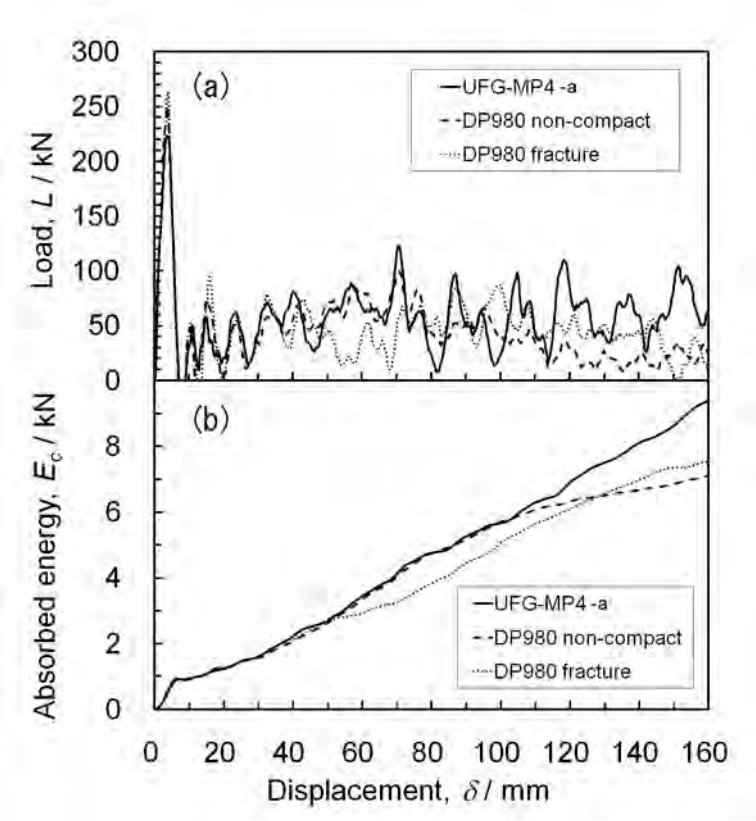

Figure 5.18 (a) Load-displacement curves and (b) absorbed energy-displacement curves of the hat columns made of the UFG-MP4-a steel deformed in compact-mode, and two DP980 columns deformed in different modes in dynamic collapse-compression tests. The appearances of the three hat columns are shown in Fig. 5.16.

Table 5.14 summarizes the maximum load, average load at a displacement range between 10 mm and 150 mm, and AE up to a displacement of 150 mm, of three columns shown in Fig. 5.16 and Fig. 5.17. The maximum load in the UFG-MP4-a column was slightly smaller than the other columns. On the other hand, the average load and AE of the UFG-MP4-a steel were the highest among three columns, due to the ideal compact-mode deformation.

Table 5.14 Maximum load, average load and absorbed energy of the columns made of UFG-MP4-a and DP980 steels having different deformation configurations in dynamic collapse tests. The thickness of the columns was 1.2 mm.

Steel	Maximum load (kN)	Average load (10-150 mm) (kN)	Absorbed Energy (0-150 mm) (kJ)
UFG-MP4-a	230	59.3	8.50
DP980 (non-compact)	250	42.0	6.86
DP980 (fracture)	264	45.9	7.36

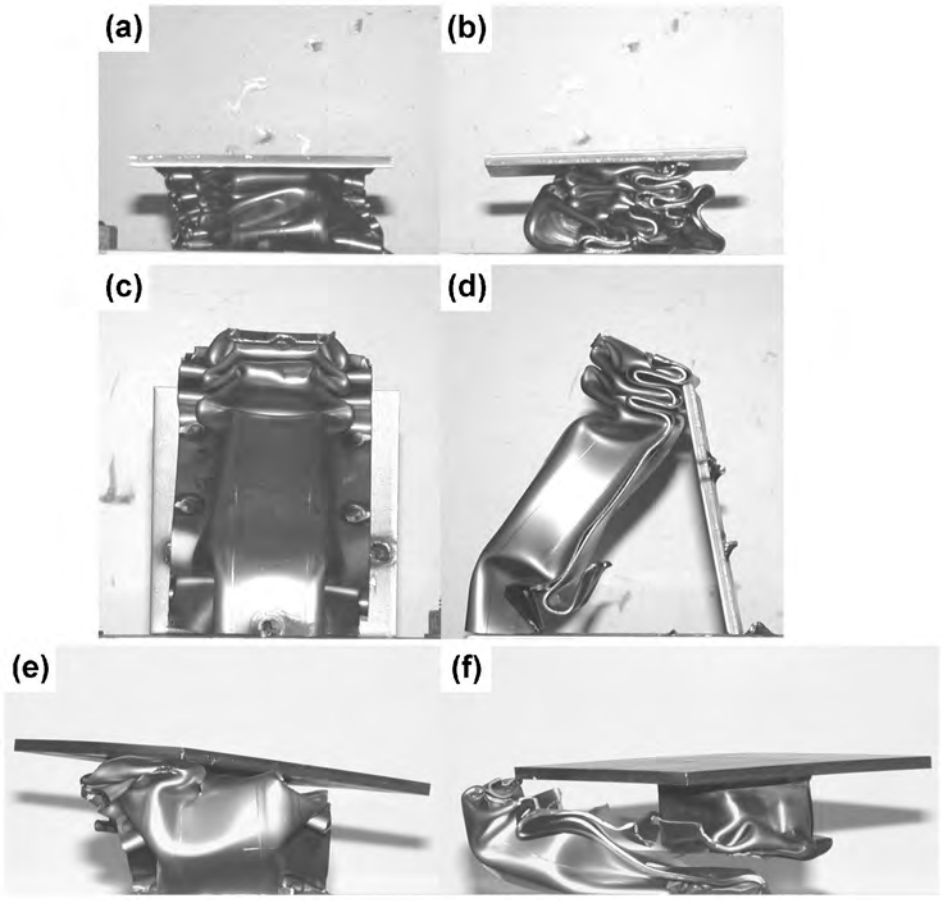

Figure 5.19 Appearances of the hat columns with a thickness of 1.0 mm after dynamic collapse tests showing various deformation shapes. (a, b) UFG-MP3 column deformed in compact-mode, (c, d) DP980 column deformed in non-compact mode, (e, f) Another DP980 column showing significant fracture in both hat part and back plate. The pictures (a, c, e) were taken from the front of the columns and (b, d, f) from the right hand side of the columns.

Next, another example for the improvement of deformation shape by applying the UFG-MP steels is shown. Figure 5.19 shows the appearance of the hat columns having a thickness of 1.0 mm, which were made by the UFG-MP3 and DP980 steels. The UFG-MP3 column exhibited “compact-mode” deformation as well. For the DP980 steel, two examples

were found. Fig. 5.19 (c, d) shows a typical “non-compact” deformation shape with remaining straight regions accompanied with falling down of the column. Some folds near the top end of the column were also observed. Another column shown in Fig. 5.19 (e, f) showed a significant fracture at the upper region of the hat wall. The lower part of the column fell down during the collapse. The column shown in Fig. 5.19 (e, f) was also categorized into a "fracture mode" because of the significant fracture.

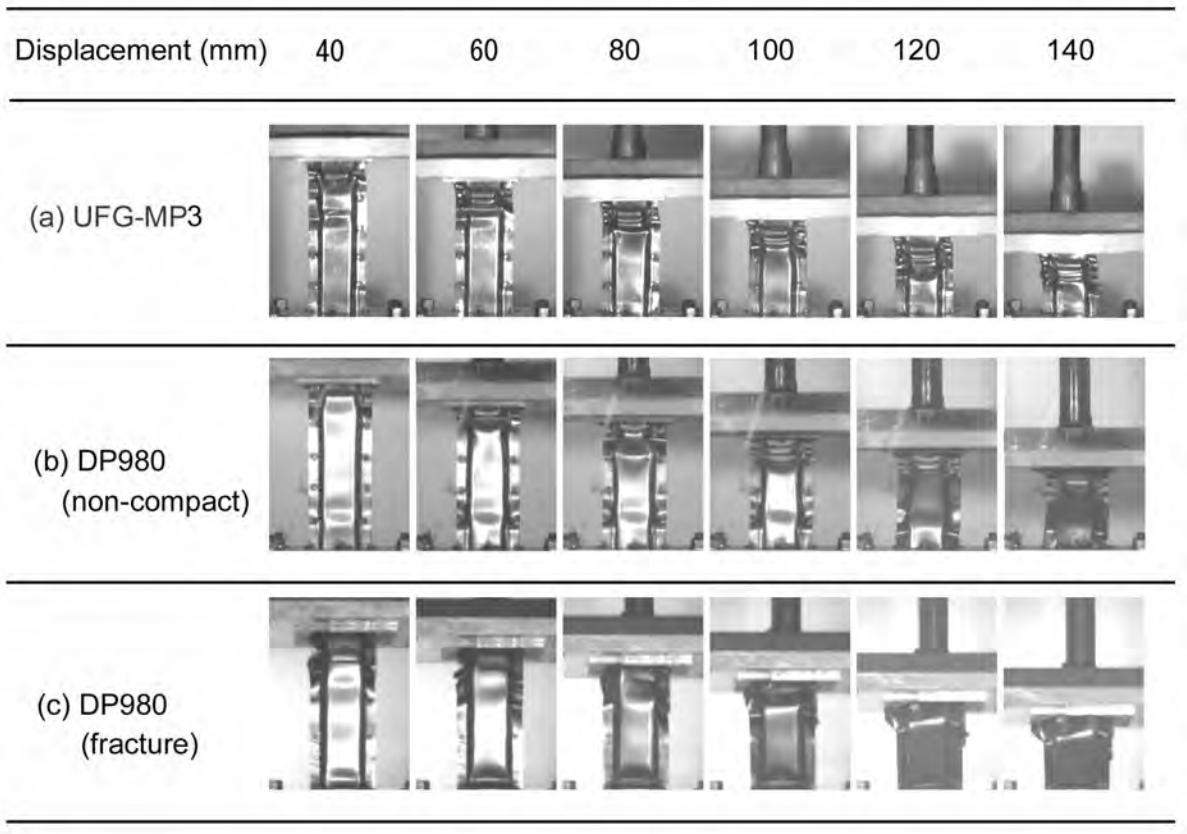

Figure 5.20 Captured images during collapse progression in the columns made of (a) UFG-MP3 column deformed in compact-mode, (b) DP980 column deformed in non-compact mode, and (c) another DP980 column showing early fracture at hat part and falling down. The appearances of three columns after the collapse tests are shown in Fig. 5. 19.

Figure 5.20 shows captured images during collapse progression of three columns shown in Fig. 5.19 taken by using high-speed camera. Figure 5.20 (a) shows a continuous formation of folds with no fracture in the UFG-MP3 steel. In Figure 5.20 (b) it is shown that in the column made of the DP980 steel, falling down of column have already started at a displacement of 120 mm although some compact folds formed before that. Another DP980 column shown in Fig. 5.20 (c) exhibited significant fracture. The first fold formed at displacement of 20 mm, but new fold formation was not observed after that. At 40 mm displacement, a fracture at the first fold had already occurred, and at 60mm, the rest of the hat column below the first fold started to fall down. As a result, the hat column was divided into two parts as shown in Fig. 5.19 (e, f).

Figure 5.21 (a) shows load-displacement curves, and Figure 5.21 (b) shows AE-displacement curves of three hat columns made of the UFG-MP3, and DP980 steels deformed in different modes. The appearances of these hat columns are shown in Fig. 5.19 and Fig. 5.20. In the UFG-MP3 column, the average load was almost constant after the first peak load although oscillation in deformation load was observed. The constant load was due to the continuous progression of compact folds. Therefore the AE continuously increased up to the displacement of 160 mm in the UFG-MP3 steel (Fig. 5.21 (b)). In the DP980 column deformed in non-compact mode, the load dropped at displacement of about 110 mm due to the occurrence of falling down of the column (Fig. 5.20 (b)), resulting in the saturation in AE after 110 mm displacement.

In the DP980 column with fracture, a significant drop in deformation load was observed at displacement around 70 to 80 mm (Fig. 5.21 (a)). This load drop corresponded to the occurrence of falling down of the column just after the occurrence of fracture (Fig. 5.20 (c)). After that the average load gradually decreased, therefore the increasing rate of AE decreased, resulting in small AE compared with the UFG-MP3 column (Fig. 5.21 (b)). It is clear that the UFG-MP3 steel showed the best axial deformation behavior with effective energy absorption among three columns. The deformation behavior in the UFG-MP3 column was the same as that in the UFG-MP4-a one shown in Fig. 5.16 and Fig. 5.17

Table 5.15 summarizes the maximum load, average load at a displacement range between 10 mm and 150 mm, and AE up to displacement of 150 mm of three columns shown in Fig. 5.19, 5.20 and 5.21. The maximum load in the UFG-MP3 column was slightly smaller than that in the DP980 column (non-compact). The maximum load in the DP980 column (fracture) was significantly smaller than those in other columns. In the DP980 column (fracture), the fracture seemed to occur at the first fold as soon as it formed. Therefore, the first peak load was lower than those in other columns. On the other hand, the average load and AE of the UFG-MP3 steel were the highest among three columns, because of the ideal compact-mode deformation.

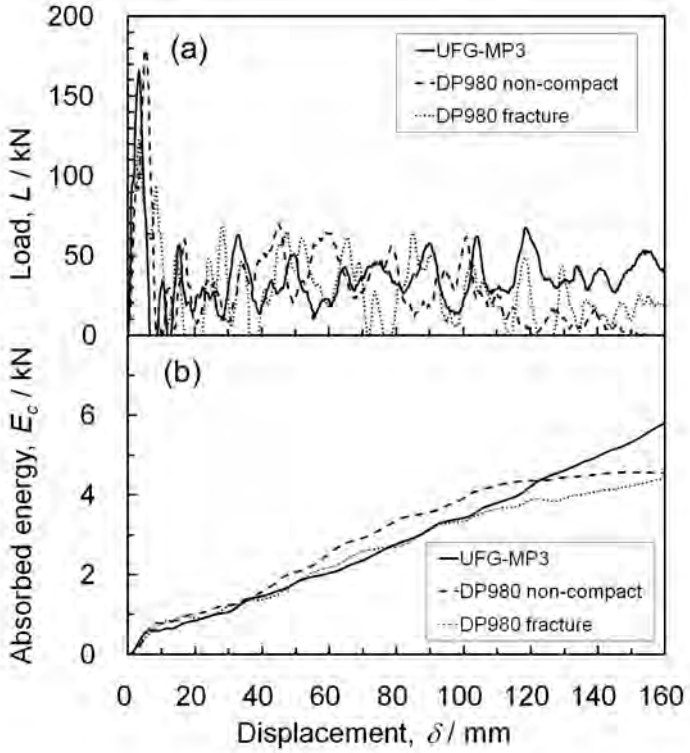

Figure 5.21 (a) Load-displacement curves and (b) absorbed energy-displacement curves of the hat columns made of the UFG-MP3 steel deformed in compact-mode, and two DP980 steels deformed in different modes in the dynamic collapse tests. The appearances of the three hat columns are shown in Fig. 5.19.

Table 5.15 Maximum load, average load and absorbed energy of the UFG-MP3 and DP980 steels sheets having different deformation configurations in dynamic collapse tests. The thickness of columns was 1.0 mm.

Steel	Maximum load (kN)	Average load (10 – 150 mm) (kN)	Absorbed Energy (0 – 150 mm) (kJ)
UFG-MP3	166	33.8	5.33
DP980 (non-compact)	180	26.6	4.56
DP980 (fracture)	123	24.8	4.23

5.3.5 Discussion

The results obtained in dynamic axial collapse tests of the UFG-MP steels and conventional HSS are discussed. The AE of the columns in the dynamic axial collapse tests, E_c, which is one of the most important properties evaluating crash worthiness of the columns, are plotted as a function of quasi-static TS in Fig. 5.22. The red symbols and blue symbols represent the UFG-MP steels and conventional HSS, respectively. The closed circles indicate the data of the columns deformed in compact-mode. The open triangles indicate the columns deformed in non-compact mode. The symbol x indicates the columns that showed significant fracture. Here, in order to compare the data of the columns having different wall thickness (1.2 mm and 1.0 mm), E_c of the 1.2 mm thick columns were converted to the E_c of the 1.0 mm columns by using following equation established in a previous study on axial collapse of rectangular hollow columns [13].

$$E = Ct^{5/3} \tag{5.1}$$

where E is the absorbed energy of the column in axial collapse, C is a constant, and t is the wall thickness of the hollow column. It is shown in Fig. 5.22 that the AE of the columns roughly depended on the quasi-static TS. Here, considering both AE and deformation mode, the data can be categorized into three groups having different features: (I) Compact-mode with high AE, (II) Non-compact mode/fracture with low AE, and (III) Non-compact mode/fracture with high AE. These three groups are indicated in Fig. 5.22, and the steels that belong to each group are summarized in Table 5.16. As described before, some "non-compact" columns were accompanied with fracture like the column shown in Fig. 5. 16 (c, d). However, they were categorized into the "non-compact" group because non-compact deformation shape was the most significant feature in those columns. The columns in the group III showed significant fracture as shown in Fig. 5.16 (e, f).

Table 5.16 Classification of hat columns in dynamic axial collapse tests.

Group	Deformation mode and AE	Steels included
I	Compact-mode with high AE	HSS (TS<800), UFG-MP (TS<1300)
II	Non-compact mode/fracture with low AE	HSS (TS> 600), UFG-MP (one example)
III	Non-compact mode/fracture with high AE	HSS (TS>1180, t=1.2), UFG-MP (TS>1300)

HSS: conventional high strength steels,

t: thiwkness of the column

The evaluation of E_c by TS of the materials, shown in Fig. 5.22 is useful for actual designing of body structures. However, as discussed in section 5.2, the impact energy absorbed by columns in dynamic axial collapse tests had good correlation to AE evaluated by dynamic tensile tests. In Fig. 5.23, the E_c is re-plotted as a function of the AE up to 7% stain evaluated by dynamic tensile tests, E_{td}. In Fig. 5.23, high efficiency of energy absorption in the steels of group I was indicated more clearly.

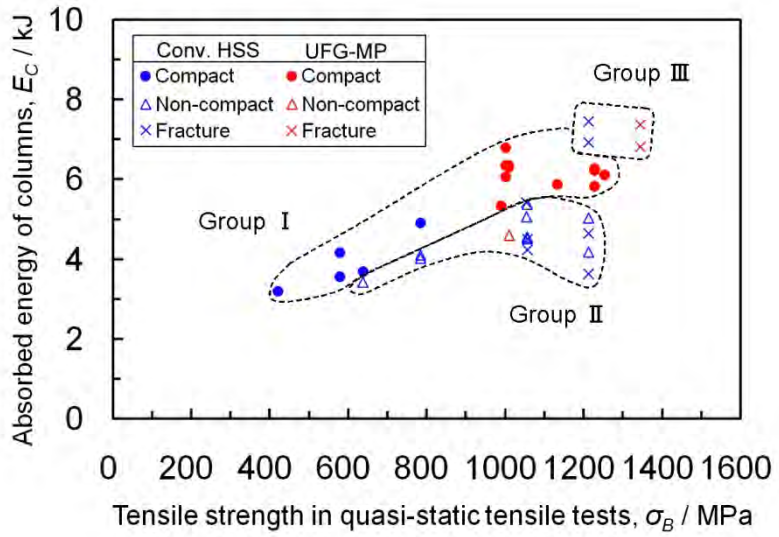

Figure 5.22 Relationship between the absorbed energy of hat columns evaluated by the dynamic axial collapse tests, E_c, and tensile strength in quasi-static tensile tests at a strain rate of 10^{-2} s^{-1}. The E_c of the 1.2 mm thick columns have been converted to the E_c supposing the 1.0 mm thickness.

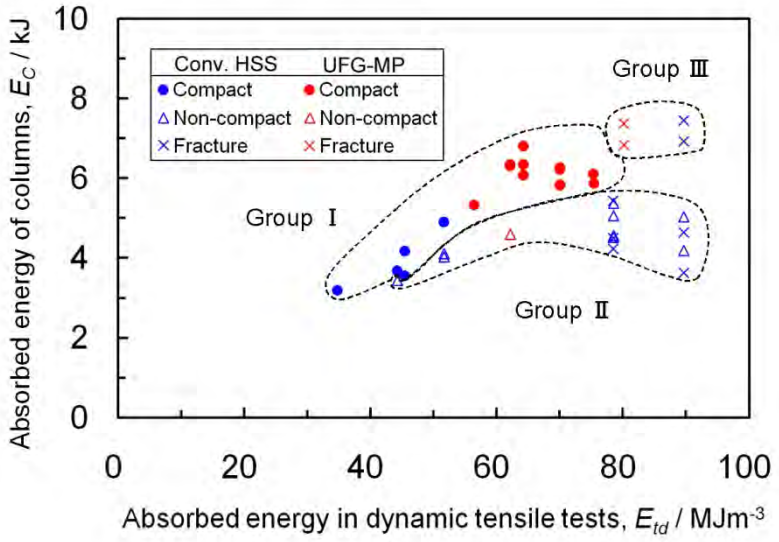

Figure 5.23 Relationship between the absorbed energy of hat columns evaluated by the dynamic axial collapse tests, E_c, and the absorbed energy evaluated by the dynamic tensile tests at a strain rate of 10^3 s^{-1}, E_{td}. The E_c of the 1.2 mm thick columns have been converted to the E_c supposing the 1.0 mm thickness.

Next, based on the data shown in Fig 5.22 and Fig. 5.23, the features of each group are described, with some examples of the deformed columns. The group I included the HSS having TS between 400 and 800 MPa, and the UFG-MP steels having TS lower than 1300 MPa. The columns in the group I were characterized by high E_c and compact-mode deformation. Especially the UFG-MP steels (shown by red symbols) had higher AE compared with conventional HSS having the same TS or E_{td}. This is because the UFG-MP steels promoted compact-mode deformation, which was not obtained in the conventional UHSS (the HSS having TS higher than 1000 MPa).

The group II contained conventional HSS having TS higher than 600 MPa, and one example for the UFG-MP steel. Some examples of the columns in the group II have been shown in Fig. 5.16 (c-f) and Fig. 5.19 (c-f). Other examples are shown here. A few columns deformed in non-compact mode but did not show falling down of the columns such as the columns shown in Fig. 5.16 and Fig. 5.19. Figure 5.24 shows two examples of such columns showing non-compact deformation without falling down. Figure 5.24 (a, b) are the pictures of columns made of the UFG-MP4-a steel. Two folds were observed, and the region between them deformed in large-sized buckling. Falling down of the column did not occur in this case. Three columns were prepared from the UFG-MP4-a steel, and the other two columns deformed in compact-mode. This is the only example that exhibited non-compact mode among the UFG-MP columns tested in these experiments. Figure 5.24 (c, d) are the pictures of columns made of the DP780 steel. A non-compact buckling was observed at upper part of the column. Another column made of the DP780 steel deformed in compact-mode. The occurrence of non-compact mode seemed to be caused by the change in collapse conditions, for example, slight difference in the precision in preparation of columns, or in the impact angle of the weight in collapse tests. However, the probability of the occurrence of non-compact mode in the UFG-MP steels was clearly smaller than that in conventional HSS having strength higher than 980MPa.

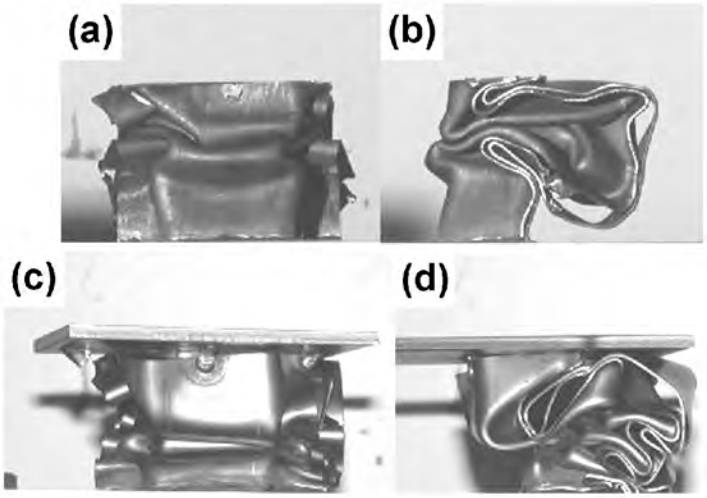

Figure 5.24 Examples of hat columns that deformed in non-compact mode but did not show falling down of columns (included in group II). (a, b) One of the columns made of the UFG-MP4-a steel with a thickness of 1.2 mm, and (c, d) one of the columns made of the DP780 steel with a thickness of 1.0 mm. The pictures (a, c) were taken from the front of the columns and (b, d) from the right hand side of the columns.

The group III included only four examples, the columns made of the 1180 steel with a thickness of 1.2 mm, and the columns made of the UFG-MP5 steel. It should be noted that other 1.2 mm thick 1180 steel columns were included in the group II, as shown in Fig 5.22. Therefore, not all the 1180 columns showed the features for the group III. Here, two examples in the group III are introduced. Figure 5.25 (a, b) shows the appearance of a column made of the UFG-MP5 steel with a thickness of 1 mm. The column showed significant fracture. Especially the side walls were split at bending corners. Figure 5.26 (a)

shows captured images during collapse progression in the UFG-MP5 column shown in Fig. 5.25 (a, b), taken by high-speed camera. It is shown that the side walls started to be split at displacement of 60 mm near the top end of the column. During the progression of the collapse, the split of the walls continued and the walls deformed in a curled-shape by further intrusion of the upper part near the top end of the column.

Figure 5.25 (c, d) shows a picture of a column made of the 1180 steel with a thickness of 1.2 mm. A long straight region with significant fractures was observed at the lower end. Figure 5.26 (b) shows captured images during collapse progression in the 1180 column shown in Fig. 5.25 (c, d). The formation of folds started at the bottom end of the column. At displacement of 80 mm, the remained straight region was observed, and its lower end had already touched the lower steel plate. It seemed that the lower end of the straight region had already been fractured at displacement of 60 mm. After that, the straight region prevented the column from further deformation by existing vertically between the bottom and top plates.

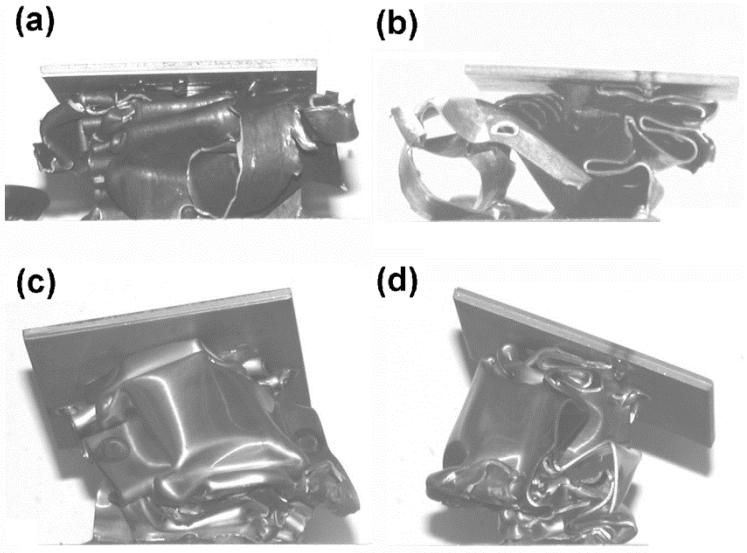

Figure 5.25 Examples of hat columns included in “group III” (non-compact mode/fracture with high AE) in dynamic collapse tests. (a, b) The UFG-MP5 steel with a thickness of 1 mm, deformed with fracture. (c, d) the 1180 steel with a thickness of 1.2 mm that deformed in non-compact mode with fracture. The pictures (a, c) were taken from the front of the columns and (b, d) from the right hand side of the columns..

Figure 5.27 (a, b) shows load-displacement curves and AE-displacement curves of hat columns made of the UFG-MP5 steel and 1180 steel. The load in the 1180 column did not drop significantly up to displacement of 160 mm On the other hand, the load gradually decreased during progression of collapse in the UFG-MP5 column.

As shown in Fig. 5.22 and Fig. 5.23, the AE of both columns were higher than those of other columns deformed in non-compact mode or deformed with fracture. The high AE of the 1180 column was caused by the straight region remained between the top and bottom plates, which were stiff and difficult to be deformed. Therefore, the observed load was high, resulting in the high AE because it was calculated as the integrated area of the load-displacement curves. However, this property seems unacceptable considering the

demands for crushable parts, which should deform in stable form and absorb crash energy. Too stiff body frame may damage the opponent car in the case of actual “car to car” collisions.

The column made of the UFG-MP5 steel showed relatively high AE in spite of significant fracture. This seemed to be because continuous tearing of the side wall requiring high load, resulting in the high energy absorption of the column. However, once fracture occurs, the performance of the column becomes unstable and uncontrollable. Actually, specially designed structures for energy absorption by tearing of material have been proposed and their constant loads during tearing have been shown [20, 21]. However, additional structures for tearing the material, such as cutting blades or dies are required. Therefore, such structures seem not to be adaptive to automobile body structures. Consequently, the columns in the group III are not suitable for body parts for energy absorption, even though the calculated AE was relatively high.

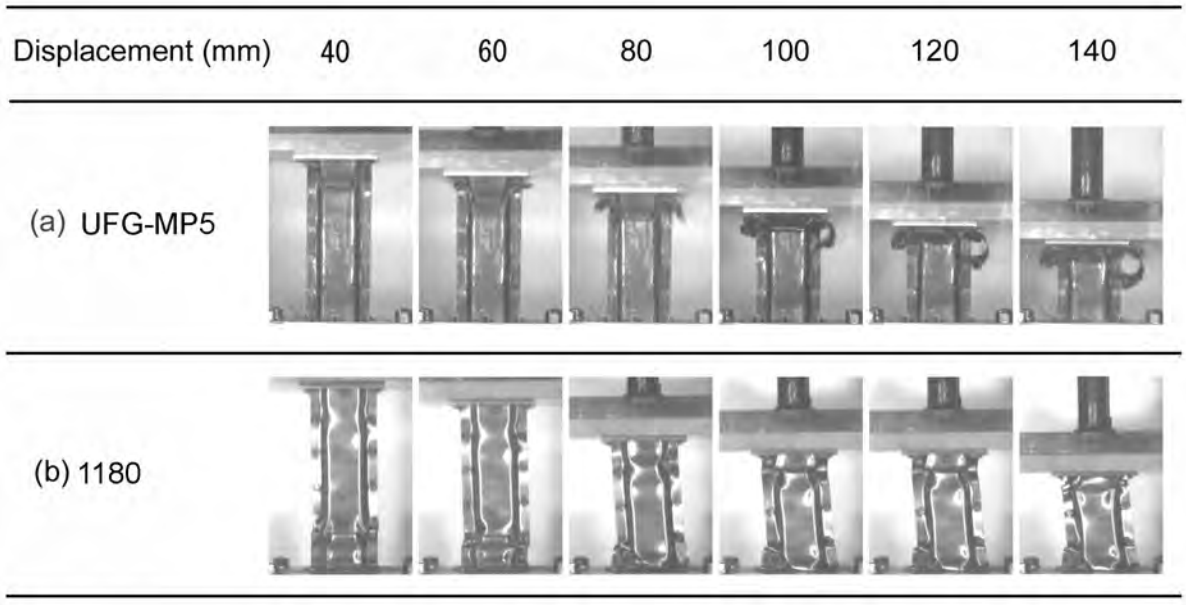

Figure 5.26 Captured images during collapse progression in the columns made of (a) the UFG-MP5 steel with a thickness of 1 mm deformed with fracture and (b) the 1180 steel with a thickness of 1.2 mm deformed with fracture. The appearances of the columns after collapse tests are shown in Fig. 5.25.

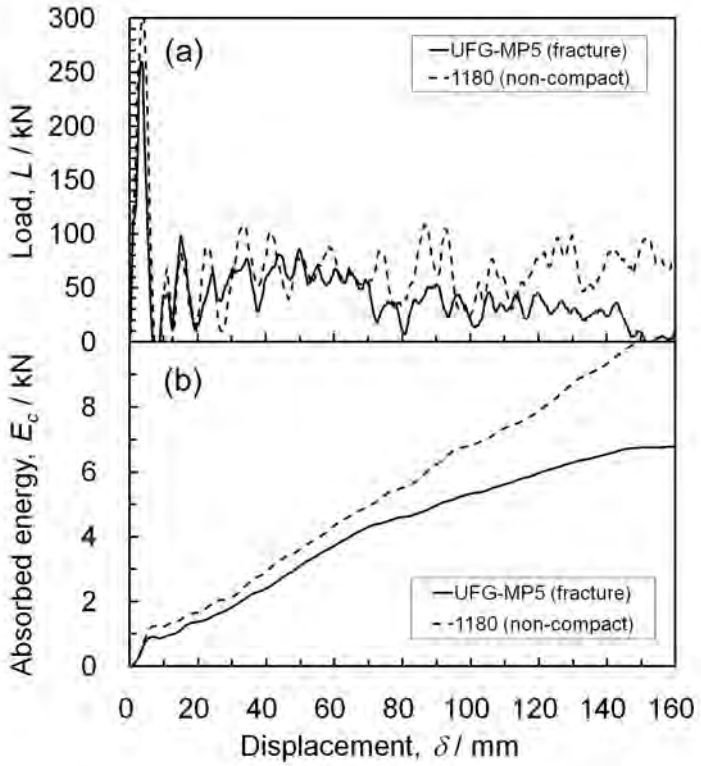

Figure 5.27 (a) Load-displacement curves and (b) absorbed energy-displacement curves of hat columns made of the UFG-MP5 steel with a thickness of 1 mm deformed with fracture and the 1180 steel with a thickness of 1.2 mm deformed with fracture. The appearances of hat columns after collapse tests are shown in Fig. 5.25.

5.3.6 Summary

In this section, dynamic collapse experiments using hat columns were carried out in order to evaluate crash worthiness of the UFG-MP steels. Various UFG-MP steels having various chemical compositions were fabricated and evaluated. The obtained results are summarized below.

(1) Most of the columns made of the UFG-MP steels deformed in “compact-mode” showing continuous progression of folds formation in axial collapse without fractures. On the other hand, the columns made of conventional HSS having TS higher than 980 MPa exhibited non-compact deformation or fracture.

(2) The absorbed energy of the columns in dynamic axial collapse depended on quasi-static TS and absorbed energy evaluated by dynamic tensile test.

(3) It was revealed that the absorbed energy in dynamic collapse of the UFG-MP columns was higher than that of the columns made of conventional HSS, when compared at the same strength.

(4) Considering both AE and deformation mode, the columns made of various steels could be categorized into three groups: (I) Compact-mode with high AE, (II) Non-compact mode/fracture with low AE and (III) Non-compact mode/fracture with high AE. The columns included in the group I had the best crash worthiness.

The UFG-MP steels showed high AE because of compact-mode deformation, which was not obtained in the conventional UHSS having TS higher than 980 MPa. It was shown that the UFG-MP steels have superior crash worthiness when applied to automobile body frame parts, and may contribute to the further weight reduction of automobile body structures.

5.4 Numerical simulation of axial collapse using steels having different work hardening rates

5.4.1 Introduction

In the former sections, it was shown that UFG-MP steels have high energy absorption performance due to the promotion of compact-mode deformation in axial collapse of hat columns. This was thought to be brought by the improved work hardening rate in the UFG-MP steels compared with conventional HSS. Uenishi et al. [19] have suggested a possibility to improve deformation mode by enhancing work hardening rate of the materials. They have carried out FEM (finite element model) simulations for axial collapse of square tubes having various work hardening rates. Figure 5.28 shows the results reported in Ref. [19]. The s-s curves of three model materials applied are shown in Fig. 5.28 (a), and the deformed shapes of square steel tubes are shown in Fig. 5.28 (b). The square tubes were axially deformed with a slanted impact direction of 2 °. If the material V3 with low work hardening rate was applied, the tube deformed in non-compact mode accompanied with falling down. If the material V1 with high work hardening rate was applied, deformation mode was certainly improved and changed from “non-compact” to “compact-mode”. However, the mechanism of the improvement of deformation shape was not discussed in Ref. [19]. In this section, the effect of the shape of s-s curves including work hardening rate on axial deformation behavior is investigated by using FEM simulation. The mechanism of the improvement of deformation shapes in axial collapse of the UFG-MP steels are discussed in detail.

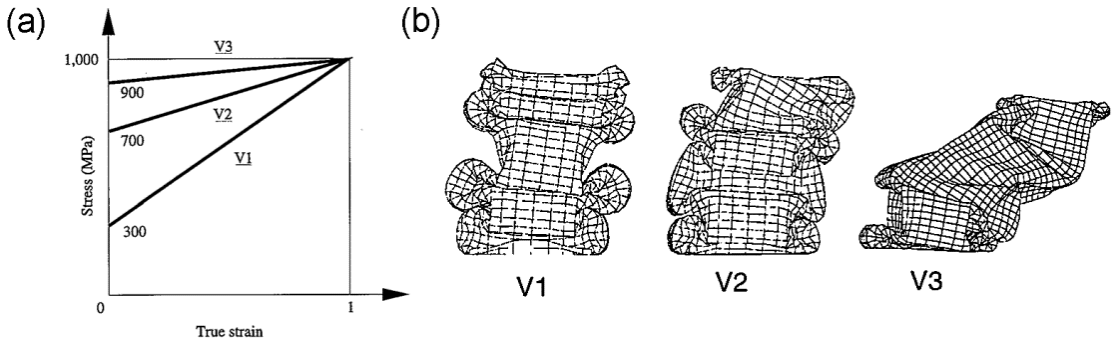

Figure 5.28 (a) The s-s curves of model materials used in the FEM simulations, and (b) deformed shapes of the square tubes axially deformed by a slanted impact direction of 2 °. Various materials having different work hardening rates were applied [19].

5.4.2 Experimental procedure

Numerical simulations were carried out using RADIOSS dynamic explicit commercial finite element code. A finite element model of a rectangular hat column was developed. The cross section and general view of the model are shown in Fig.5.29. The hat column was composed of a hat part bent by a corner radius of 5 mm and a flat back plate, both of which are connected by spot-welding which is expressed by rigid beams binding the facing nodes on the flanges. The thickness of the material was 1 mm, and the pitch of spot-welding was 40 mm. On the bottom end of hat column, all nodes were constrained for all translation, while on the top end, several nodes were constrained for rotation in four places. A rigid wall having a mass of 110 kg hit the top of hat column at a velocity of 50 kmh^{-1}.

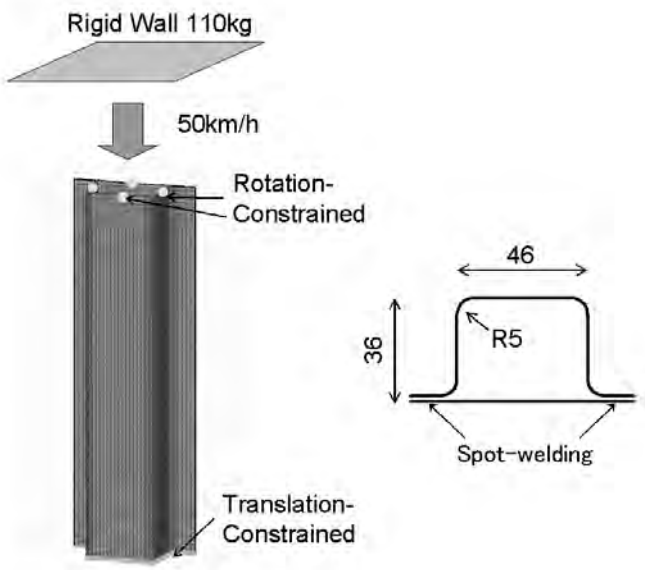

Figure 5.29 General views of the finite element model and conditions.

In order to clarify the effect of work hardening rate of the materials on the deformation behavior, three sets of material parameters were generated to explain different s-s curves having various combinations of yield strength and work hardening rate. The equation expressing s-s curves was defined by using Ludwik type static s-s curve and Cowper-Symonds type strain rate sensitivity index expressed as

$$\sigma = (a + b\varepsilon^n)\left(1 + \left(\frac{\dot{\varepsilon}}{D}\right)^{\frac{1}{p}}\right) \tag{5.2}$$

where a, b and n are the parameters describing the static s-s curve, D and p are strain rate sensitivity parameters, and $\dot{\varepsilon}$ is strain rate. Besides those parameters, σ_{max} was defined for each material to explain the maximum stress permitted. The material parameters for three model materials and calculated 0.2% offset stress are listed in Table 5.17. In Fig. 5.30, true stress-plastic strain curves at a strain rate of 0.01 s^{-1} that were calculated using the three

parameter sets in Table 5.17 are shown. Material A had a relatively low 0.2% offset stress and significant work hardening up to a strain around 0.07. Material D had the same maximum stress as material A and low work hardening rate. Material H had the highest 0.2% offset stress and low work hardening rate. The 0.2% offset stress is represented as the yield strength (YS) hereafter. Using three material parameter sets, deformation shape of the hat columns, load and absorbed energy were evaluated in the FEM simulations.

Table 5.17 Material parameters and calculated 0.2% offset stress of three different model materials for FEM simulation.

Material	a (MPa)	b (MPa)	n	D (s^{-1})	p	σ_{max} (MPa)	0.2% offset stress (MPa)
A	392	2058	0.3	10^9	6.53	1299	711
D	392	1960	0.15	10^9	6.53	1299	1164
H	784	1960	0.15	10^9	6.53	1621	1556

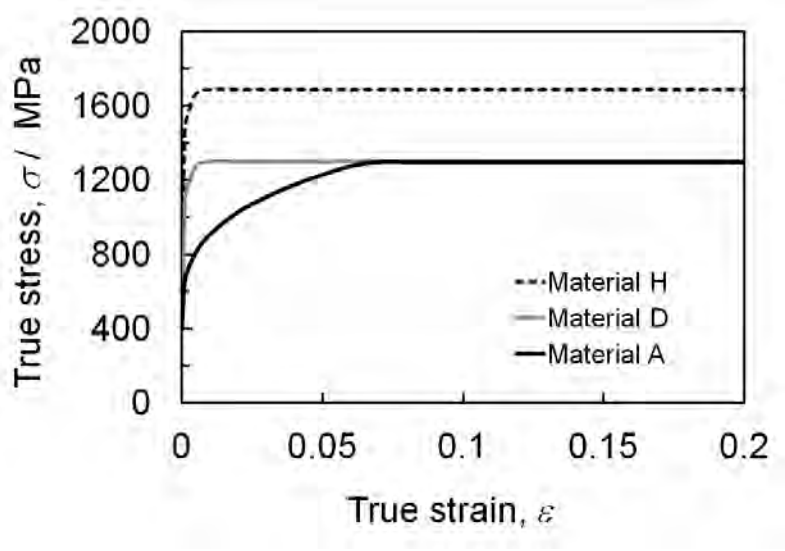

Figure 5.30 Stress-strain curves of the model materials having different work hardening rate.

5.4.3 Results and discussion

The effects of 0.2% offset stress

Figure 5.31 (a, b) shows stress distributions in the deformed hat columns before the occurrence of first buckling: (a) for material A and (b) for material H. The stress (von Mises stress) shown in the figure has been normalized by following equation and.

$$\sigma_N = \sigma/\sigma_m \tag{5.3}$$

where σ_N is the normalized stress, σ is the calculated stress in each element, and σ_m is the maximum value of stress observed in each material. The calculating periods (the time after the impact of rigid wall) are also shown in the figure. Stress waves traveling downward

from the top of the column to the bottom were observed at 0.04 msec in both materials. At 0.08 msec, stress waves amplified by reflection at the bottom end were seen going upward. Then at 0.13 msec, next reflected waves were going downward. Figure 5.31 (c, d) shows strain distributions in both columns. It is seen that plastic deformation of the column began near the top end in material A at 0.19 msec, while in material H, it began near the bottom end. This seemed to be caused by the difference in YS of the materials. In the material A, the column began deforming at the top end after the second reflection of the stress wave between 0.13 and 0.19 msec. On the other hand, in the material H, the amplitude of the stress wave after the second reflection at the top end seemed to be smaller than YS, so that plastic deformation did not occur at the top end, but occurred at the bottom end after the next reflection at the bottom end. After the third reflection of the stress wave, the amplified stress wave seemed to exceed YS (0.19 msec). This difference in deformation behavior affected the deformation shape at 7 msec. The column made of the material A exhibited stable progressive buckling, and each wrinkle generated by buckling piled up like accordion. This is called “compact-mode” [16, 17] as mentioned before. On the other hand, in the column made of material H, the straight regions between deformed areas remained because the buckling occurred simultaneously at the top and bottom ends. This is called “non-compact” behavior [16, 17]. In Fig. 5.31 (d), strain concentration at buckling area was observed, which will be discussed later. It was shown that the difference in the first buckling position occurred depending on YS of the materials in axial collapse of hat columns. Therefore, it is suggested that one of the reasons buckling at the bottom end shown in Fig. 5.16 and Fig. 5.19 was high YS in the UHSS.

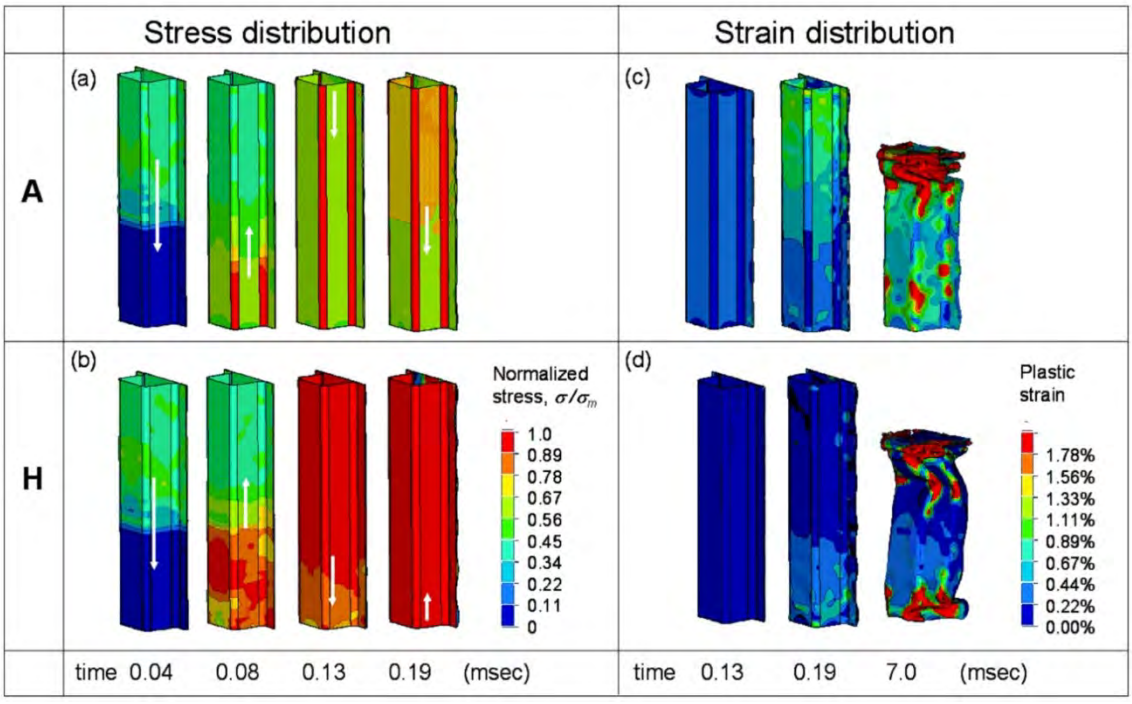

Figure 5.31 Changes of stress and strain distributions at early stages of axial deformation. Stress distributions in (a) material A, and (b) material H. Strain distributions in (c) material A, and (d) material H

The effects of work hardening rate

In order to clarify the effect of work hardening rate of materials on the deformation behavior, strain distributions of the columns with different materials are shown in Fig.5.32. Two pictures before and after the formation of a new buckling fold are shown for each material. White arrows in the figure indicate the areas that are in progress of buckling and are expected to form next folds. In materials A and D, the first fold near the top end had already formed, and the second one was just forming. In material H, in addition to the folds at the top end, another buckling at the bottom end was observed. In material A, continuous strain distribution along hat corner was observed in the area between the existing fold and new fold. On the other hand, in materials D and H, strain distributions in this region was not continuous, and large strain was concentrated into the small region at the new buckling area. When the deformation progressed, the new buckling completed in compact-mode in material A. On the other hand, the region between the existing fold and new fold was almost straight and had small plastic strains in the materials D and H.

Figure 5.33 shows side views of the columns with the material A and material H, at deformation periods of 5 and 8 msec. The red lines indicate cross sections at the center of the front planes. The bending radius of the second buckling area was smaller in the material H compared with the case of the material A, which caused stress concentration in the buckling area. As a result, the column of material H showed non-compact behavior at 8 msec. Consequently, it was indicated in the analysis of stress and strain distributions that the material having low YS and high work hardening rate tended to deform in compact-mode.

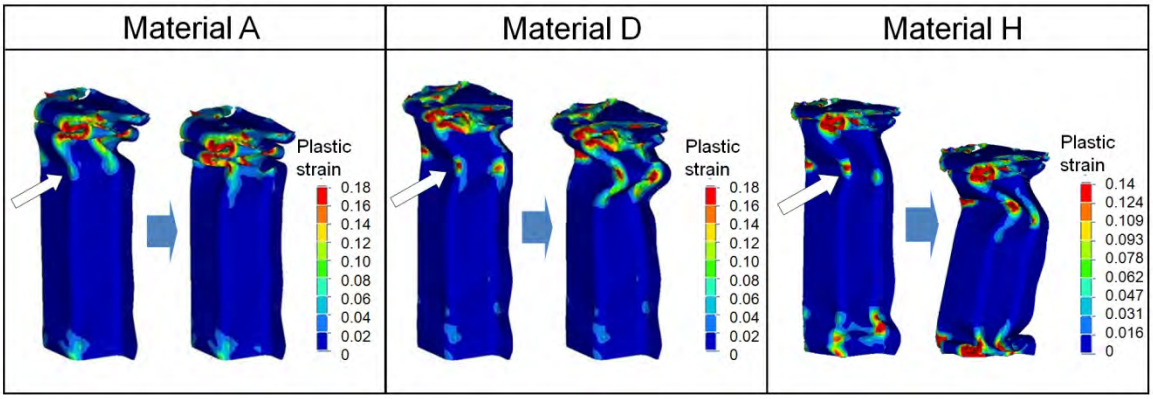

Figure 5.32 Plastic strain distributions in the columns of materials A, D and H. White arrows show the following deformation areas (second buckling areas).

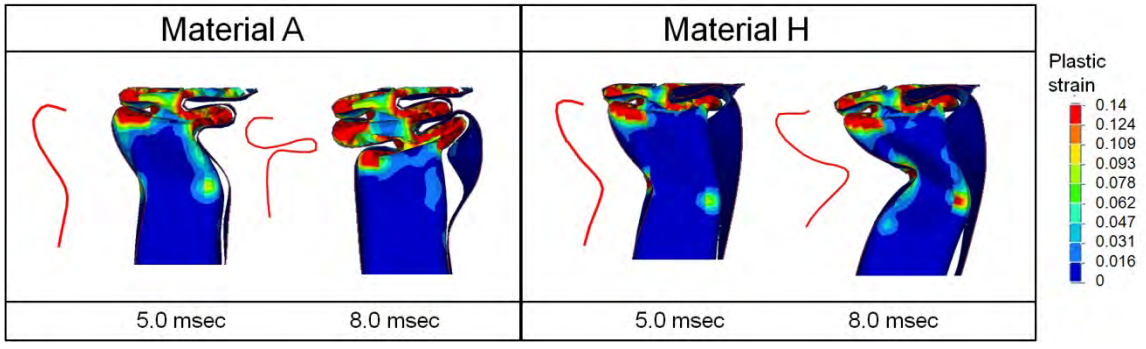

Figure 5.33 Plastic strain distributions in the columns of materials A and H, at deformation periods of 5.0 and 8.0 msec. Red lines indicate cross sections at the center of the front planes.

The load and absorbed energy

Figure 5.34 shows relationship between load and deformation period of two hat columns with different materials. Before 7 msec, higher deformation load was observed in the material H. However, after 8 msec corresponding to the second buckling, the load in the material H significantly dropped. On the other hand, the load remained almost the same during buckling progress after 4 msec in the material A. Table 5.18 shows the maximum load, average load between displacement (deformation length) of 20 and 150 mm, and AE up to 150 mm displacement. The maximum load (peak load before 1 msec) was higher in the material H, but the average load and AE was higher in the material A. This result indicates that high YS is not always effective for improving AE in axial collapse, but a combination of relatively low YS and high work hardening rate is favorable for stabilizing deformation shape (promotion of compact-mode), and improving AE.

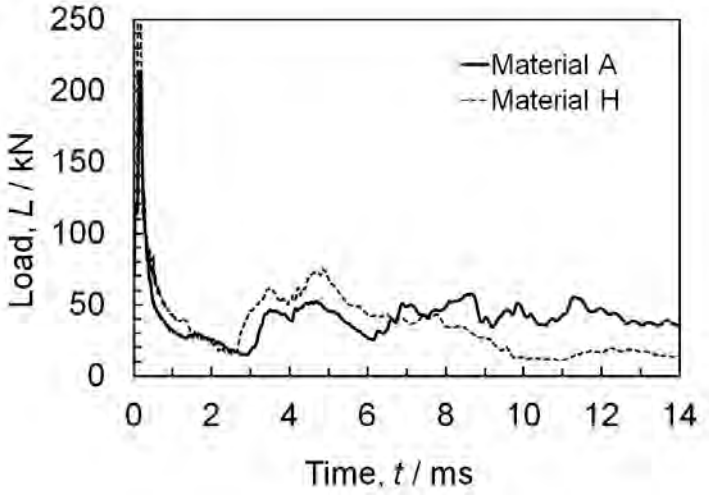

Figure 5.34 Load-time curves of hat columns using the materials A and H obtained by FEM simulations.

Table 5.18 Maximum load, average load and absorbed energy of hat columns using the materials A and H obtained by FEM simulations.

Material	Maximum load (kN)	Average load (20-150 mm) (kN)	Absorbed Energy (0-150 mm) (kJ)
A	214	39.8	6.31
H	342	32.4	5.94

5.4.4 Summary

The effects of yield strength (YS) and work hardening rate of materials on axial collapse performance were investigated using FEM simulation. The obtained results are summarized below.

(1) The propagation of stress wave at the top end of column and its multiplication at the top and bottom ends were observed. In the analysis conditions in this section, the material A having low YS showed first buckling at the top end when the amplitude of the stress wave exceeded YS of the material. On the other hand, in the material H having high YS, first buckling occurred at the bottom end later than the occurrence of buckling in the material A. This was because one more reflection was required for exceeding the high YS of the material H. In this case, due to the buckling near the bottom end, the column tended to show unstable “non-compact mode” deformation.

(2) In the material A having high work hardening rate, continuous strain distribution between two buckling folds was observed. On the other hand, in the materials D and H having low work hardening rate, strain was concentrated into a small region at the buckling fold. This difference in strain distributions was thought to be caused by the difference in work hardening rate of the materials. The continuous strain distribution in the material A promoted stable “compact-mode” deformation during the progression of axial collapse. It is indicated that the materials with high work hardening rate tend to promote favorable “compact-mode” configuration.

5.5 Stamping and spot-welding performances of ultrafine grained multi-phase steels

5.5.1 Introduction

Most of the parts in automobile body structures are formed by stamping of sheet metals, and jointed by spot-welding. Spot-welding, which is one of the electric resistance welding methods using a pair of electrodes, is widely applied in assembling process of automobile bodies. New techniques for forming and welding procedures, such as roll-forming and hydroforming (forming of a metal pipe by hydro pressure applied to the inside of it), and laser-welding assembly, have been applied and gradually expanding. However, stamping and spot-welding are still the most popular manufacturing methods.

In this section, the performances in stamping and spot-welding of the UFG-MP steels are investigated. For evaluating stamping performance, deep-drawing was chosen among various modes of forming. Actual body parts need different forming modes such as bending, drawing and stretching simultaneously. This is due to the complex shape in actual parts. Among those forming modes, the drawability is especially important, because more complex part shapes become possible by improving drawability. Actually, conventional UHSS have poor drawability due to their low elongation and work hardening rate. On the other hand, the UFG-MP steels developed in this study showed large tensile elongation and work hardening rate, therefore they are expected to show improved drawability. In the first part of this section, using a prototyping die set for deep-drawing, stamping performance of the UFG-MP steels are shown and discussed.

For spot-welding joints, strength in various load directions (from parallel to perpendicular to the sheet normal) is required. The most popular and basic mode which should be investigated at first is the tensile shear strength (TSS), which is the maximum load at fracture of the joints of which direction is perpendicular to the normal direction (ND) of sheets. In the second part of this section, TSS of the weld joints using the UFG-MP steels as well as conventional HSS are investigated and discussed.

5.5.2 Experimental procedure

Materials fabrication

Three types of UFG-MP steels were prepared. Table 5.19 summarizes the chemical compositions of the prepared steels: the UFG-MP2, UFG-MP3 and UFG-MP4 steels. The chemical compositions of these steels are substantially the same as the steels listed in Table 5.11. In addition, commercially available DP980 and 1180 sheet steels listed in Table 5.19 were used for comparison. Figure 5.35 shows a schematic drawing of the fabricating process of the UFG-MP steels. The fabricating conditions are summarized in Table 5.20. Steel ingots

prepared by vacuum-melting were hot-rolled to a thickness of 5 mm at various FT in austenite region. The cooling condition after hot-rolling was chosen from two patterns. The one is air-cooling to room temperature, which was applied to the UFG-MP2 and UFG-MP4 steels. The other is water-cooling to room temperature after air-cooling to 350 °C corresponding to two-phase region of ferrite and austenite. This pattern was applied to the UFG-MP3 steel. All the hot-rolled sheets showed complex microstructures composed of ferrite and hard phases.

After mechanical grinding to a thickness of 3.5 mm, the hot-rolled sheets were warm-rolled or cold-rolled. The warm-rolling (WR) was composed of reheating at 500 °C for 1 hour and rolling without additional reheating. The WR was applied to the UFG-MP2 and UFG-MP4 steels. The hot-rolled sheet of the UFG-MP3 steel was cold-rolled at room temperature with lubrication. The final thicknesses and rolling reduction in WR/CR were 1.2 mm and 66%, respectively. The sheets after WR/CR were annealed at various temperatures (T_s) between 685 and 700 °C corresponding to intercritical regions of ferrite and austenite. The condition after intercritical annealing for each steel was chosen from two patterns: water-cooling to room temperature, or subsequent annealing (over-aging: OA) at 400 °C for 300 sec. Two salt baths of which temperatures were set at the T_s and OA temperature (400 °C) were used. After annealing at intercritical region for 120 s, the sheets were moved to another bath for OA treatment, kept for 300 s and then air-cooled to room temperature.

Tensile properties were investigated using JIS No. 5 tensile specimens having gauge length of 50 mm and gauge width of 25 mm. Two specimens, of which tensile direction was parallel to RD, were tested in each steel at a strain rate of 3.3×10^{-3}. In tensile tests, the gauge length and width were measured using a video-type extensometer, and *n*-value and *r*-value (Lankford value) was calculated. The calculation method of *n*-value has been shown in the equations (4.5) and (4.6). The *r*-value, representing plastic anisotropy of sheet metals during tensile deformation, is expressed as

$$r = ln\left(\frac{w}{w_0}\right)/ln\left(\frac{t}{t_0}\right) = ln\left(\frac{w}{w_0}\right)/ln\left(\frac{l_0 w_0}{lw}\right) \quad (5.4)$$

where w_0 and w are width of gauge section before and after tensile deformation, respectively; t_0 and t are thickness before and after tensile deformation, respectively; and l_0 and l are gauge lengths before and after tensile deformation, respectively. In this study, *r*-value was calculated using the gauge length and width under an assumption that the volume of gauge section in tensile specimen is constant. For measurement of *r*-value, tensile specimens having various tensile directions were tested, and average *r*-value, r_m was calculated as

$$r_m = \frac{1}{4}(r_0 + 2r_{45} + r_{90}) \quad (5.5)$$

where r_0, r_{45} and r_{90} are *r*-values along directions of 0°, 45 ° and 90 ° from RD, respectively. Applied tensile strains for the measurement of *r*-value were 5% and 10% in conventional HSS and the UFG-MP steels, respectively.

Table 5.19 Chemical compositions of the UFG-MP steel and the HSS used for stamping and spot-welding experiments (mass%).

Steel	C	Si	Mn	P	S	Al	Nb	N
UFG-MP2	0.152	0.55	4.0	0.001	0.0011	0.024	0.047	0.0019
UFG-MP3	0.206	0.02	3.0	0.002	0.001	0.013	0.023	0.0014
UFG-MP4	0.150	1.42	4.0	0.001	0.001	0.026	0.054	0.0021
DP980	0.157	0.51	2.4	0.009	0.002	0.03	-	0.004
1180	0.151	0.51	2.6	0.007	0.001	0.032	-	-

-: Not measured

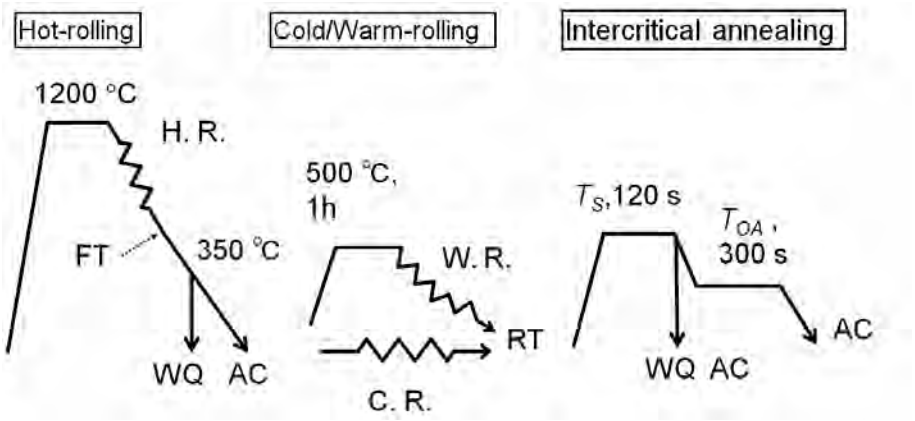

Figure 5.35 Schematic drawing of the process for fabricating the UFG-MP steels used for stamping and spot-welding experiments.

Table 5.20 Fabricating conditions of the UFG-MP steels used for stamping and spot-welding experiments.

Steel	FT (°C)	Cooling after HR	CR/ WR	*t* (mm)	*R* (%)	T_S (°C)	T_{OA} (°C)
UFG-MP2	770	AC	WR	1.2	66	685	400
UFG-MP3	770	WQ from 350 °C	CR	1.2	66	700	(WQ)
UFG-MP4	850	AC	WR	1.2	66	690	400

FT: Finishing temperature in hot-rolling,

HR: Hot-rolling, CR: cold-rolling, WR: warm-rolling,

AC: Air-cooling, WQ: Water-cooling,

t: Thickness after the cold/warm-rolling, *R*: Reduction in the cold/warm-rolling,

T_S: intercritical annealing temperature, T_{OA}: over-aging temperature

Deep-drawing experiments

A model part for investigating deep-drawability of the materials was designed, and a prototyping die set for forming the model part was prepared. A schematic drawing and dimensions of the model part is shown in Fig. 5.36. The upper view is shown in Fig. 5.36 (a). The cross section profile between A and A' is shown in Fig. 5.36 (b). The outer profile of the part is formed by deep-drawing. Embosses at top plane of the part require stretch formability rather than drawability. Therefore, in addition to deep-drawability, stretch formability of the materials can be evaluated using this model part and die set. In Fig. 5.37 (a), a schematic illustration showing stamping process by the prototyping die set is shown. The blank sheets for stamping of which shape and dimensions are shown in Fig. 5.37 (b) were cut from the steel sheets by CO_2 laser. The blank sheets were set on the blank-holder of the die set and then stamped to a drawing height of 30 mm with lubrication. The period of one cycle of stamping motion was about 4 sec. A servo-type stamping machine driven by a stepping motor was used. Generally, deep-drawability is affected by the blank-holding force (the force of clamping the blank sheet by the blank-holder and upper die). In this experiment, the blank-holding force was represented by the air pressure applied to the blank-holders that varied from 0.2 to 0.5 MPa. After stamping, cracking and wrinkling were investigated visually. The UFG-MP3, UFG-MP4, DP980 and 1180 steels in Table 5.19 were evaluated.

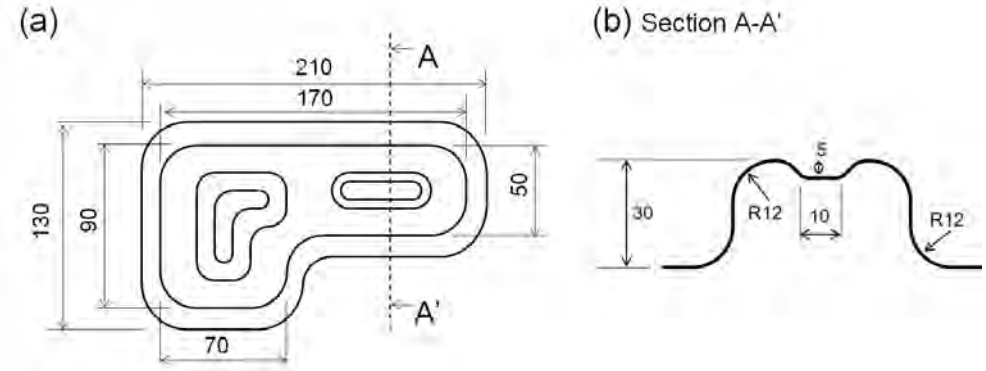

Figure 5.36 Schematic drawing of the model part for evaluating deep-drawability.

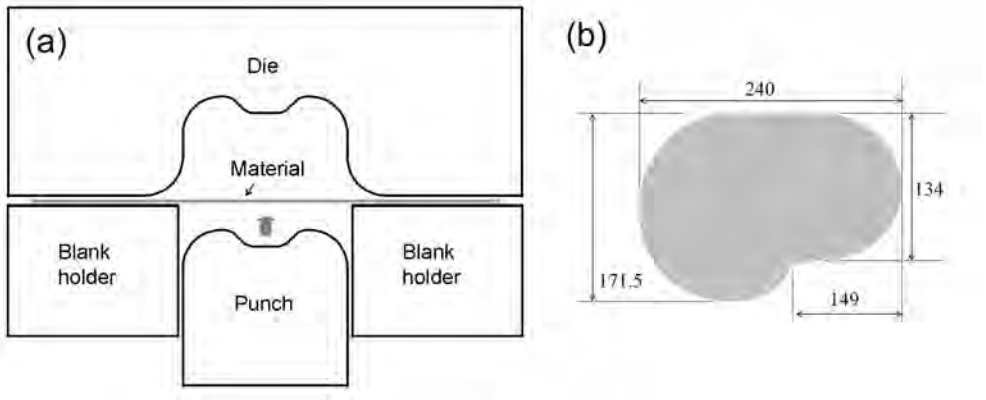

Figure 5.37 (a) Schematic illustration showing stamping process by the prototyping die set, and (b) shape and dimensions of the trimmed steel sheet prepared for stamping experiments.

Spot-welding experiments

Spot-weldability of the UFG-MP2 and 1180 steels shown in Table 5.19 was evaluated. As basic properties for evaluating spot-weldability of the steels, weld-nugget quality and TSS of spot-weld joints were investigated. For investigating weld-nugget quality, two 50 mm square sheets were piled and spot-welded at the center of the sheets. The welding conditions are summarized in Table 5.21. Two conditions using electrodes having different tip diameters were applied. Dome-radius (DR) type electrodes, made of Cu-Cr alloy, were used. The appearance and dimensions of the electrodes used in this study are shown in Fig. 5.38. Various weld joints having various nugget diameters were prepared by changing welding current. The spot-weld specimens were cut at the center of weld-nugget, and the cross sections were observed by using optical microscopy. The size of nuggets was measured, and existence of defects such as voids or inclusions was investigated. Microstructures near weld-nuggets were observed by SEM using the cut specimens. Vickers hardness distribution on weld-nuggets was measured using the cut specimens, along a line that was parallel to the interface of the sheets, and 0.1 mm far from the interface. The load in hardness measurement was 500 gf.

TSS was measured using a standard specimen of JIS. The appearance and dimensions are shown in Fig. 5.39. Two sheets having 30 mm width and 100 mm length were piled at a 30 mm square region as shown in the figure, and then spot-welded at the center of the lapped region. Tensile tests of the prepared TSS specimens were carried out using a gear-driven type tensile test machine at a test speed of 0.17 mms^{-1}. The tensile direction was parallel to the longitudinal direction of the TSS test specimens.

Table 5.21 Spot-welding conditions applied to the UFG-MP4, DP980 and 1180 steels.

Condition	Electrode	Clamping force (kN)	Welding current (kA)	Welding time (msec)
1	DR8	6	6-10	240
2	DR6	5	6-9.5	240

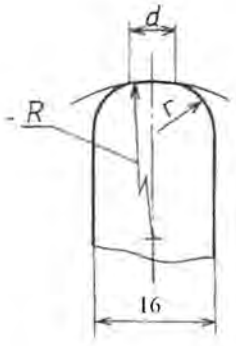

	R (mm)	d (mm)	R (mm)
DR6	40	6	8
DR8	50	8	10

Figure 5.38 Schematic illustration showing appearance and dimensions of the DR type electrodes used in this section.

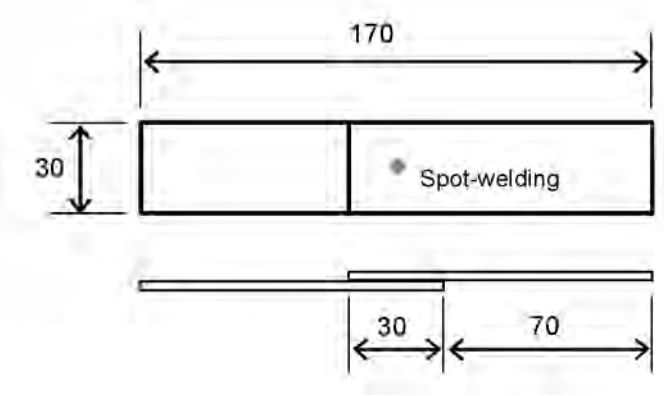

Figure 5.39 Schematic illustration of the tensile shear specimen applied.

5.5.3 Stamping performance of ultrafine grained multi-phase steels

The fabricated UFG-MP steels exhibited complex microstructures composed of sub-micrometer ferrite matrix and second phases. Table 5.22 summarizes thickness and quasi-static mechanical properties of the fabricated UFG-MP steels and conventional DP980 and 1180 steels. TS of the steels varied from 1030 to 1212 MPa. The UFG-MP steels have significantly higher elongation and *n*-value than those in conventional HSS. Generally, deep-drawability of sheet steels is strongly affected by *r*-value of sheet metals [22-24]. However, as shown in Table 5.22, the *r*-values of both the UFG-MP steels and conventional HSS were under 1.0, which were much smaller than that in mild steels. For example, EDDQ (extra deep drawing quality) grade IF (interstitial free) steel has *r*-value around 2.0 [22]. Therefore, the "deep-drawability" of the steels listed in Table 5.22 mainly depends on elongation and *n*-value.

Table 5.22 Mechanical properties at quasi-static strain rate (10^{-2} s^{-1}) of the steels used for stamping experiments. JIS No.5 specimen was used.

Steel	Thickness (mm)	0.2% offset stress (MPa)	Tensile strength (MPa)	Uniform elongation (%)	Total elongation (%)	*n*-value at 5-10%	r_m-value
UFG-MP3	1.2	531	1030	14.8	19.2	0.356	0.45
UFG-MP4	1.2	972	1088	16.3	20.5	0.184	0.46
DP980	1.0	755	1079	7.5	13.4	0.052	0.75
1180	1.0	985	1212	5.0	9.2	-	0.78

Figure 5.40 shows appearances of all the model parts stamped by the prototyping die set, using the UFG-MP steels and conventional HSS. Table 5.23 summarizes the features observed in the stamped model parts. At a blank-holding pressure of 0.2 MPa represented by air pressure, wrinkles throughout the outer flanges were observed in the DP980, 1180 and

UFG-MP4 steels. The wrinkles were also observed in the UFG-MP3 steel at limited regions. In the DP980 and 1180 steels, large cracks were observed simultaneously. When the blank-holding pressure increased up to 0.4 MPa, wrinkles at the flanges decreased, but large cracks still remained in the DP980 and 1180 steels. It meant that the optimum stamping conditions without wrinkles and cracks did not exist in the DP980 and 1180 steels. On the other hand, in the UFG-MP3 and UFG-MP4 steels, wrinkles significantly decreased without occurrence of cracks at 0.4 MPa. Under this condition, the model parts of the UFG-MP steels were successfully formed. Figure 5.41 shows magnified photographs of the model parts formed at a blank-holding pressure of 0.4 MPa. In the DP 980 steel (Fig. 5.41 (c)), a large crack was observed at punch shoulder region. In the 1180 steel (Fig. 5.41 (d)), in addition to a large crack at the right hand side, another crack was observed also at punch shoulder in the center region. These cracks were caused by the lack of deep-drawability in conventional HSS. On the other hand, as shown in Fig. 5.41 (a, b), no cracks were observed in the UFG-MP steels. When the blank-holding pressure increased up to 0.5 MPa, small cracks at embosses on the top plane were observed even in the UFG-MP steels (Fig. 5.40). This was because of the eliminated material flow due to the high blank-holding pressure. However, those cracks were not so large in the UFG-MP steels. It was clearly shown in this experiment that the UFG-MP steels have higher performance in deep-drawability.

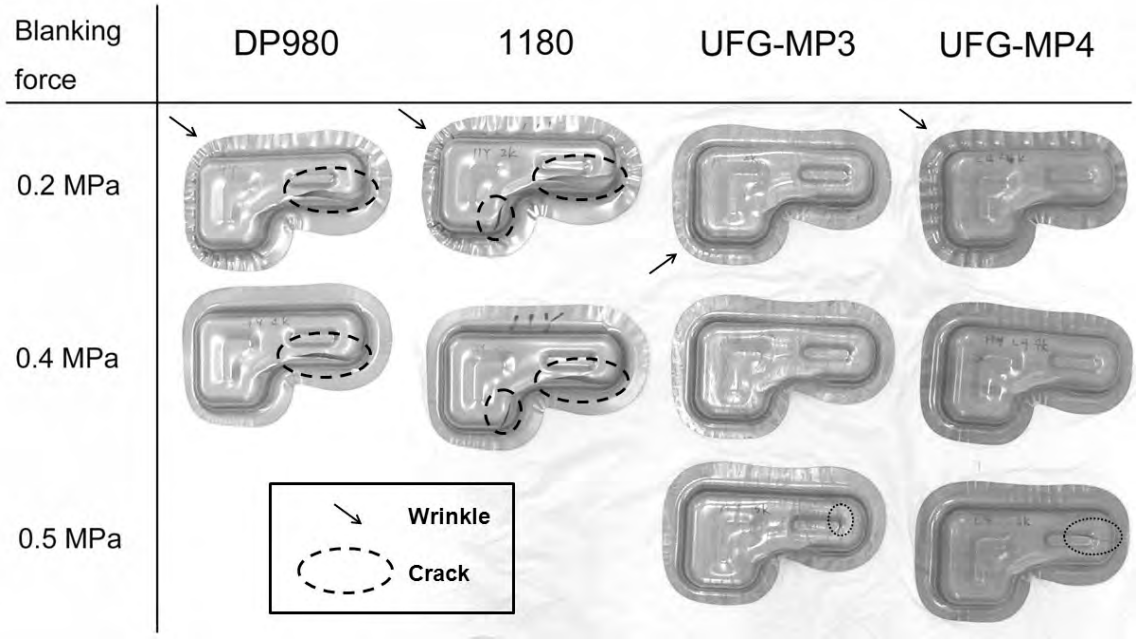

Figure 5.40 Appearances of all the model parts stamped using the prototyping die set. The dotted circles and black arrows indicate cracks and wrinkles, respectively.

Table 5.23 Features observed in the stamped model parts of the UFG-MP steels and conventional HSS. The appearances of the parts are shown in Fig. 5.40.

Blank-holding pressure (MPa)	Materials			
	DP980	1180	UFG-MP3	UFG-MP4
0.2	wrinkling	wrinkling	wrinkling	wrinkling
0.4	cracking at punch shoulder	cracking at punch shoulder	OK	OK
0.5	-	-	cracking at emboss	cracking at emboss

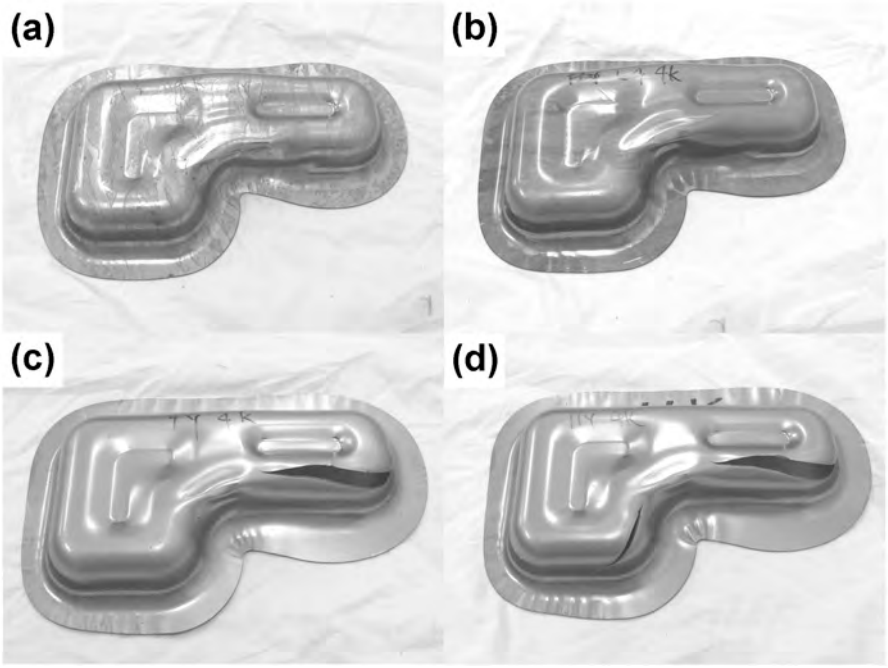

Figure 5.41 Appearances of the model parts stamped at a blank-holding force of 0.4 MPa. The blank-holding force is represented by the air pressure for holding the blank sheet. (a) UFG-MP3, (b) UFG-MP4, (c) DP9890 and (d) 1180 steels. The UFG-MP steels showed no cracks (a, b). The DP980 and 1180 steels showed significant cracks at one or two regions (c, d).

5.5.4 Spot-welding performance of ultrafine grained multi-phase steels

Table 5.24 summarizes thickness and quasi-static mechanical properties of the steels used for spot-welding experiments, the UFG-MP2 steel and conventional 1180 steel. The 1180 steel, one of the typical UHSS, was used for comparison. Figure 5.43 shows optical micrographs of cross-sections of spot-weld nuggets of the UFG-MP2 steel (Fig. 5.42 (a, b)) and 1180 steel (Fig. 5.42 (c, d)). Two spot-weld joints for each steel prepared under different conditions are shown. The specimens shown in Fig 5.42 (a, c) were prepared applying

condition 2 in Table 5.21 (DR6 electrodes, 7.8 kA) while the specimens shown in Fig. 5.42 (b, d) were prepared under condition 1 (DR8 electrodes, 8.9 kA). The light gray regions at the center of the pictures across two stacked sheets are the weld-nuggets, which once melted and solidified during spot-welding process. No defects such as voids or inclusions were observed in the weld-nuggets of both steels.

Table 5.24 Mechanical properties at a quasi-static strain rate (10^{-2} s^{-1}) of the steels used for spot-welding experiments. Measured using JIS No. 5 specimens having tensile direction parallel to RD.

Steel	Thickness (mm)	0.2% offset stress (MPa)	Tensile strength (MPa)	Uniform elongation (%)	Total elongation (%)	*n*-value at 5-10%
UFG-MP2	1.2	1010	1132	13.4	17.2	0.165
1180	1.2	1038	1254	4.5	7.5	-

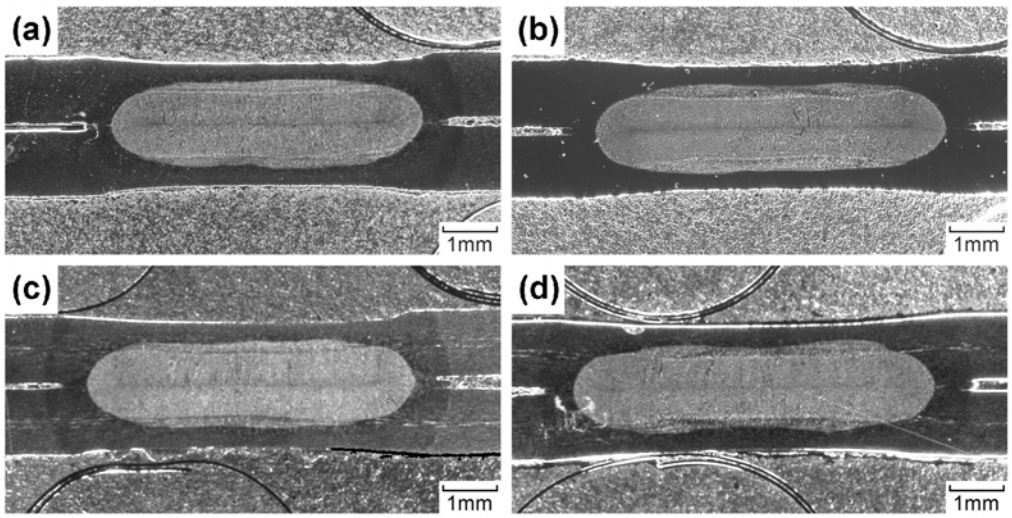

Figure 5.42 Optical micrographs of cross-sections of spot-weld nuggets of (a, b) the UFG-MP2 and (c, d) 1180 steels. The welding conditions are (a, c) DR6 electrodes, 7.8 kA, and (b, d) DR8 electrodes, 8.9 kA.

Figure 5.43 shows hardness distribution on the weld-nugget along horizontal direction in the UFG-MP2 and 1180 steels. The welding condition 2 (DR6 electrodes) in Table 5.21 with a welding current of 7.8 kA was applied. Optical micrographs of the weld-nuggets are shown in Fig. 5.42 (a, c). In Fig. 5.43, the regions of weld-nugget and heat-affected zone (HAZ) measured on optical micrographs are indicated. The hardness of weld-nugget was high, and a part of HAZ surrounding the weld-nugget showed also high hardness in both steels. On the other hand, the outer region of HAZ showed low hardness. The inner part of HAZ with high hardness is called as “HAZ1”, while the outer part is called as “HAZ2” hereafter. The

high hardness in HAZ1 was due to the fact that the temperature reached to austenite region and then transformed to martensite during the welding. On the other hand, the hardness in HAZ2 regions showed different features among two steels. In the conventional 1180 steel, the hardness in HAZ2 region was significantly lower than that in the base metal. Such soft regions were not observed in the UFG-MP2 steel.

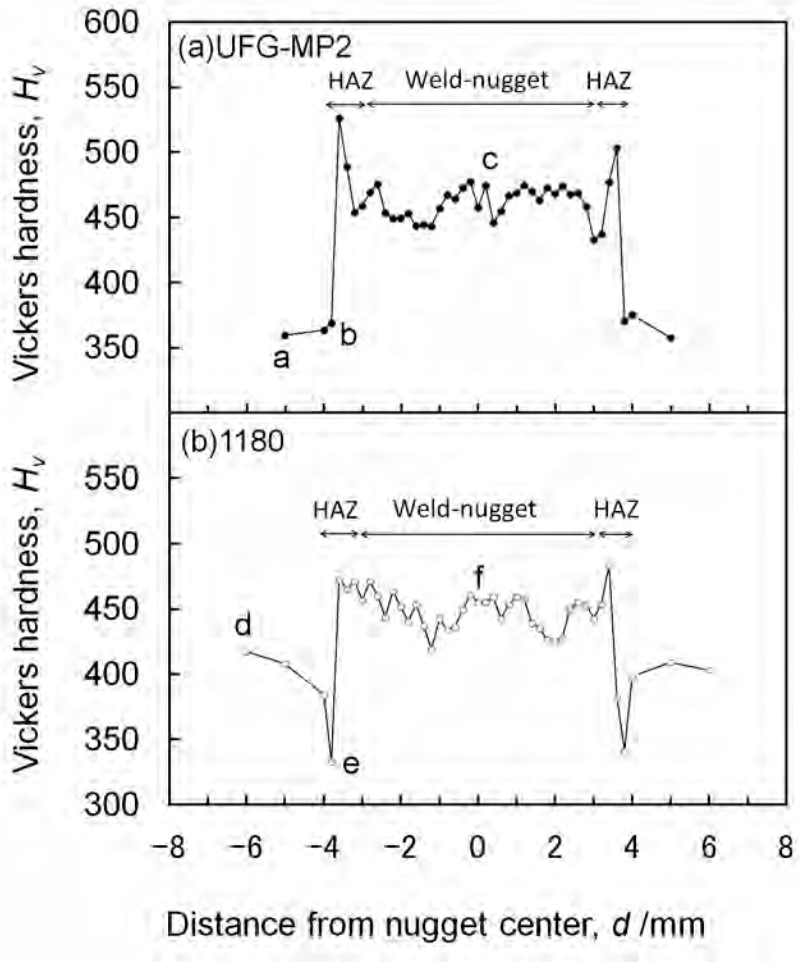

Figure 5.43 Hardness distributions near weld-nuggets in the UFG-MP2 and 1180 steels. Vickers hardness was measured on cross sections of the weld-nuggets along a line near the interface of the sheets, with a load of 500 gf. The spot-weld nuggets were prepared applying the condition 2 in Table 5.21 (DR6 electrodes, 7.8 kA).

In order to clarify the difference in hardness in HAZ2, microstructures near the weld-nuggets are shown in Fig. 5.44. The observed regions in Fig. 5.44 (a-f) correspond to the points indicated by the letters “a” to “f” in Fig. 5.43. First, the microstructures in the UFG-MP2 steel are described. The base metal of the UFG-MP2 steel had a multi-phase microstructure composed of sub-micrometer ferrite and second phases (Fig. 5.44 (a)). The HAZ2 area had also a complex microstructure with higher fraction of second phases than that of the base metal (Fig. 5.44 (b)). This was because the temperature reached to intercritical region of ferrite and austenite during the welding process. However, both the ferrite matrix and second phases kept sub-micrometer size. As discussed in section 4.2, the existence of fine second phase particles at ferrite grain boundaries in the base metal might

prevent grain growth of ferrite. In addition, the heating and cooling rate during the welding process seemed to be very high. Therefore, grain growth was suppressed and the HAZ2 area in the UFG-MP2 steel did not show heat-affected softening. The weld-nugget had full-martensite microstructure (Fig. 5.44 (c)). The microstructure in the HAZ1 region, which was not shown in the figure, was also full-martensite.

Next, the microstructures in the 1180 steel are explained. The base metal exhibited almost full-martensite containing a slight amount of ferrite (Fig. 5.44 (d)). The HAZ2 area, which was softer than the base metal, exhibited a duplex microstructure composed of relatively coarse ferrite and martensite (Fig. 5.44 (e)). However, in contrast to the UFG-MP2 steel, grain growth occurred in the HAZ2 area of the 1180 steel. In the martensite single-phase microstructure, the grain growth could not be suppressed during the heating to intercritical region. Consequently, the hardness in the HAZ2 region in the 1180 steel was significantly lower than that in the base metal. The weld-nugget showed full-martensite microstructure (Fig. 5.44 (f)). It was revealed that heat-affected softening in HAZ did not occur in the UFG-MP2 steel, while significant grain growth and softening was observed in the conventional 1180 steel.

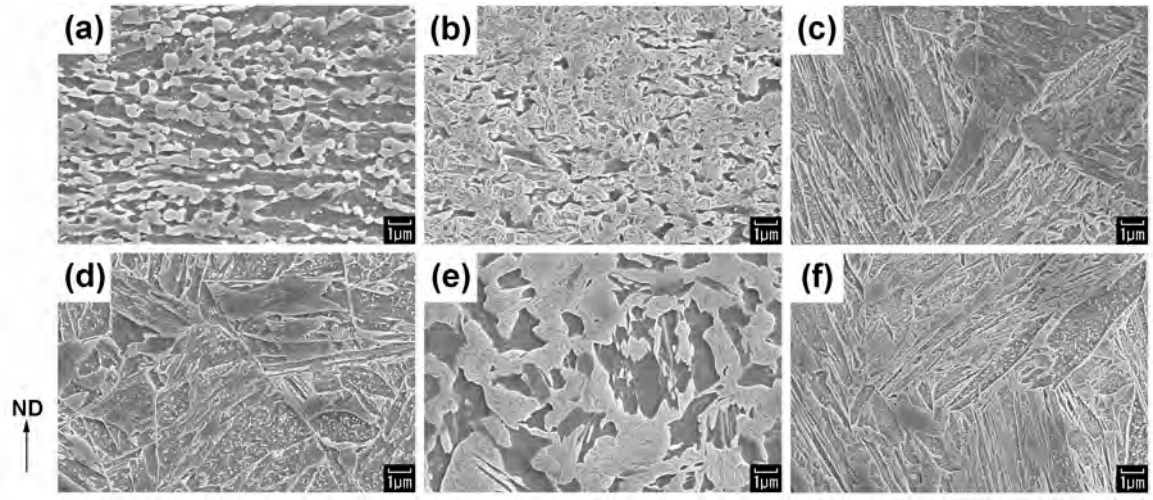

Figure 5.44 SEM microstructures of cross-sections near the weld-nuggets of the (a, b, c) UFG-MP2 and (d, e, f) 1180 steels. The images were taken at (a, c) base metal, (b, d) heat affected zone (HAZ2) close to the base metal and (c, e) the center of weld-nugget. The welding condition 2 in Table 5.21 (DR6 electrodes, 7.8 kA) was applied. The corresponding places for the images are indicated in Fig. 5.43.

Next, the effect of welding condition on nugget size and TSS is shown. Figure 5.45 shows the nugget diameter and TSS of the weld joints as a function of welding current. The welding condition 1 in Table 5.21 was applied. Figure 5.45 (a) shows the nugget diameter. The occurrence of expulsion is indicated in the figure. Generally, expulsion tends to occur when the welding current is too high, and it often decreases nugget quality and strength of the weld joint. The welding current where expulsion occurred was lower in the UFG-MP2 steel than that in the 1180steel.

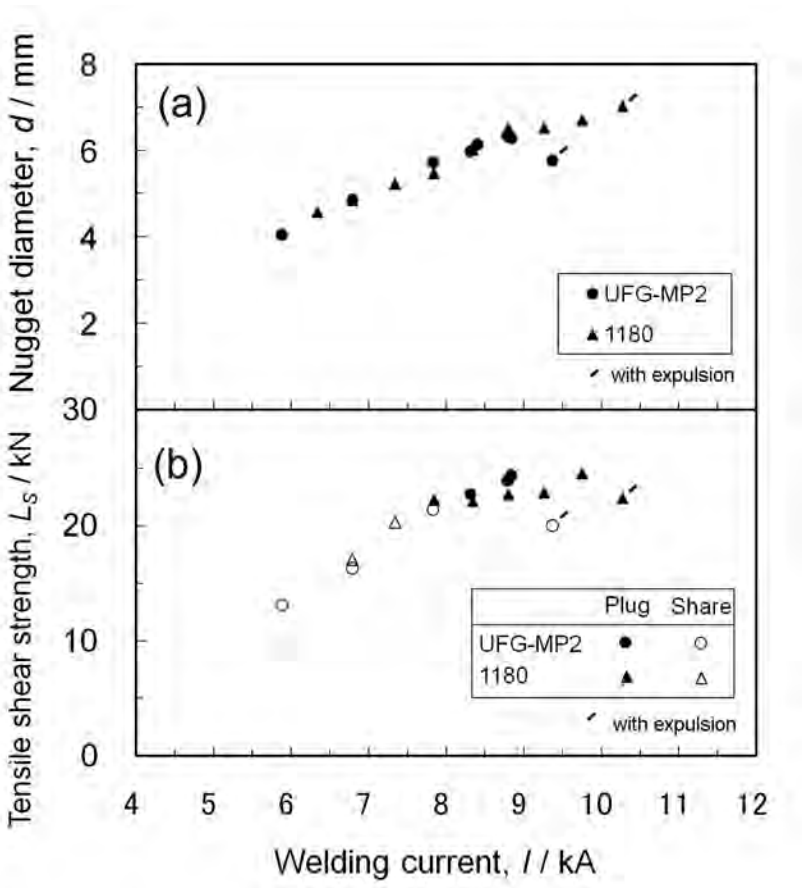

Figure 5.45 (a) Nugget diameter and (b) tensile shear strength (TSS) in the UFG-MP2 1180 steels as a function of welding current. The welding condition 1 in Table 5.21 was applied. The occurrence of expulsion of melt metal during the welding is indicated in the figures. In (b), the solid symbols indicate “plug fracture”, and the open symbols indicate “share fracture”.

Figure 5.45 (b) shows the relationship between TSS and welding current. The solid symbols indicate “plug fracture” where the weld-nuggets remained as a button-shape at one side of the fractured specimen. The open symbols indicate “share fracture” where the weld-nuggets were shared by two sheets and no buttons were observed. It was shown that UFG-MP2 steel had the same TSS as that in the 1180 steel, as long as expulsion did not occur. Generally at low welding current, share fracture tends to occur and decreases strength of weld-joints. The weld current range, where the nuggets show plug fracture without expulsion, was 8.5 to 9.0 kA in the UFG-MP2 steel, while 7.3 to 8.8 kA in the 1180 steel. The optimum welding current range was narrower in the UFG-MP2 steel. However, it is noteworthy that TSS of the UFG-MP2 steel was almost the same as that in the conventional 1180 steel in spite of high Mn content of the UFG-MP2 steel.

5.5.5 Summary

Stamping and spot-welding performances of the UFG-MP steels were shown and discussed. The UFG-MP steels, having complex microstructures composed of ultrafine ferrite and second phases, and tensile strengths between 1030 and 1212 MPa were fabricated. In order to evaluate stamping performance, a prototyping die set for stamping a model part was designed. Deep-drawability of the UFG-MP steels was evaluated. The obtained results are summarized below.

(1) For the conventional DP980 and 1180 steels, wrinkles or cracks were observed in all the stamping conditions. On the other hand, the UFG-MP steels were successfully stamped without cracks and significant wrinkles at a blank-holding pressure of 0.4 MPa.
(2) Good performance in deep-drawing of the UFG-MP steels seemed to be caused by high elongation and work hardening rate compared with conventional HSS.

Next, nugget quality and tensile shear strength (TSS) of weld-joints of the UFG-MP steel were evaluated. Using dome-radius type electrodes, spot-weld joints were prepared at various welding currents. Observation of the cross section of the nuggets and TSS measurements were carried out. The obtained results are summarized below.

(1) In the weld-nuggets of the UFG-MP2 steel, no defects such as voids or inclusions were observed.
(2) Softening in heat affected zone (HAZ), which is often observed in the conventional HSS was not observed in the UFG-MP2 steel. Microstructure at HAZ exhibited an UFG complex microstructure with increased second phase fraction. Grain growth in HAZ was suppressed in the UFG-MP2 steel. On the other hand, the microstructural change from martensite to coarse grained dual-phase in HAZ occurred in the conventional 1180 steel, which decreased the hardness of HAZ.
(3) The optimum welding current range in the UFG-MP steel was narrower than that in the conventional 1180 steel. However, as far as the optimum welding conditions were selected, the weld joint of the UFG-MP2 steel showed the same TSS as the conventional 1180 steel in spite of high Mn content of the UFG-MP2 steel.

5.6 Conclusions

In this chapter, the performances of the UFG steels when applied to automobile body structures were shown and discussed. First, crash worthiness of the UFG-FC and UFG-MP steels was investigated and discussed. In the UFG-FC steels, using their high strain rate dependence of flow stress, high energy absorption in dynamic collapse was achieved. This was because the UFG-FC steels had higher dynamic strength than conventional HSS (high strength steels) having the equivalent quasi-static strength. In other words, when the steel for body structures is replaced by the UFG-FC steel having the same quasi-static strength, the energy absorption during car collisions is expected to be improved. This may contribute to further weight reduction by reducing the thickness. However, in the UFG-FC microstructures, TS was limited under 1000 MPa. Therefore, the UFG-FC microstructures cannot satisfy the demands for very high strength such as UHSS (ultrahigh strength steels). In addition, the poor uniform elongation in UFG-FC steels should be improved when considering stamping processes for actual body parts.

Next, the UFG-MP steels having both high strength and high work hardening rate were evaluated by dynamic axial collapse. Stable “compact-mode” deformation, which was not achieved in conventional UHSS, was achieved in the UFG-MP steels. The compact-mode deformation improved the energy absorption in axial collapse. It was clarified that the UFG-MP steels having very high strength as those in UHSS could be applied to crushable parts. By the numerical analysis for axial collapse of hat columns focusing on stress-strain relationship of the materials, it was confirmed that improvement of deformation shapes was brought by the high work hardening rate in the UFG-MP steels.

Finally, stamping and spot-welding performances of the UFG-MP steels, which are important in manufacturing of automobile body structures, were evaluated. It was shown that the UFG-MP steels had superior deep-drawability compared with the conventional UHSS. This result was brought by the high work hardening rate (*n*-value) as well as the large uniform elongation. In spot-welding experiments, it was revealed that quality of the nuggets and tensile shear strength were almost the same as those in the conventional UHSS, as far as the optimum welding condition was taken. Consequently, the UFG-MP steels showed superior performances in stamping and dynamic collapse, without decreasing spot-weld strength. It was confirmed that the UFG-MP steels are the promising material that can contribute to the further weight reduction of automobile body structures.

5.7 References

[1] H. Takechi, JOM 60 No. 12 (2008) 22.
[2] World Steel Association, Advanced High Strength Steel (AHSS) Application Guidelines Version 4.1. 2009. Available from: http://www.worldautosteel.org [Accessed 14 October 2011].
[3] National Agency for Automotive Safety & Victim's Aid (NASVA), Available from: http://www.nasva.go.jp [Accessed 2 November 2011].
[4] N. Fujita, T. Nonaka, T. Tomokiyo, H. Taniguchi, K. Goto, K. Yamazaki, SAE Technical Paper 2007-01-0341, SAE International, Warrendale, 2007.
[5] R. Z. Mallen, J. Odell, B. O'Hara, SAE Technical Paper 2009-01-0088, SAE International, Warrendale, 2009.
[6] D. W. Fan, B. C. De Cooman, ISIJ Int. 50 (2010) 1713.
[7] B. Lüdke, M. Pfestorf, in: S. Hashimoto, S. Jansto, H. Mohrbacher, F. Siciliano (Eds.), International Symposium on Niobium Microalloyed Sheet Steel for Automotive Applications. TMS, Warrendale, 2006, pp. 27.
[8] R. Sohmshetty, K. Malella, O. Faruque, P. Geck, SAE Technical Paper, 2006-01-1587, SAE International, Warrendale, 2006.
[9] M. S. Walp. SAE Technical Paper 2007-01-0342, SAE International, Warrendale, 2007.
[10] A. Otubushin, Int. J. Impact Eng. 21 (1998) 349.
[11] S. Simunovic, P. Kumar, V. Nukala, J. Fekete, D. Meuleman, M. Milititsky, SAE Technical Paper 2003-01-1383, SAE International, Warrendale, 2003.
[12] K. Sato, A. Yoshitake, Y. Hosoya, T. Yokoyama, SAE Technical Paper, 1997-20-0115, SAE International, Warrendale, 1997.
[13] T. Wierzbicki, W. Abramowicz, J. Appl. Mech. 50 (1983) 727.
[14] M. D. White, N. Jones, Int. J. Mech. Sci. 41 (1999) 179.
[15] X. M. Chen, M. F. Shi, G. Chen, M. Kamura, K. Watanabe, Y. Omiya, SAE Technical Paper 2005-01-0354, SAE International, Warrendale, 2005.
[16] H. F. Mahmood, A. Paluszny, SAE Technical Paper, 811302, SAE International, Warrendale, 1981.
[17] S. R. Reid, T. Y. Reddy, M. D. Gray, Int. J. Mech. Sci. 28 (1986) 295.
[18] M. Takahashi, A. Uenishi, H. Yoshida, Y. Kuriyama, SAE Technical Paper 2003-01-2765, SAE International, Warrendale, 2003.
[19] A. Uenishi, Y. Kuriyama, M. Takahashi, Nippon Steel Tech. Rep. 81 (2000) 17.
[20] X. Huang, G. Lu, T. X. Yu, Thin-walled structures 40 (2002) 153.
[21] S. Y. Jin, W. Altenhof, SAE Technical Paper, 2010-01-0380, SAE International, Warrendale, 2010.
[22] H. Takechi, ISIJ Int. 34 (1994) 1.
[23] W. B. Hutchinson, Int. Met. Rev. 29 (1984) 25.
[24] G. Krauss, STEELS Processing, Structure, and Performance, ASM International, Materials Park, 2005, pp. 226.

CHAPTER 6

CONCLUSIONS

In the present study, focusing on ultrafine grained ferrite steels, their fabrication, mechanical properties and application were widely studied. The results obtained in this study are summarized in this chapter.

In Chapter 1, the background of this study was reviewed. First, the increasing demands for improving fuel efficiency of automobiles aiming for reducing greenhouse gases emission were emphasized. Advanced high strength steels (AHSS) are expected to contribute to further weight reduction of automobile bodies, and ultrafine grain refinement is considered as one of the important technologies in next generation of AHSS. Two subjects for applying the ultrafine grain refinement to automobile steels were pointed out. One is improving productivity in fabricating process of bulky ultrafine grained (UFG) metals, which have been generally fabricated by using severe plastic deformation (SPD) processes. The other is optimizing mechanical properties concerning automobile body applications. It was emphasized that the properties required for future steels for automobile body structures are dynamic deformation properties (e.g. crash worthiness) and adequate balance of strength and elongation. Finally, the method for evaluating crash worthiness, i.e. dynamic collapse, which was applied in this thesis was introduced.

In Chapter 2, a new route to fabricate UFG ferritic steels without severe plastic deformation (SPD) was proposed. Fully-annealed UFG ferrite microstructures were successfully obtained by applying the new process composed of conventional cold-rolling and annealing procedure. The feature of the process was the rolling of duplex microstructures composed of ferrite and martensite, and the key factor was strain distribution between soft ferrite matrix and hard martensite during rolling. First, the concept of this process was introduced, and the UFG ferrite formation behavior was investigated and discussed. It was suggested that the UFG ferrite formed by continuous coarsening of the very fine regions having various orientations in the deformed microstructure. Secondly, the effects of process conditions on UFG ferrite formation were investigated. It was revealed that the higher cold-rolling reduction and lower annealing temperature was favorable to obtain finer ferrite microstructures. It was also shown that the refinement of microstructure before cold-rolling was effective to reduce the necessary cold-rolling reduction. Finally, the optimum martensite volume fraction in the starting microstructures to obtain uniform UFG ferrite microstructures was clarified to be 40 to 65 %.

In Chapter 3, quasi-static and dynamic tensile properties of the fabricated UFG-FC and UFG-IF steels as well as conventional sheet steels were shown and discussed. The conventional strengthening ways by solid solution, precipitation, and introduction of hard phases significantly decreased $\Delta\sigma$ (difference in flow stress between dynamic and

quasi-static strain rates) in steels. On the other hand, the UFG-FC and UFG-IF steels showed higher $\Delta\sigma$ compared with conventional HSS. It was indicated that grain refinement of ferrite is a good way to strengthen steels, which does not decrease the $\Delta\sigma$ so much. However, it was revealed that the ultrafine grain refinement of ferrite-cementite microstructures significantly decreased uniform elongation, which might result in poor stamping formability of the steels in fabricating automobile parts. This was due to the lack of work hardening in the sub-micrometer ferrite single-phase microstructure.

In Chapter 4, attempts to improve ductility of the UFG ferrite microstructures were made. An introduction of hard second phases into ultrafine ferrite matrix was considered. For suppressing grain growth of ferrite matrix, transformation temperatures of the steels were decreased by Mn addition, therefore the necessary intercritical annealing temperature could be decreased. Based on this concept, the UFG-MP microstructures having both ultrafine ferrite matrix and hard second phases were successfully obtained through the process proposed in this thesis. The fabricated UFG-MP steels showed superior strength-ductility balance, which was brought by high work hardening rate in the microstructures. Deformation induced martensite transformation of retained austenite in the UFG-MP steel was directly observed by *in-situ* neutron diffraction, and it was concluded that the deformation induced martensite contributed to improve the work hardening rate. It was shown that work hardening rate was kept high up to high tensile strains when the stability of retained austenite against straining was high. In addition, it was shown that the microstructural refinement improved the work hardening rate of the UFG-MP steels compared with coarse-grained MP microstructures. It was suggested that the ultrafine grain refinement of ferrite matrix as well as the refinement of retained austenite contributed to the improvement of work hardening rate. Finally, it was confirmed that strength-ductility balance of the UFG-MP steels existed within the target area for the third generation AHSS, indicating that the UFG-MP steels are one of the important candidates for the next generation AHSS.

In Chapter 5, performances of the UFG steels as automobile body parts were shown and discussed. First, crash worthiness of the UFG-FC and UFG-MP steels were investigated and discussed in detail. In the UFG-FC steels, due to the high $\Delta\sigma$ of the UFG-FC steels, higher energy absorption in dynamic collapse compared with conventional steels having equivalent quasi-static strength was achieved. This result might contribute to further weight reduction by reducing the thickness of the steel applied to automobile body structures. However, the UFG-FC steels could not satisfy the demands for very high strength such as UHSS (ultrahigh strength steels). In addition, the poor uniform elongation in the UFG-FC steels should be improved when considering stamping processes for fabricating body parts. The UFG-MP steels were expected to satisfy such demands. In axial collapse experiments, it was shown that stable “compact-mode” deformation, which was not achieved in conventional UHSS, was obtained in the UFG-MP steels. The improved deformation configuration also improved the efficiency of energy absorption in axial collapse. It was clarified that the UFG-MP steels having very high strength as those in UHSS could be applied to crushable parts.

Finally, stamping and spot-welding performances of the UFG-MP steels were

evaluated. It was shown that the UFG-MP steels had superior deep-drawability compared with conventional UHSS. For spot-weldability, it was revealed that the quality of the nuggets and the tensile shear strength of the UFG-MP steels were almost the same as those of conventional 1180 steel, as far as the optimum welding condition was taken. Consequently, the UFG-MP steels showed superior performances in stamping deformation and dynamic collapse without decreasing spot-weld strength.

In this thesis, fabrication of the UFG sheet steels with high productivity, their mechanical properties at dynamic strain rates, improvement of mechanical properties and performances as automobile body parts were systematically investigated and discussed. It was confirmed that the UFG-MP steels are the promising material, which can contribute to the further weight reduction of automobile body structures. Finally, it is expected that the research in the UFG steels would progress furthermore in both academic and engineering aspects, and could contribute to the further weight reduction of automobiles and the decrease of greenhouse gasses emission.

ACKNOWLEDGEMENTS

On finalizing this thesis, I would thank all the people who have supported me.

This research was carried out in collaboration with Prof. Nobuhiro Tsuji of Kyoto University. I would thank Prof. Tsuji for fruitful discussions throughout this research, and great support and supervision during the preparation of this thesis.

Prof. Shojiro Ochiai, Prof. Haruyuki Inui, Prof. Akira Sakai and Prof. Isao Tanaka of Kyoto University are preferentially acknowledged for useful advises which improved this thesis.

Important parts of this study were carried out with Dr. Naoki Takata of Tokyo Institute of Technology. The study on the mechanisms of the microstructure formation and dynamic deformation in the UFG steels were not achieved without this collaboration. I would thank Dr. Takata for his helps and useful discussions.

The neutron diffraction experiments were carried out at J-PARC (Japan Proton Accelerator Research Complex). Prof. Yo Tomota of Ibaraki University, Dr. Stefanus Harjo of J-PARC, and the researchers in Tomota laboratory in Ibaraki University are to be gratefully acknowledged for the operation of the experiments and fruitful discussions.

During the period when the research equipments in our company were shut down after the great east-Japan earthquake, I have got great helps in the operation of some experiments. I am grateful to Prof. Rintaro Ueji of Kagawa University for help in dynamic tensile tests and useful discussions. Dr. Daisuke Terada of Kyoto University is also gratefully acknowledged for help in EBSD measurement as well as useful discussions.

I would thank Dr. Yoshiaki Nakazawa of Sumitomo Metal Industries, LTD. for useful discussions on the results of FEM analysis.

This study cannot be completed without helps by the colleagues in Honda R&D Co., Ltd. I would thank Mr. Tadashi Naito for FEM simulation, Mr. Naoki Takaki, Mr. Tomoaki Sugiura and Ms. Yumiko Sawada for helps in the experiments for materials evaluation.

Finally, I am grateful to my wife and daughter for their patience and encouragement during the preparation of this thesis.

PUBLICATION LIST

JOURNAL PAPER

[1] Y. Okitsu, N. Takata and N. Tsuji, “Mechanical properties of ultrafine grained ferritic steel sheets fabricated by rolling and annealing of duplex microstructure”. Journal of Material Science, 43 (2008) pp. 7391-7396.

[2] Y. Okitsu, N. Takata and N. Tsuji, “A new route to fabricate ultrafine grained structures in carbon steels without severe plastic deformation”. Scripta Materialia, 60 (2009) pp. 76-79.

[3] Y. Okitsu, T. Naito, N. Takaki, T. Sugiura and N. Tsuji, “Mechanical Properties and Crash Worthiness of Ultrafine Grained Multi-Phase Steel Sheets for Automotive Body Applications”. SAE International Journal of Materials and Manufacturing, 3 (2010) pp. 237-245.

[4] Y. Okitsu, N. Takata and N. Tsuji, “Dynamic deformation behavior of ultrafine grained iron produced by ultrahigh strain deformation and annealing”, Scripta Materialia, 64 (2011) pp. 896-899.

[5] N. Takata, Y. Okitsu and N. Tsuji, Dynamic deformation behavior of ultrafine grained aluminum produced by ARB and subsequent annealing. Journal of Material Science, 43 (2008) pp. 7385-7390.

[6] K. Asoo, Y. Tomota, S. Harjo and Y. Okitsu, “Tensile Behavior of a TRIP-aided Ultra-fine Grained Steel Studied by Neutron Diffraction”, ISIJ International, 51 (2011) pp. 145-150.

BOOKS CHAPTER

[1] Y. Okitsu, T. Naito and N. Tsuji, “Two Concepts to Improve Crash Worthiness of Hat Columns by Applying Ultrafine Grained Steel Sheets”. in: M. F. Kody (Ed.) Automobiles: Performance, Safety Assessment and Energy Consumption. Nova Science Publishers, Inc., New York, 2010.

[2] Y. Okitsu and N. Tsuji, “Applying nanostructured steel sheets to automotive body structures”. in: S. H. Whang (Ed.) Nanostructured Metals and Alloys: Processing, Microstructure and Mechanical Properties. Woodhead Publishing, London, 2011.

[3] Y. Okitsu and N. Tsuji, “Nanostructured steel for automotive body structures”. in: J. Rowe (Ed.) Advanced materials in automotive engineering. Woodhead Publishing, London, 2012.

CONFERENCE PROCEEDINGS (INTERNATIONAL)

[1] Y. Okitsu, N. Takata and N. Tsuji, “Ultrafine grained multi-phase steel with high strength and high ductility fabricated by rolling and annealing of duplex microstructure”. in: Proceedings of International Symposium on Giant Straining Process for Advanced Materials (GSAM-2008), Fukoka, 2008, pp. 19.

[2] Y. Okitsu and N. Tsuji, “Mechanical Properties of Ultrafine Grained Multi-Phase Steel Sheets Aiming for Automobile Body Applications”. in: Proceedings of the 2nd International Symposium on Steel Science (ISSS 2009), Kyoto, 2009, pp. 253.

[3] Y. Okitsu, T. Naito, N. Takaki, T. Sugiura and N. Tsuji, “Mechanical Properties and Crash Worthiness of Ultrafine Grained Multi-Phase Steel Sheets for Automotive Body Applications”. SAE Technical Paper, 2010-01-0438, SAE World Congress, Detroit, 2010.

CONFERENCE PROCEEDINGS (DOMESTIC)

[1] Y. Okitsu, N. Takata, N. Tsuji and H. Kitahara, “Dynamic Deformation Behavior of Ultra-Fine Grained IF steel”. in: Proceedings of JIM annual meeting (2007) / CAMP-ISIJ 20 (2007) p.596. (In Japanese).

[2] Y. Okitsu, N. Takata and N. Tsuji, “Dynamic Deformation Behavior of Ultra-Fine Grained Ferrite-cementite steel”. in: Proceedings of JIM annual meeting (2007) / CAMP-ISIJ 20 (2007) p.597. (In Japanese).

[3] N. Takata, Y. Okitsu and N. Tsuji, “Dynamic Deformation Behavior of Ultra-Fine Grained Aluminium”. in: Proceedings of JIM annual meeting (2007) / CAMP-ISIJ 20 (2007) p.597. (In Japanese).

[4] Y. Okitsu, N. Takata and N. Tsuji, “Mechanical Properties of Ultrafine Grained Ferritic Steel Sheets Fabricated by a New Process without Severe Plastic Deformation”. in: CAMP-ISIJ 20 (2007) p.1389. (In Japanese).

[5] Y. Okitsu, N. Takata and N. Tsuji, “Dynamic Collapse Property of Ultrafine Grained Ferritic Steel Sheets”. in: Proceedings of JIM annual meeting (2007) / CAMP-ISIJ 20 (2007) p.1390. (In Japanese).

[6] Y. Okitsu, N. Tsuji and N. Takata: “Mechanical Properties of Ultrafine Grained Dual-Phase Steel Sheets Fabricated by a New Process without Severe Plastic Deformation (Study on Nano-DP steel -1)”. in: CAMP-ISIJ 21 (2008) p. 706. (In Japanese).

[7] A. Narui, Y. Tomota and Y. Okitsu, “Deformation Analysis of Ultrafine Grained TRIP Dual-Phase Steel by In Situ Neutron Diffraction (Study on Nano-DP steel -2)”. in: CAMP-ISIJ 21 (2008) p. 707. (In Japanese).

[8] Y. Okitsu, N. Takata and N. Tsuji, “Mechanical Properties and Dynamic Collapse Properties of Low-C Ultrafine Grained Multi-Phase Steel Sheets

(Study on Nano-DP steel -3)". in: CAMP-ISIJ 21 (2008) p. 521 (In Japanese).

[9] N. Takaki, Y. Okitsu, H. Fujii and N. Tsuji, "Microstructures of Friction Stir Welded High-C Ultrafine Grained Multi-Phase Steel Sheets". in: CAMP-ISIJ 22 vol.1 (2009) J-22 (In Japanese).

[10] Y. Okitsu, T. Sugiura, N. Takaki and N. Tsuji, "Effect of Mn Addition on Mechanical Properties of Ultrafine Grained Multi-Phase Steel Sheets (Study on Nano-DP steel -4)". in: CAMP-ISIJ 22 vol.2 (2009) J-32 (In Japanese).

[11] N. Takaki, Y. Okitsu and H. Fujii, "Dynamic Collapse Properties of Friction Stir Welded High-C Ultrafine Grained Multi-Phase Steel Sheets". in: CAMP-ISIJ 22 vol.2 (2009) J-33 (In Japanese).

LECTURE

[1] Y. Okitsu, "Potential of Ultrafine Grained Steel Sheets as Automobile Materials" in: JIM seminar "Bulk Nanostructured Metals - New Potential for Structural Metallic Materials', Tokyo, 2011, p.49. (In Japanese).

AWARD

[1] "SAE/AISI 2010 Sydney H. Melbourne Award for Excellence in the Advancement of Automotive Sheet Steel" for SAE Technical Paper 2010-01-0438 by Y. Okitsu, T. Naito, N. Takaki, T. Sugiura and N. Tsuji. (Apr. 2011).